

**PREDICTION METHODS FOR NEAR FIELD
NOISE ENVIRONMENTS OF VTOL AIRCRAFT**

*L. C. SUTHERLAND
D. BROWN*

Distribution limited to U. S. Government agencies only; test and evaluation, statement applied 24 March 1972. Other requests for this document must be referred to AF Flight Dynamics Laboratory (FY), Wright-Patterson AFB, Ohio 45433.

FOREWORD

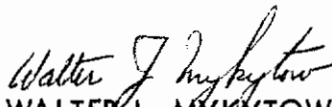
The research described in this report was conducted by the Research Staff of Wyle Laboratories, El Segundo, California for the Aero-Acoustics Branch, Vehicle Dynamics Division, Air Force Flight Dynamics Laboratory, Wright-Patterson Air Force Base, Ohio, under Contract F33615-69-C-1407. The work was directed under Project 1471, "Aero-Acoustic Problems in Air Force Flight Vehicles," Task 147102, "Prediction and Control of Noise Associated with USAF Flight Vehicles." Mr. D. L. Smith of the Aero-Acoustics Branch was the Project Engineer.

The analysis of VTOL jet noise was carried out by L. C. Sutherland. The propeller noise prediction method was developed by D. Brown. The authors wish to extend their appreciation to R. Potter and V. Mason, who assisted during initial stages of the VTOL jet noise study, J. B. Ollerhead, who conducted the initial development of the rotating-blade noise study, C. L. Munch, who conducted the computer programming and experimental propeller noise investigations, and Mrs. M. Brisbin, who typed the manuscript.

This report covers work performed from February 1969 to October 1971. Wyle Laboratories Report Number is WR 71-19.

Manuscript was released by the authors on 1 November 1971 for publication as an AFFDL Technical Report.

This Technical Report has been reviewed and is approved.


WALTER J. MYKYTOW
Assist. for Research and Technology
Vehicle Dynamics Division

ABSTRACT

The objective of this report is to establish a consistent set of first-generation prediction methods which may be used to estimate near field noise levels for jet-powered and rotor/propeller-powered VTOL aircraft operating in close proximity to the ground. The methods provided utilize available theory, where appropriate, augmented extensively by experimental data which was available or which was developed during preparation of this report.

For jet-powered VTOL aircraft, the principal sources of near field noise are the direct and ground-reflected noise of the jet exhaust, the aerodynamic noise from the wall jet formed by the deflected exhaust flow and the noise of the impinging jet. These principal sources are analyzed in detail and several of their basic characteristics for VTOL jet noise are established. Emphasis is placed on the change in acoustic power and near field levels due to their combined effect. The general nature of the deflected flow and other potential sources of noise are also considered. A prediction method for near field noise of VTOL jets is then developed in the form of additive corrections to apply to near field levels for the undeflected jet. These corrections have a maximum value of about 15 to 20 dB near resonance frequencies of vehicle skin panels.

The near field sound pressures for rotor/propeller systems are examined by reference to data on full scale propellers and by detailed measurements obtained from small model propeller tests. A data correlation, based on thrust per blade, blade tip speed and rotor diameter, is made which allows estimation of the harmonic pressures within one diameter of the rotor center over a tip speed range of $0.2 \leq M_t \leq 1.0$. Directivity patterns are derived from rotating point source theory and are shown to provide good correlation with test data in regions away from the rotor plane. Suitable corrections are made for the near plane regions.

The final near field noise prediction methods developed under this study are presented in Section VI. These were developed to allow a preliminary analysis of near field environments of VTOL aircraft using a simplified procedure suitable for manual calculations.

The experimental effort carried out in support of this report consisted of extensive noise measurements in the near field of a model propeller (Appendix B) and a subsonic jet in a free and vertical deflected configuration (Appendix C). Ground reflection correction factors for a simple source are tabulated in Appendix D along with the computer program listing.

Contrails

TABLE OF CONTENTS

	<u>Page</u>
I. INTRODUCTION	1
1. VTOL Propulsion Systems and General Noise Characteristics	2
2. Organization of Report	6
II. CRITERIA FOR PREDICTION OF ACOUSTIC LOADS ON VTOL STRUCTURE	8
1. Introduction	8
2. Criteria for Analytical Prediction Methods	8
3. Criteria for Experimental Methods	11
4. Criteria for Frequency Range of Primary Importance	11
III. NEAR FIELD NOISE FOR JET-POWERED VTOL AIRCRAFT – A REVIEW OF THE STATE-OF-THE-ART	14
1. Noise Sources	14
2. Flow Properties of a Deflected Jet	14
a. Mean Flow – Subsonic Jet	14
b. Mean Flow – Supersonic Jet	24
c. Turbulent Flow in a Wall Jet	34
d. Summary of Wall Jet Flow Characteristics	36
3. Jet Noise	38
a. Acoustic Power of VTOL Jets	39
b. Acoustic Power of Free Jets	44
c. Jet Density Effects	48
d. Excess Acoustic Power of VTOL Jets	49
e. Acoustic Power Spectra of VTOL Jets	51
f. Directivity of VTOL Jets	53
4. Ground Reflection Effects for VTOL Jets	58
a. Effect of Wall Jet on Ground Reflection	72
b. Ground Reflection for Propeller Noise	76
c. Effect of Ground Plane on Radiation Efficiency	76

TABLE OF CONTENTS (Continued)

	<u>Page</u>
5. Comparison of Predicted Ground Reflection for VTOL Jets with Experimental Data	78
6. Other Noise Sources of VTOL Jets	92
a. Radiation from Impingement Area	94
b. Direct Radiation by Wall Jet	97
c. Vortex Noise from Deflector Vanes	100
d. Discrete Ring Tones	101
e. Shock-Turbulence Interaction Noise	105
f. Buffeting Noise	105
7. Development of a Prediction Model	107
a. Qualitative Review of Source Predictions	107
b. Contour Summation Method	108
c. Total Sound Field Contour Method	109
d. The Δ Method	109
e. Development of the Δ Method	110
f. Comparison of Predictions with Full Scale Data	115
IV. NEAR FIELD NOISE OF PROPELLER SYSTEMS	120
1. Free Rotors and Propellers	120
a. Review of Propeller Noise Prediction Methods	120
b. Comparison with Experimental Data	127
2. Ducted Fans	135
a. Review of Theory	135
b. Comparison with Experimental Data	144
V. NOISE REDUCTION CONCEPTS FOR VTOL AIRCRAFT	146
1. Jet Noise Reduction	146
2. Fan Noise Reduction	148
3. Rotor or Propeller Noise Reduction	150

TABLE OF CONTENTS (Concluded)

	<u>Page</u>
VI. NEAR FIELD NOISE PREDICTION METHODS	152
1. Prediction of VTOL Jet Near Field Noise Levels	152
a. Sound Pressure Levels for the Undelected Jet	153
b. Sound Pressure Levels for the VTOL Jet	157
2. Prediction of Propeller/Rotor Near Field Noise Levels	162
a. Free Propellers	162
b. Corrections for Ducted Systems	167
VII CONCLUSIONS	170
1. Prediction Methods for Jet-Type Propulsion Systems	170
2. Prediction Methods for Propeller-Type Propulsion Systems	171
REFERENCES	172
APPENDIX A SUMMARY OF REPRESENTATIVE VTOL AIRCRAFT (CURRENT OR PROPOSED)	180
APPENDIX B PROPELLER NEAR FIELD NOISE EXPERIMENTS	181
APPENDIX C SUMMARY OF EXPERIMENTAL STUDY OF MEAN FLOW PROPERTIES AND NOISE GENERATION BY SIMULATED VTOL JET	192
APPENDIX D TABLES AND COMPUTER PROGRAM FOR REFLECTION OF OCTAVE BANDS OF WHITE NOISE FROM A RIGID REFLECTING PLANE	212

LIST OF ILLUSTRATIONS

<u>Figure</u>		<u>Page</u>
1.	Family of Possible Propulsion Systems for VTOL Aircraft	3
2.	Approximate Trend in Overall Sound Power Level or Maximum Far Field Sound Level for Various Propulsion Systems at Constant Thrust (Adopted from Reference 1).	4
3.	Conceptual Illustration of Representative VTOL Aircraft Configurations.	9
4.	Trend in Normalized Octave Band Stress Levels Measured on XV-4B Hummingbird Aircraft During VTOL and CTOL Operation (Data from Reference 5).	12
5.	Conceptual Illustration of Potential Noise Sources for Jet-Powered VTOL Aircraft.	16
6.	Geometry and Flow Parameters for Radial Wall Jet	17
7.	Comparison of Theory and Experimental Data for Exponent (a) for Decay of Maximum Radial Velocity in Turbulent Radial Wall Jet where $U_{\max} \sim R^a$.	19
8.	Idealized Model for Radial Velocity Decay and Growth of Thickness of Wall Jet.	20
9.	Variation in Length of Potential Core with Exit Mach No.	23
10.	Measured Variation in Maximum Radial Velocity at 0°, 90° and 180° Azimuth Angles for Jet at 70° Incidence Compared to Radial Velocity for 90° Incidence (Data from Appendix C).	25
11.	Change in Mach Number and Velocity Across Normal Shock Wave	28
12.	Supersonic Length vs Exit Mach Number Compared to Potential Core Length	29
13.	Comparison of Observed Decay in Axial Velocity for Subsonic Jets with Experimental Data for Supersonic Jets. (Data Points Calculated from Experimental Data in Reference 17 for $M_E = 1.4 - 3.5$ and $M_c < 1$).	31

LIST OF ILLUSTRATIONS (Continued)

<u>Figure</u>		<u>Page</u>
14.	Estimated Initial Radial Velocity of Wall Jet Relative to Jet Exit Velocity as a Function of Nozzle Elevation and Exit Mach Number for Supersonic Jet. D_E = Fully Expanded Jet Diameter.	33
15.	Fluctuating Pressures on Ground Under a Vertical and Grazing Subsonic Air Jet (Data from Reference 12).	35
16.	Relative Octave Band Levels for Pressure Fluctuations under Wall Jet.	37
17.	Overall Power Level Per Unit Nozzle Area (A_e) for VTOL Model and Full Scale Jets Versus Nozzle Elevation.	41
18.	Normalized Axial Distribution of Measured Sound Power in Sonic and Supersonic Jets. (Area Under Each Curve is Unity.)	43
19.	Calculated and Observed Change With Nozzle Elevation in Overall Power Level for VTOL Jets. Calculated Change Based on Integration of Power Distribution in Figure 18.	45
20.	Overall Power Level per Unit Exit Area versus Exit Velocity.	46
21.	Summary Comparison of Normalized Sound Power for Free Sonic or Subsonic Jets (Closed Symbols) and Excess Power for VTOL Jets (Open Symbols) at Nozzle Elevations of 0.5 (/ Flag) 1.0 (No Flag) or 1.5-2 (\ Flag) Core Lengths. (Basic Symbol Code Same as in Figures 17 and 19.)	50
22.	Relative Octave Band Power Level Spectra for the Free Jet Configurations. [D_E = Fully Expanded Nozzle Diameter, U_e = Fully Expanded Jet Velocity, c^* = Speed of Sound at Throat of Nozzle, c_o = Ambient Speed of Sound, after Eldred].	52
23.	Normalized Octave Band Power Level Spectra for Subsonic Free and Deflected Ambient Air Jets. ($M_E = 0.85$.)	54
24.	Normalized Octave Band Power Level Spectra for Free and Deflected Ambient Air Jets ($M_E = 0.6$).	55

LIST OF ILLUSTRATIONS (Continued)

<u>Figure</u>		<u>Page</u>
25.	Normalized Octave Band Power Level Spectra for Supersonic Free (Closed Symbol) and Deflected (Open Symbol) Ambient Jet and Rocket at Various Nozzle Elevations.	56
26.	Directivity Index Measured at Radius of 24 Nozzle Diameters from Exit of Free (Closed Symbols) and Deflected (VTOL) Jet (Open Symbols) at 9 to 10, 5 to 6 and 2 to 3 Diameters Elevation.	57
27.	Typical Directivity of Overall Sound Level for Ambient Air Jets, Turbojets and Rockets.	59
28.	Simplified Model for Ground Reflection of VTOL Jets Illustrated by Contours of Direct, Reflected and Combined Field. Reflected Field Simulated by Image Jet Source as Illustrated by Insert.	60
29.	Comparison of Experimental Directivity Data for Ambient and Heated Jets with Semi-Empirical Prediction.	65
30.	Change in Octave Band Level Due to Reflection from Rigid Plane for Monopole Source. λ = Wavelength at Center Frequency of Band of White Noise.	66
31.	Change in Octave Band Level Due to Reflection from Rigid Plane for "Point" Source with Directivity of an Ambient Air Jet. λ = Wavelength at Center Frequency of Band of White Noise.	68
32.	Change in Octave Band Level Due to Reflection by Rigid Plane for Point Source with Directivity of a Turbojet. λ = Wavelength at Center Frequency of Band of White Noise.	70
33.	Contours of Computed Octave Band Levels for Point Source Simulating a VTOL Jet. Space Average Octave Band Level = 100 dB at Radius = H' , λ = Wavelength at Center Frequency of Band of White Noise.	71
34.	Model for Reflection of Plane Waves by Wall Jet Flow over a Rigid Ground Plane.	73

LIST OF ILLUSTRATIONS (Continued)

<u>Figure</u>		<u>Page</u>
35.	Separation of Reflection from Flow Interface into Three Regions. For Uppermost Region, Angle of Incidence Exceeds the Critical Angle Defined by Equation 31. At Upper Boundary of Lower Region, Reflection is Zero and $M = (1 - \tan \alpha)/\sin \alpha$. (From Reference 57.)	75
36.	Illustration of Typical Possible Shift in Lateral Position of Reflected Rays from VTOL Jet Due to Wall Jet Flow. Δy is Positive for Ray P_1 and Negative for Ray P_2 Relative to Reflected Ray (Dashed Line) in Absence of Wall Jet.	77
37.	Contours of Constant Octave Band Sound Level for Free Ambient Air Jet (from Appendix C).	79
38.	Contours of Constant Octave Band Sound Level for VTOL Ambient Air Jet (from Appendix C).	80
39.	Comparison of Estimated (Dashed Lines) and Measured (Solid Lines) Contours of Octave Band Sound Level at 4000 Hz for Mach 1 Ambient Air VTOL Jet at 6 Nozzle Diameters Elevation and 10° Offset from Vertical. (From Appendix C.)	81
40.	Change with Nozzle Height in Position of Near Field Contours (a, b) and Overall Sound Level (c) for Mach 1.88 VTOL Air Jet (Data from Reference 37).	83
41.	Change in Octave Band Level Forward of Exit for Cold and Hot Model VTOL Jet Relative to Free Field Level - $H/D = \infty$ (Data from Reference 4).	84
42.	Summary of Model Data on Change in Octave Band Sound Level for VTOL Jet Relative to Level for Free (Undeflected) Jet. (See Legend at End of Figure.)	85
43.	Variation in Δ (Change in Near Field Octave Band Levels Re Free Jet) in 4000 Hz Octave Band for 3 Different Mach Numbers. (Data from Appendix C.)	89

LIST OF ILLUSTRATIONS (Continued)

<u>Figure</u>		<u>Page</u>
44.	Variation Over Near Field Region of Maximum Value of Δ at 4000 Hz. (For Mach 1 Ambient Air Jet, $fD/U_e = 0.24$ - Data from Appendix C.)	90
45.	Change in Octave Band Power Levels and Near Field Octave Band Levels Relative to Free (Undelected) Jet for VTOL Ambient Air Jet at 6 Nozzle Diameters Elevation. (Δ for Mach 1, \circ for Mach 0.85, \square for Mach 0.6 - Data from Appendix C.)	91
46.	Envelope of Maximum Value of Change in Octave Band Levels for Model VTOL Jet Relative to Levels for Free Jet. (Δ for Mach 1, \circ for Mach 0.85 and \square for Mach 0.6 - Data from Appendix C.)	93
47.	Simplified Illustration of Growth in Total Acoustic Power (W_a) Generated by Primary Jet and by Wall Jet as Nozzle Elevation Increases. (Based on Idealized Versions of Power per Unit Length, Figure 18, Velocity Decay of Wall Jet, Figure 8, and Wall Jet Velocity for Supersonic Jet, Figure 14, and Assuming Acoustic Power Proportional to U^8 in all Cases.)	99
48.	Typical One-Third Octave Band Spectrum Measured with and without Ring Tone Present. Exit Mach No. = 1.0, Exit Velocity = 1045 ft/sec., Exit Diameter = 0.75 in.	103
49.	Typical Example of One-Third Octave Band Levels vs Angle to Exhaust of VTOL Jet with Ring Tone (Solid Lines) and with Ring Tone Suppressed (Dashed Lines). $M_E = 1.0$, $U_e = 1045$ ft/sec, $H/D = 6$, $D = 0.75$ in., Radius from Jet Exit, $R/D = 34$.	104
50.	Illustration of Typical Sources of Buffeting on VTOL Aircraft Structure from Recirculation or Upflow from Jet Exhaust (from Reference 9).	106
51.	Illustration of Effect of Correcting Measured Octave Band Level Contours for Ground Reflection ("Measured" Contour from Reference 36).	111

LIST OF ILLUSTRATIONS (Continued)

<u>Figure</u>		<u>Page</u>
52.	Adjusted Values for Δ from the Ambient Air Model Tests in Appendix C.	113
53.	Nozzle Configuration and Test Point Location for the Full Scale Measurements on a P1127 VTOL Aircraft (from Reference 43).	116
54.	Comparison of Measured and Predicted Octave Band Levels on P1127 VTOL Aircraft at 92.5% Power and 9.7 Nozzle Diameter Elevation (Measured Data from Reference 43).	117
55. (a)	Measured Variation in Overall Sound Pressure Level with Total Engine Thrust for Noise Measurements Made on P1127 VTOL Aircraft at 9.7 Nozzle Diameter Elevation (Data from Reference 43, Measurement Locations Shown in Figure 53).	118
55. (b)	Comparison of Measured and Calculated Octave Band Power Levels for P1127 VTOL Aircraft (Measured Data from Reference 43. Predicted Levels Based on Reference 49 for Free Jet Noise Power of Bypass and Primary Exhaust Streams.	119
56.	Spatial Coordinate System for Rotor Noise Calculations	122
57.	Comparison of Theory and Experiment for First Two Harmonics of 2 and 3 Bladed Model Propellers ($R/D = 0.55$, $D = 0.75$ feet, Data from Appendix B).	125
58.	Effect of Distance From Effective Source on Propeller Noise First Harmonic Levels.	130
59.	Dependence of the In-Plane Near Field Corrected First Harmonic Levels L_T and L_D , on Tip Mach Numbers.	131
60.	Decay of Propeller Noise Harmonics at Different Tip Speeds and Near Field Radii (In-Plane Levels).	133
61.	Harmonic Level Decay with Normalized Field Radius as a Function of Harmonic Number.	134
62.	Effects of Thrust/Drag Ratio and Blade Velocity on Propeller Noise Directivity (Theory).	136

LIST OF ILLUSTRATIONS (Continued)

<u>Figure</u>		<u>Page</u>
63.	Directionality Corrections for mB Harmonics (r/D Constant)	138
64.	Comparison of Measured and Theoretical Decay of Harmonic Sound Levels in a Propeller Duct (from Reference 84).	141
65.	Typical Example of Maximum Octave Band Sound Levels at 1000 ft Slant Range (Normalized to 10,000 lb Thrust) During Takeoff of Current Commercial Aircraft with Turbojet and Turbofan Engines. (From References 88 and 89.)	147
66.	Illustration of Typical Attenuation of Fan Noise Source Achieved by Duct Lining (Reference 90).	149
67.	Current Design Approaches to Helicopter Noise Reduction (Reference 93).	151
68.	Demonstrated Noise Reduction of a Heavy-Helicopter Twin-Rotor System for Hover and Two Flight Speeds (Reference 94).	151
69.	Contours of Octave Band Sound Pressure Level in dB re $20\mu\text{N/m}^2$ for Free Jet with Exit Velocity of 1930 ft/sec and Exit Mach Number of 1.13 (Adopted from Reference 36 with Corrections for Ground Reflection).	154
70.	Contours of Overall Sound Pressure Level in dB re: $20\mu\text{N/m}^2$ for Same Jet as in Figure 69 at Two Power Settings (from Reference 36).	156
71.	Δ_{max} , Maximum Change in Near Field Octave Band Sound Pressure Levels for VTOL Jets Relative to Levels for Undelected Jets.	159
72.	Change in Δ Relative to its Maximum Value for Near Field of VTOL Jet as a Function of Nozzle Elevation and Normalized Frequency	160
73.	Partial Sound Pressure Level, L_1 , in Terms of Rotor Diameter and Thrust per Blade.	163
74.	Sound Level Correction, $\Delta L^{(1)}$, for Required Observation Radius from Rotor Center, r/D.	165

LIST OF ILLUSTRATIONS (Continued)

<u>Figure</u>		<u>Page</u>
75.	Sound Level Correction, $\Delta L_m^{(2)}$, for Harmonic Order m , in terms of Tip Mach Number M_t , and Observation Radius, r/D .	165
76.	Sound Harmonic Level Correction $\Delta L_{mB}^{(3)}$, ψ for Azimuthal Angle, ψ Degrees, from Rotor Plane. (m = Harmonic Order, B = Blade Numbers).	166
B-1.	Model Propeller Installation (Top View)	182
B-2.	Model Study Instrumentation	183
B-3.	Azimuthal Distributions of Harmonic Sound Pressure Levels Near 9-inch Model Propeller. B = Number of Blades = 2, r/D = Radius in Propeller Diameters = 0.555, N = Rotational Speed, rpm, M_t = Tip Mach No.	186
B-4.	Azimuthal Distributions of Harmonic Sound Pressure Levels Near 9-inch Model Propeller. $B = 2$, $r/D = 0.667$.	187
B-5.	Azimuthal Distributions of Harmonic Sound Pressure Levels Near 9-inch Model Propeller. $B = 2$, $r/D = 0.833$.	188
B-6.	Azimuthal Distributions of Harmonic Sound Pressure Levels Near 9-inch Model Propeller. $B = 2$, $r/D = 1$.	189
B-7.	Azimuthal Distributions of Harmonic Sound Pressure Levels Near 9-inch Model Propeller. $B = 3$, $r/D = 0.555$.	190
B-8.	Azimuthal Distributions of Harmonic Sound Pressure Levels Near 9-inch Model Propeller. $B = 3$, $r/D = 0.667$.	191
C-1.	Decay in Axial Velocity (U_c) of Free Jet or Maximum Radial Velocity (U_{max}) of Simulated VTOL Jet (Mach 0.18, Total Temperature = 100 Degrees F).	194
C-2.	Velocity Profiles Through Free and Deflected Jet	195
C-3.	Variation with Azimuth Angle of Maximum Radial Velocity in Fully Developed Flow Region for Oblique Incidence	198
C-4.	Variation in Dynamic Pressure of Radial Flow Along Radial Line of Symmetry for Wall Jet with Oblique Incidence Jet.	198

LIST OF ILLUSTRATIONS (Continued)

<u>Figure</u>		<u>Page</u>
C-5.	Inverse Square Law Measurements in the Anechoic Room Using Full-Octave Bands of Random Noise.	199
C-6.	Block Diagram of Acoustic Data Acquisition System	200
C-7.	Model Nozzle and Plenum Chamber Assembly Setup to Simulate VTOL Operation.	200
C-8.	Graphic Record of Total Pressure Profile at Exit Plane of Nozzle with Exit Mach Number of 1.0 (data from Reference 95).	202
C-9.	Octave Band Power Level Spectra for Model Jet (from Measurement at 170 Diameter Radius, Reference 95).	203
C-10.	Directivity Pattern for Horizontal Free Jet at 170 Nozzle Diameters (from Reference 95).	204
C-11.	Typical Graphic Record of Angular Variation in Octave Band Level, Horizontal Jet, Mach 0.85, Microphone Radius 13.3 Nozzle Diameters.	205
C-12.	Typical Octave Band Sound Level Contours.	206
C-13.	Contours of Octave Band Sound Pressure Level, dB re $20\mu\text{N}/\text{m}^2$, Mach 1, Free Horizontal Jet.	207
C-14.	Contours of Octave Band Sound Pressure Level, dB re $20\mu\text{N}/\text{m}^2$, Mach 1, VTOL Jet, H/D = 2, Jet Impingment Angle, 80° .	208
C-15.	Contours of Octave Band Sound Pressure Level, dB re $20\mu\text{N}/\text{m}^2$, Mach 1, VTOL Jet (H/D = 4), Jet Impingment Angle = 80° .	209
C-16.	Contours of Octave Band Sound Pressure Level, dB re $20\mu\text{N}/\text{m}^2$, Mach 1, VTOL Jet (H/D = 6), Jet Impingment Angle = 80° .	210
C-17.	Contours of Octave Band Sound Pressure Level, dB re $20\mu\text{N}/\text{m}^2$, Mach 1, VTOL Jet (H/D = 9), Jet Impingment Angle = 80° .	211

LIST OF ILLUSTRATIONS (Continued)

<u>Figure</u>		<u>Page</u>
D-1.	Geometry for Reflection by Rigid Plane of Octave Bands of White Noise from Directional Point Source. Wavelength at Center Frequency of Band = λ .	213

LIST OF TABLES

<u>Table</u>		<u>Page</u>
I.	Synopsis of Potential Acoustic Noise Sources for Jet-Powered VTOL Aircraft.	15
II.	Summary of VTOL Jet Test Data.	40
III.	Measured Values of the Change in Octave Band Level (Δ) Relative to Levels for an Undeflected Jet. $H/D = 6$, $M_E = 1.0$ (From Tests Described in Appendix C).	114
IV.	Summary of Propeller Noise Near Field Experimental Data Cases	129
V.	Cut-Off Values of $(k_{\ell}^{(r)} \cdot R)$ for Duct Sound Transmission (from Reference 80).	143
VI.	Measured Near Field Noise Levels (at $R/D = 1.0$) of a Tip-Turbine Fan (Reference 87).	144
C-1.	Flow Parameters for Model VTOL Tests.	201
D-1.	Change in Octave Band Level Due to Reflection from Rigid Plane for Monopole Source at Elevation H with Wavelength λ at Center Frequency of Band.	218
D-2.	Octave Band Level for Monopole Source of White Noise at Elevation H Above Rigid Plane with Space Average Octave Band Level = 50 dB at Radius = H ($H/\lambda = 100$).	220
D-3.	Listing for Program to Compute Ground Reflection Tables.	221

LIST OF SYMBOLS

a	Velocity decay exponent
A	Correction for ground reflection
A_e	Exit area of jet, ft^2
A_d	Propeller disc area, ft^2
b	Ratio of Δf to f_c
B	Number of blades
c_o	Ambient speed of sound
C	Correlation coefficient
C_v	Velocity correction, dB
d	Rotor-stator separation distance
D	Jet exit diameter
D	Propeller disc diameter
D_E	Fully-expanded jet diameter
D_r	Drag force, lb
$D(\theta)$	Directivity factor at angle θ
E	Energy dissipation of jet
f	Frequency, Hz
f_c	Characteristic frequency, center of band
F	Force
G	Ratio of source height to wavelength
H	Height of nozzle exit above ground
H'	Height of point source above ground
$J_{mB}(x)$	Bessel Function of first kind, of order (mB) and argument x
k	Wave number ($= 2\pi f/c_o$)
K	Constant
l	Tangential acoustic mode number in duct
L	Sound pressure level, or increment, dB

Contrails

m	Harmonic number (integer)
M	Mach number
M_E	Jet exit Mach number
N	Revolutions per minute
p	Acoustic pressure
\tilde{p}	rms acoustic pressure
P	Static pressure
P_H	Shaft horsepower
q	Dynamic pressure
r	Ratio of reflected to direct pressure
r	Observer radius from disc center, ft
r_o	Effective radius of acoustic point source from disc center, ft
R	Radial position in wall jet
R	Distance from source to receiver
R	Duct radius
s	Observer distance from acoustic point source, ft
S	Integer
S_N	Strouhal Number = $f D/U_e$
t	Time
T	Thrust
T_T	Total jet temperature
\tilde{u}	rms fluctuating pressure
U	Mean flow velocity
U_c	Axial jet velocity
U_e	Jet exit velocity
U_{max}	Maximum radial velocity in wall jet
W_a	Acoustic power
$W(X)$	Acoustic power per unit length
x	Vertical cartesian coordinate relative to ground plane

Contrails

X	Axial position on jet axis re exit
X_f	Length of potential core
X_s	Supersonic length
y	Horizontal cartesian coordinate relative to ground plane
Y	Lateral position normal to jet axis
Z	Thickness direction in wall jet
$Z_{1/2}$	Wall jet thickness at $U/U_{\max} = 0.5$

Greek

α	Correction term in directivity factor
α	Angle of incident ray reflected from wall jet
β	Incidence angle of VTOL jet re: ground plane
γ	Incidence angle of VTOL jet re: normal to ground
δ	Azimuth angle in ground plane
Δ	Correction to add to free jet sound levels to predict VTOL jet noise
Δ_{\max}	Maximum value of Δ
η	Acoustic efficiency
θ	Angle re: jet exhaust
κ	Ratio of specific heats
λ	Wavelength
ρ	Density in jet, $\text{lb sec}^2/\text{ft}^4$
ρ_e	Jet exit density
ρ_o	Ambient air density
σ	Hub to tip radius ratio
ϕ	Blade rotation angle
ϕ	Half-angle of jet boundary
ψ	Azimuth angle in plane normal to propeller disc
Ω	Rotational speed, radians/second

Contrails

SECTION I

INTRODUCTION

The vertical takeoff and landing (VTOL) aircraft offers a unique operational advantage for military and civilian flight operations by virtue of its flexible takeoff and landing capability. The propulsion systems for such aircraft are generally heavier than for conventional aircraft due to the higher thrust requirements. The requirement for takeoff thrust to weight ratios of the order of 1.1 to 1.3 for VTOL aircraft, compared to ratios of the order of 0.18 to 0.36 for conventional takeoff and landing (CTOL) transport aircraft and 0.4 to 0.67 for current CTOL fighter aircraft, implies that the propulsion system in a VTOL is generally a significantly higher proportion of aircraft weight than in a CTOL aircraft. It is highly desirable, therefore, that this weight penalty not be compounded by any additional weight penalties associated with the anticipated sonic environments generated by the propulsion system during takeoff and landing operations. Thus, reliable estimates of acoustic environments for VTOL aircraft can be more critical than for conventional aircraft.

The sources of noise generated by the propulsion system for VTOL aircraft can be grouped into two main categories — noise from jet-type propulsion systems deriving thrust from high velocity jet efflux and noise from propeller-type systems deriving thrust from aerodynamic lift on rotating blades. Although reasonable prediction methods have been available for predicting the near noise field from such sources for conventional aircraft, the effect on the near noise field of operating such systems in close proximity to the ground with the thrust axis nearly vertical has not been well established. Therefore, the objective of this report is to establish a consistent set of first-generation prediction methods which may be used to estimate near field noise levels for all types of VTOL aircraft operating in close proximity to the ground. The prediction procedures are intended for preliminary design purposes and utilize techniques suitable for manual calculation.

The methods provided utilize available theory, where appropriate, augmented extensively by experimental data which was available or which was developed during preparation of this report. The experimental effort carried out in support of this report consisted of extensive noise measurements in the near field of a model propeller (Appendix B) and a subsonic jet in a free and vertical deflected configuration (Appendix C).

The near noise field generated by VTOL aircraft may be influenced by several factors not necessarily present for conventional aircraft. These factors include:

- The effects of ground reflection of the vertically-oriented noise field.
- Change in a jet noise source due to drastic alteration of the exhaust flow by the ground.
- Noise generated by the turbulent flow impinging on the ground.
- Vortex noise in a jet exhaust due to presence of exhaust deflector vanes utilized to achieve vertical lift for a normally horizontal propulsion engine.
- The basic transient nature of the VTOL noise field during initial climb-out to the cruise configuration.
- Potentially higher near field noise levels for a given aircraft weight due to the higher thrust to weight ratio for VTOL aircraft.
- Potential buffeting loads from upward deflected exhaust or wake between multiple VTOL engine installations.

The prediction methods developed in this report will account for these effects to the extent possible within the current state-of-the-art.

1. VTOL PROPULSION SYSTEMS AND GENERAL NOISE CHARACTERISTICS

VTOL aircraft propulsion, as presently conceived, will normally consist of air breathing reaction systems. Many different types of such lifting devices have now been proposed, varying from direct lift rotor systems through lifting fans to bypass jet engines. Each of these lift methods has been combined in many ways to produce an astonishingly wide variety of proposed VTOL aircraft types. Figure 1 illustrates some of the possible types grouped into the two broad categories mentioned earlier. This variety of possible configurations adds significant complexity and difficulty to the task of predicting the noise characteristics of VTOL aircraft.

There are wide possible differences in the noise characteristics of these propulsion systems. However, in general, it may be anticipated that the application of any given type of propulsion system to a VTOL aircraft will result in more severe sonic loading than if it were applied to a CTOL aircraft. There are two principal reasons for this increase in severity. First, to achieve stable VTOL operation, the engines must be mounted so that the liftoff thrust vector passes through the aircraft's center of gravity. Thus, many of the configurations used to reduce sonic loading on CTOL aircraft, such as tail mounting, cannot be employed. Second, the thrust requirement for a VTOL aircraft is generally higher than that for a CTOL aircraft. This implies that the acoustic power for a propulsion system of a given type and technology will be greater, all else being equal. Such an increase could, of course, be overcome by selecting an inherently less noisy propulsion system (e.g., converting from pure turbojet to high

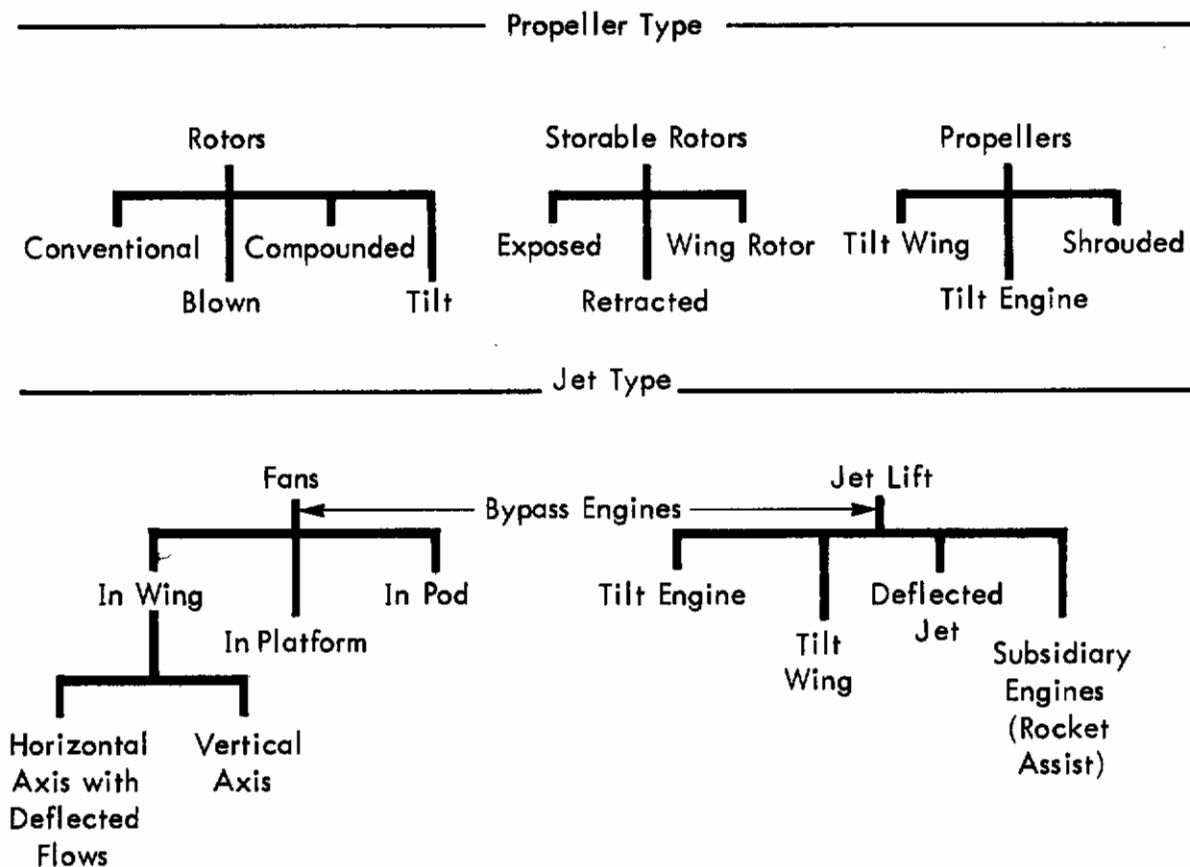


Figure 1. Family of Possible Propulsion Systems for VTOL Aircraft

bypass ratio turbofan propulsion systems). Figure 2 illustrates the approximate trend in overall sound power levels (or maximum far field sound levels) for various types of propulsion systems delivering the same thrust.

No such simple portrayal can be defined for the near field noise levels for VTOL aircraft due, in part, to the reasons discussed earlier. However, some trends can be identified for their maximum value.

In all cases, the maximum sonic loading in the near field of VTOL propulsion systems will occur in the so-called hydrodynamic or non-radiating field. For jet-type devices, this would occur for any structure located in the immediate vicinity of the undeflected jet exhaust. An approximate upper bound for this fluctuating pressure near a jet can be defined as the unsteady part of the dynamic pressure of the exhaust.

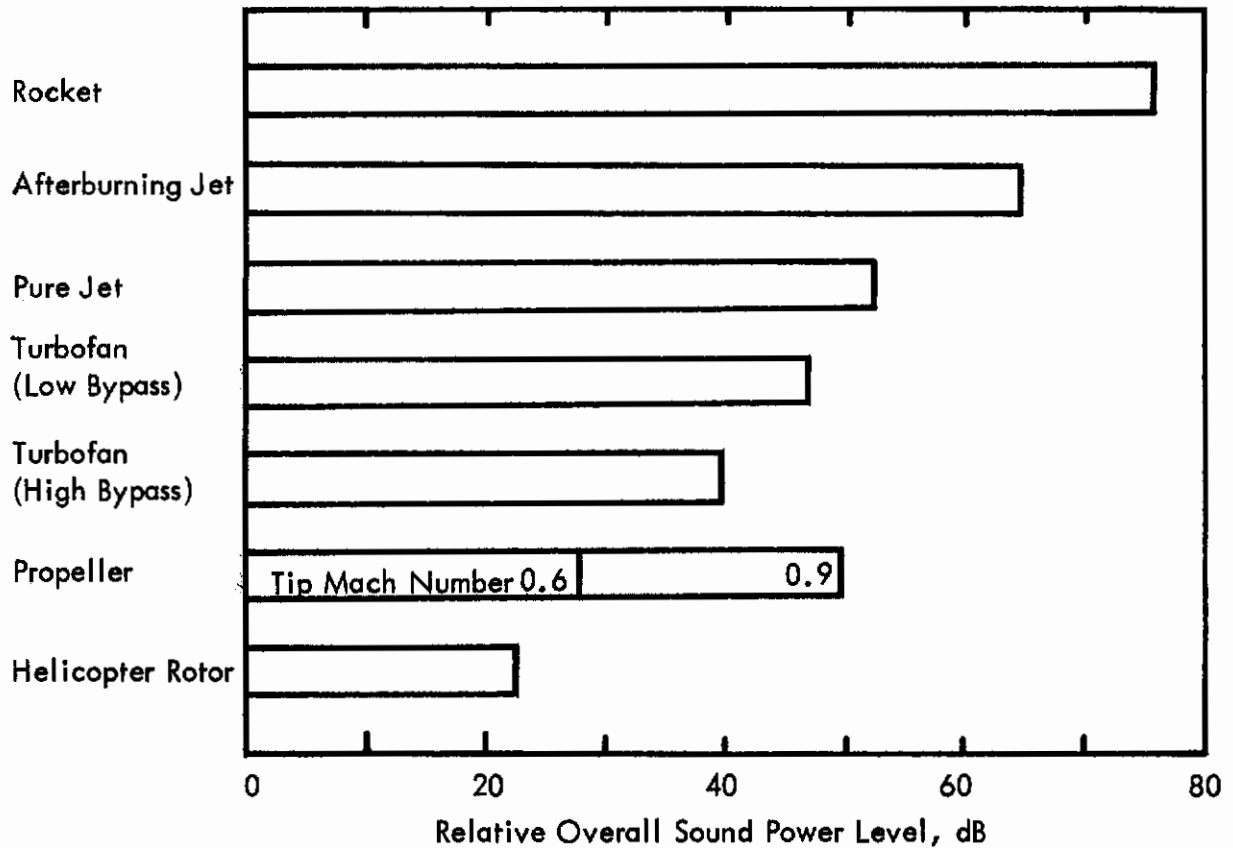


Figure 2. Approximate Trend in Overall Sound Power Level or Maximum Far Field Sound Level for Various Propulsion Systems at Constant Thrust (Adopted from Reference 1).

Considering only velocity fluctuations, this time-varying dynamic pressure can be expressed as

$$P = 1/2 \rho (U + u)^2 \quad (1)$$

where

ρ = density of jet exhaust

U = local mean velocity

u = local rms turbulent velocity fluctuation

Contrails

From measurements in turbulent jets, it is known that the maximum turbulence intensity (u/U) is of the order of 0.1 and that this occurs near the region in the flow where the local mean velocity is approximately 1/2 of the maximum exit velocity U_e .^{2*} Thus, the unsteady pressure will be of the order of

$$p \approx \rho U \tilde{u} = \rho U_e^2 \left(\frac{U}{U_e} \right) \left(\frac{\tilde{u}}{U} \right) \approx \frac{1}{40} \rho U_e^2 \quad (2)$$

The quantity ρU_e^2 is simply the net thrust per unit area for the jet exhaust. This can vary from about 8 psi for high bypass ratio turbofans to 120 psi for rockets. Thus, applying the preceding expression, an approximate upper bound for the fluctuating pressures in the hydrodynamic field of these propulsion systems can be summarized as follows.

<u>Engine Type</u>	<u>Typical Thrust/Exit Area</u>	<u>Approximate Maximum Fluctuating Pressures</u>
● High Bypass Ratio Turbofan	~ 6 psi	0.15 psi = 154 dB
● Turbojets and Low Bypass Ratio Turbofans	~ 28 psi	0.7 psi = 167 dB
● Rockets	~ 115 psi	2.9 psi = 180 dB

The estimate for rockets is very conservative since it neglects the observed decrease in turbulence intensity of supersonic jets.³ Including this effect reduces the estimated upper bound for fluctuating pressures in the hydrodynamic field of rockets to about 175 dB. These rough estimates are consistent with the limited data on fluctuating pressures in or immediately adjacent to a jet exhaust flow. For propeller-type systems, the quantity ρU_e^2 can be equated to the thrust per unit disc area (e.g., the disc loading) of the propeller where U_e is the effective wake velocity immediately downstream of the propeller disc. The following table summarizes the maximum fluctuating pressures that would occur in this region due to this wake. In this case, it was assumed that the turbulent velocities would be of the order of $0.2 U_e$.

<u>Propeller Type</u>	<u>Typical Disc Loading</u>	<u>Maximum Fluctuating Pressures in Wake</u>
● Conventional	0.35 psi	0.017 psi = 135 dB
● Rotor (Helicopter)	0.06 psi	0.003 psi = 120 dB

*Superscripts indicate references listed on pp 172-179.

Fluctuating pressures of the order of 20 to 30 dB higher are, of course, observed in the vicinity of rotating propellers or rotors. The noise from the propeller or rotor wake is not the major source. As discussed in more detail in Section IV, the dominant noise source is associated with the fluctuating thrust and drag forces generated by the rotating propeller. However, under certain conditions, the deflection of a vertically-directed propeller or rotor wake by the ground could present a source of significant buffeting loads on the fuselage.

Except for this last phenomenon, no specific consideration has been given to VTOL aircraft in this crude analysis of upper bounds in near field pressures. This, in fact, is the point – the severity of the near field noise environment for VTOL aircraft cannot be simply scaled up from levels observed in the near field of CTOL aircraft. The maximum near field noise levels expected for VTOL aircraft can be greater or less than those experienced by CTOL aircraft. The configuration of the vehicle system and the influence of the ground surface is very different for VTOL aircraft and leads to a requirement for new prediction methods or modified application of existing methods for predicting the near noise fields.

2. ORGANIZATION OF REPORT

The remainder of this report is organized to present these prediction methods in the following manner.

Section II outlines the basic criteria for the parameters required to adequately define near field noise levels for VTOL aircraft. Compromises required in this specification, dictated by the current state-of-the-art, are defined.

Sections III and IV review existing prediction methods and experimental data for jet-type and propeller-type near noise fields respectively and provide the necessary background and validation for the prediction methods selected. The nature of potential buffeting loads associated with the deflected wake from prop-, rotor- or fan-in-wing-type engines will be considered in Section III in conjunction with the consideration of these loads from ground-deflected jet exhausts. The basic methodology for analyzing the effect of ground reflection on propeller noise is also treated in Section III, since the same basic concepts are applicable for both jet and propeller-type noise sources.

Section V briefly summarizes some of the noise reduction techniques that can be applied to reduce near field noise levels for VTOL aircraft.

Section IV presents the basic method for predicting near field noise levels of VTOL aircraft in the form of simple expressions and graphs for each of the two general types of propulsion systems (jet and propeller systems).

Contrails

Finally, Section VII contains a brief summary of conclusions. Appendix A presents a table of the major characteristics of several existing VTOL aircraft. Appendices B and C present a summary of the major results obtained from the near field noise measurements conducted for this report near a model propeller (Appendix B) and a free and deflected subsonic jet (Appendix C). Appendix D presents tables of correction factors for ground reflection of octave bands of white noise and includes the program listing used to generate the tables. The latter are presented uniquely in a geometrically scaled array useful for direct physical interpretation.

SECTION II

CRITERIA FOR PREDICTION OF ACOUSTIC LOADS ON VTOL STRUCTURE

1. INTRODUCTION

The integrity of VTOL aircraft structure can be influenced by acoustic loads generated by the propulsion system. These loads must be determined, therefore, for adequate structural design of VTOL aircraft. This determination is preferably made by analytical (empirical or theoretical) methods during the preliminary design stage. During subsequent design phases, the predictions should be refined, where necessary, and supported by experimental data to insure that structural loads are adequately defined within acceptable design margins. The ultimate objective of this process should be the establishment of a structural design which reduces to an acceptable minimum any risks of system malfunction due to sonic fatigue of structure or equipment vibration, and achieves acceptable internal noise levels. An acceptable design must satisfy these constraints without unduly penalizing the overall performance of the aircraft due to weight penalties or design complexity.

The acoustic loads on VTOL structure should ideally be specified as a function of time and position in terms of:

- Overall sound pressure level
- Frequency spectrum
- Spatial correlation

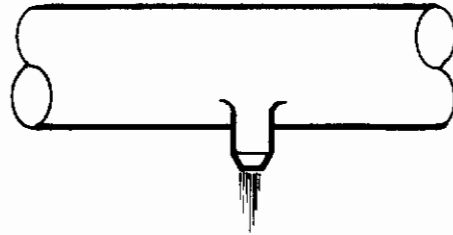
Within the current state-of-the-art of VTOL propulsion system noise, it will be necessary to limit the definition of near field noise levels for VTOL aircraft to predictions of noise levels in the frequency range critical for structural design (approximately 50 to 2000 Hz). Estimates of spatial correlation of this noise field cannot be provided at this time. As more experience is gained in the future with the evaluation of VTOL noise fields, improvements in the accuracy and detail of the noise predictions can be expected.

2. CRITERIA FOR ANALYTICAL PREDICTION METHODS

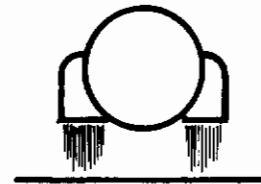
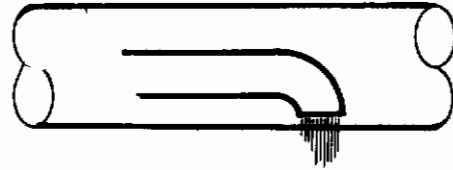
Based on a critical review of the current state-of-the-art, summarized in the next sections, the following parameters have been selected as necessary and sufficient for the prediction of VTOL near field noise levels as developed in this report. These parameters apply to the representative VTOL aircraft configurations illustrated conceptually in Figure 3.

Jet-Powered VTOL Aircraft

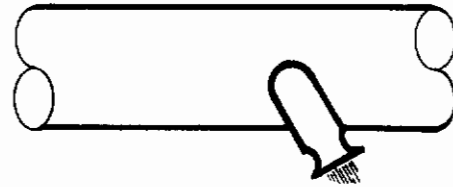
Lift Jet or Turbofan



Vectored Thrust

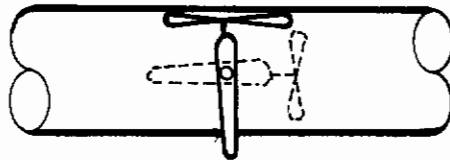


Rocket Assist

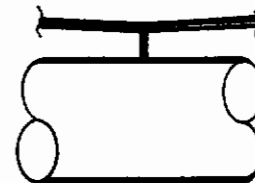


Propeller or Rotor-Powered VTOL Aircraft

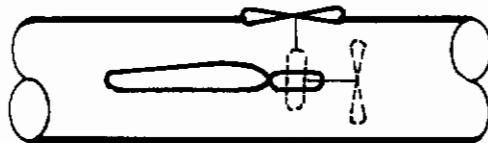
Tilt Wing



Rotor



Tilt Prop



Fan in Wing

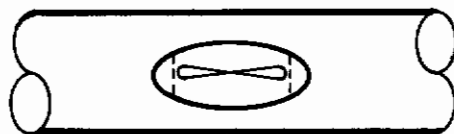


Figure 3. Conceptual Illustration of Representative VTOL Aircraft Configurations

Jet-Type Propulsion Systems

- **Basic Operating Parameters**
 - Jet Type (e.g., fan exhaust, non-afterburning jet, rocket)
 - Jet Thrust
 - Jet Velocity
 - Jet exit diameter
 - Jet temperature
- **Acoustic Field Parameters**
 - Jet exhaust – ground plane elevation
 - Multiple nozzle configuration
 - Nozzle exit – aircraft structure configuration
- **Atmospheric Parameters**
 - Ambient temperature
 - Ambient pressure

Propeller or Rotor-Type Propulsion Systems

- **Basic Operating Parameters**
 - Rotor diameter
 - Blade number
 - Tip Mach number
 - Thrust
- **Acoustic Field Parameters**
 - Duct geometry (if applicable)
 - Ground plane
 - Propeller – structure geometry
- **Atmospheric Parameters**
 - Ambient temperature
 - Ambient pressure

The three groups of parameters are qualitatively the same for each type of propulsion system. The first group is required to define the noise field for the propulsion system in a free unobstructed field. The second group is required to account for modification of the field due to the presence of the vehicle and ground plane, while the third group is used to apply any necessary corrections to the noise field due to significant changes in the propulsion system noise generation and radiation as a result of changes in atmospheric parameters. The significance of these three groups of input parameters is in descending order – that is, the most important parameters are those required to define the sound field characteristics in the absence of any boundaries.

3. CRITERIA FOR EXPERIMENTAL METHODS

When the accuracy of analytical methods is inadequate to define acoustic loads for VTOL aircraft within acceptable design margins, a more detailed evaluation of structural design-propulsion system noise tradeoffs will require the use of experimental tests. Application of scaled models is preferred during preliminary phases to allow economical evaluation of alternate design configurations.

The optimum modeling technique for evaluating acoustic loads involves duplicating all parameters of the propulsion system except size. A single dimensional scale factor is applied to all geometrical parameters. The net result, ideally, is that the same near field sound levels are measured at scaled distances as would be expected in the full scale version. The only change is that the frequency spectrum of the noise is shifted up in direct proportion to the dimensional scale factor. The result is that the product of any characteristic frequency of the noise, f_c , (e.g., peak frequency in jet spectrum or propeller fundamental) and a characteristic dimension, d , is constant. The non-geometrical parameters which are critical can be taken from the preceding paragraphs on criteria for analytical prediction methods. Thrust or horsepower parameters are, of course, duplicated on a per-unit area basis in the scale model.

Further details of experimental modeling techniques for jet-type systems are covered in Reference 4. Illustration of an application of modeling techniques for propeller noise is presented in Appendix B. The potential application of other modeling techniques will become clear in Sections III and IV as the scaling parameters for near field noise of VTOL aircraft propulsion systems are considered.

4. CRITERIA FOR FREQUENCY RANGE OF PRIMARY IMPORTANCE

The frequency range of primary concern for analysis of VTOL near field noise levels must include the frequencies which control structural stress, equipment vibration and crew environments. Structural stress levels on aircraft will generally be a maximum in the frequency range of lower order resonance frequencies of secondary structure and skin panels with some additional contribution due to resonant response of primary airframe structure.

This trend is illustrated in Figure 4 by the normalized octave band stress levels measured on the XV-4B experimental VTOL aircraft during VTOL and CTOL ground tests.⁵ The rms octave band stress levels, approximated from the narrow band spectra reported in Reference 5, have been normalized by the corresponding rms acoustic pressures measured at microphones adjacent to the strain gauges. For VTOL operation, the data obtained on the fuselage and wing area show a dominant peak in stress response around 200 to 500 Hz in the region of panel resonance frequencies. During CTOL operation, the engine exhaust was close to the tail surfaces which exhibited a similar

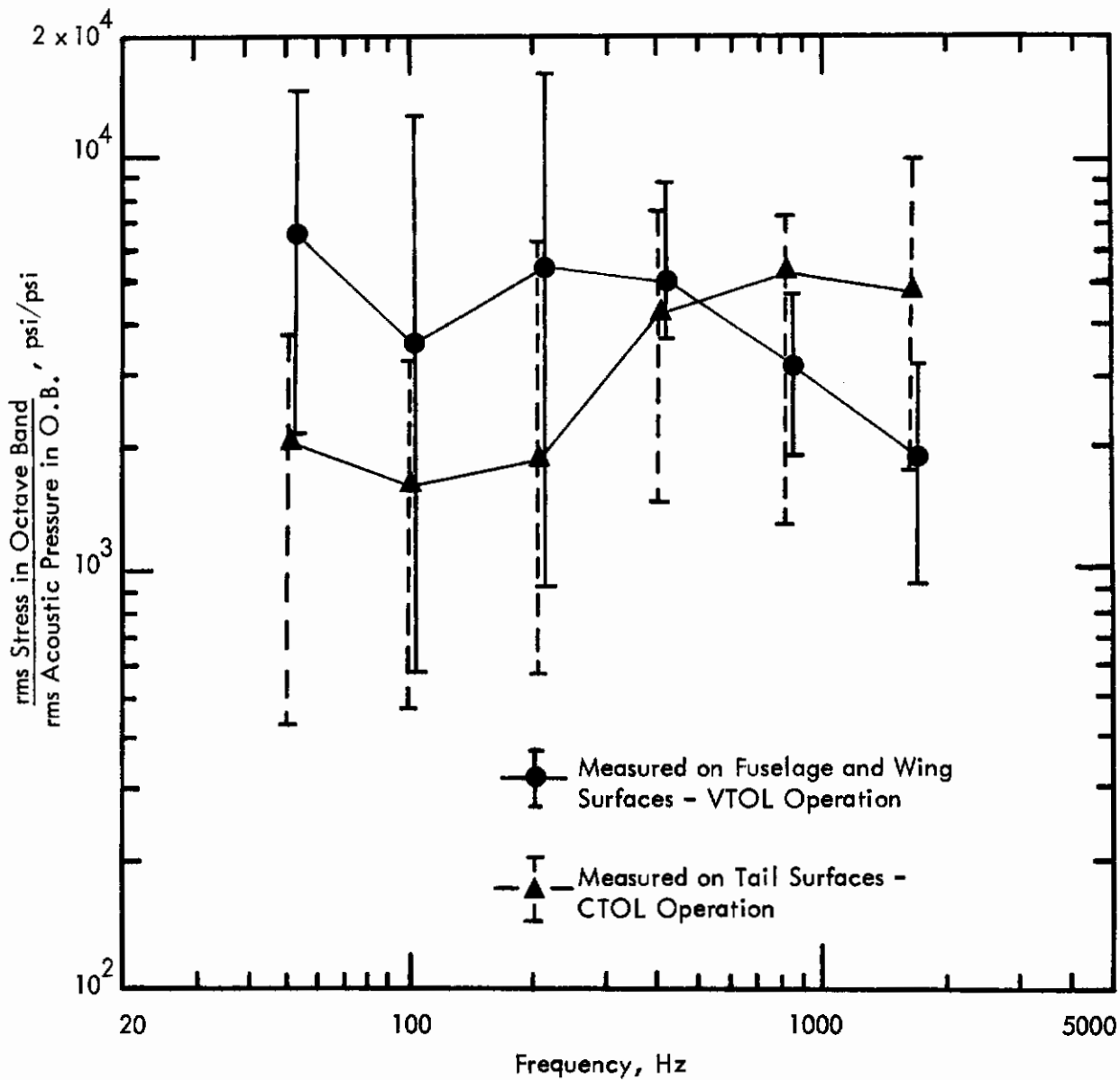
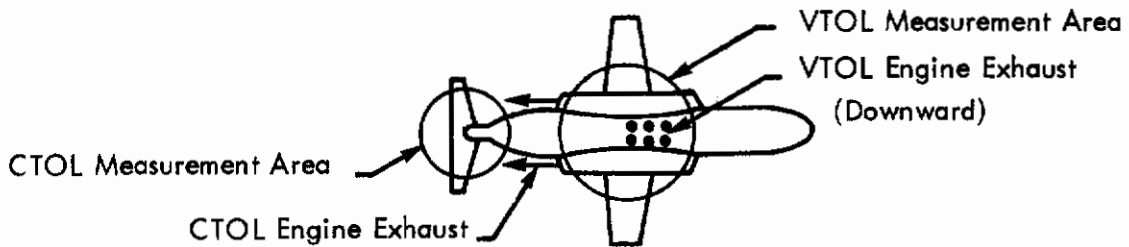


Figure 4. Trend in Normalized Octave Band Stress Levels Measured on XV-4B Hummingbird Aircraft During VTOL and CTOL Operation (Data from Reference 5).

average magnitude of normalized stress response but shifted to higher frequencies. This reflects, in part, the smaller structural dimensions in this area and correspondingly higher structural resonance frequencies. The rise in response below 100 Hz is attributed to resonant response in primary structure induced by acoustical and mechanical excitation from the engines. Approximately 50 Hz is considered a reasonable lower bound for significant acoustically-induced response in these primary modes for VTOL aircraft.

Normally, VTOL engines will be located near the center of gravity of the vehicle where structural modes will tend to have resonance frequencies below 1000 Hz. Since near field noise levels will also tend to be higher near the VTOL engines, it is reasonable to expect that dominant stress levels on VTOL aircraft will have a relative response pattern similar (in frequency range) to that illustrated in Figure 4 for the VTOL condition.

Equipment vibration levels in VTOL aircraft will be dominated by peaks in the acceleration response spectra at equipment mounting points. The data in Figure 4 provide little evidence of this response. However, some qualitative trends can be estimated. Applying the concept by Hunt that structural strain (or stress) response at resonance is proportional to peak structural velocity, the data in Figure 4 suggest that the relative octave band acceleration response spectra at the surface of the structure would be highest near or above 2000 Hz.⁶ However, allowing for structural filtering effects to internal equipment, one can expect peak internal acceleration levels to occur at frequencies below 2000 Hz.

Crew comfort criteria for noise can be based, to a first approximation, on speech interference levels.⁷ These are defined by the arithmetic average of octave band sound pressure levels at 500, 1000 and 2000 Hz, using the currently preferred octave bands.

In summary, the dominant frequency range for analysis of VTOL near field noise environments is expected to fall between 50 to 2000 Hz. Methods for predicting the near field noise environment developed in this report will emphasize this range.

SECTION III

NEAR FIELD NOISE FOR JET-POWERED VTOL AIRCRAFT –
A REVIEW OF THE STATE-OF-THE-ART

1. NOISE SOURCES

The noise generated by a vertical jet exhaust impinging on the ground can originate from several sources. These are illustrated conceptually in Figure 5. The basis for identification of these potential sources is summarized in Table I. The potential noise sources identified correspond to those illustrated in Figure 5 and are listed in estimated decreasing order of significance for vibroacoustic loads on VTOL aircraft.

Clearly, direct and reflected jet noise from the undeflected flow will be present as the principal near field noise source common to both VTOL and CTOL jet aircraft.³ The other sources identified are considered unique to VTOL jet aircraft. These are: the noise radiation from the deflected flow (wall jet noise), noise from the turbulent flow impacting the ground, noise generated by turning vanes in vectored thrust VTOL lift jets, noise from the interaction of jet turbulence convected through a normal standing shock above the ground for a supersonic VTOL jet, and discrete-frequency ring tones generated by impinging jets near the ground. Based on an evaluation of pertinent experimental data, it will be shown that the first three sources listed in Table I appear to dominate the near field for jet-powered VTOL aircraft. One exception to this rule would be the intense discrete frequency ring tones which have been noted in several model studies of simulated VTOL jets. However, as discussed later in part 6(d) of this section, these tones probably can be or are inherently suppressed on full-scale systems. In the remainder of this section, after reviewing the nature of the deflected flow, prediction methods for evaluating each of these sources will be established with emphasis on design prediction methods suitable for the first three sources.

2. FLOW PROPERTIES OF A DEFLECTED JET

a. Mean Flow – Subsonic Jet

The actual flow properties of a vertical jet impinging onto a ground plane can be conveniently illustrated with the case of a subsonic jet. Figure 6 illustrates the basic geometry and flow parameters of interest for this configuration. The figure illustrates the case where the nozzle elevation is slightly greater than the length of the uniform non-turbulent flow region called the potential core which is present in any fully expanded free jet. The velocity within the potential core is equal to the exit velocity (see, for example, References 2, 3, 14-16 for further details of jet flow).

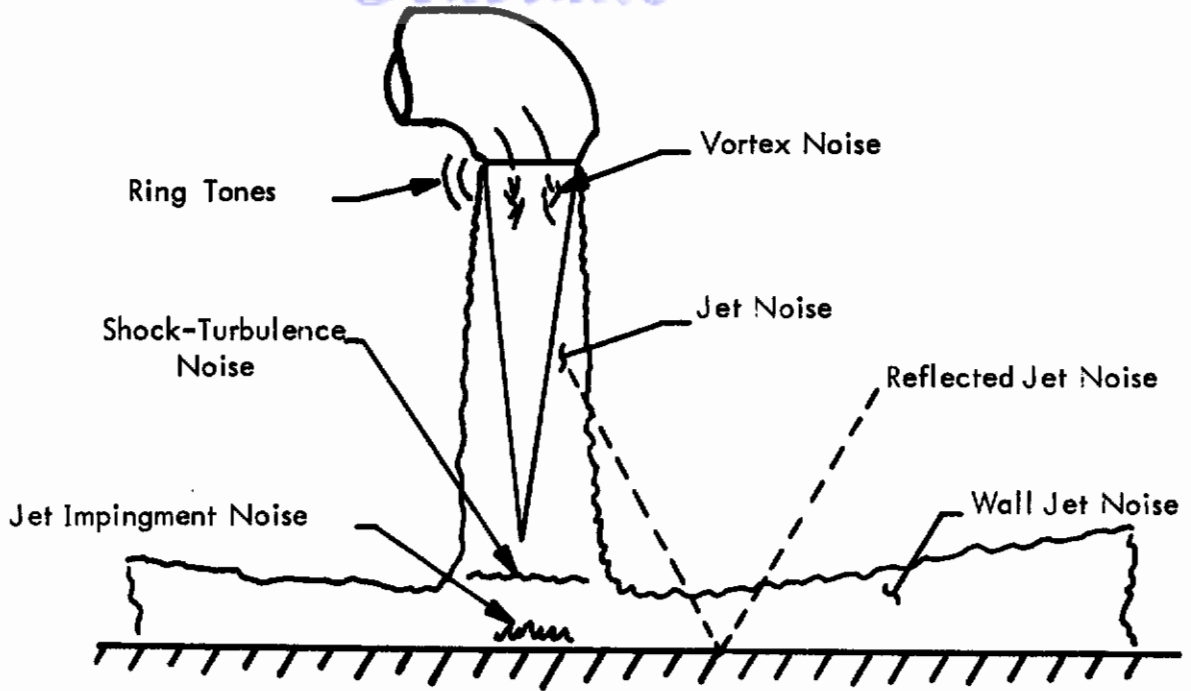
TABLE I
SYNOPSIS OF POTENTIAL ACOUSTIC NOISE SOURCES FOR JET-POWERED VTOL AIRCRAFT

Noise Source	Basis for Identification	Available Prediction Models (1)				Available Experimental Data (2)		Probable Significance for VTOL Aircraft Near Ground
		Far Field		Near Field		FF	NF	
		T	E	T	E			
1. Direct noise radiation from undeflected jet	Known noise source	X	X	X	X	X	X	High
2. Jet noise reflected by ground	Classical theory	X		X		X	X	High
3. Direct radiation from deflected flow (wall jet)	Theoretical expectation	X		X		X(3)	X(3)	Unknown
4. Radiation from impingement area of turbulent flow	Theoretical expectation	X				X(3)	X(3)	Unknown
5. Vortex Noise from jet exhaust deflector vanes	Theoretical expectation	X			X	X	X	Unknown
6. Discrete ring tones from vertical jet close to ground	Experimental observation					X	X	Low
7. Shock-turbulence interaction from deflected supersonic jet	Known noise source	X				X		Low
8. Buffeting from reverse flow for multiple impinging jets	Observation of flow	NA	NA			NA	X	Depends on configuration (suppressed by design)

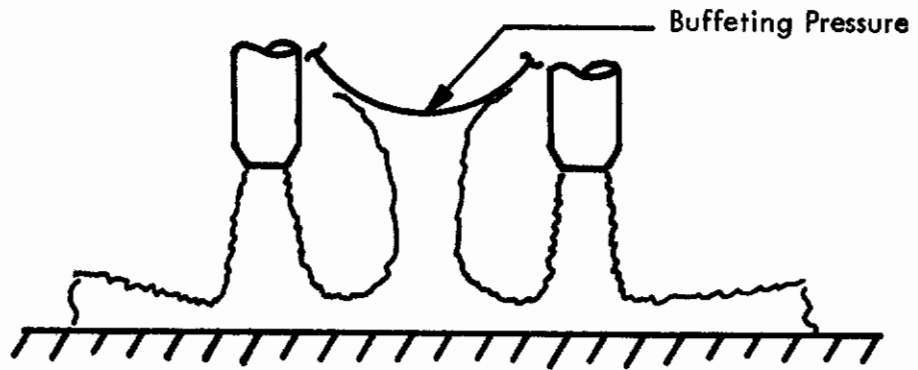
(1) T - Theoretical
E - Empirical
NA - Not Applicable

(2) FF - Far Field
NF - Near Field
(3) Not isolated in experimental data

Contrails



a) Sources of Noise for Single Impinging Jet



b) Buffeting Pressure Fluctuations from Reverse Flow for Multiple Nozzles

Figure 5. Conceptual Illustration of Potential Noise Sources for Jet-Powered VTOL Aircraft

Contrails

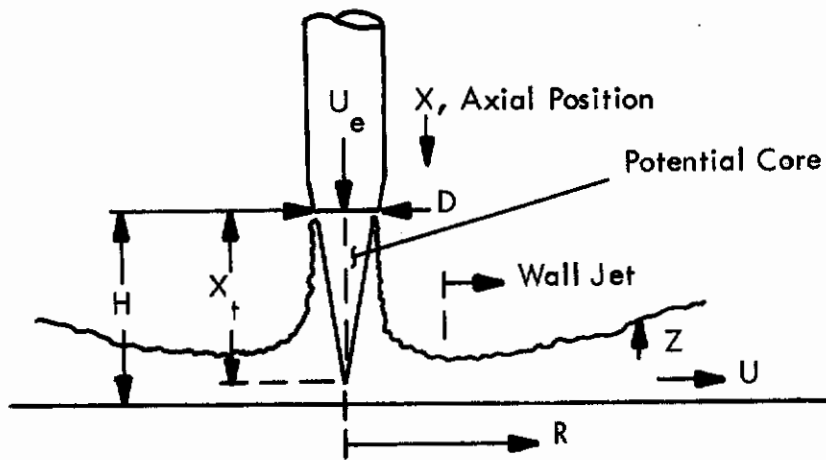


Figure 6. Geometry and Flow Parameters for Radial Wall Jet

The deflected flow along the ground is called a radial wall-jet. Glauert presented an analysis of the fluid dynamics of the wall jet in 1956.⁸ Skifstad has reviewed subsequent experimental and theoretical studies of the fluid dynamics of wall jets and impinging jets in his thorough summary (containing over 100 references) of the aerodynamics of VTOL jets.⁹ Key results from this summary, plus additional material from References 10-12, and results from a brief experimental study of mean flow properties of a subsonic wall jet are considered here.

Utilizing basic principles of flow similarity and fluid dynamics theory, Glauert defined several idealized models for the flow in a wall jet. The decay in maximum velocity (U_{\max}) of the wall jet with radius (R) from the jet axis and the growth in thickness (Z) with R , are defined by the following three simple flow models.

<u>Flow Model</u>	<u>Velocity Decay</u>	<u>Thickness Growth</u>
Laminar Flow	$U_{\max} \sim R^{-3/2}$	$Z \sim R^{5/4}$
Turbulent Flow (neglecting wall friction)	$U_{\max} \sim R^{-4/3}$	$Z \sim R$
Turbulent Flow (wall friction included)	$U_{\max} \sim R^{-1.38}$	$Z \sim R^{1.08}$

The flow in a wall jet from a VTOL aircraft will certainly be turbulent so that the laminar flow model is clearly not applicable. Glauert derived a fourth refined model for the turbulent radial wall jet which included wall friction effects. This model showed that the perfect similarity in the flow profiles was not retained as a function of radial distance R . The result is that the wall jet velocity and thickness vary as a power of the radius R . However, the exponents vary slightly with Reynolds number when the latter is based on the maximum velocity in the wall jet and its thickness.

The values of the velocity decay exponents predicted by Glauert are compared in Figure 7 with the available experimental data. Glauert's refined theoretical model agrees reasonably with the very limited data. The reason for the higher exponent (more rapid decay) for the test data given in Appendix C is not clear. It may be due to the higher turbulence anticipated at the nozzle exit for this test. A low decay exponent has been observed when the jet exit was surrounded by a large flange extending several diameters in radius.^{10,11} The presence of such a flange would tend to reduce the induction of air into the wall jet and hence reduce its decay rate. This effect was minimized for the flow test reviewed in Appendix C.

The refined theory by Glauert predicts that the thickness of the wall jet (a measure of a typical eddy size) increases as R^b where b varies from 1.019 at a Reynolds number of 1200 to 1.005 at a Reynolds number of 1.4×10^6 . The experimental data (References 9 through 11 and Appendix C) indicate that the exponent b , varies from 0.0 to 1.0, in general agreement with the theoretical values.

The Reynolds number for a radial wall jet formed by vertical ground impingement of a full scale jet or turbofan engine exhaust would normally exceed 10^6 . Based on Glauert's refined theoretical model, Figure 7 indicates that the decay in maximum velocity will approach a simple $1/R$ law, the same as for the decay in axial velocity of a fully developed jet. This relationship will be used, therefore, as a conservative prediction model of wall jet velocity decay for evaluating noise radiated by the wall jet itself. The thickness of the wall jet or typical eddy size will be assumed to increase directly with R .

This assumed variation in radial velocity and wall jet thickness for a full scale subsonic VTOL jet is compared in Figure 8 with the trend that was observed in the model experiments discussed in Appendix C. The radial velocity decay is shown in Figure 8(a) on a normalized scale relative to the exit velocity (U_e) of the subsonic jet.

The figure shows that the initial radial velocity of the wall jet is constant out to a radius of about 1 to 1.5 nozzle diameters. For nozzle elevations greater than 1 nozzle diameter above the ground, this initial radial velocity (U_{max_0}) is essentially the same as the axial velocity of the impinging jet. This observation, based on the experimental data reported in Appendix C, indicates that there is no significant loss in kinetic energy of the subsonic jet as a result of its being deflected by the ground plane. It also appears that the presence of the ground plane does not significantly influence the undeflected jet flow for nozzle heights above the ground greater than about 1 diameter. This important point has been noted by several other investigators of VTOL model jets.⁹ This initial radial velocity of the wall jet can be defined approximately as follows:

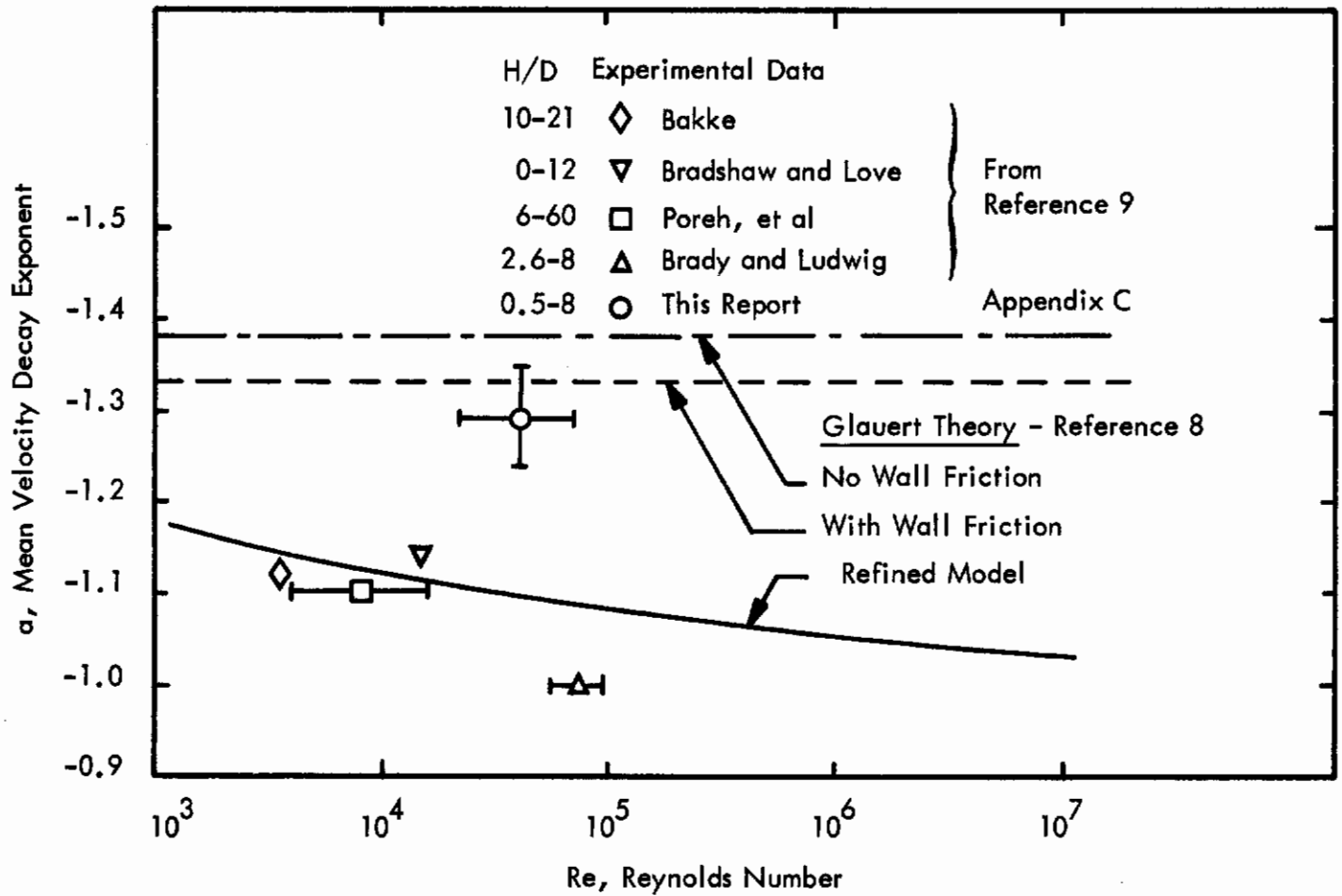
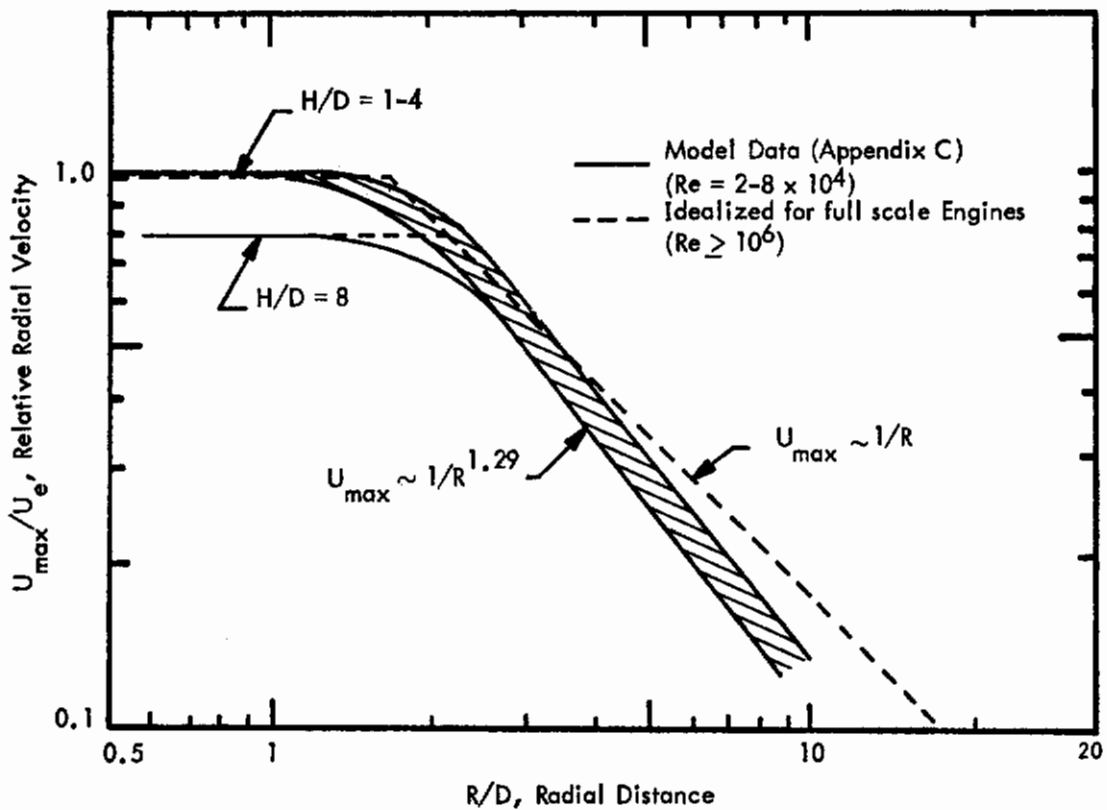
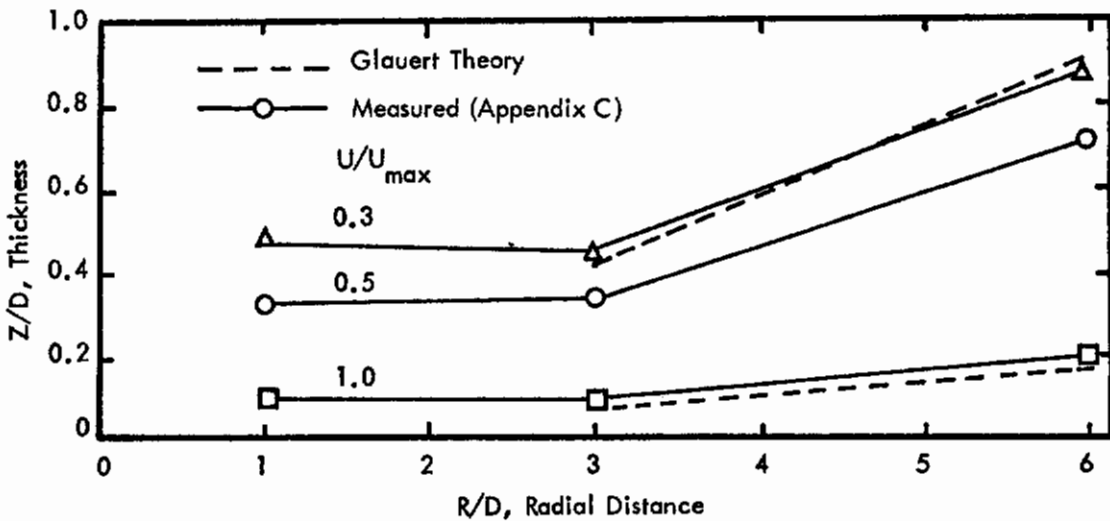


Figure 7. Comparison of Theory and Experimental Data for Exponent (α) for Decay of Maximum Radial Velocity in Turbulent Radial Wall Jet where $U_{\max} \sim R^\alpha$.



a) Decay in Radial Velocity of Wall Jet



b) Growth in Thickness of Wall Jet

Figure 8. Idealized Model for Radial Velocity Decay and Growth of Thickness of Wall Jet

Contrails

for $1 < \frac{H}{D} < \frac{X_t}{D}$, $U_{\max_o} \approx U_e$ (3)

and

for $\frac{H}{D} > \frac{X_t}{D}$, $U_{\max_o} \approx U_e \left[1 + \left(\frac{H}{1.5X_t} \right)^6 \right]^{-1/6}$ (4)

where

H = axial distance from nozzle exit to ground impingement point

X_t = length of potential core

U_e = exit velocity of subsonic jet

Equation (4) is an empirical expression which closely approximates the decay in axial velocity observed in a free subsonic jet downstream of the potential core (see Appendix C). It describes the observed velocity decay in the transition region of a free jet as well as the well-known decay rate of $1/X$ in the fully developed flow region for such a jet where X is the axial position on the jet axis downstream of the jet exit.^{3, 13-15}

At radii greater than 1.5 diameters, the observed decay in radial velocity approaches a single decay curve for nozzle elevations between 1 and 8 diameters (see Appendix C). For full scale VTOL aircraft, it will be assumed that this trend is described approximately by the empirical expression:

for $\frac{R}{D} > 1.5$, $U_{\max} \approx U_e \frac{1.7}{R/D}$ (5)

Combining Equation (5) with (3) or (4), this inverse decay law would apply for radial distances greater than

$$\frac{R}{D} > 1.7 \quad \text{for} \quad 1 < \frac{H}{D} < \frac{X_t}{D}, \quad \text{or greater than}$$

$$\frac{R}{D} > 1.7 \left[1 + \frac{H}{1.5X_t} \right]^{1/6} \quad \text{for} \quad \frac{H}{D} > \frac{X_t}{D}$$

Figure 8(b) illustrates the growth in thickness of the wall jet based on the very limited data for one nozzle height ($H/D = 4$) reported in Appendix C. Contours of constant relative velocity are shown based on vertical velocity profile measurements at radial distances of 1, 3 and 6 diameters. At each station, the velocity was normalized to the local maximum velocity U_{\max} . Glauert's theoretical model for the vertical velocity profile of the wall jet defines the shape of this profile in terms of the thickness ($Z_{1/2}$) at which $U/U_{\max} = 0.5$.⁸ By using the measured values for this reference thickness, theoretical values for the thickness at $U/U_{\max} = 0.3$ and 1.0 have been determined and plotted in Figure 8(b). The agreement with data is very good for radii of 3 and 6 diameters where the wall jet has fully developed. Note that projection of the contours of constant relative velocity in Figure 8(b) back to zero thickness suggests that the virtual origin of the fully developed wall jet is very close to the axis of the jet.⁹ Therefore, it will be assumed that a suitable characteristic dimension of the fully developed wall jet is equal to $Z_{1/2}$. This parameter can be estimated from Figure 8(b) by the expression

$$\frac{Z_{1/2}}{D} \approx K \frac{R}{D} \quad (6)$$

where

$$K \approx 0.12$$

Although this estimate is based on data for only one nozzle elevation ($H/D = 4$), the uniformity of the decay in axial velocity for $H/D = 1$ to 8 strongly suggests that the wall jet thickness will be essentially independent of nozzle heights in this range. Lyon observed a value for K of about 0.085 for H/D varying from 1 to 2 for a wall jet with a large flange (flange diameter = 3.7 nozzle diameters) at the exit plane.¹¹

Returning now to Equation (4), Eldred, et al, have shown that the length of the potential core (X_t) can be predicted from the empirical expression:¹⁵

$$X_t = 3.45 D_E \left[1 + 0.38 M_E \right]^2 \quad (7)$$

where

D_E = exit diameter for a fully expanded jet

M_E = exit Mach number (exit velocity/speed of sound in the flow).

This expression is plotted in Figure 9 along with available data which cover a range of jet temperatures from -300°F to 2000°F . No influence of temperature is apparent in

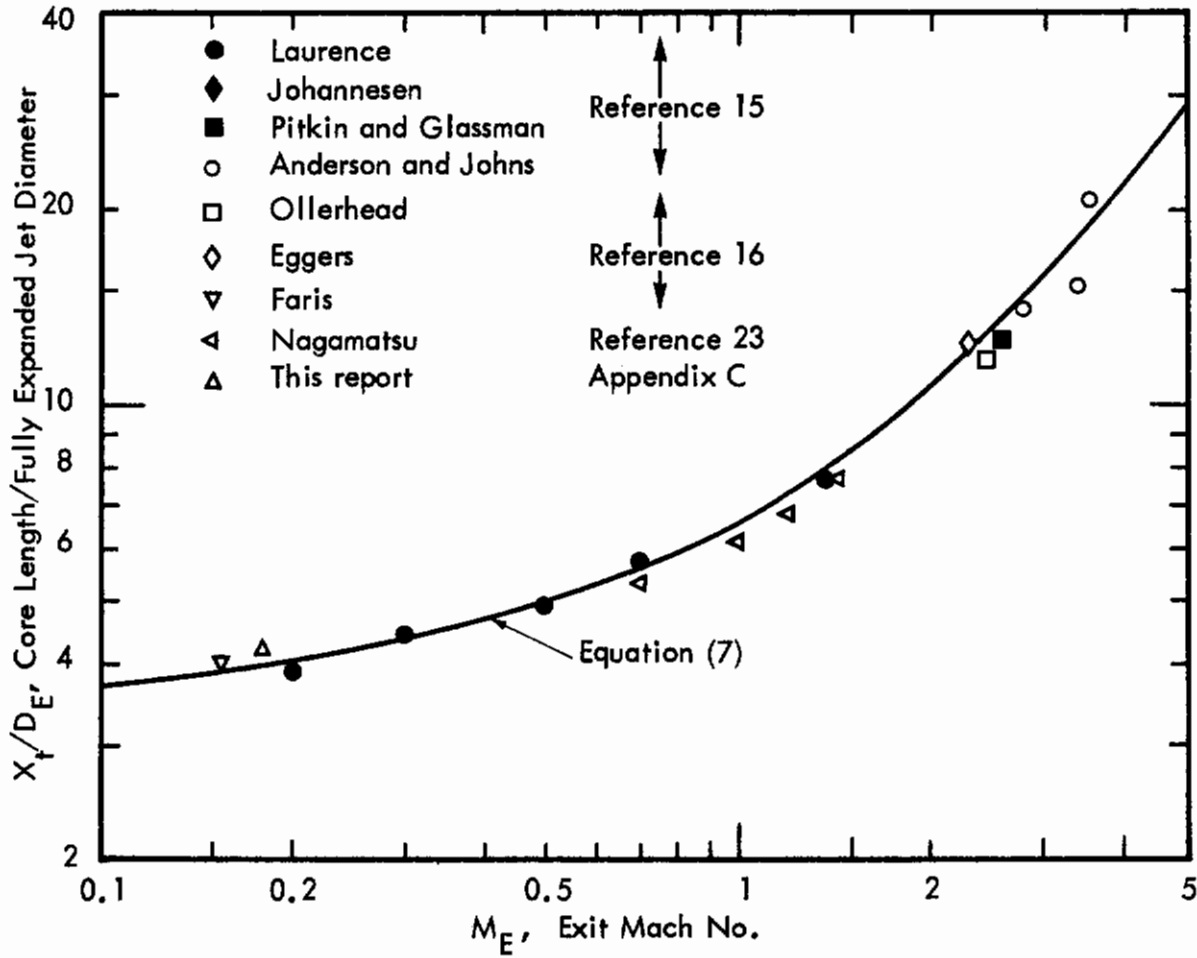


Figure 9. Variation in Length of Potential Core with Exit Mach No.

the data thus indicating that Equation (5) can be used for estimating the potential core length for full scale engines. This characteristic length can be expected to have a strong influence on the manner in which noise changes from a VTOL jet as nozzle elevation (H) changes.

For jet-powered VTOL aircraft, the incidence angle of the jet with the ground during the initial lift-off or terminal landing phase of flight may vary as much as $\pm 20^\circ$ from the vertical.⁴² Results from a brief experimental evaluation of the flow for an oblique incidence angle are summarized in Figure 10. (See Appendix C for additional details.) The maximum velocities in the downstream and upstream directions for an incidence angle of 70° have nearly the same initial values and essentially the same rate of decay with radius ($\sim R^{-1.27}$) as observed for 90° incidence. However, in the region of fully developed flow ($R/D > 3$), the absolute magnitudes of the velocities in the upstream and downstream directions are different. Based on the limited measurements discussed in Appendix C, the following expression was found to satisfactorily approximate the observed variation in maximum velocity in the fully developed flow region as a function of incidence and azimuth angles.

$$U_{\max}(\delta) \approx U_{\max}(90^\circ) [1 + \cos \beta \cos \delta] \quad (8)$$

where

$U_{\max}(90^\circ)$ = maximum radial velocity for $\beta = 90^\circ$ in fully developed flow region

β = incidence angle of jet

δ = azimuth angle (see Figure 10)

Although this expression is based on very limited data, it is consistent with a simple physical concept that the change in maximum radial velocity in the fully developed flow region is proportional to the radial vector component ($\sim \cos \beta \cos \delta$) of the incident jet velocity. Additional details on mean flow properties of oblique incidence jets may be found in the studies cited in Reference 9.

b. Mean Flow – Supersonic Jet

For some VTOL aircraft, lift-type turbojet engines have been employed which have exit velocities of the order of 1800 to 2200 ft/sec with corresponding exit Mach numbers of the order of 1.05 to 1.2. Solid rocket engines have also been considered for boosting the takeoff thrust of VTOL aircraft. Exit Mach numbers generally range from 2.5 to 3.5 for such engines. Available information on deflected supersonic jets emphasize flow characteristics for rocket launch stand deflectors where the incidence

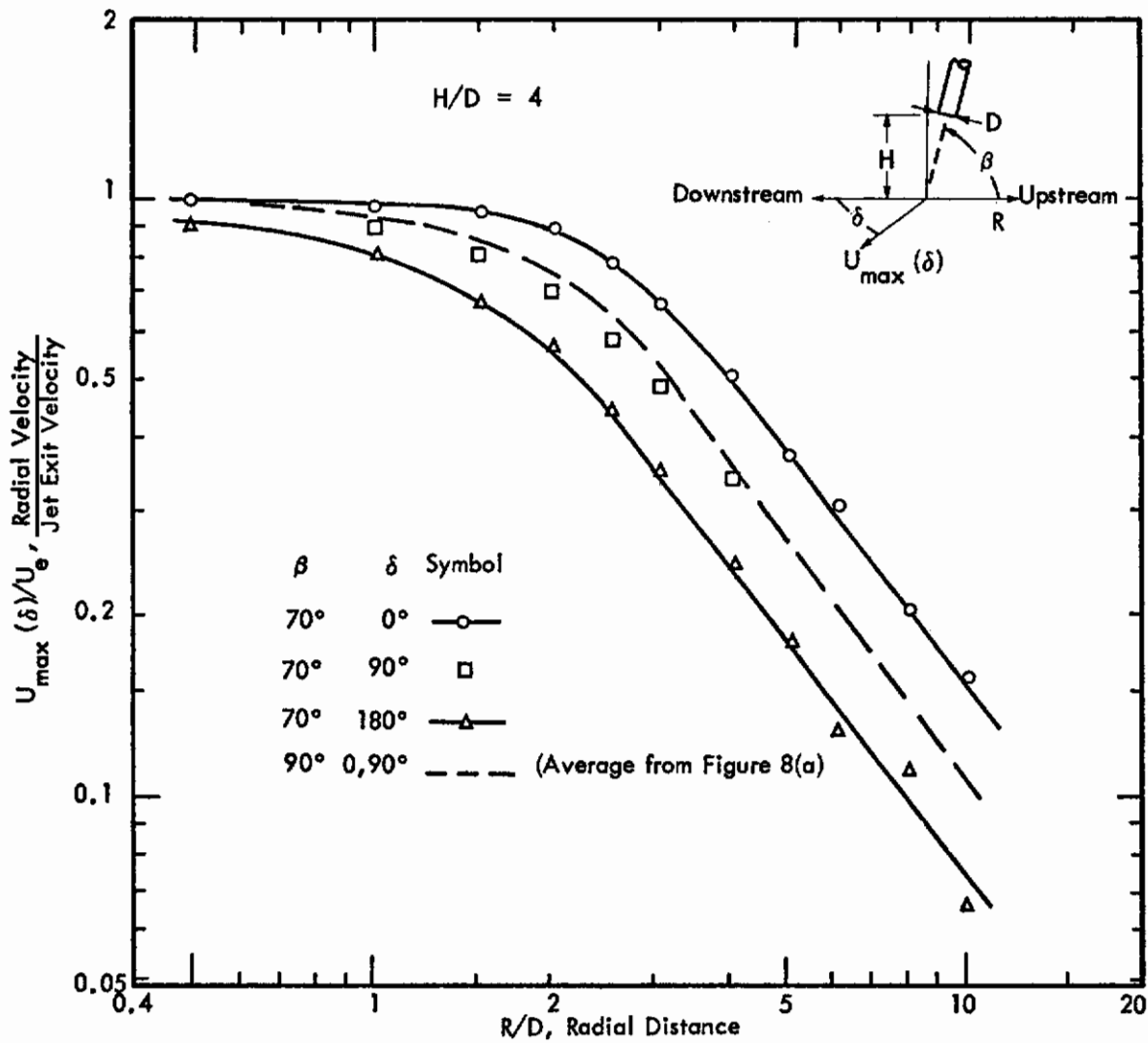


Figure 10. Measured Variation in Maximum Radial Velocity at 0°, 90° and 180° Azimuth Angles for Jet at 70° Incidence Compared to Radial Velocity for 90° Incidence. (Data from Appendix C)

angle of the flow is generally less than 60° .^{17,18} For small (near grazing) impingement angles of a supersonic flow, a shock wave is formed which attaches to the impinging surface and the deflected flow travels only in the downstream direction. However, for impingement angles greater than about 40° for a Mach 3 flow, this shock detaches from the deflection surface and some of the deflected flow begins to travel upstream.¹⁸ Thus, as the impingement angle approaches 90° , as for a supersonic VTOL jet, a strong shock wave will be formed in the flow just above the ground plane. This situation was illustrated conceptually in Figure 5. Although the structure of this shock wave will not be uniform due to the non-uniform velocity profile of the impinging jet, some reasonable estimates of the resulting wall jet can be made by assuming the incident flow is uniform. By treating the shock as a normal shock wave and applying standard aerodynamic theory for the velocity drop across such a normal shock, an estimate can be made of the velocity of the flow which actually impinges on the ground. Since the flow is always aerodynamically subsonic downstream of a normal shock wave, this incident velocity will be subsonic (less than the speed of sound in the flow).

The Mach number (M_2) downstream of a normal shock with an upstream Mach number of M_1 is given by¹⁹

$$M = \left[\frac{(\kappa - 1) M_1^2 + 2}{2 \kappa M_1^2 - (\kappa - 1)} \right]^{1/2} \quad (9)$$

where κ = ratio of specific heats.

Assuming constant mass flow through the normal shock wave and no change in cross section of the flow at this point, then the product of density (ρ) times velocity (U) must be constant on each side of the shock. Thus, using the known relationship for density ratio across a normal shock, the velocity ratio is given by

$$\frac{U_2}{U_1} = \frac{\rho_1}{\rho_2} = \frac{(\kappa - 1) M_1^2 + 2}{(\kappa + 1) M_1^2} \quad (10)$$

where subscripts 1 and 2 denote upstream and downstream values respectively. Similarly, the dynamic pressure changes across the shock by the same ratio as shown by

$$\frac{\rho_2 U_2^2}{\rho_1 U_1^2} = \frac{\rho_2}{\rho_1} \left(\frac{\rho_1}{\rho_2} \right)^2 = \frac{\rho_1}{\rho_2} = \frac{U_2}{U_1} \quad (11)$$

Equations (10) and (11) are plotted in Figure 11 for three values of κ encompassing the range that would be encountered for ambient air jets ($\kappa = 1.4$), turbojets ($\kappa \approx 1.35$) and rockets ($\kappa \approx 1.2$). Although direct experimental evidence was not available for the change in velocity of a supersonic VTOL jet, shadowgraphs of such a flow configuration and limited flow velocity data for a 90° elbow-type deflector tend to confirm this expected phenomena.²⁰ This change in velocity of the impinging flow for a supersonic VTOL jet will only occur for nozzle elevations less than the supersonic length (X_s), the point where the flow on the centerline of the jet has decayed to Mach 1. This length must, of course, be greater than the length of the potential core (X_t) for any exit Mach number (M_E) greater than 1 since the flow Mach number is equal to M_E within the potential core. Figure 12 shows available experimental data for the supersonic length compared to the potential core length. A reasonable fit for the experimental values for X_s is provided by the following expression if the data below the potential core length line is discounted.

$$\frac{X_s}{D_E} \approx 6.5 M_E^{1.5}, \quad M_E \geq 1 \quad (12)$$

The experimental data cover a wide range of jets with total temperatures at the exit ranging from ambient to 4000°R. Although temperature probably has some influence on the supersonic length, there is no discernable pattern for such effects. Thus, it is assumed that exit Mach number alone can be used for estimating this length.

Three characteristic ranges for the nozzle elevation of a supersonic VTOL jet can now be recognized. The axial velocity at the impingement point or the maximum initial velocity U_{\max_o} of the radial wall jet will vary accordingly as follows

- $H < X_t$, $U_{\max_o} = U_e \left[\frac{U_2}{U_1} \right]$
- $X_t < H < X_s$, $U_{\max_o} = U_c \left[\frac{U_2}{U_1} \right]$
- $H > X_s$, $U_{\max_o} = U_c$

where

U_e = the exit velocity (assuming full expansion)

U_c = the axial velocity of the free jet downstream of X_t

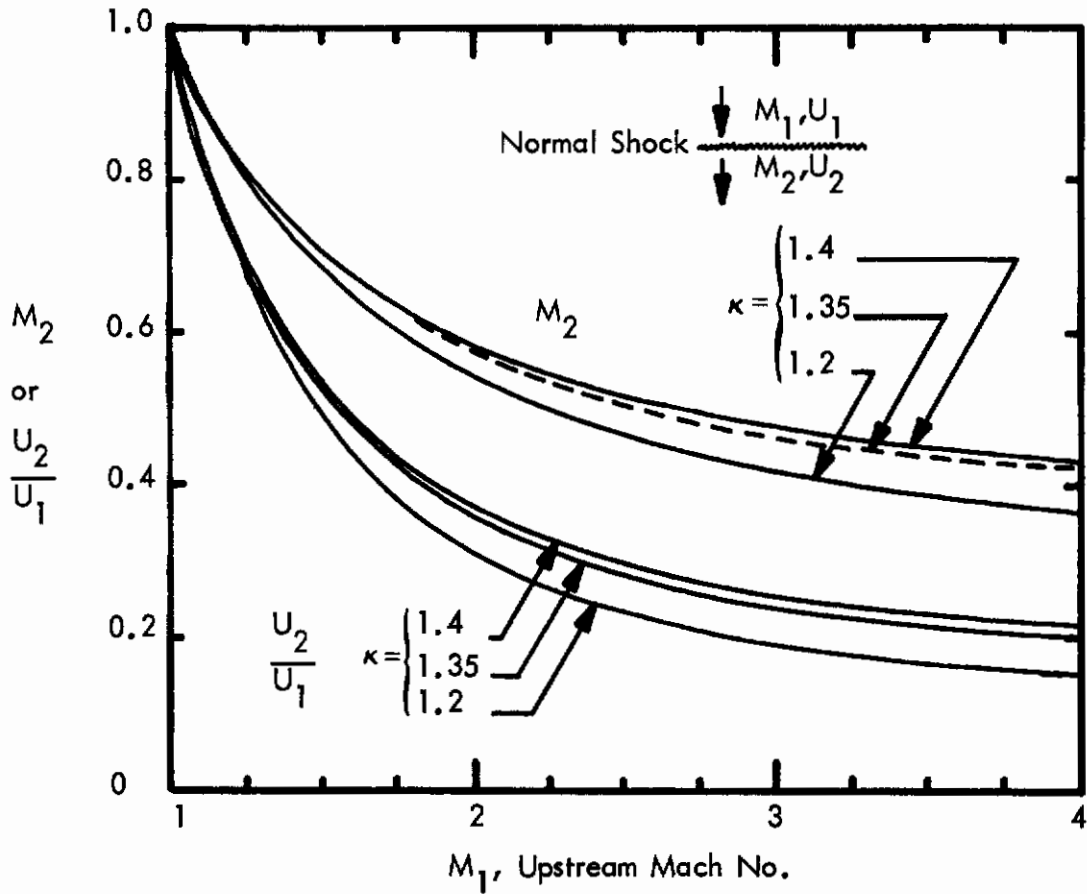


Figure 11. Change in Mach Number and Velocity Across Normal Shock Wave

Contrails

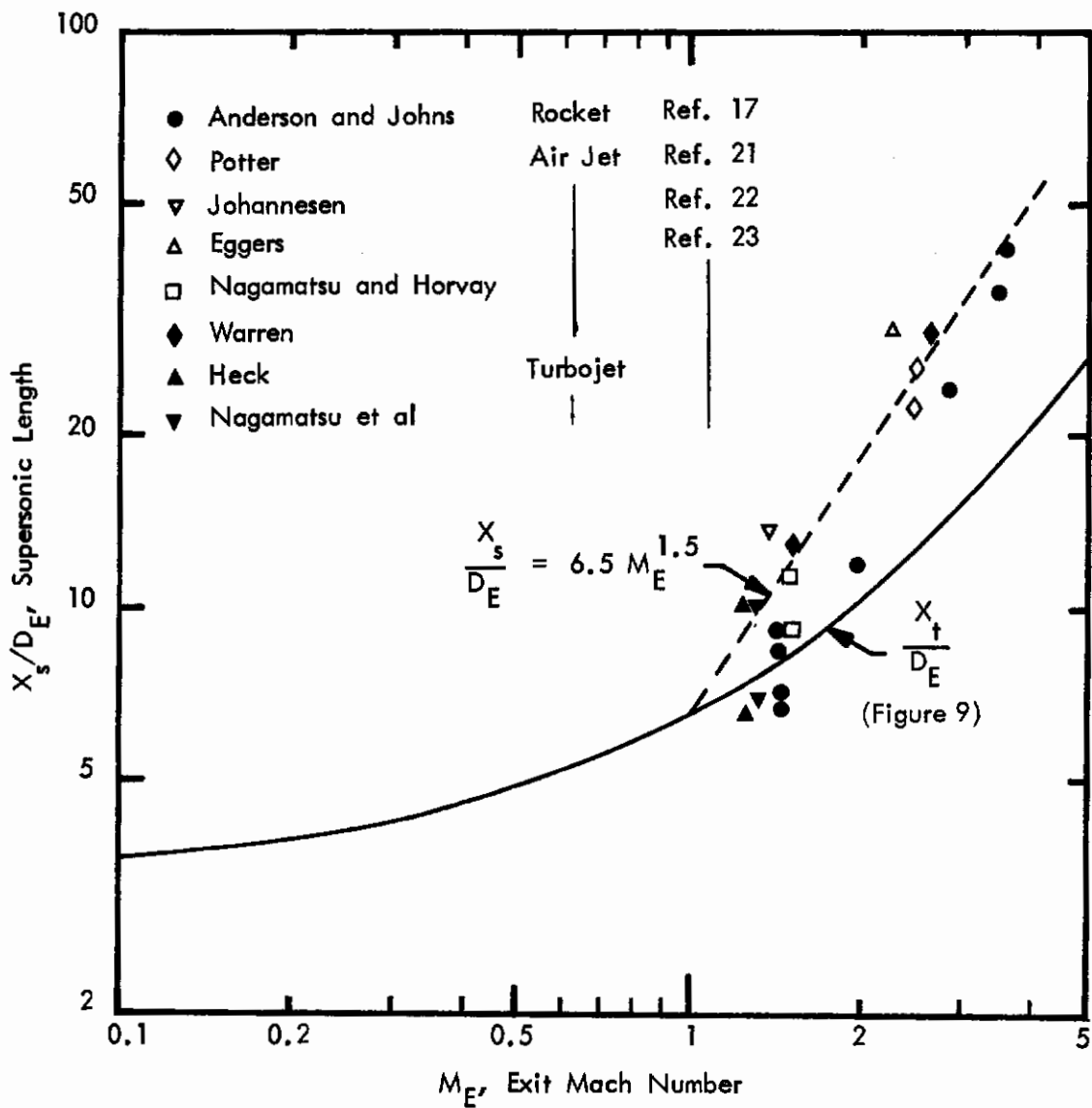
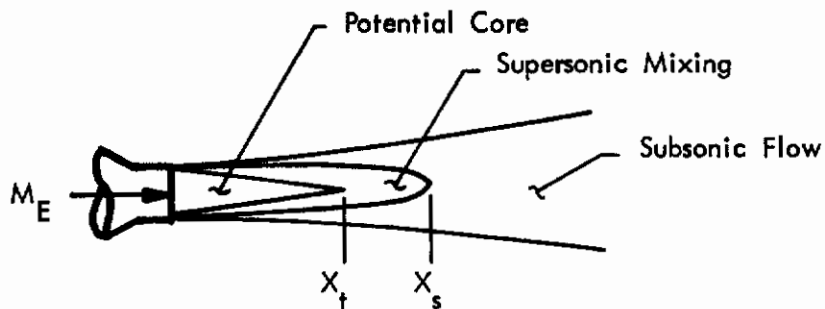


Figure 12. Supersonic Length vs Exit Mach Number Compared to Potential Core Length

Contrails

U_2/U_1 = the velocity ratio from Figure 11 for $M_1 = M_E$ or M_c respectively.

M_c = the axial Mach number downstream of the potential core.

It is necessary, therefore, to define U_c and M_c for a supersonic free jet in order to estimate the maximum velocity in the wall jet.

The axial decay in velocity of a fully expanded (shock free) supersonic jet might be expected to vary in a manner similar to that for a subsonic jet. This indeed appears to be the case as indicated in Figure 13. The graph shows the decay in the ratio U_c/U_e as a function of axial position relative to the potential core length specified in Figure 5. Experimental data for supersonic jets from References 17, 23 and 24 have been reduced to this same form for comparison with the subsonic results. The uppermost line represents the empirical fit to the observed decay for subsonic jets as discussed in Appendix C. The results from Reference 23 and 24 are shown by the dashed lines representing smooth values from the raw data. The data from Reference 17 covered experimental measurements from Mach 1.4 to about 3.5. However, the original data in Reference 17 covered the subsonic region only and were presented in the form of axial velocities relative to the axial velocity at the end of the supersonic length. Axial distance was normalized by the jet diameter at this point. This diameter was assumed equal to twice the "1/2 velocity" diameter of the jet. The reference velocity at the end of the supersonic length was assumed equal to the sonic velocity at the throat of the nozzle. With these assumptions and the data on jet spreading in Reference 17, it was possible to compute the values shown in Figure 13 by data points. The trend in decay of U_c/U_e for supersonic jets is bounded by the upper line in this figure and, with the exception of results from Reference 24, shows approximately the same $1/X$ slope as for subsonic jets. Again, it is important to note that the data cover a wide range of jet temperatures with no effect of temperature discernable. However, there is a distinct trend toward lower values of the relative velocity at a given axial position as Mach number increases. Based on the data in Figure 13, this effect can be accounted for, to a first approximation, by the following empirical expression for axial velocity decay of supersonic jets.

$$\frac{U_c}{U_e} \approx \left[1 + \left(\frac{M_E^{0.25}}{1.5} \frac{X}{X_t} \right)^6 \right]^{-1/6} \quad (13)$$

where X_t is given by Equation (7).

The axial Mach number upstream of the potential core is equal to the exit Mach number. Downstream of the supersonic length X_s , the flow is subsonic so that the flow Mach number is not required to define the wall jet velocity. Between these two points, the

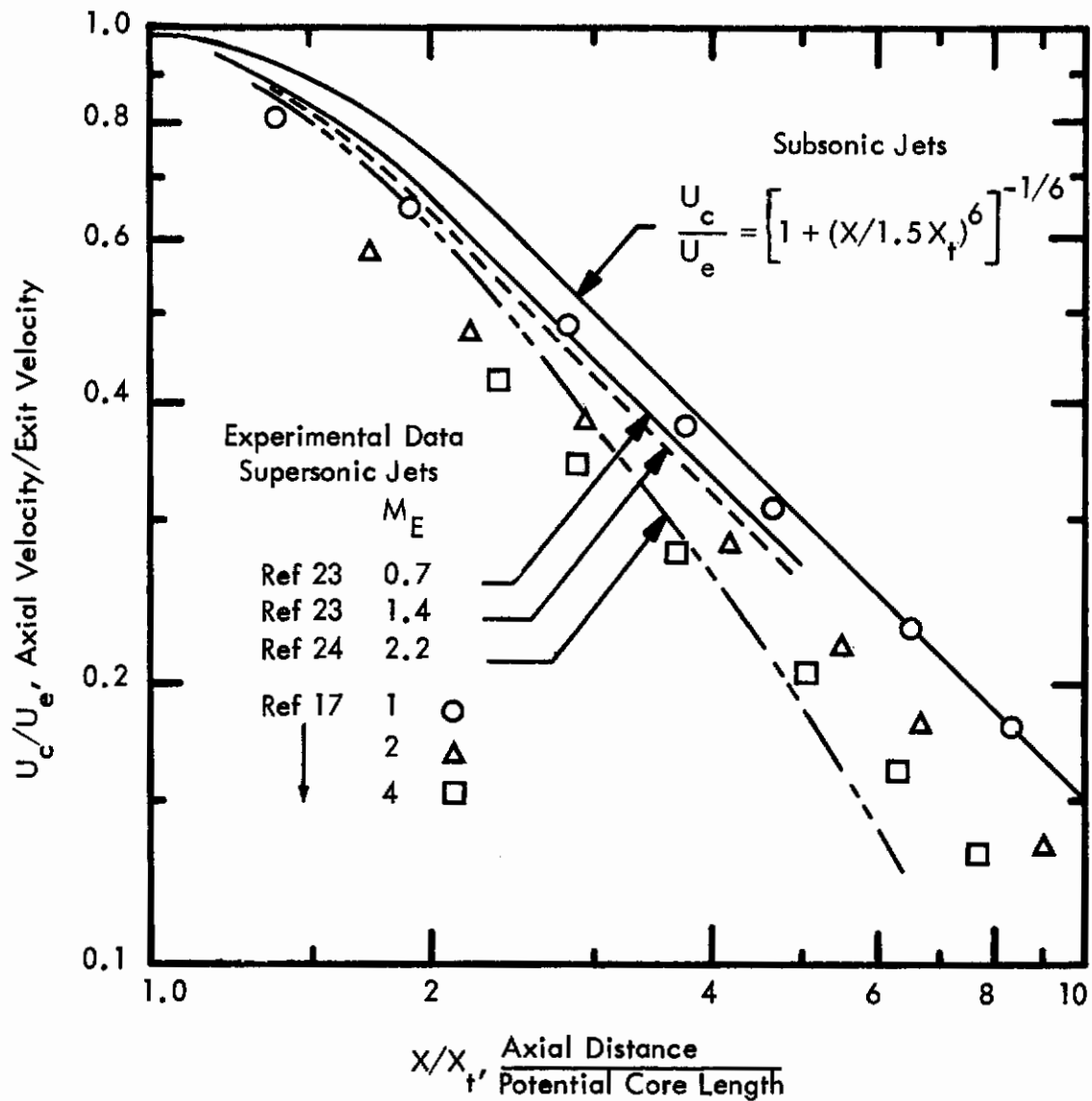


Figure 13. Comparison of Observed Decay in Axial Velocity for Subsonic Jets with Experimental Data for Supersonic Jets. (Data Points Calculated from Experimental Data in Reference 17 for $M_E = 1.4 - 3.5$ and $M_c < 1$)

limited data on decay in axial Mach number of supersonic jets indicates that a simple linear decay rate with the dimensionless position X/X_t can be assumed.^{23,24} That is, for axial positions between X_t and X_s , the axial Mach number (M_c) can be approximated by

$$M_c = M_E - \frac{(M_E - 1)^6}{X_s - X_t} (X - X_t) \quad (14)$$

While further refinements on this topic are possible, they are not warranted for this report. The flow in supersonic jets is often complicated by the presence of shock patterns due to lack of ideal expansion to the atmosphere at the nozzle exit. Thus, this analysis, based on a simple correlation of available experimental data, should be considered only as a rough approximation which can be used for estimating mean flow conditions for supersonic VTOL jets. References 15, 16, 18 and 23 are representative sources containing a more detailed discussion of jet flow properties relative to their noise generation.

To illustrate the significance of the preceding concepts, the maximum initial radial velocity for a 90° incidence supersonic VTOL jet has been estimated as a function of nozzle elevation for four representative cases. Each represents a condition for which noise data are available.

- $M_E = 1$ (Typical for subsonic turbojets)
- $M_E = 1.15$ (Typical for turbojets)
- $M_E = 1.88$ (Applicable to supersonic VTOL model jet data)
- $M_E = 3.25$ (Typical for rockets)

The results are shown in Figure 14 by the initial wall velocity relative to the jet exit velocity. The principal result immediately apparent is that for nozzle exit Mach numbers much greater than 1, the initial wall jet velocity should be substantially less than the nozzle exit velocity. For supersonic jets, the maximum value of this wall velocity will occur when the nozzle elevation is equal to the supersonic length X_s . Thus, considering this initial velocity as a preliminary measure of the noise output of the wall jet relative to its parent free jet, it is clear that the wall jet noise from supersonic VTOL jets should contribute much less to the total noise output than would a sonic or subsonic jet. This will subsequently be shown to be the case.

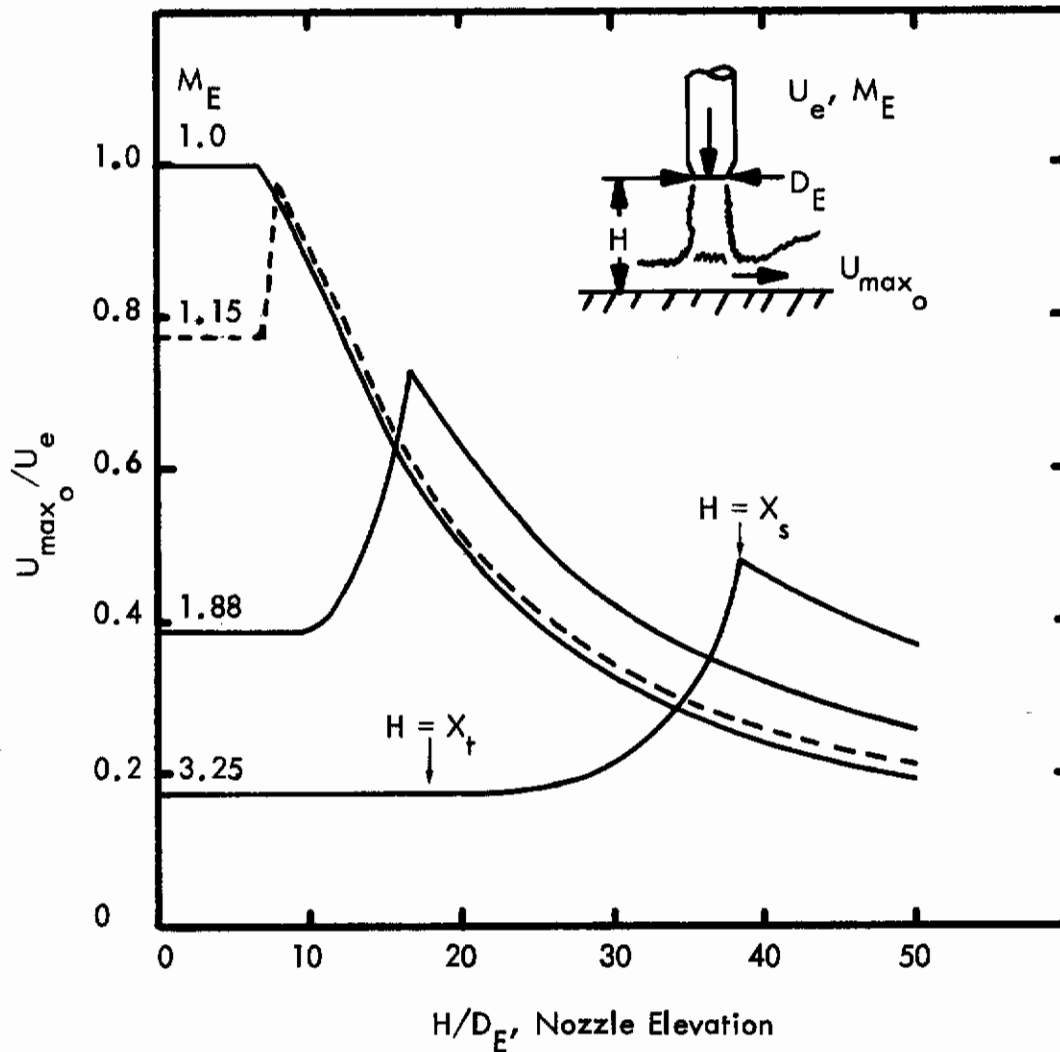


Figure 14. Estimated Initial Radial Velocity of Wall Jet Relative to Jet Exit Velocity as a Function of Nozzle Elevation and Exit Mach Number for Supersonic Jet. $D_E =$ Fully Expanded Jet Diameter.

c. Turbulent Flow in a Wall Jet

Aerodynamic noise generated by the wall jet will be a function of the turbulence intensity and scale in the flow. Although data on these parameters in wall jets were not available, related information is provided by measurements of fluctuating pressures on the surface of a "ground" plane under an impinging subsonic ambient air jet.¹⁰⁻¹² The rms amplitude (\tilde{p}) of these pressure fluctuations varies with nozzle elevation (H), radius from the impingement point (R), and incidence angle (β). The ratio of \tilde{p} to the dynamic pressure ($1/2 \rho U_e^2$) at the exit for a jet of 90 degrees incidence is shown in Figure 15 for several values of H/D and for a limited range of R/D. According to the data in Reference 12, the fluctuating pressures did not change appreciably for incidence angles from 70 to 90 degrees. However, Figure 15 shows that at a slant nozzle elevation of 7 diameters, and grazing incidence ($\beta = 3^\circ$), the fluctuating pressure is essentially independent of radius and equal to 1/4 to 1/2 of the level observed for the vertical jet at the same nozzle-ground plane distance. Note that if \tilde{p} were normalized to the local dynamic pressure in the flow, the ratio of fluctuating to dynamic pressure would increase for nozzle elevations beyond about 3.8 diameters which is the estimated length (X_1) of the potential core for this Mach 0.12 jet.

As noted by Hodgson, the fluctuating pressure under a wall jet, for a vertical nozzle elevation of about 0.5 diameters, decreased with radius such that the ratio of \tilde{p} to local dynamic pressure in the wall jet was constant, and defined by¹⁰

$$\frac{\tilde{p}}{1/2 \rho U_{\max}^2} = 0.134 \quad (15)$$

where U_{\max} = local maximum radial velocity of wall jet.

An estimate can be made of the turbulence intensity in the wall jet if it is assumed that the fluctuating pressure is of the order of $\rho U \tilde{u}$, where \tilde{u} is the rms fluctuating velocity. Thus, based on the work by Hodgson

$$\frac{\tilde{p}}{1/2 \rho U_{\max}^2} = \frac{\rho U_{\max} \tilde{u}}{1/2 \rho U_{\max}^2} = 2 \frac{\tilde{u}}{U_{\max}} = 0.13 \quad (16)$$

If the maximum local velocity fluctuations occur at the 1/2 velocity point in the wall jet, then, the intensity of this local turbulence would be about 0.13; slightly greater than an intensity of 0.1 observed in the mixing zone of free jets.²

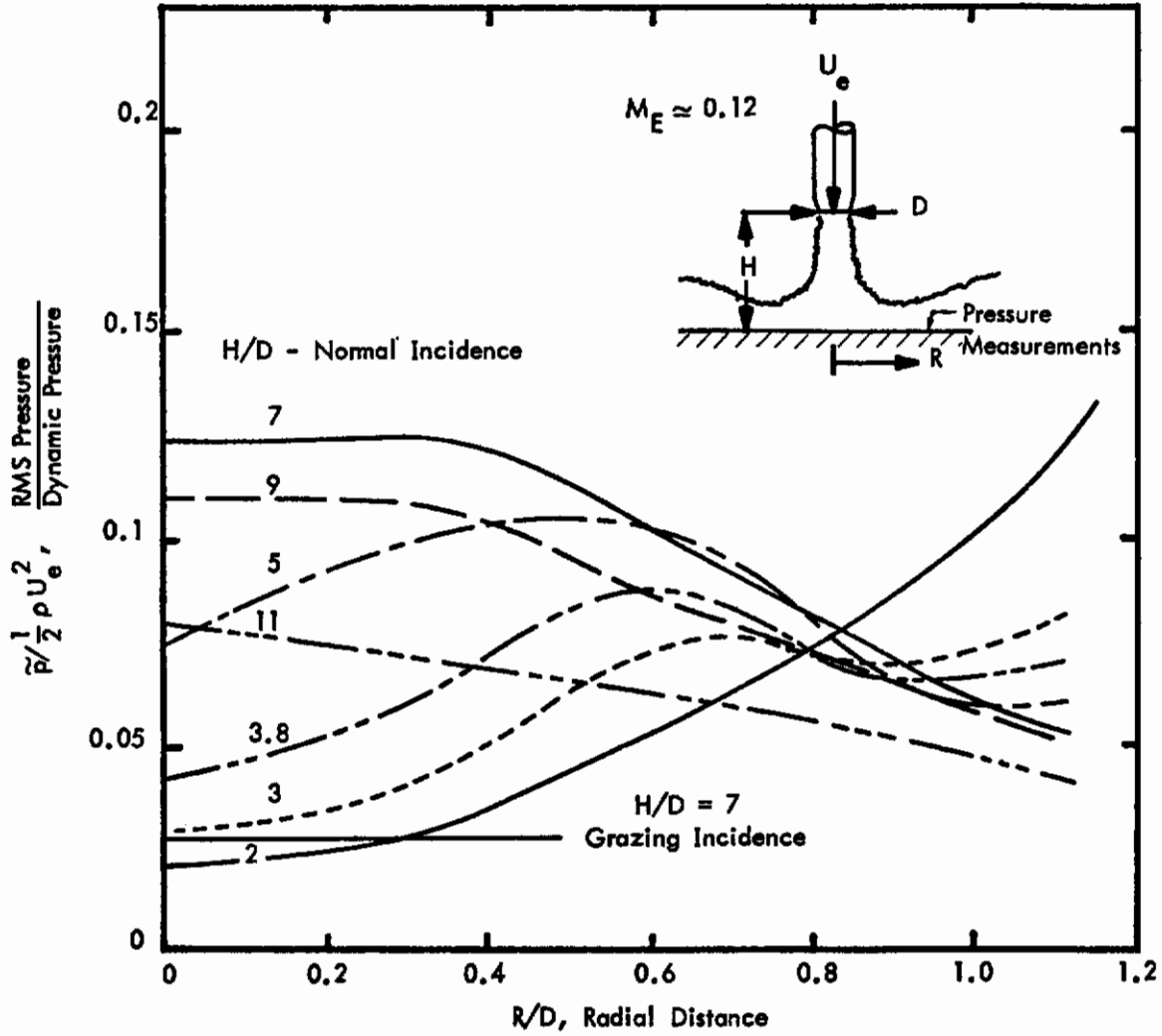


Figure 15. Fluctuating Pressures on Ground Under a Vertical and Grazing Subsonic Air Jet (Data from Reference 12)

From cross-correlation measurements of the fluctuating pressures, a characteristic length or scale of the pressure field was shown to be of the order of 0.6 to 1.0 nozzle diameters for positions within one nozzle diameter of the impingement point.¹² According to Figure 8(b), the 1/2 velocity thickness ($Z_{1/2}$) was approximately 0.33 D for $R/D < 3$ at a nozzle elevation of 4 diameters. Thus, $Z_{1/2}/D$ is close to the range observed for a correlation length, verifying that $Z_{1/2}$ is a suitable measure of a characteristic length in the wall jet flow.

The spectrum of the fluctuating pressure provides an estimate of the noise spectrum radiated by the wall jet. Available spectrum measurements are compared in Figure 16, in terms of relative octave band levels, on a non-dimensional frequency scale given by the Strouhal number $fZ_{1/2}/U_{\max}$.^{10,12} The spectrum levels reported in Reference 12 were originally normalized to a frequency scale given by fD/U_e . This scale was converted to that in Figure 16 by assuming $Z_{1/2} \approx 0.33 D$ and $U_{\max} \approx 0.785 U_e$. These conversion factors were computed with the procedures outlined in part (a) of this section for the case where $R/D = 1$ and $H/D = 7$.

The relative spectrum data in Figure 16 indicate a peak for $fZ_{1/2}/U_{\max} \approx 0.1$ to 0.2 from both sets of measurements involving two substantially different nozzle elevations. Again, this confirms that characteristic dimensions of the wall jet tend to be independent of nozzle height. The same conclusion is reached in a study of structural response to a wall jet.¹¹ The limited data in Figure 16 do not clearly establish the spectrum shape below the peak frequency. However, one would expect that levels below the peak frequency would be higher (i.e., lower rate of roll-off) for higher nozzle elevations where the larger scale eddies in the parent impinging jet would have developed.

d. Summary of Wall Jet Flow Characteristics

The principal characteristics of the flow properties of a deflected jet have been reviewed to establish simplified models or concepts useful for analyzing the noise generation from such jets. The availability of the new experimental data in Appendix C assisted greatly although there are many details of the flow as yet undefined. The principal findings may be summarized as follows:

- The deflection by the ground of a vertical jet forms a wall jet whose major dimensions are proportional to the exit diameter of the parent jet and nearly independent of the nozzle elevation.
- The ground plane does not influence the parameters of the undeflected flow.
- The maximum radial velocity (U_{\max}) of the wall jet is equal, initially, to the axial velocity of the incident jet and then decays as R^{-a} , where a is ~ 1.1 to 1.3 for small jets and is expected to approach 1.0 for full scale jets (Figures 7, 8(a)).

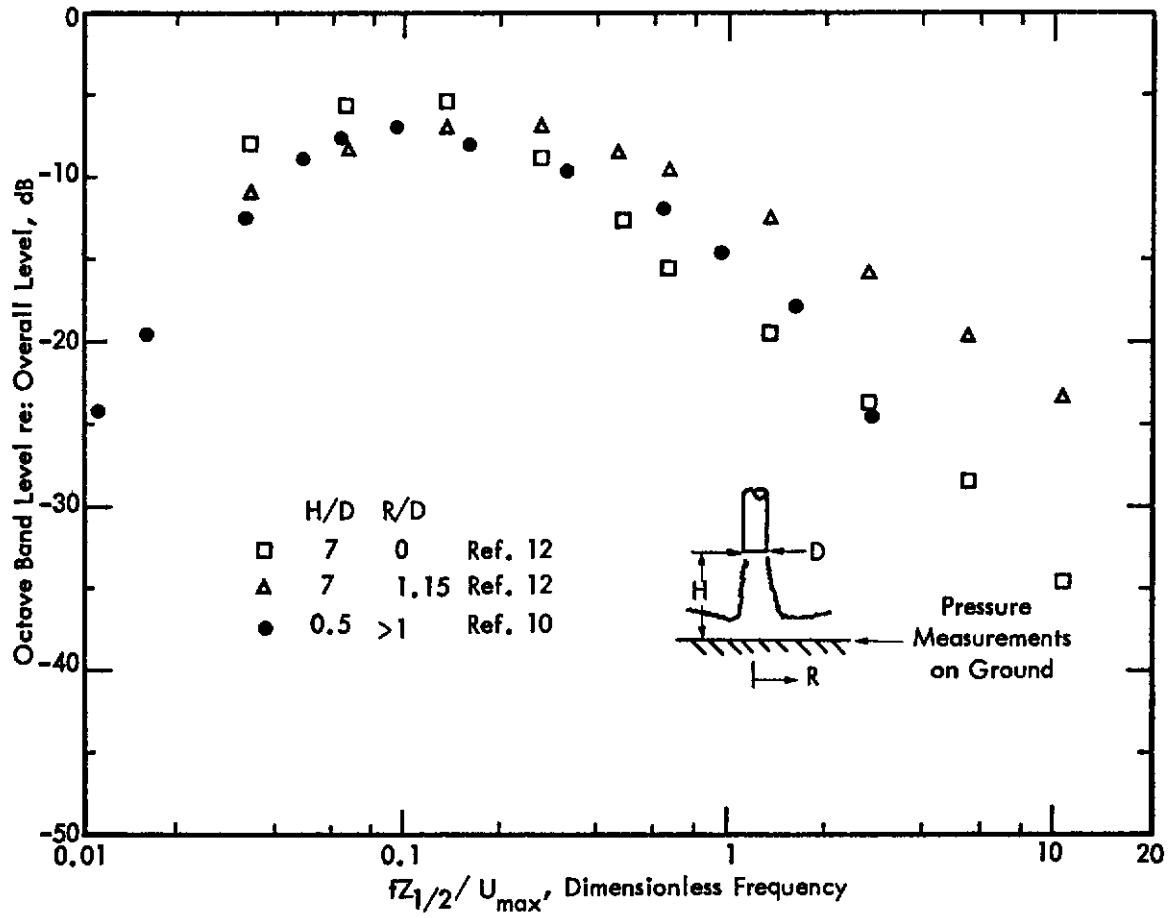


Figure 16. Relative Octave Band Levels for Pressure Fluctuations under Wall Jet.

- The characteristic thickness or scale of the wall jet is given by the thickness of the $1/2$ velocity point ($Z_{1/2}$). This thickness remains approximately constant for a radius of about 1 to 1.5 nozzle diameters and then increases directly with radius (Figure 8(b)).
- The velocity decay of free subsonic jets is expected to collapse on a single curve related to the length of the potential core (Figures 9, 13).
- A compilation of data on velocity decay of supersonic jets, combined with the above concept, provides a preliminary basis for estimating the initial radial velocity for wall jets formed from supersonic jets (Figures 11 through 14). Wall jet velocities are expected to always be subsonic, or at least never supersonic for vertically impinging supersonic jets.
- Pressure fluctuations on the ground under a wall jet are 2 to 4 times greater than those in a free jet at comparable axial positions (Figure 15).
- The spectra of these pressure fluctuations, presumed representative of the spectra of noise radiated by the jet, show a consistent peak Strouhal number given by $fZ_{1/2}/U_{\max} \sim 0.15$ (Figure 16).

3. JET NOISE

Near field noise levels for jet-powered VTOL aircraft will be dominated by the direct and reflected noise generated by the turbulent exhaust. The foundation of jet noise theory was formulated by Lighthill nearly twenty years ago when he showed that a fluctuating gas flow generates, in the atmosphere outside the flow, an acoustic field equivalent to that produced in a stationary medium by a system of externally applied stresses.^{3, 25} Subsequent refinements to the theory have improved its application to the specific case of turbulent jets. This has included the distinction by Lilley of the two mechanisms, self-noise and shear noise, generally responsible for low frequencies and high frequencies, respectively, in subsonic jet noise generation.²⁶ Other refinements have been proposed by Ffowcs Williams, Ribner, Lighthill and Pao among others, on the effect of eddy convection and on the efficiency and directional characteristics of subsonic and supersonic jets.^{27, 28, 3, 29} However, development of purely theoretical approaches to jet noise prediction is seriously hindered by requiring that acoustic sources be defined in terms of specific turbulence properties which vary widely over the extended noise generating region in the jet. This extended nature of the source is, in fact, the single most important feature of jet noise that must be accounted for when predicting the near field noise field. It will be particularly important for VTOL jets.

Relying heavily on dimensional analysis of flow similarity in a jet, and with support from experimental data, semi-empirical methods have been developed for jet noise prediction which partially bridge this gap between theory, based on discrete sources, and practical methods which account for the extended source. Ribner, Powell, Franken et al, Eldred et al, Potter and Crocker and Nagamatsu, among others, have utilized this approach to analyze the noise from jets and rockets.^{30, 31, 32, 15, 18, 23} Extensive experimental data supporting this approach are available.^{15, 18, 21, 23, 32-35}

Before attempting to develop a near field prediction method for VTOL jets, it is desirable to examine the experimentally observed trend in their noise characteristics as a function of nozzle height and exit Mach number. This will clearly establish several overriding features which will provide a proper perspective for evaluation of the dominant noise sources.

a. Acoustic Power of VTOL Jets

Consider first the total acoustic power radiated by a VTOL jet. The available experimental data on change in acoustic power with nozzle height for VTOL jets is shown in Figure 17. Table II summarizes the available sources of VTOL jet noise data, some of which were utilized for this figure. This includes the results from the acoustic model tests of a vertical air jet described in Appendix C.

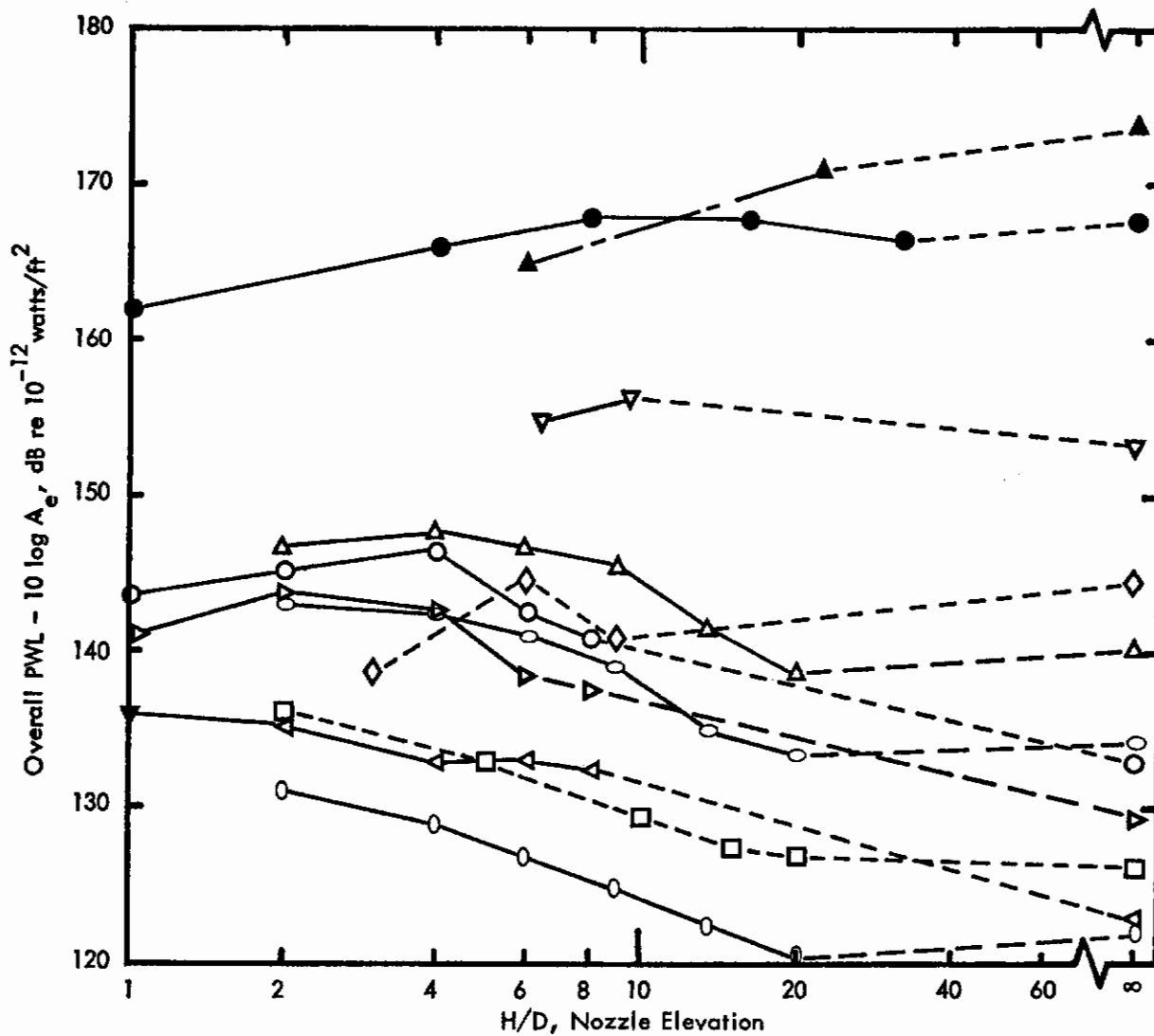
The data shown in Figure 17 are drawn primarily from model tests of ambient air jets.^{4, 37, 39-41} Results are also shown for one simulated VTOL rocket test using a 1000 lb thrust solid rocket.³⁸ With the exception of the full scale data from tests on a VTOL turbofan, acoustic power level data were also available for the undeflected jet condition. For the full scale data, an estimated free field power level was used to relate change in power level to distance above the ground.⁴³ The full significance of the data in Figure 17 can be better appreciated with the aid of the following analysis.

The noise generated per unit length for a subsonic jet is normally assumed to be approximately constant along the mixing length between the exit plane and the end of the potential core.^{15, 30, 31} Downstream of this point, in the fully developed turbulent flow region where similarity laws hold, the acoustic power radiated per unit length is predicted to follow an X^{-7} law or alternately $X^{-6} \ell^{-1}$, where X is the axial distance from the exit and ℓ is a characteristic mixing length.³⁰ As suggested by Lighthill, this decay law may reduce to essentially X^{-6} since the characteristic mixing length in a fully developed jet is expected to change slowly within the first 20 nozzle diameters.³ For a supersonic jet, the initial mixing process of the jet is delayed by the supersonic flow velocities which do not allow mixing flow disturbances to propagate as effectively as in a subsonic jet.²¹ This effect, perhaps compounded by the reduced acoustic efficiency of the high speed flow near the exit, apparently causes the rate of acoustic generation per unit length ($W(X)$) to increase initially, reaching a peak somewhere

TABLE II
SUMMARY OF VTOL JET TEST DATA

Reference	Investigator	Nozzle Diameter inches	Exit Mach Number	Exit Velocity ft/sec	Nozzle Elevation N.D. (a)	Near Field Data	Far Field Data	Model	T _t °R (j)	A ₀ Slugs/ft ³ x 10 ⁻³ (k)	X _r /D(l)
Model Data											
37	Oas	1.38	1.88	1620	1-32	Contours	PWL	Air	520(c)	4.04	10.2
38	Cole, et al	2.6	3.25	5500	6, 22	2(b)	PWL, D(m)	Rocket	2910	0.94	17.2
4	Morgan, et al	3	1.15	1900	1-16	1	-	Heated Air	1460	1.07	7.1
			1.6	1900					880	2.13	9.0
39	Marth	1.5	0.66	735	2-20	-	PWL, D	Air	560	2.4	5.4
40	Plumlee	3.5	1.0	1175	3-9	Contours	PWL(c)	Air	575	2.14	6.5
41	Potter and Ollerhead	2.5	0.41	460	1-8	-	PWL(n)	Air	530(c)	2.41	4.6
			0.62	675	1-8	-	-	Air	2.51	5.3	
			0.85	896	1-8	-	-	Air	2.66	6.2	
Full Scale Data	This report	0.75	0.60	660	2-20	Contours	PWL, D	Air	545	2.42	5.2
			0.85	910					2.59	6.0	
			1.0	1045					2.72	6.5	
5	Rose and Sailors	11.5(c)	1.1(e)	2200	2.2, 12.5	6(b)	-	XV-48(f)	2100(e)	0.71	7.0
42	Fleming and Scholten	18.5(c) 14.4(c)	(Turbofan)	-	5.1, 70	-	(d)	DO-31(g)	-	-	6.0
			(Lift Jet)	2100(g)							
43	Smith and McFarland	18.5(c) 18.1	0.817(e)	1447(jet)	6.5, 9.7	Contours	PWL, D	P1127(h)	1458	0.95	6.0
			0.832	1035(fan)						721	1.95

(a) Data also available for free or horizontal jet.
 (b) Number of near field test points designated by number.
 (c) Estimated.
 (d) Octave band levels on ground at 328 foot radius.
 (e) Data also available for 3 lower power settings.
 (f) With 6 J-85 Turbojets.
 (g) With 2 Pegasus 5 Turbofan and 8 RB-162-4 Turbojet Engines.
 (h) With 1 Pegasus Turbofan (2 exhaust ducts each for by-pass and primary jets)
 (i) Estimated PWL from Near Field Data.
 (j) Total temperature of exhaust.
 (k) Exit density.
 (l) Estimated length of potential core (Figure 9).
 (m) D signifies directivity data available.
 (n) Corrected for discrete ring tones.



Symbol	M _E	Reference
●	1.88	37
▲	3.25	38
□	0.66	39
◇	1.0	40

Symbol	M _E	Reference
○	0.85	41
▷	0.62	41
◁	0.41	41
▽	0.8	43

Symbol	M _E	Reference
▲	1.0	This Report
○	0.85	This Report
○	0.6	This Report

Figure 17. Overall Power Level Per Unit Nozzle Area (A_e) for VTOL Model and Full Scale Jets Versus Nozzle Elevation

between the end of the potential core (X_c) and the supersonic length (X_s). Experimental verification of this concept for axial distribution of the power in jets is illustrated in Figure 18 with model data for a supersonic ambient gas jet from Potter and for a sonic heated jet from Simcox and Grande.^{21,35} The latter limited data contained only the peak octave band power level for a model heated air jet simulating typical turbojet engine conditions. The experimental technique was the same for both tests and employed a direct reverberation room measurement of source power distribution. The distribution in power per unit length in Figure 18 is expressed in non-dimensional form as power per unit core length relative to the total power (i.e., the area under each curve, when plotted on a linear scale, is unity).

The data for the sonic jet closely follow the expected X^{-6} trend. The supersonic jet data indicate nearly the same roll-off in power distribution beyond the core tip but show an $X^{1.4}$ increase along the initial mixing region. It should be pointed out that Eldred has shown that power distribution for a full scale jet engine (comparable to the Mach 1.04 model jet in Figure 18) has roughly a constant power per unit length up to the core tip but decreases more like X^{-3} downstream of this point.¹⁵

Either of the curves in Figure 18 can be roughly approximated by two straight line segments. The following will illustrate roughly how the power is distributed upstream or downstream of the intercept point X_c of these two segments. For either curve:

Case 1, $X \leq X_c$

$$\text{let } W(X) = W_c \left[\frac{X}{X_c} \right]^m, \quad m \geq 0 \quad (17)$$

where W_c = power per unit length at intercept point X_c .

Case 2, $X \geq X_c$

$$\text{let } W(X) = W_c \left[\frac{X_c}{X} \right]^n, \quad n > 1 \quad (18)$$

For either segment, the partial power generated within the segment will be

$$W = \int_{X_1}^{X_2} W(X) dX \quad (19)$$

where $X_1, X_2 = 0, X_c$ for Case 1 and X_c, ∞ for Case 2 respectively.

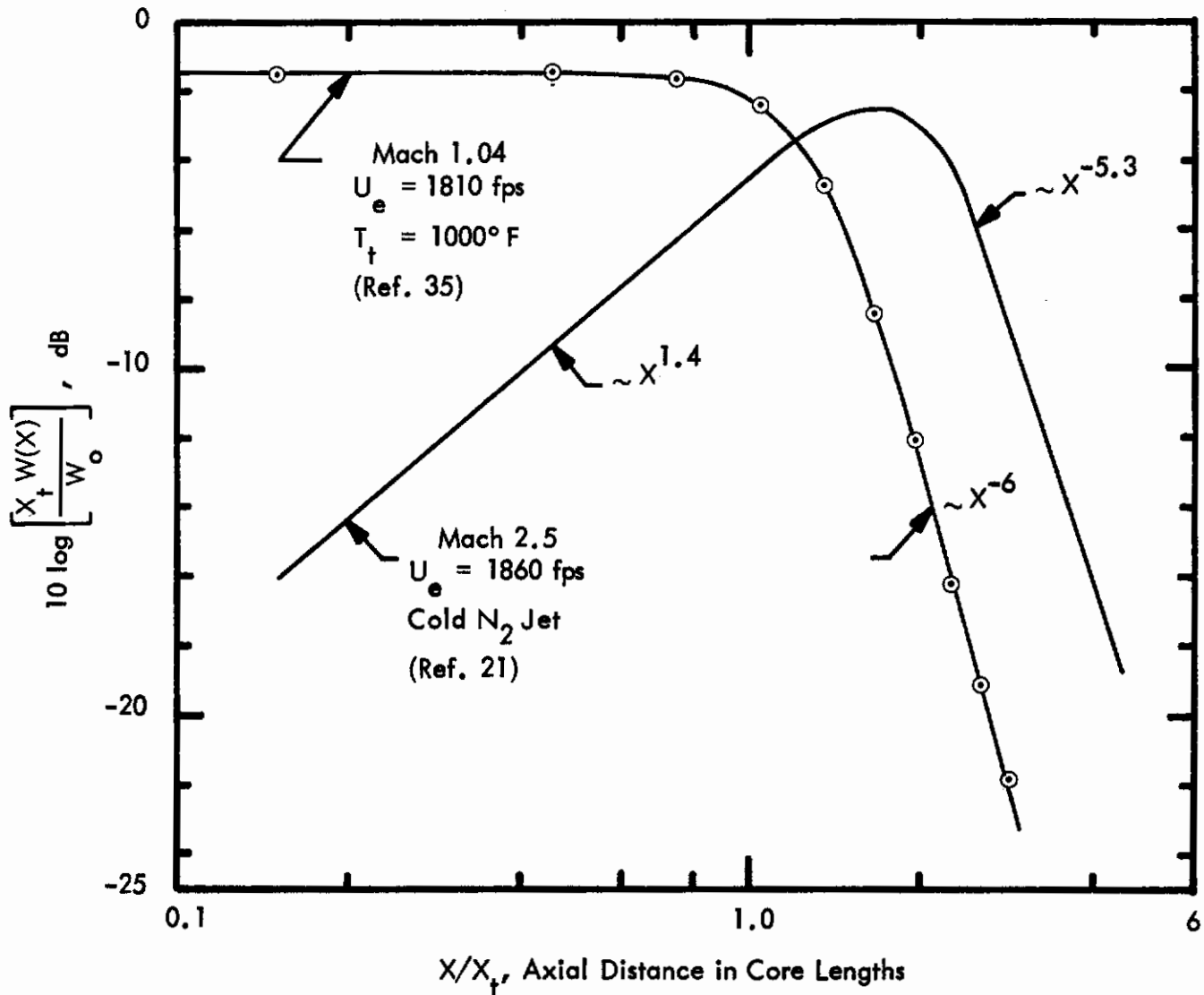


Figure 18. Normalized Axial Distribution of Measured Sound Power in Sonic and Supersonic Jets. (Area Under Each Curve is Unity.)

Carrying out this integration, the ratio of power generated upstream (W_1) ($X < X_c$) to that generated downstream (W_2) of the peak can be approximated by

$$\frac{W_1 (X < X_c)}{W_2 (X > X_c)} \approx \frac{n - 1}{m + 1} \quad (20)$$

Thus, for the sonic and supersonic jet data in Figure 18, this ratio becomes

Sonic Jet	$m \approx 0$ $n \approx 6,$	$\frac{W_1}{W_2} \approx 5$
Supersonic Jet	$m \approx 1.4$ $n \approx 5.3,$	$\frac{W_1}{W_2} \approx \frac{4.3}{2.4} \sim 2$

The implication for VTOL jets is that the noise power generated by the free (undeflected) flow for sonic and subsonic jets would not be significantly reduced until the nozzle elevation is substantially less than the core tip length. However, for a supersonic VTOL jet (such as a booster rocket), one would expect a substantial decrease in the total jet noise power generated for nozzle elevations comparable to the core length.

Figure 18 can now be applied to the data in Figure 17. By carrying out an integration of the power distribution curve from the nozzle exit up to any given axial distance equal to the nozzle height H , the expected decrease in free jet noise power alone can be estimated for various nozzle elevations. This simply assumes that that portion of the jet beyond the nozzle elevation distance is destroyed and no longer contributes to the basic jet noise generation. The result of this evaluation is compared, in Figure 19(a) and (b) for supersonic and sonic or subsonic jets respectively, to the data from Figure 17. For the sake of comparison, the latter have been normalized to the change in power level relative to the free field value as a function of nozzle elevation expressed in estimated potential core length units. This key figure clearly shows that power is actually increased, rather than decreased for subsonic jets with $H/X_c < 2$. Apparently, another source of sound power is present when such jets are deflected by a ground plane.

b. Acoustic Power of Free Jets

Available measured values for the overall power level for the free (undeflected) jets generally agreed within 1.5 dB with values predicted by the dashed line in Figure 20. This figure summarizes data on overall sound power level per unit exit area of subsonic and supersonic free jets as a function of exit velocity, assuming full expansion of the jets. For jets with exit velocities less than about 2000 ft/sec, the total power is

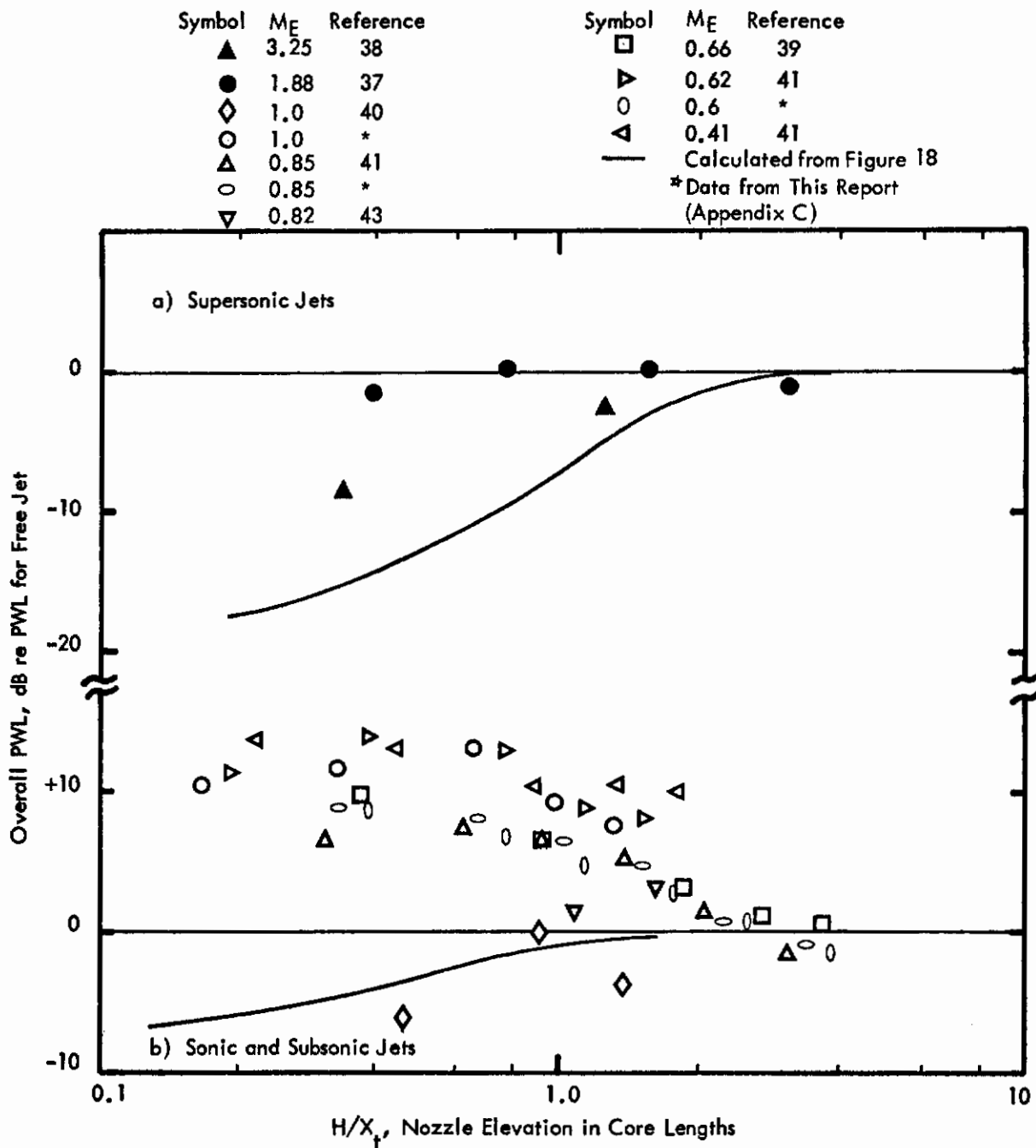


Figure 19. Calculated and Observed Change With Nozzle Elevation in Overall Power Level for VTOL Jets. Calculated Change Based on Integration of Power Distribution in Figure 18.

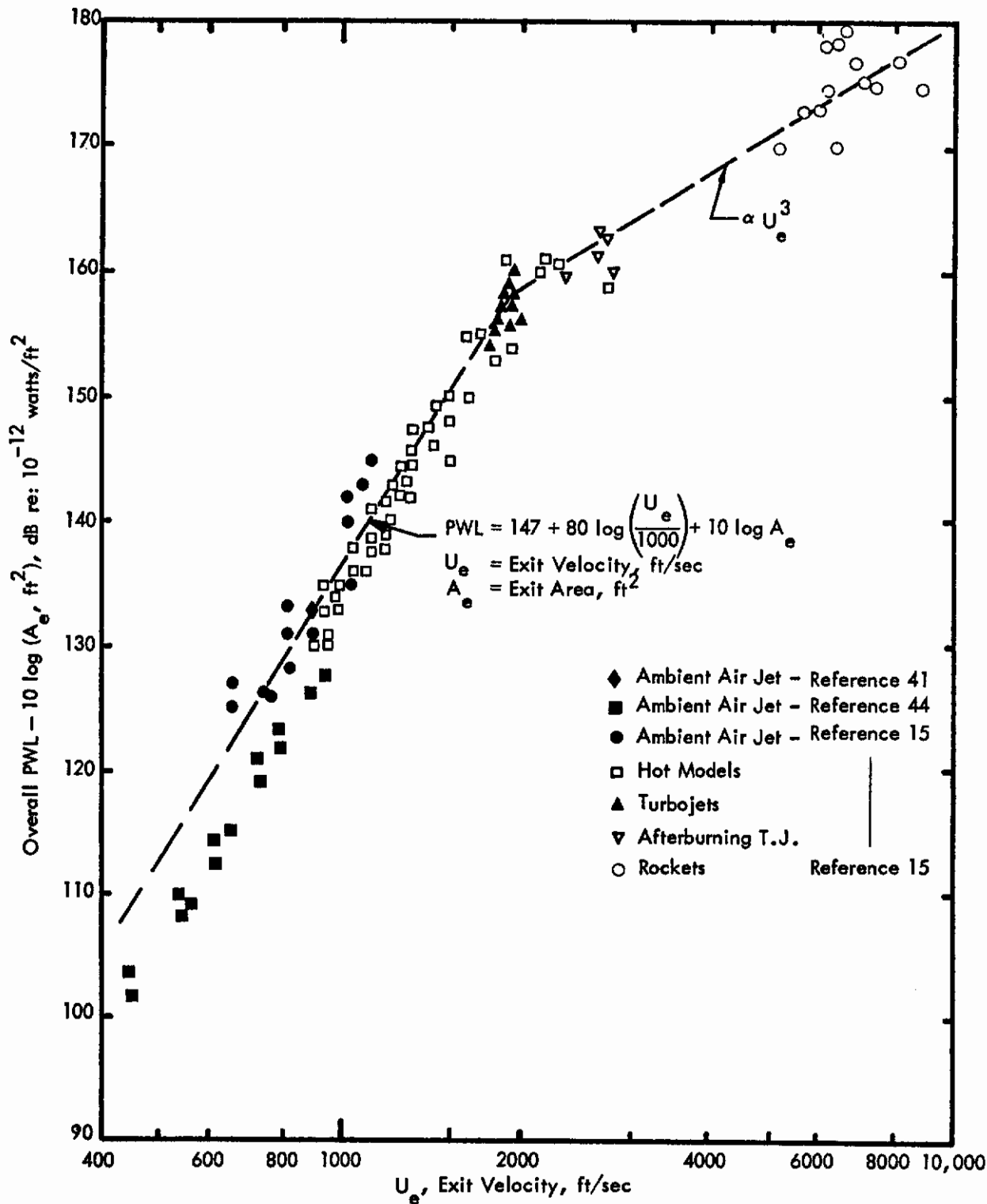


Figure 20. Overall Power Level per Unit Exit Area versus Exit Velocity

Contrails

predicted fairly well by the simplified U^8 law noted in the figure. This expression was used for predicting the overall power level for the undeflected jet case for the full scale data from Smith and McFarland.⁴³ The expression is equivalent to Lighthill's equation for sound power of ambient low speed jets given by

$$W_o = K \rho_o A_e U_e^8 / c_o^5, \quad \text{watts} \quad (21)$$

where

$$A_e = \text{exit area, ft}^2$$

$$\rho_o = \text{ambient air density, lb sec}^2/\text{ft}^4$$

$$U_e = \text{exit velocity, ft/sec}$$

$$c_o = \text{ambient speed of sound, ft/sec}$$

$$K = \text{constant}$$

According to the expression shown in Figure 20, for jets with exit velocities less than 2000 ft/sec, the constant K in Equation (21) is 3.66×10^{-5} for W_o in watts. This agrees, within 0.5 dB, with the value of K reported by Howes.⁴⁶ The scatter about the mean line is not entirely due to experimental error but represents, in part, the known influence of other effects such as velocity profile at the jet exit, turbulence level at the exit, and jet density.^{31, 44, 3, 45, 47, 48}

Rocket boosters for VTOL aircraft, such as JATO bottles, have exit velocities well above 2000 ft/sec. For this type of rocket, the acoustic power is approximately equal to 1/4% of the mechanical power in the exhaust, or

$$W_o \approx 0.0017 \rho_e A_e U_e^3, \quad \text{watts} \quad (22)$$

where ρ_e, A_e, U_e = jet density, area and exit velocity in the same units as for Equation (21)

Thus, for rockets, the acoustic power varies as the third power of the exit velocity as indicated in Figure 20.

c. Jet Density Effects

According to Lighthill's theory, the acoustic power for a jet with a density different from the ambient air, should vary as the square of the jet density. Hubbard and Lassiter show agreement with this theoretical prediction according to measurements on unheated gas jets differing in density by over 25 to 1.⁴⁷ Industry practice for predicting jet noise on the ground from aircraft also utilizes a similar density correction.⁴⁹ However, the effect of density becomes less well defined for high temperature jets. Experimental data are reported by Plumlee, et al, for heated air jets with exit velocities ranging from 600 to 1400 ft/sec and exit static temperatures ranging from 540°R to 1100°R (equivalent to a 2 to 1 change in exit density).⁴⁸ For these data, the overall acoustic power varies approximately as the first power of jet density and eighth power of exit velocity.

A deviation from the theoretically predicted influence of jet density is expected for heated jets, since other effects have been neglected. These include the counteracting effects of convection of jet turbulence (tending to increase acoustic output), and the decrease in turbulence intensity (decreases acoustic output).^{3, 27-29} Density and temperature gradients in heated jets are also expected to influence the directivity and acoustic power output of a jet.^{15, 50} As suggested by Lighthill, the net result is that the acoustic power of heated jets is expected to vary approximately as the first power of jet density.³ Thus, an expression which can be used for scaling the overall power of jet noise for free jets at various operating conditions would be

$$PWL = 147 + 10 \log \frac{\rho_e}{\rho} + 80 \log \frac{U_e}{1000} + 10 \log A_e \quad (23)$$

where

ρ_e = jet density

ρ = a reference density

and

U_e = exit velocity – less than 2000 ft/sec.

Application of this density correction to free jet power level data, such as shown in Figure 20, does not appear to improve the data collapse significantly. Assuming ρ is the ambient density of air, the density correction ranges from about -4 to +1 dB for typical heated air jets, turbojets and smaller solid propellant rockets. Thus, Equation 23 can be used to estimate the change in overall power level for a given jet for

changing exit conditions. The reference density would be set equal to the jet density at a convenient reference condition, such as maximum power.

d. Excess Acoustic Power of VTOL Jets

Returning to Figure 19, it is clear that nearly all the data indicate that a VTOL jet generates substantially more acoustic power than expected from the free jet alone for nozzle elevations less than 1 to 2 core lengths. The solid line in Figure 19(b) represents the expected decrease in power level for a free subsonic jet alone as a function of nozzle elevation. The difference between this line and the observed power levels represents an estimate of the excess power generated by the deflected jet configuration. This excess power is clearly dependent on nozzle height but would also be expected to vary with velocity of the jet. The power level data on subsonic jets, presented earlier in Figures 17 and 19, have been utilized to compute this excess power.

(The Mach 1 VTOL jet data from Reference 40 were not utilized since they were based on rough estimates of sound power from near field measurements and the results do not appear to fit the trend of the other sonic or subsonic data. Supersonic VTOL data were not analyzed by this process due to lack of sufficient creditable data to establish trends. The free jet power level for the supersonic ambient jet data from Oas were approximately 14 dB above the expected values, and hence were not considered reliable for analysis of excess power for the VTOL configuration.³⁷⁾

The results are summarized in Figure 21 in terms of power level (normalized by the jet exit area) as a function of jet exit velocity. Data are shown for the free jet sound power by the closed symbols. The open symbols show the excess power computed from the measured values for VTOL configurations. For the latter, values are shown for nozzle height to core length ratios of 0.5, 1 and 1.5 to 2. The individual data sets plotted in Figures 18 and 19 were used (with interpolation to the 3 nozzle height conditions) to determine the deflected jet power levels for each case. Additional data at lower power conditions from the full scale tests, reported by Smith and McFarland, not plotted in Figures 18 and 19, are also included in Figure 21. Free jet power levels for these full scale VTOL data were calculated from Equation 23. Each open symbol in Figure 21 represents the computed power level (normalized to the exit area of the nozzle) necessary to make up the difference between the measured VTOL power level and the estimated remaining jet power level according to the solid line in Figure 19(b).

The model data fall approximately into 2 groups:

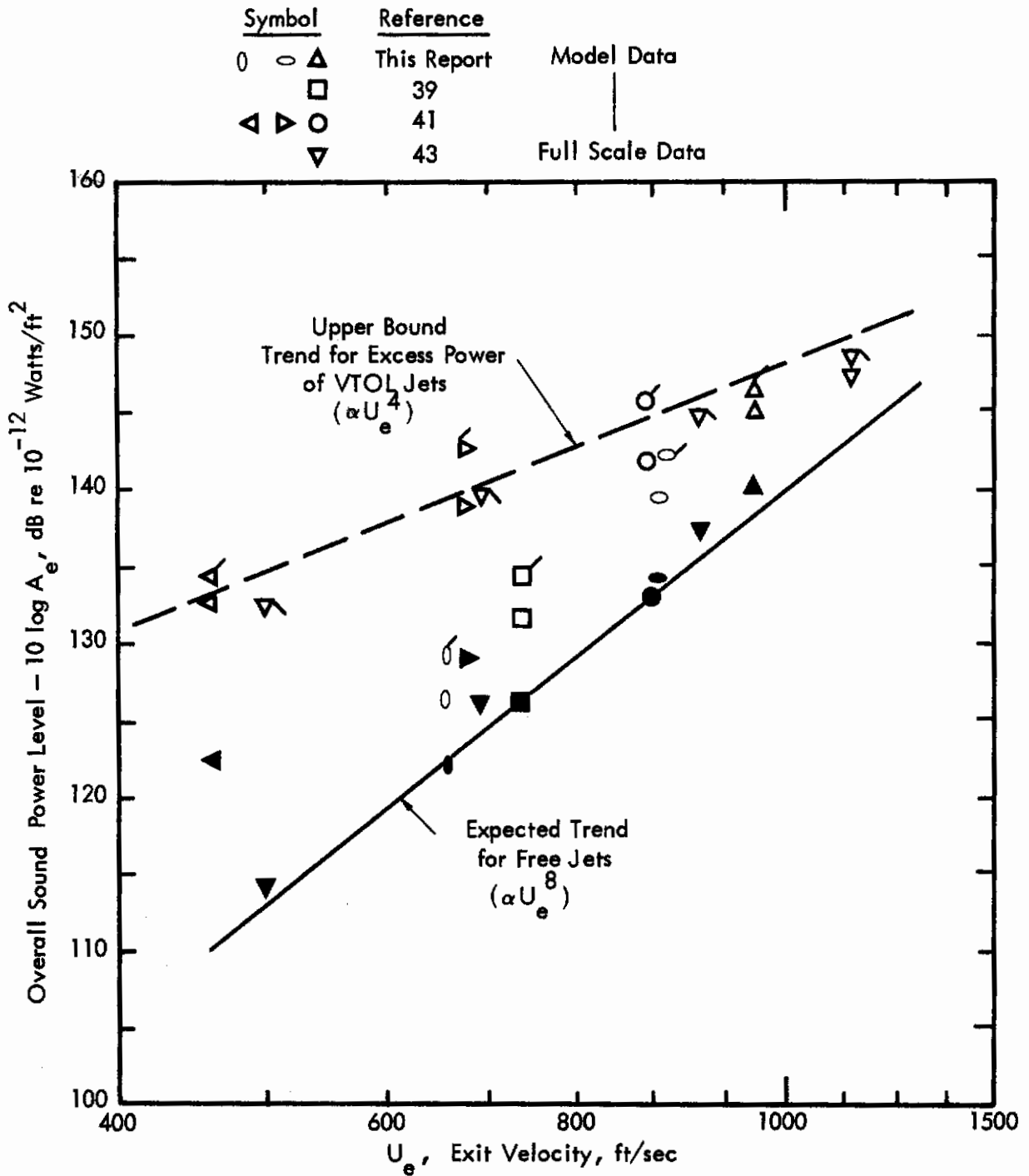


Figure 21. Summary Comparison of Normalized Sound Power for Free Sonic or Subsonic Jets (Closed Symbols) and Excess Power for VTOL Jets (Open Symbols) at Nozzle Elevations of 0.5 (/ Flag) 1.0 (No Flag) or 1.5-2 (\ Flag) Core Lengths. (Basic Symbol Code Same as in Figures 17 and 19)

Conclusions

- For free jets with measured power levels close to the expected values, the excess power level for a VTOL configuration is approximately 4 to 8 dB above the U^8 line. This approximate difference did not change with velocity according to results from this report. This suggests the excess noise is radiated as aerodynamic (jet) noise from the wall jet.
- Results from one test showed free jet power levels differing substantially from the expected U^8 trend, at lower velocities. In this case, the excess power levels for the VTOL configurations are bounded by a U^4 line. This suggests the excess power level was due to simple source (monopole) noise from fluctuations in the exhaust flow, or from acoustic sources within the exhaust.⁵¹ The measured sound power levels for the one set of full scale data available follow this same trend. Note that the full scale data were obtained on a dual-exhaust bypass fan engine. For purposes of plotting in Figure 21, an effective single-exhaust velocity was used which was equal to that of an engine with the same total thrust and mass flow.
- The basic trends observed for the model and full scale data are not changed substantially if the estimated jet impingement velocity is used instead of the exit velocity for correlating the excess power of the VTOL configurations. This impingement velocity is about 70 to 75% of the exit velocity for the full scale data.

Any attempt to generalize these limited results is certainly subject to change when more full scale data are available. However, there is a strong indication from the results that turbulence at the nozzle exit or internal noise generated upstream of the exit may strongly influence the overall noise power radiated by a VTOL jet.

e. Acoustic Power Spectra of VTOL Jets

Further evidence of the difference between VTOL noise levels for jets with differing upstream conditions is offered by examining their power spectra. Figure 22 shows, for reference, the relative octave band power level spectra for the free jet configurations for which VTOL power level spectra were available. The octave band frequencies have been normalized by the non-dimensional parameter shown, after the method proposed by Eldred.⁴⁵ The relative shape of the spectra for the free jets show a reasonable collapse.

Normalized octave band power level spectra from two independent data sources, each with free and vertically deflected jets at 4 nozzle diameters elevation, are compared in Figure 23 (Mach 0.85) and Figure 24 (M 0.61). The normalized frequency scale employed for these plots is the conventional Strouhal number equal to frequency (f)

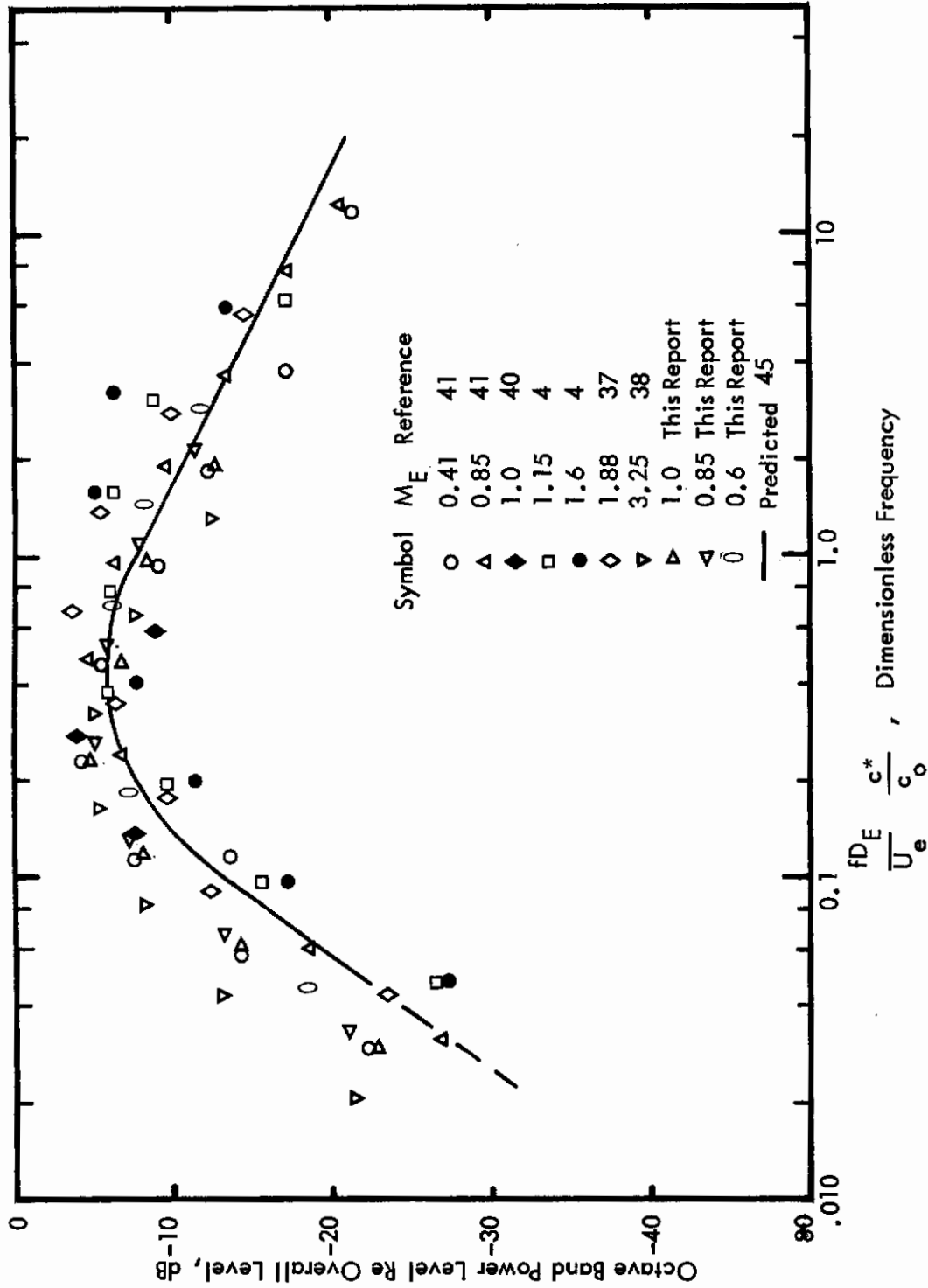


Figure 22. Relative Octave Band Power Level Spectra for the Free Jet Configurations. [D_E = Fully Expanded Nozzle Diameter, U_E = Fully Expanded Jet Velocity, c* = Speed of Sound at Throat of Nozzle, c_o = Ambient Speed of Sound, after Eldred 45]

times exit diameter (D) divided by exit velocity (U). For the Mach 0.85 case in Figure 23, the free jet spectra for the two sets of data are in excellent agreement. (The absolute levels are also close to the expected levels as indicated on Figure 21.) However, the deflected jet spectra from Reference 41 are consistently higher than results from this report by about 5 dB. This is attributed to the use of a more effective muffler and low turbulence plenum for the latter data (see Appendix C). These differences become more significant in Figure 24 for the Mach 0.6 results. Now, the free undeflected spectra from Reference 41 are substantially greater than expected, and show an even greater increase in spectra levels in the VTOL configuration. This trend is identical to that noted earlier in Figure 21. Jets with power levels greater than predicted by the U^8 law for the undeflected condition exhibited a greater increase in power for the VTOL condition.

The octave band power spectra for supersonic VTOL jets exhibit a substantially different trend as illustrated in Figure 25(a) and (b). In these two cases for which VTOL spectra data are available, the octave band spectrum levels for the VTOL condition are generally less than for the free or undeflected condition. The limited data in Figure 25 are not considered adequate to draw any further general conclusions regarding power spectra of supersonic VTOL jets. (Note that the frequency scale in Figure 25 is normalized by the usual Strouhal number but this fails to collapse the spectral shape for the supersonic ambient jet (part (a)) with the supersonic rocket data (part (b)). This has been well recognized by others.^{15, 16, 18, 45}

In summary, available model data indicate that the acoustic power generated by sonic or subsonic VTOL jets is substantially greater than expected according to the difference between the observed power and the calculated power of the undeflected portion of a VTOL jet. This excess power, which exhibits a broadband spectrum, is attributed to several possible mechanisms depending, potentially, on the turbulence conditions or internal noise at the exhaust plane. A source of discrete noise, found in several of the model tests, was excluded from the data considered here. It will be treated later in part 6(d) of this section.

f. Directivity of VTOL Jets

Near field sound levels for VTOL aircraft will obviously be strongly dependent on the directivity of the noise field. Figure 26 summarizes the overall directivity index measured for sonic or subsonic free and deflected jets at a radius of about 24 nozzle diameters according to data in Appendix C and other sources.^{39, 40, 40} The directivity index, equal to the difference between the observed level at a specified radius and angle to the jet exhaust, and the space average sound level at this same radius, is shown, for the VTOL condition, for 3 different ranges of nozzle elevation. The directivity index for the free jet condition is based on the average of the measurements cited for ambient jets and is shown on each plot for comparison.

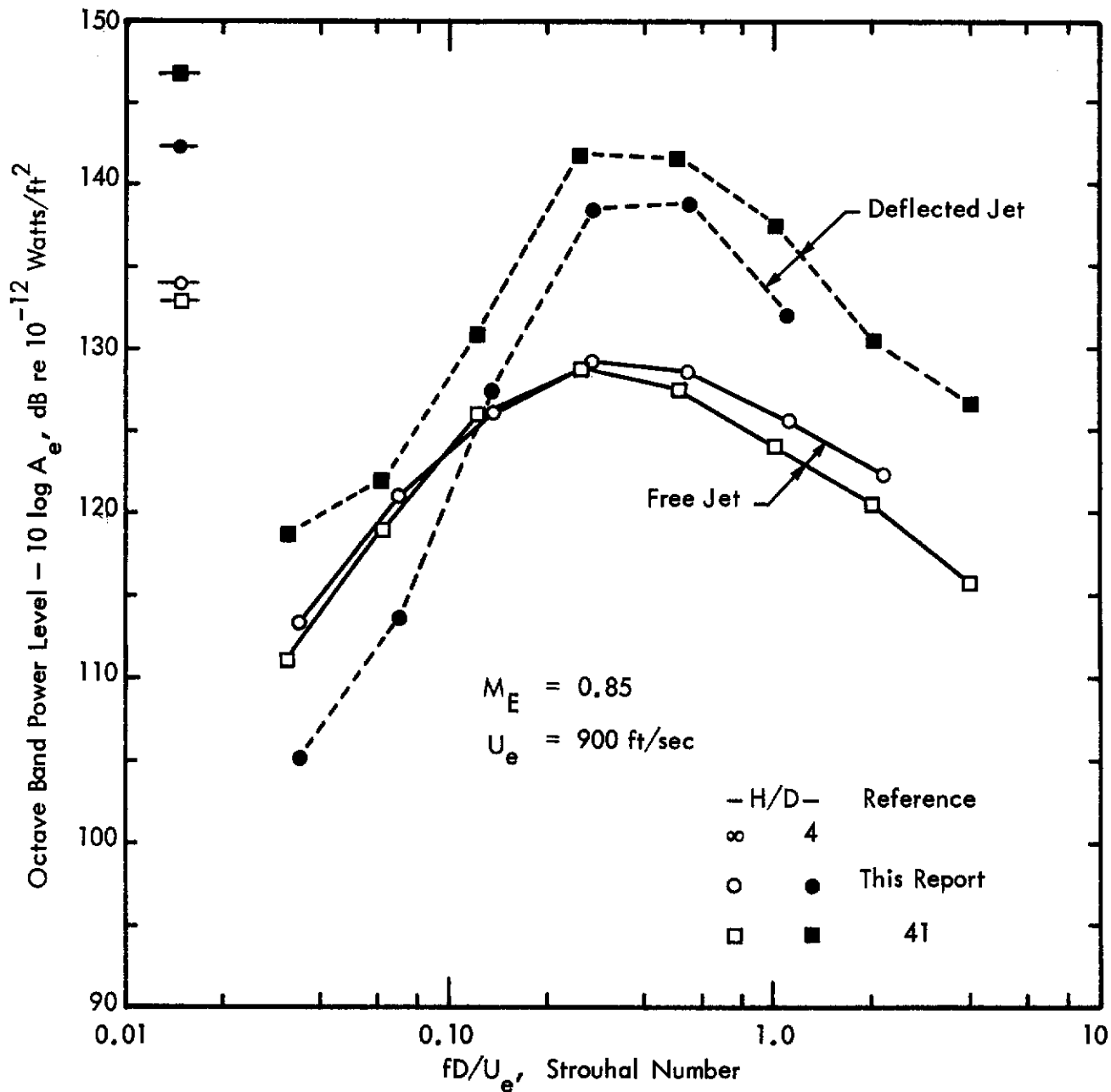


Figure 23. Normalized Octave Band Power Level Spectra for Subsonic Free and Deflected Ambient Air Jets. ($M_E = 0.85$).

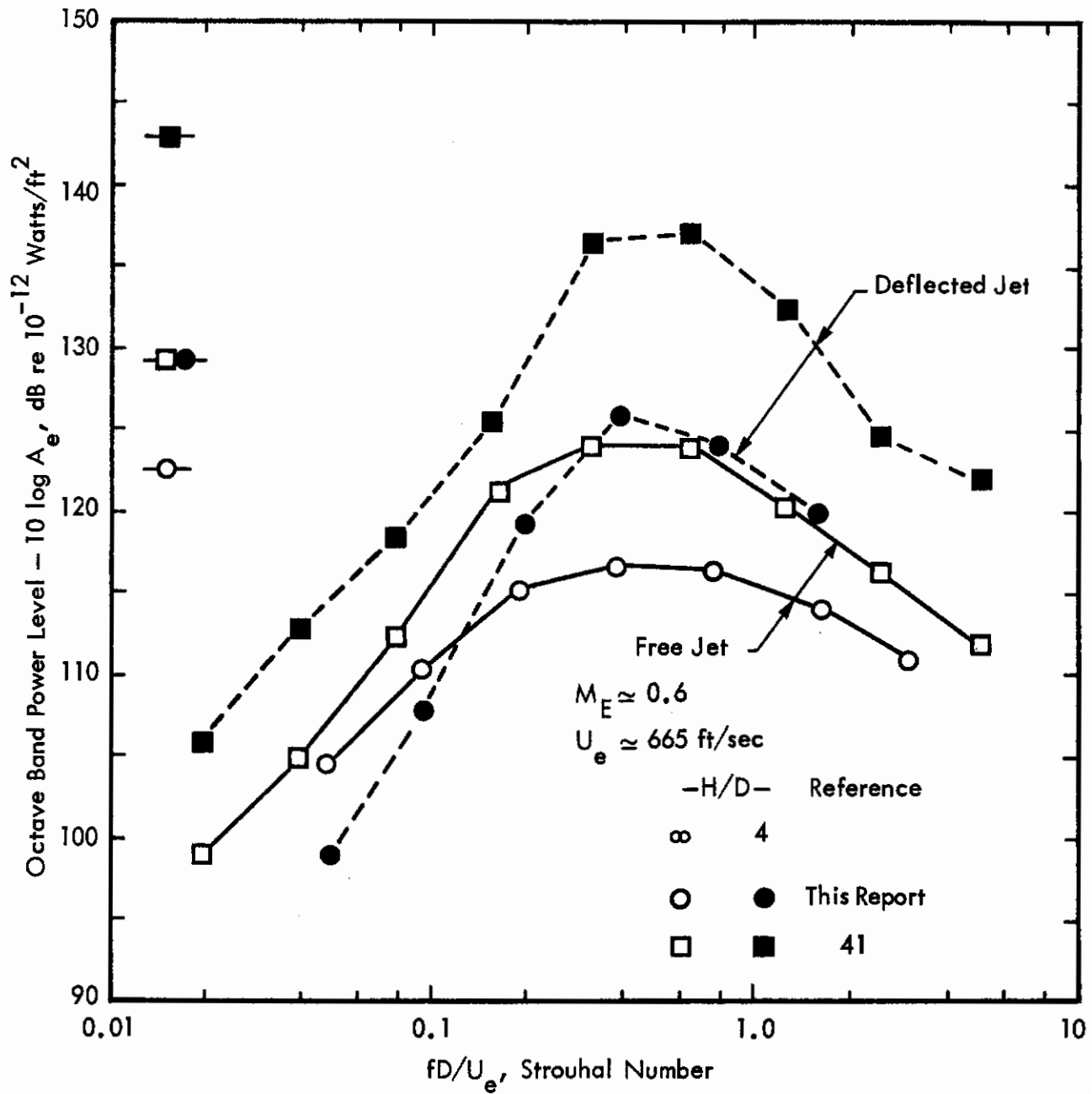


Figure 24. Normalized Octave Band Power Level Spectra for Free and Deflected Ambient Air Jets ($M_E = 0.6$)

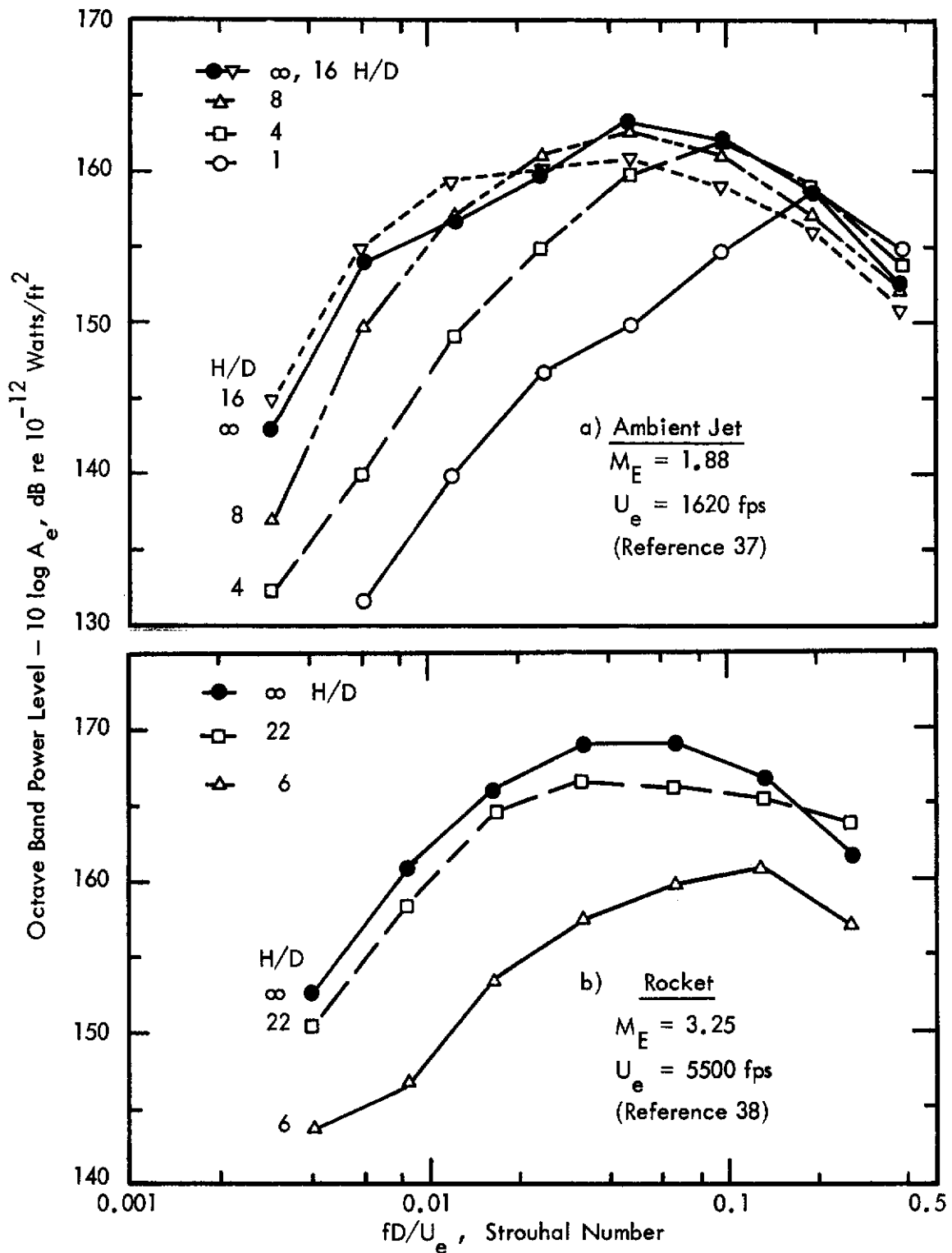


Figure 25. Normalized Octave Band Power Level Spectra for Supersonic Free (Closed Symbol) and Deflected (Open Symbol) Ambient Jet and Rocket at Various Nozzle Elevations

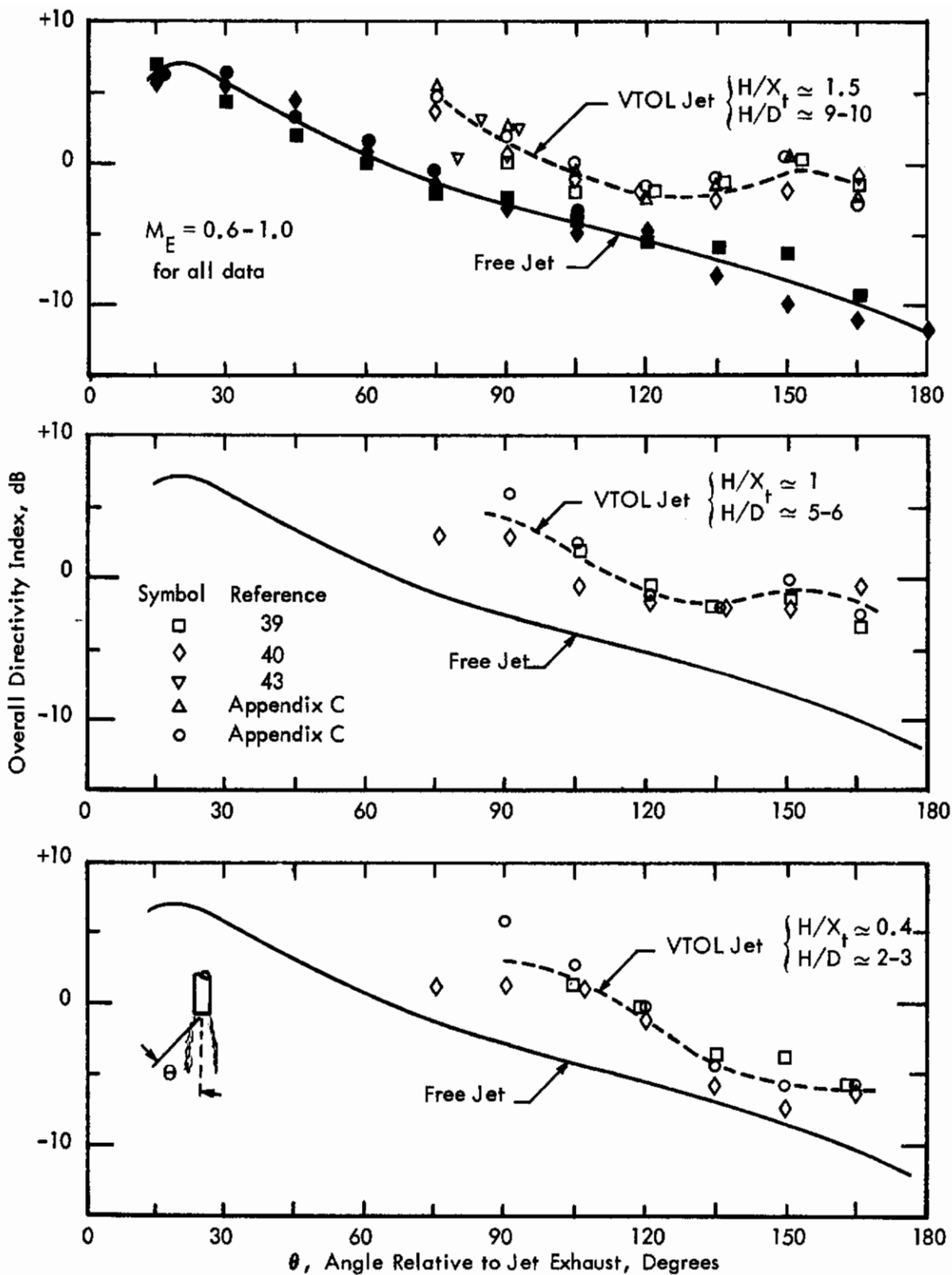


Figure 26. Directivity Index Measured at Radius of 24 Nozzle Diameters from Exit of Free (Closed Symbols) and Deflected (VTOL) Jet (Open Symbols) at 9 to 10, 5 to 6 and 2 to 3 Diameters Elevation.

At any given angle, the difference between the overall directivity indices for the VTOL and free jet conditions (from Figure 26) plus the difference in overall power levels for the two conditions (from Figure 19) corresponds approximately to the change in the overall sound level due to the change from a free to VTOL condition. According to Figure 19 and Figure 26, this difference in overall sound levels ranges from about 8 to 16 dB along an arc from 90 degrees to 165 degrees to the jet exhaust at a radius of about 24 nozzle diameters from the exit. This provides an indication of the order of magnitude of the change in near field sound levels for a VTOL jet relative to corresponding levels for a free jet.

Examination of the directivity plots in Figure 26 strongly suggests that near 150 degrees to the VTOL jet exhaust, the increase in the directivity relative to that of a free jet, may be due to ground reflection. However, the directivity index for a free ambient air jet data is substantially different from that of normal jet engines. This well-known difference, illustrated in Figure 27, is attributed to the combined effects of source convection and refraction on directivity of a heated jet exhaust.^{3,15,28,50} Thus, as the next step in development of a VTOL near field noise prediction method, it is desirable to critically examine the available VTOL air jet model data for the influence of ground reflection so that these model results can be realistically extrapolated to full scale VTOL jets. Consider first, the expected effects of ground reflection.

4. GROUND REFLECTION EFFECTS FOR VTOL JETS

If there were no other noise sources for a VTOL jet except the undeflected flow, the near field noise contours at nozzle elevations of one or more core lengths would be similar to the pattern illustrated conceptually in Figure 28. This represents the overall noise field contours as the sum of the direct noise radiation from the undeflected flow and the ground reflected noise. The latter is defined, to a first approximation, by an equivalent image jet neglecting effects of cancellation or reinforcement of the combined sound field. Clearly, the sound field forward of the jet exit is dominated by the reflected sound field. The simplified model illustrated assumes that the jet nozzle elevation is sufficiently high to prevent any significant decrease in the total noise generation by the undeflected flow. The potential influence of the deflected wall jet flow on the reflection at the ground is also ignored. With these exceptions, the use of an image jet to represent the reflected field is physically reasonable. Application of an image source is, in fact, the usual method for accounting for specular reflection of jet noise from a rigid ground plane.^{4,15,53,54} This method is applied in the following brief analysis of ground reflection for the highly directive noise field of a jet. The effect of refraction by the wall jet on this ground reflection is treated later.

Referring to the insert in Figure 28, the mean square sound pressure at a receiver in the sound field of a point source and corresponding image source can be expressed as⁴

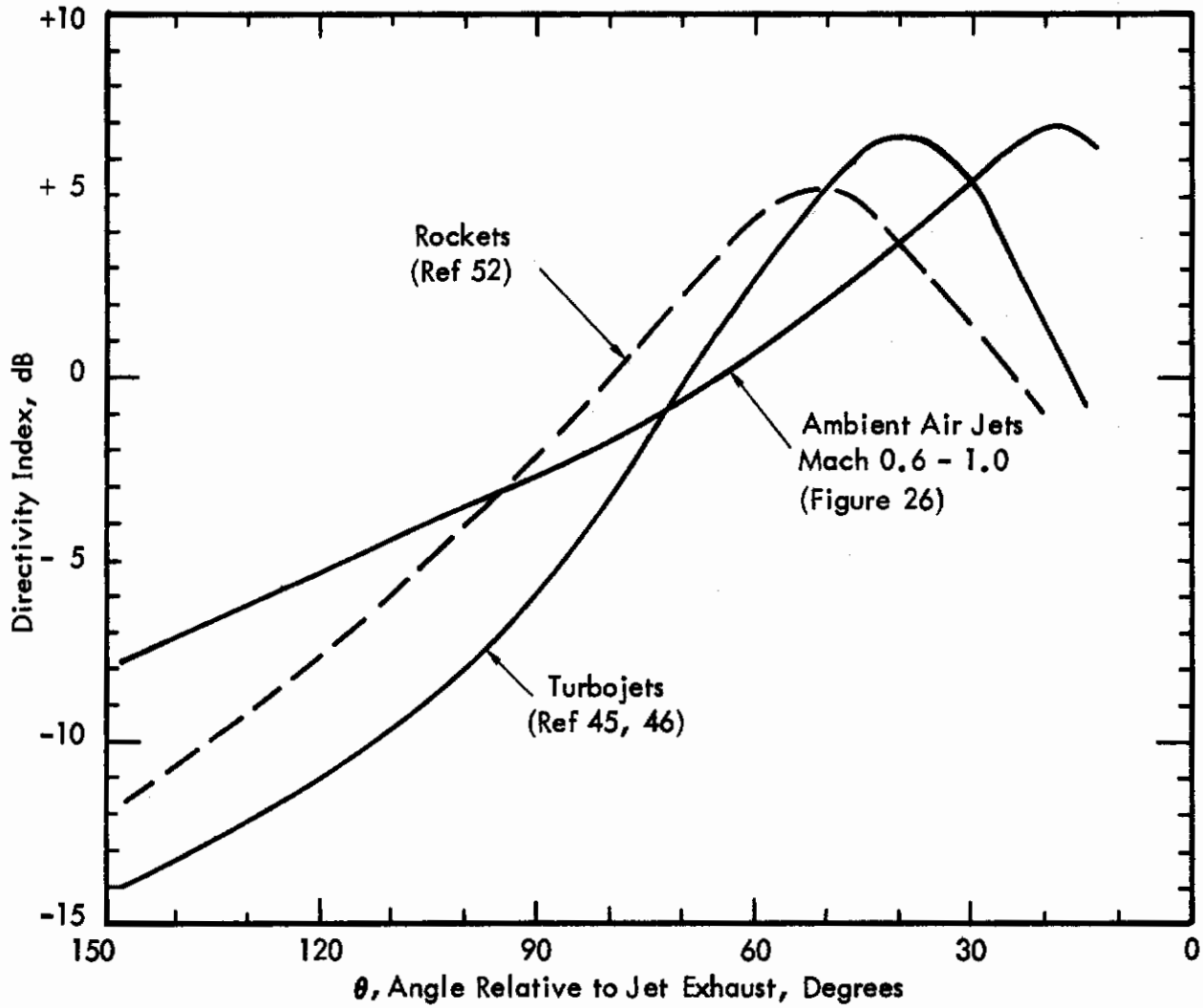


Figure 27. Typical Directivity of Overall Sound Level for Ambient Air Jets, Turbojets and Rockets.

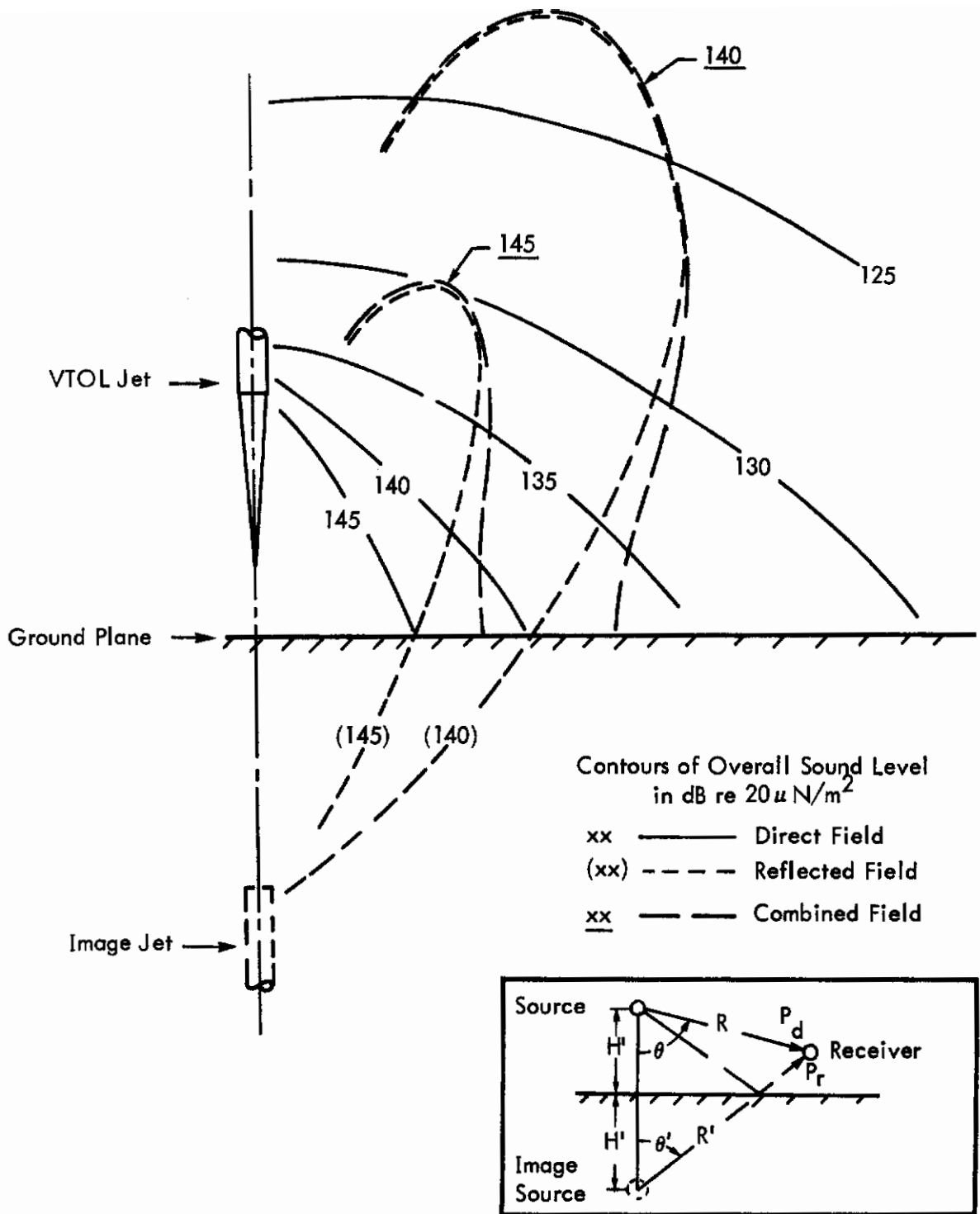


Figure 28. Simplified Model for Ground Reflection of VTOL Jets Illustrated by Contours of Direct, Reflected and Combined Field. Reflected Field Simulated by Image Jet Source as Illustrated by Insert.

Contrails

$$\bar{P}^2 = (\overline{P_d + P_r})^2 = \bar{P}_d^2 [1 + r^2 + 2rC] \quad (24)$$

where

P_d, P_r = direct and reflected pressures respectively at the receiver

$r^2 = \bar{P}_r^2 / \bar{P}_d^2$, ratio of mean square reflected to direct pressures

$C = \frac{\overline{P_d P_r}}{\sqrt{\bar{P}_d^2 \bar{P}_r^2}}$, the correlation coefficient between P_d and P_r

and $\bar{\quad}$ signifies a long time average.

For a directive point source with a directivity factor $D(\theta)$, the ratio r^2 is given by

$$r^2 = \frac{R^2}{(R')^2} \cdot \frac{D(\theta')}{D(\theta)} \quad (25)$$

where

$R' = R \left[1 + 4 \left(\frac{H'}{R} \right)^2 - 4 \left(\frac{H'}{R} \right) \cos \theta \right]^{1/2}$, the distance from the image source to the receiver

$\theta' = \tan^{-1} \left[\sin \theta / \left(2 \frac{H'}{R} - \cos \theta \right) \right]$, the angle between the source-image axis and the radius R'

and

H' = source elevation above the ground plane

If the source consists of an ideal band of white noise, the correlation coefficient C can be shown to be^{54, 4}

Contrails

$$C = \frac{\sin \left[\pi f_c \tau b \right]}{\pi f_c \tau b} \cos \left[2\pi f_c \tau \sqrt{1 + (b/2)^2} \right] \quad (26)$$

where

$$\tau = (R' - R)/c_o, \quad \text{time delay between direct and reflected signals}$$

$$b = \Delta f/f_c$$

$$f_c = \text{center frequency of band}$$

$$\Delta f = \text{bandwidth of noise (ideal filter)}$$

$$c_o = \text{ambient speed of sound}$$

For plotting purposes, it is convenient to transform the coordinate system to rectilinear coordinates x, y where x is the vertical distance below the jet exit plane, and y is the lateral distance parallel to the ground plane. Furthermore, by expressing distances in terms of nozzle height and frequencies in terms of the ratio of source height (H') to wavelength $\lambda = c_o/f_c$, then for an octave band of noise, $b = 0.707$ and one obtains

$$r^2 = \frac{(R/H')^2}{\left[(R/H')^2 + 4(1 - x/H') \right]} \frac{D(\theta')}{D(\theta)} \quad (27)$$

$$C = \frac{\sin B}{B} \cos 3B$$

where

$$B = \pi G \left[\sqrt{(R/H')^2 + 4(1 - x/H')} - R/H' \right] / \sqrt{2}$$

$$G = f \cdot H'/c_o = H'/\lambda, \quad \text{the ratio of source height to wavelength}$$

$$R/H' = \left[(x/H')^2 + (y/H')^2 \right]^{1/2}$$

$$\theta = \cos^{-1} \left(\frac{x/H'}{R/H'} \right)$$

and

$$\theta' = \tan^{-1} \frac{y/H'}{2 - x/H'}$$

Equations (27) and (28) were used in Equation (24) to plot contours of constant values of the quantity

$$A = 10 \log \left[1 + r^2 + 2r C \right], \quad \text{dB} \quad (29)$$

This is simply the change in sound level in decibels due to introduction of the ground planes. Contours of this reflection correction were computed for three general cases:

- (1) A nondirective point source
- (2) A "point source" simulating the far field directivity of an ambient air jet
- (3) A "point source" simulating a turbojet engine as a heated jet

For the nondirectional (monopole) source, $D(\theta) = D(\theta') = 1$. For an ambient air jet source, the directivity factor can be approximated as

$$D(\theta) = \frac{K(1 + \cos^4 \theta)}{\left[(1 - M \cos \theta)^2 + (\alpha M)^2 \right]^{5/2} \left[1 + C_4 e^{-C_5 \theta} \right]} \quad (30)$$

where

$K = 0.56$, an arbitrary constant selected so that $\int D(\theta) \sin \theta = 1$

$M = 0.3$, a typical convection Mach number of an ambient air jet

$\alpha^2 = 0.3$, a correction factor for finite eddy decay time

$C_4 = 2$, an empirical constant

$C_5 = 12.3$ per radian, an empirical constant

This directivity factor is based on the theoretical model derived by Ribner and modified by an empirical exponential term in the manner proposed by Plumblee to account for the decrease in directivity near the jet axis.^{28,40}

The following constants are used in Equation (30) to simulate the far field directivity of a full scale turbojet engine.

$$\left. \begin{array}{l} K = 0.37 \\ M = 0.75 \\ \alpha^2 = 0.3 \\ C_4 = 310 \\ C_5 = 9 \end{array} \right\} \text{Directivity constants for heated jet}$$

Figure 29 shows that the resulting computed values of directivity index for these two types of jets fits experimental data quite well. However, the constants, C_4 and C_5 were adjusted empirically to obtain the good fit for values of θ near zero.

Equation (29) has been used to compute the relative change in octave band levels for a point source of white noise. The results are shown in Figure 30 for the non-directional source and in Figures 31 and 32 for the two types of jets. Since it was desirable to simulate actual experimental VTOL conditions, the jet axis was assumed to be 10 degrees off the vertical for the latter two cases. This oblique angle was used for the model tests reported in Appendix C and is approximately equal to typical conditions for a full scale VTOL jet.^{42,43} This oblique incidence is accounted for in the preceding expressions by subtracting the offset angle (10°) from the angles θ and θ' which are taken relative to the jet axes of the actual and image source respectively.

The figures show the effect of ground reflection in the form of contours of constant values of the correction factor A that would be observed in a vertical plane containing the source and its axis of symmetry. For the two jet cases, the contours show only the quadrant forward of the source position. Distances in this plane are normalized by the height (H') of the source above the ground. Plots are shown for several frequencies by varying the ratio H'/λ . The shaded areas in each figure represent the regions where the value of A is negative - in other words, where destructive interference of the direct and reflected waves is a maximum. The general pattern of these contour maps of ground reflection effects varies substantially for the three types of sources.

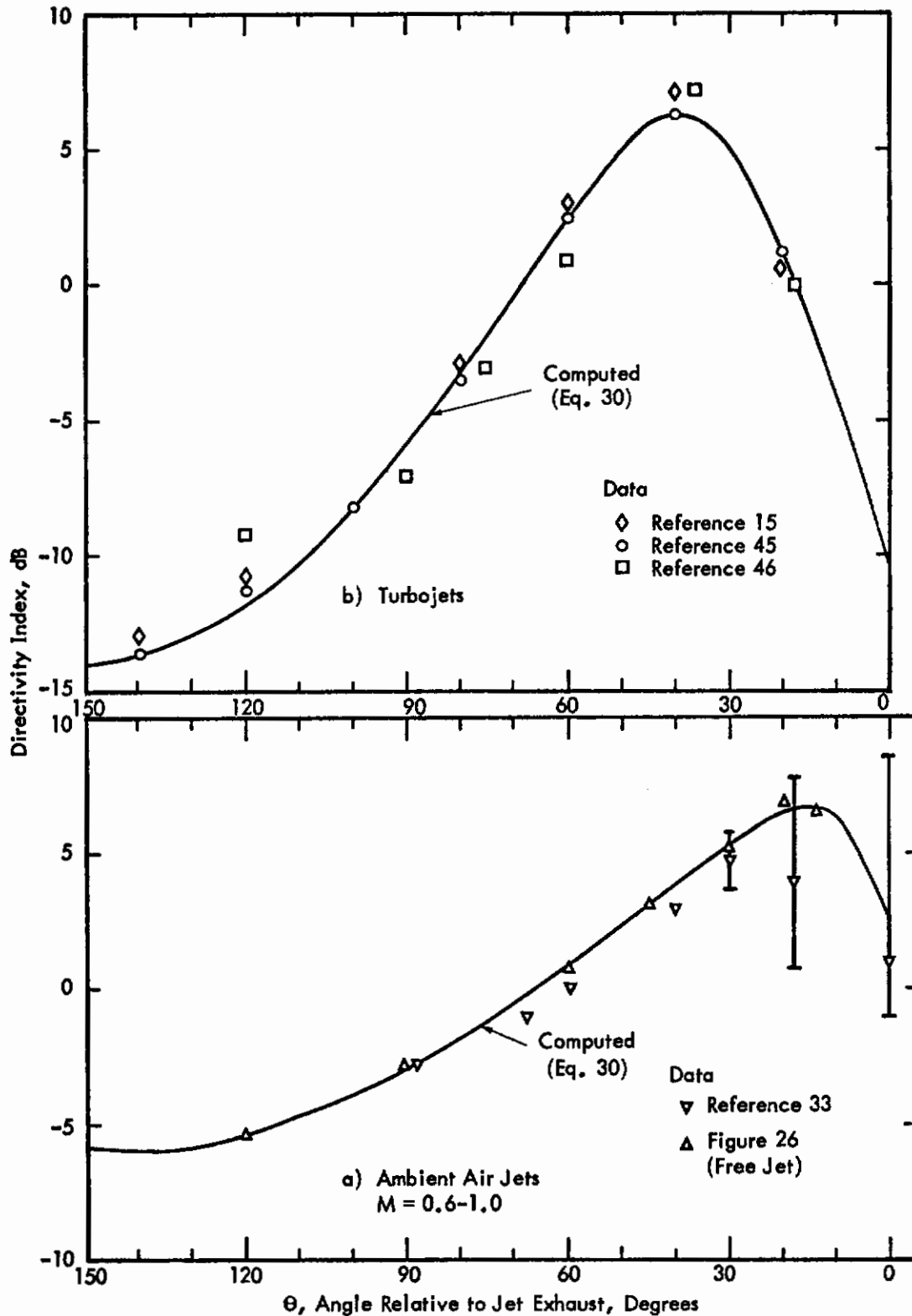


Figure 29. Comparison of Experimental Directivity Data For Ambient and Heated Jets with Semi-Empirical Prediction.

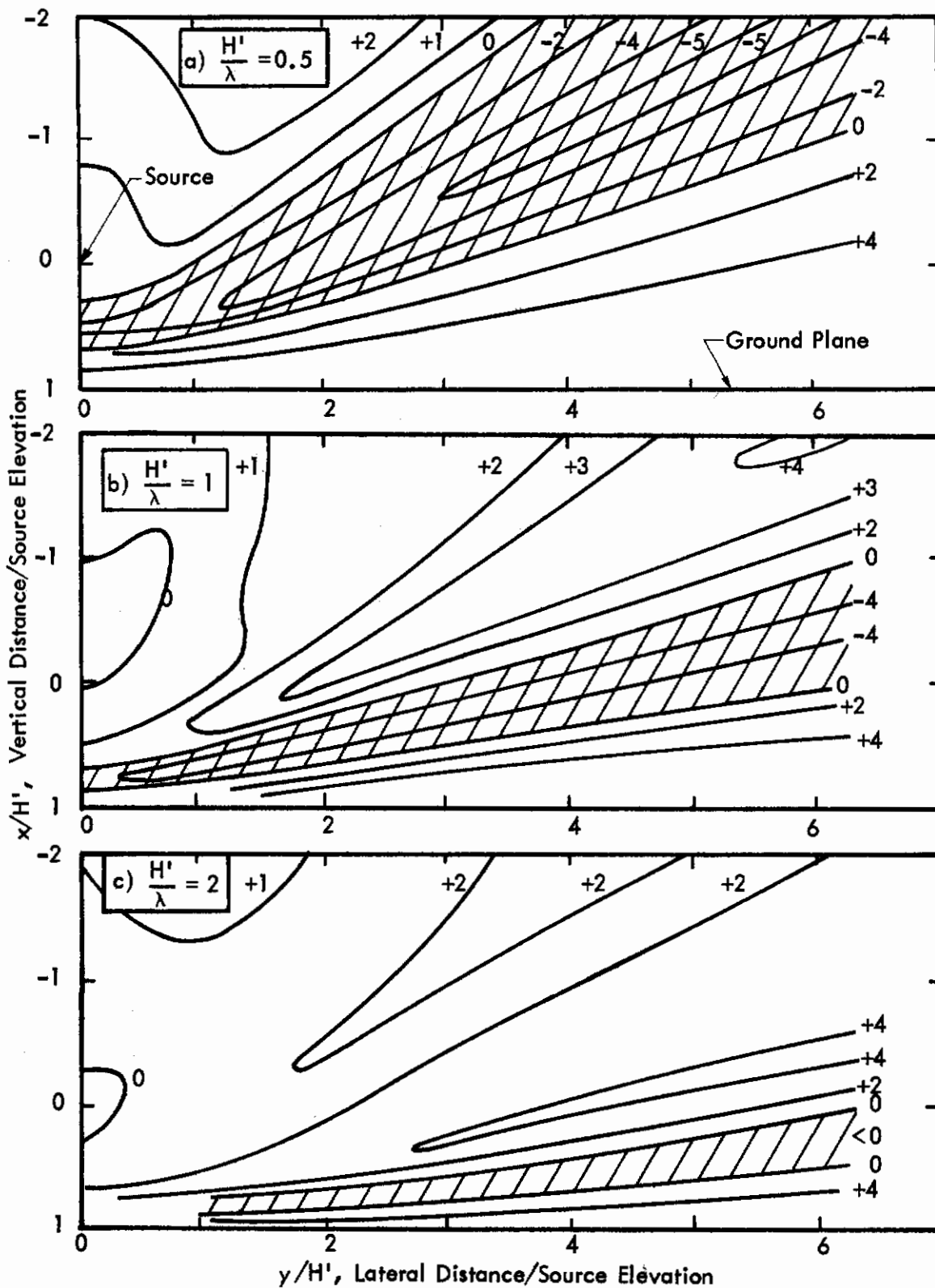


Figure 30. Change in Octave Band Level Due to Reflection from Rigid Plane for Monopole Source. λ = Wavelength at Center Frequency of band of White Noise.

For the monopole source, the region of destructive interference occupies a fan-shaped zone which approaches ever closer to the ground plane and which becomes narrower as frequency increases. A more complete tabulation of the values plotted in Figure 30 is given in Appendix D along with a computer program listing used to generate the tables.

For the ambient jet case, shown in Figure 31, destructive interference effects are apparent for values of $H'/\lambda < 1$ with the greatest effect being observed near the vertical axis. However, the assumed directivity model is least accurate for values of θ near 0 and 180 degrees so that the value of the contours near the x axis are suspect. Nevertheless, based on the assumptions made for this point source model for a jet, the general pattern indicated for the ground reflection effect is considered qualitatively reasonable. A comparison of the data in Figure 30 for the monopole source and the ambient jet source shows in fact the same trends in the shift of the maximum interference pattern with frequency. Figure 31(d) shows, in dashed lines, the ground reflection correction for $H'/\lambda = 100$. This corresponds to the case where the reflected pressure is no longer coherent with respect to the directly radiated pressure so that their correlation coefficient (C) approaches zero. The net result is that the direct and reflected pressures add as their mean square values on an intensity basis only.

The same general pattern of ground reflection effects observed for the ambient jet model is repeated in Figure 32 for the simulated "turbojet" point source. Figure 32(a) shows the condition for $H'/\lambda = 0.225$, the source elevation for maximum interference effects directly above the source.⁴ Figure 32(b) shows the case for $H'/\lambda = 1$ (solid lines) and $H'/\lambda = 100$ (dashed lines). For the latter figure, the contours for the ground reflection correction are very similar and are still within a few dB of the values in Figure 32(a) at lateral positions greater than $y/H' = 2$.

The principal conclusion to be drawn from Figures 31 and 32 is that variations in the ground reflection effect due to destructive interference patterns are relatively minor compared to the major influence of reflection by a highly directional source. Comparison of the ground reflection contours for the case of $H'/\lambda = 100$ with the other cases in Figures 31 and 32 for lower values of H'/λ shows that they all exhibit the same general pattern. Considering the relatively crude model of the near field of a jet represented by this "point source" version, it is probably reasonable to ignore the phase effects and consider only the basic ground reflection of the highly directive jet noise field in terms of an intensity summation when considering reflection of VTOL jet noise by a ground plane.

Figure 33 illustrates more clearly the implications of this possible approach. Figure 33(a) shows the total sound field predicted by the model for the VTOL turbojet with $H'/\lambda = 0.225$ and the absolute source level defined, arbitrarily, to give a space average sound level of 100 dB at a radius equal to the source elevation (H'). The

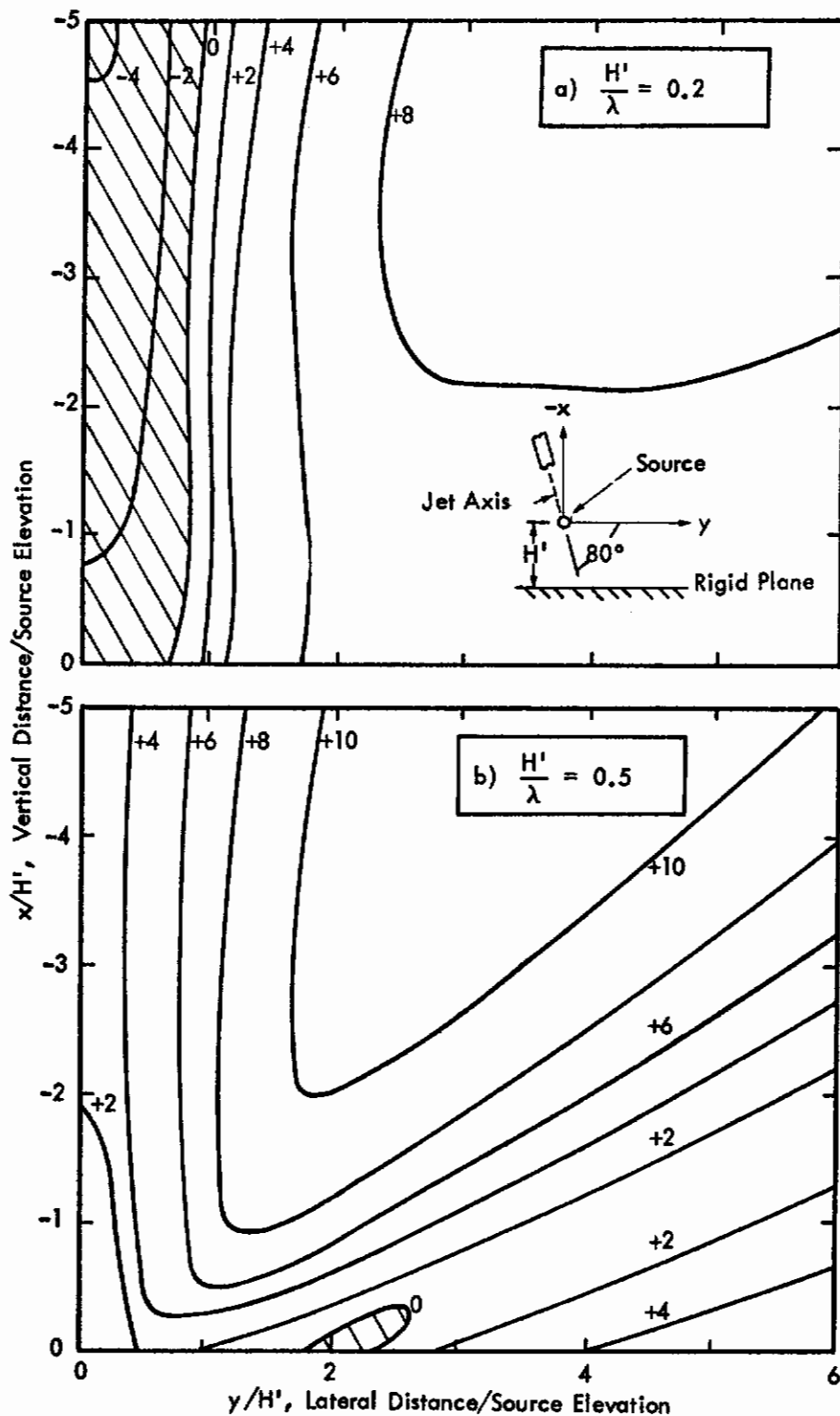


Figure 31. Change in Octave Band Level Due to Reflection from Rigid Plane for "Point" Source with Directivity of an Ambient Air Jet. $\lambda =$ Wavelength at Center Frequency of Band of White Noise

Continued.....

Contours

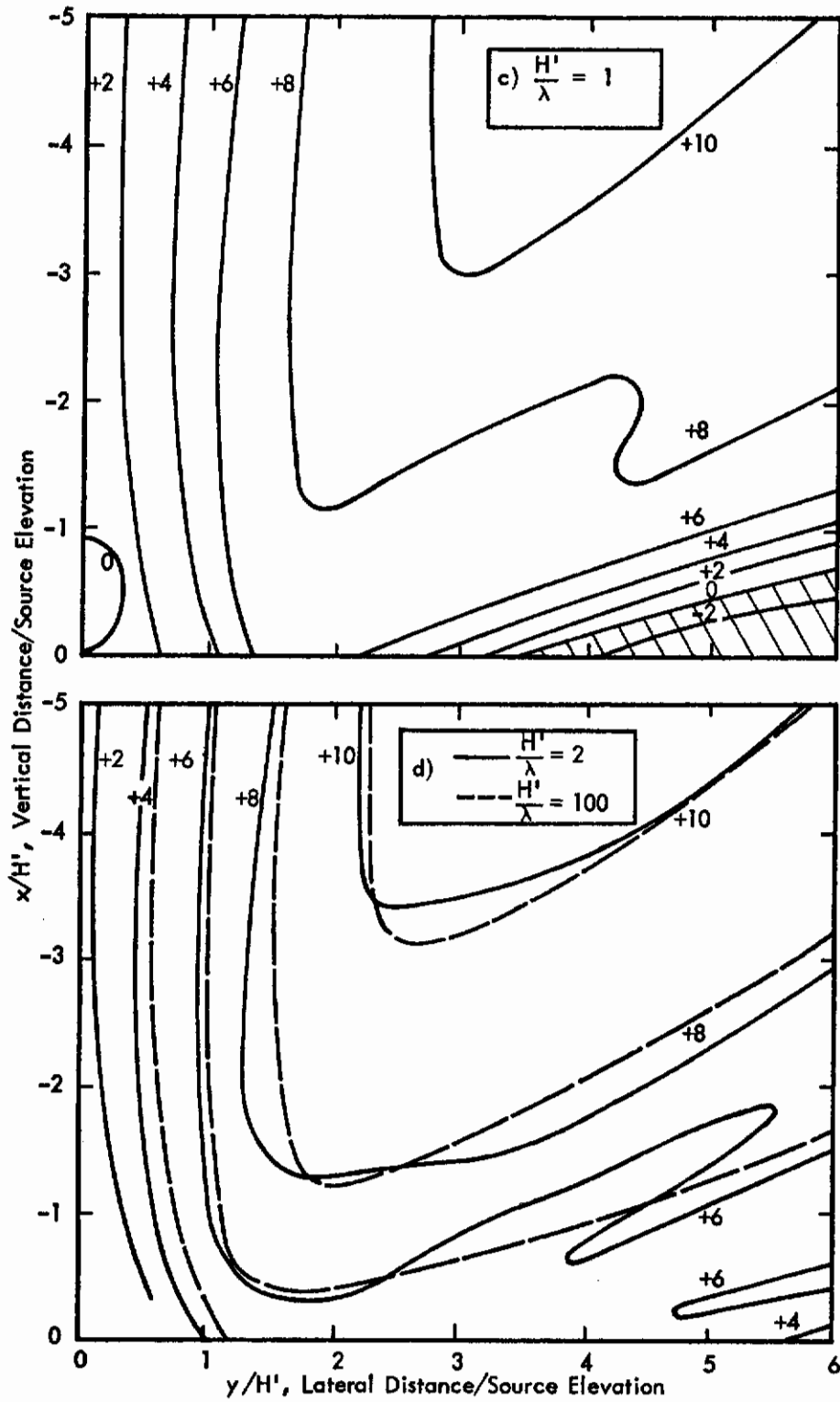


Figure 31 (Concluded)

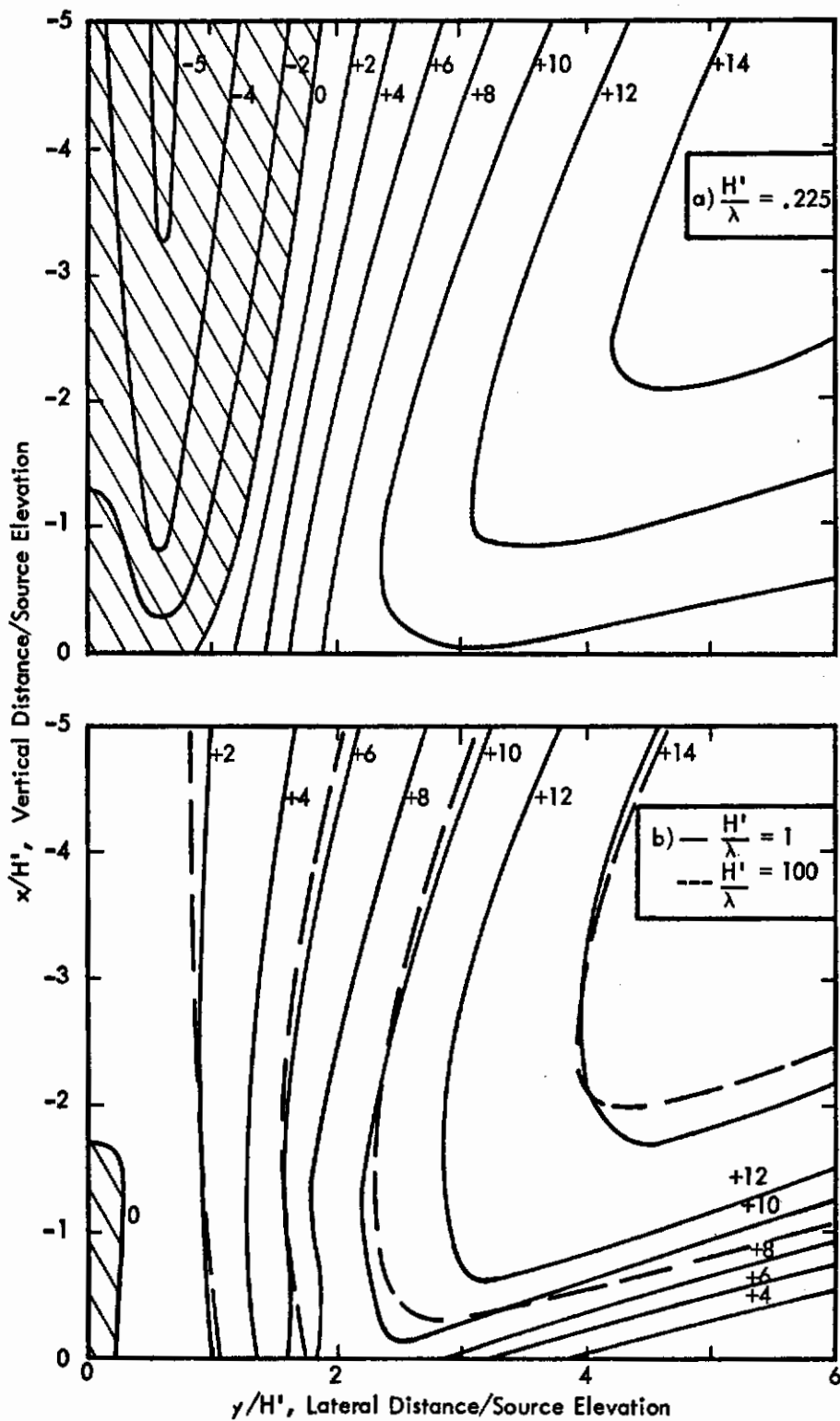


Figure 32. Change in Octave Band Level due to Reflection by Rigid Plane for Point Source with Directivity of a Turbojet. λ = Wavelength at Center Frequency of Band of White Noise.

Contrails

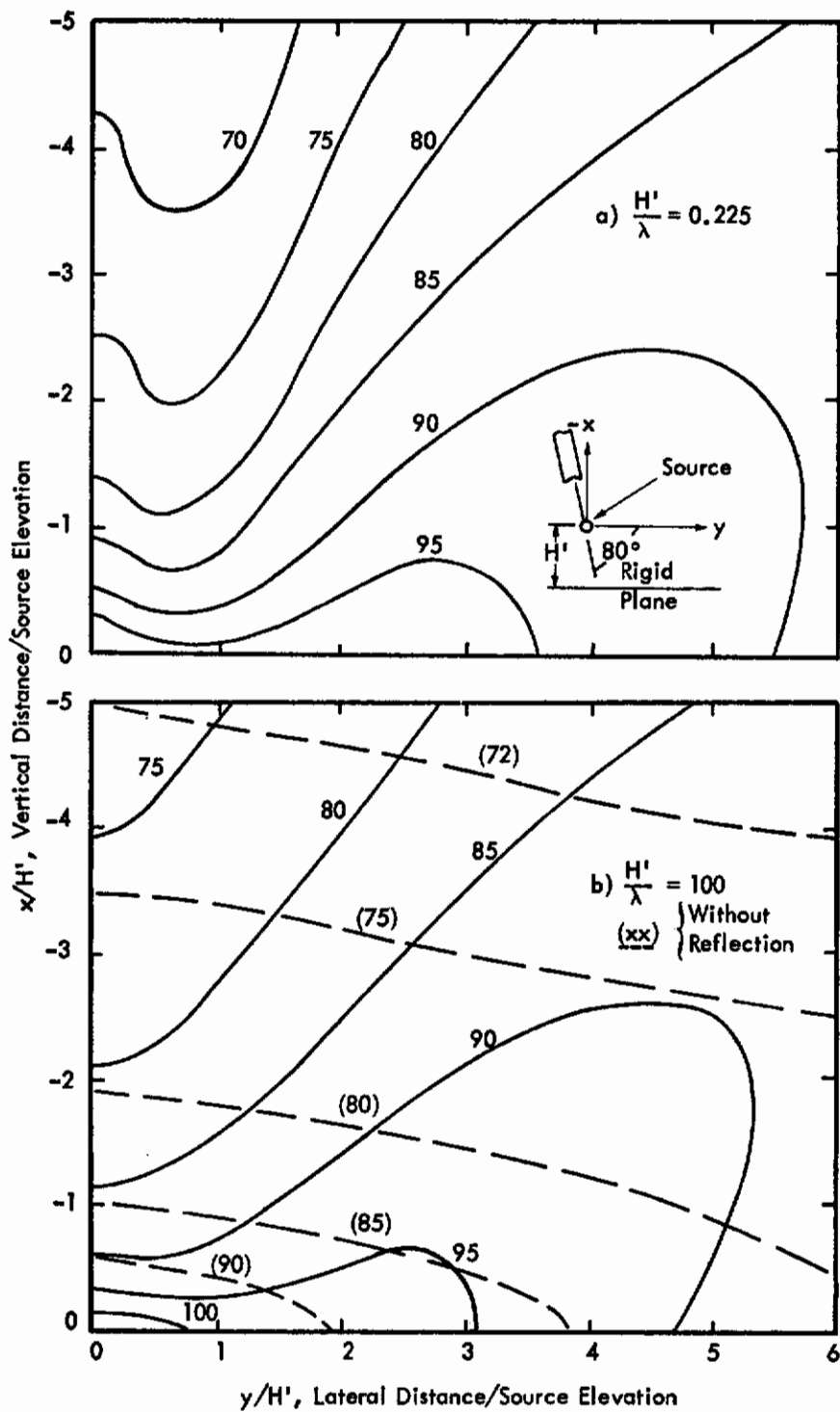


Figure 33. Contours of Computed Octave Band Levels for Point Source Simulating a VTOL Jet. Space Average Octave Band Level = 100 dB at Radius = H' , λ = Wavelength at Center Frequency of Band of White Noise.

lower figure shows the case for $H'/\lambda = 100$, with the ground plane (solid lines), and without the ground plane (dashed lines). Again, the effect of simply adding the intensity of the reflected field is shown to be far more significant than the differences due to phase or destruction interference effects as indicated by comparing the solid lines in Figure 33(a) and (b). These results on ground reflection effects are only illustrative and not directly applicable to the near field noise prediction model. The concept of a point source with a far field directivity of a jet fails to account for the changing directivity of the distributed sources in the near field of a jet.^{15, 40}

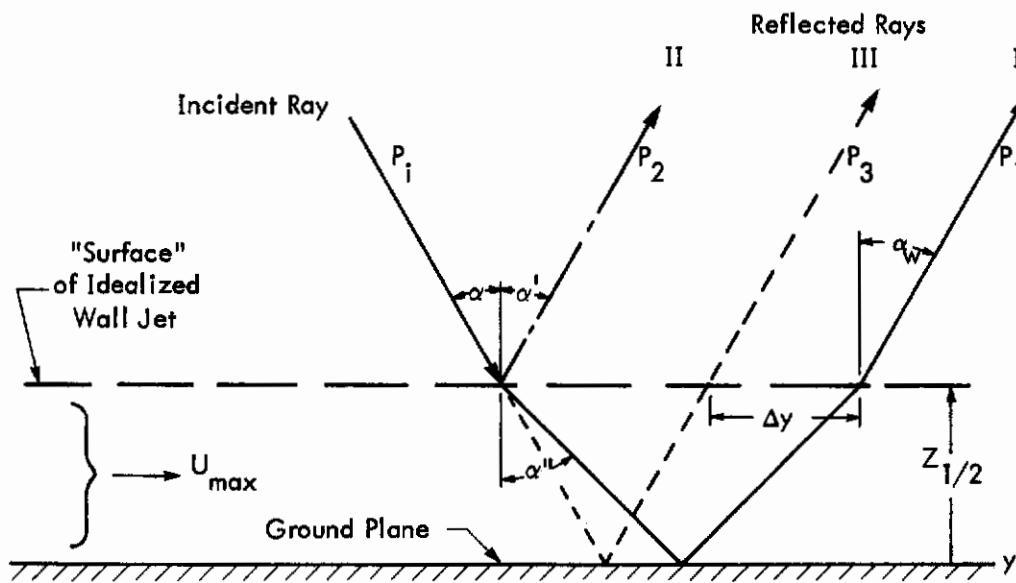
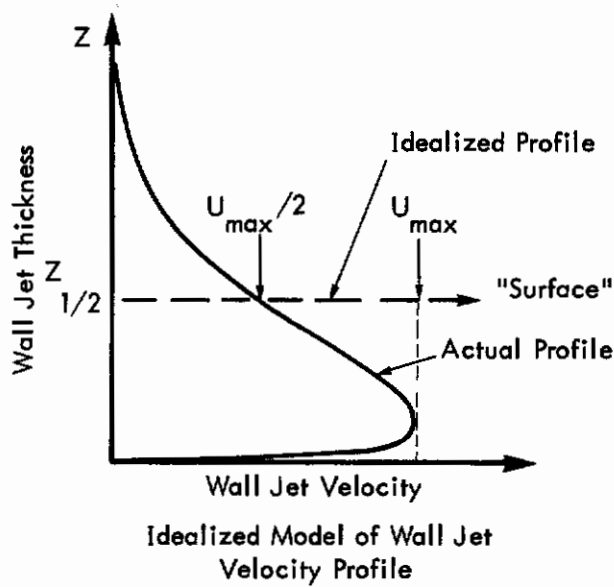
However, the significance of this analysis of ground reflection for the near field of a VTOL jet is to suggest that a reasonable approximation to account for ground reflection for this near field may be possible by utilizing the image concept suggested earlier in Figure 28. This simply involves folding the near field contours about the ground "mirror" plane to approximate the intensity-reflected field of the image jet.

a. Effect of Wall Jet on Ground Reflection

The effect of ground reflection will be altered by refraction of the incident sound waves passing through the wall jet flow. However, it will be shown in the following simplified analysis that an incident sound ray would be expected to be either reflected totally from the wall jet flow, as if it were a rigid surface, or shifted downstream and reradiated at the same "mirror image" angle. A physical picture of the phenomena is illustrated in Figure 34.

A theoretical model for refraction of plane waves of sound at a flow interface, developed by Ribner, is used to indicate, qualitatively, the probable effect of this refraction.⁵⁷ The predicted results using this model are limited by the following assumptions.

- The incident sound field is treated as a plane wave instead of a spherical or curved wave front.
- The actual wall jet velocity profile, illustrated in the upper part of Figure 34, is idealized by a rectangular profile with a maximum velocity U_{\max} equal to the maximum radial velocity in the wall jet and a thickness $Z_{1/2}$ equal to the 1/2 velocity thickness of the wall jet mixing thickness. (Flow parameters of the wall jet were discussed in part 1 of this section.)
- In the near field region of interest, the wall jet velocity decays with radial distance from the impingement point whereas, for refraction effects, the flow model considers the idealized velocity as constant over a given region.



- Rays I, II - Reflected from Ground and "Surface" of Wall Jet Respectively ($\alpha_w = \alpha' = \alpha$)
- Ray III - Reflected from Ground in Absence of Wall Jet
- Δy - Lateral Shift in Position of Reflected Ray I

Figure 34. Model for Reflection of Plane Waves by Wall Jet Flow over a Rigid Ground Plane

Contrails

According to the theoretical development by Ribner, a plane wave incident on an infinitely thin flow interface will be totally reflected if the angle of incidence α exceeds a critical angle α_c given by⁵⁷

$$\alpha_c = \sin^{-1} \left[\frac{1}{1 + M} \right] \quad (31)$$

where M = the ratio of the relative flow velocity at the interface to the speed of sound.

As the incidence angle falls below this critical angle for a given value of M , an incidence angle is reached for which the reflection is zero. This divides the reflection from the flow interface into three regions, as illustrated in Figure 35. For incidence angles less than the critical angle, the reflected wave from the interface is very weak (except as α approaches very close to α_c), while the transmitted wave is refracted by the angle α'' equal to

$$\alpha'' = \sin^{-1} \left[\frac{\sin \alpha}{1 - M \sin \alpha} \right] \quad (32)$$

However, for the assumed case of a uniform flow sheet over a rigid boundary, this transmitted wave is also reflected from this rigid boundary and upon leaving the flow, is refracted again but in the opposite direction so that the angle α_w that this wave has with the wall is identical to the original incidence angle α . This can be readily shown by applying Equation (31) twice to solve for α_w with α set equal to α'' and $M = -M$ for the second refraction. As indicated in Figure 34, this shifts the ray downstream by the distance Δy beyond its position that would exist for no flow over the ground. This lateral shift Δy can be expressed in terms of the flow thickness $Z_{1/2}$ as

$$\frac{\Delta y}{Z_{1/2}} = 2 [\tan \alpha'' - \tan \alpha] \quad (33)$$

where α'' is given by Equation (32).

Beyond this point, the problem becomes awkward to generalize for application to the near field of a VTOL jet since the flow Mach number and incidence angles can take on a wide range of values depending on the jet exit velocity, nozzle height and location of the source of the incident rays.

As an illustration of the possible effects, the empirical expressions developed in part I for the flow velocity (U_{max}) and thickness ($Z_{1/2}$) of a VTOL wall jet have been utilized to estimate the magnitude of the lateral shift in the reflected ray for incidence

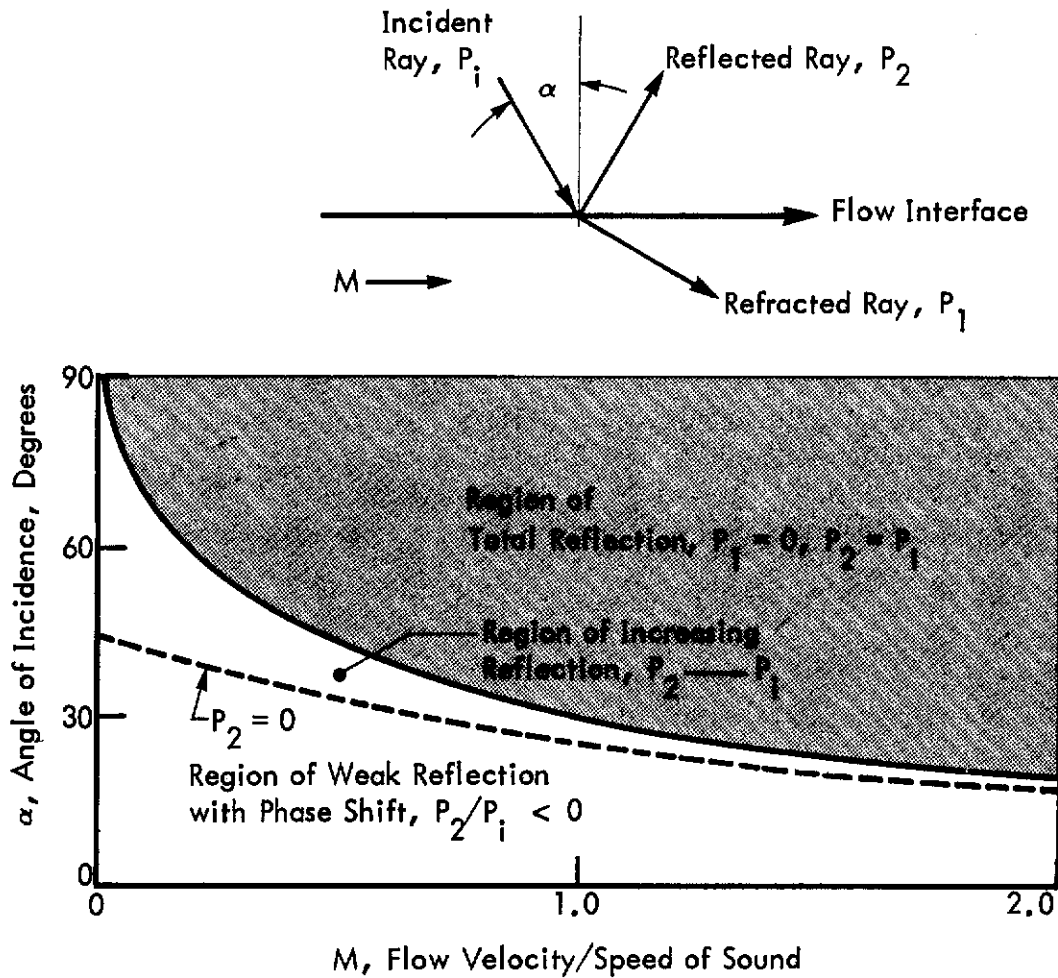


Figure 35. Separation of Reflection from Flow Interface into Three Regions. For Uppermost Region, Angle of Incidence Exceeds the Critical Angle Defined by Equation 31. At Upper Boundary of Lower Region, Reflection is Zero and $M = (1 - \tan \alpha) / \sin \alpha$. (From Reference 57)

angles less than α_c . The result is shown in Figure 36 for a case where the "source" was assumed to be at a height of 4 nozzle diameters above the ground. In general, the shift is expected to be less than the elevation of the source for nozzle elevations which correspond to maximum near field noise levels. Clearly, however, there are additional complications to account for — the source location in the jet as a function of both frequency and nozzle elevation. While the problem warrants further consideration, it was considered unlikely that a practical approach could be developed for a simple VTOL near field noise prediction method which would account for this "double refraction" or reflection of waves by the wall jet. Therefore, the influence of the wall jet on ground reflection will not be considered in the development of the prediction method.

b. Ground Reflection for Propeller Noise

While Section IV considers near field noise prediction of propeller-driven VTOL aircraft, ground reflection effects are not treated in that section since the concepts developed here are fully applicable. It is worth pointing out, however, that down-wash flow along the ground under a helicopter or tilt-wing propeller disc will be substantially less than for VTOL jets.⁵⁸ Thus, the preceding complication to the ground reflection problem will tend to be minimized for propeller noise.

c. Effect of Ground Plane on Radiation Efficiency

The presence of a rigid reflecting plane near a dipole or quadrupole source has been shown theoretically, to increase the radiation efficiency, and hence acoustic power, of the source.^{55, 56} However, the effect is limited to an increase of +3 dB when the source is within 1/6 to 1/2 of a wavelength from a rigid reflecting plane where the distance is a function of the type of source.

It was shown in Figure 19 that for a nozzle elevation equal to one core length, the observed increase in power output of a sonic or subsonic VTOL jet varies from 0 to 10 dB with an average of about 7 dB. Part of this increase could, indeed, be due to this increase in efficiency of a VTOL jet at this elevation. Since the "source" location for the peak frequency of a sonic jet occurs near the core tip, the effective jet noise source would be very close to the ground plane.^{3, 15} Further, since the source position is of the order of one wavelength from the exit, the source elevation above the ground would be much less than a wavelength.¹⁵ However, at lower nozzle elevations, the expected marked decrease in power output, as the primary jet structure is destroyed, does not occur. The excess power of the VTOL jet is substantially greater than the 3 dB increase predicted by this radiation efficiency effect. It is concluded, therefore, that the effect is not a significant source of excess power for a VTOL jet.

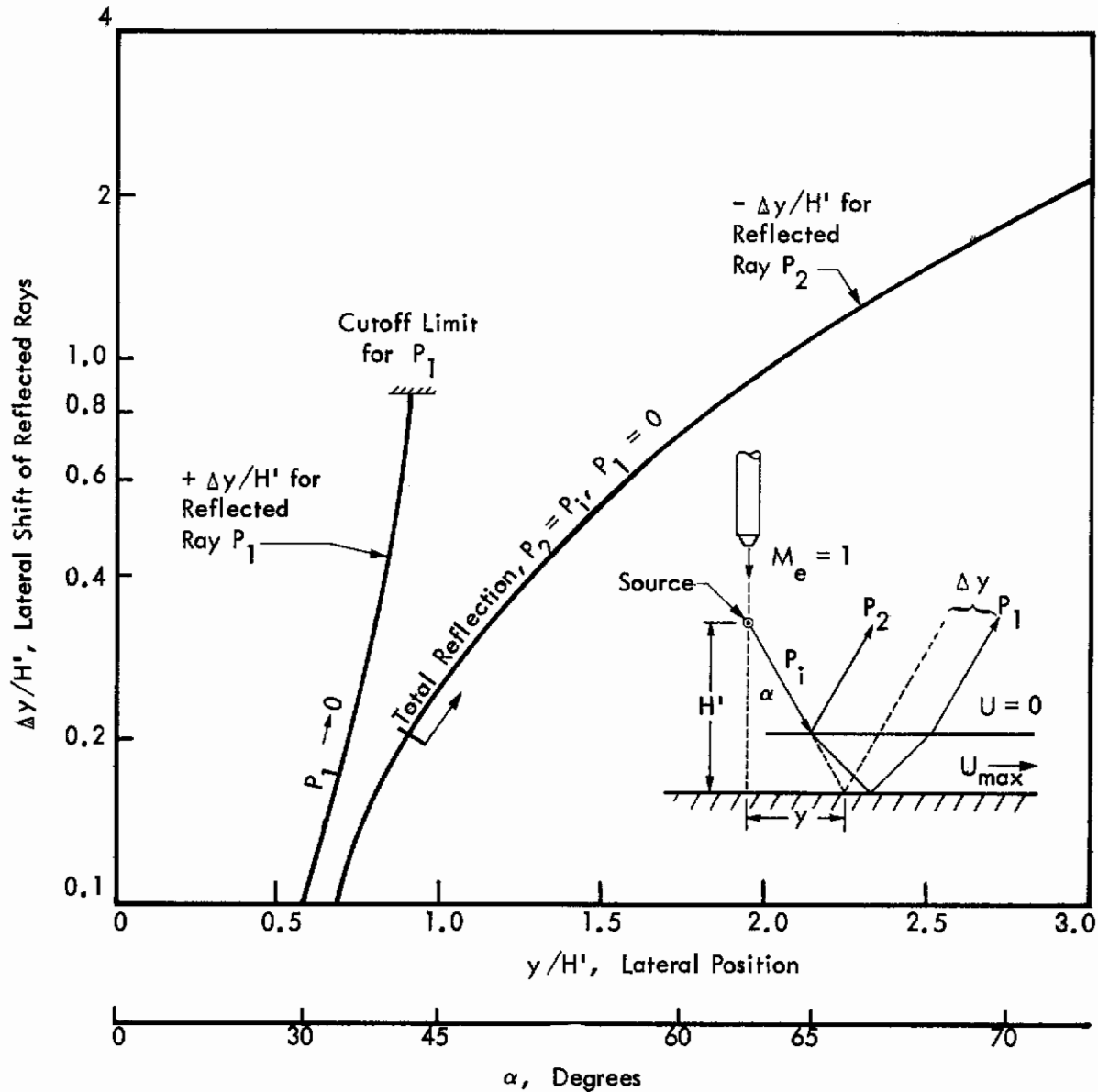


Figure 36. Illustration of Typical Possible Shift in Lateral Position of Reflected Rays from VTOL Jet Due to Wall Jet Flow. Δy is Positive for Ray P_1 and Negative for Ray P_2 Relative to Reflected Ray (Dashed Line) in Absence of Wall Jet.

5. COMPARISON OF PREDICTED GROUND REFLECTION FOR VTOL JETS WITH EXPERIMENTAL DATA

To evaluate the relative significance of the preceding analysis of ground reflection and to set the stage for consideration of other possible sources of VTOL near field noise, it is appropriate now to compare the data on actual near field sound levels for VTOL jets with predicted values using the concepts developed to this point.

Figures 37 and 38 show representative near field sound level contours for the 4000 Hz octave band from the model tests summarized in Appendix C. The data correspond to the condition for $M_E = 1$ and $fD/U_e \approx 0.24$ (near the peak frequency for this jet). The contours in Figure 37 are for the free field case while those in Figure 38 correspond to the VTOL configuration at 6 nozzle diameters elevation.

The concept of a mirror image jet (using intensity summation) was applied to estimate the reflected field. The resulting estimate is shown in Figure 39 along with the actual observed contours from Figure 38. These results are generally representative for the data reported in Appendix C. The results suggest that near the jet axis, a simple intensity addition of the reflected field using the image jet concept, provides a reasonable first approximation to the near field levels. The predicted levels in this region are about 3 to 4 dB lower than the observed values, although the contour shapes are very similar. Since the convected source in the jet is located very close to the ground, say, within 1/10 of a wavelength, this difference in level could be due to: pressure doubling (+6 dB) instead of the intensity doubling (+3 dB) assumed or an increase in radiation efficiency of up to 3 dB, as discussed in the preceding paragraphs. However, at greater distances from the jet axis, a totally different pattern emerges. While the previously discussed lateral shift of rays reflected from the wall jet could be partially responsible, it is not considered the most probable cause of this difference in contour shape for two reasons:

- (1) Incidence angles of the direct jet noise will tend to be greater than 50 to 60 degrees at positions well removed from the jet axis. In this case, for the range of wall jet velocities encountered, reflection is expected to occur predominantly from the surface of the wall jet, thus preventing the outward lateral shift of reflected rays due to refraction by the wall jet flow (see Figure 35).
- (2) "Jet" noise generated by the wall jet itself has not been accounted for yet. This source is considered more likely to be responsible for the difference between measured and predicted contours in this region well removed from the jet axis.

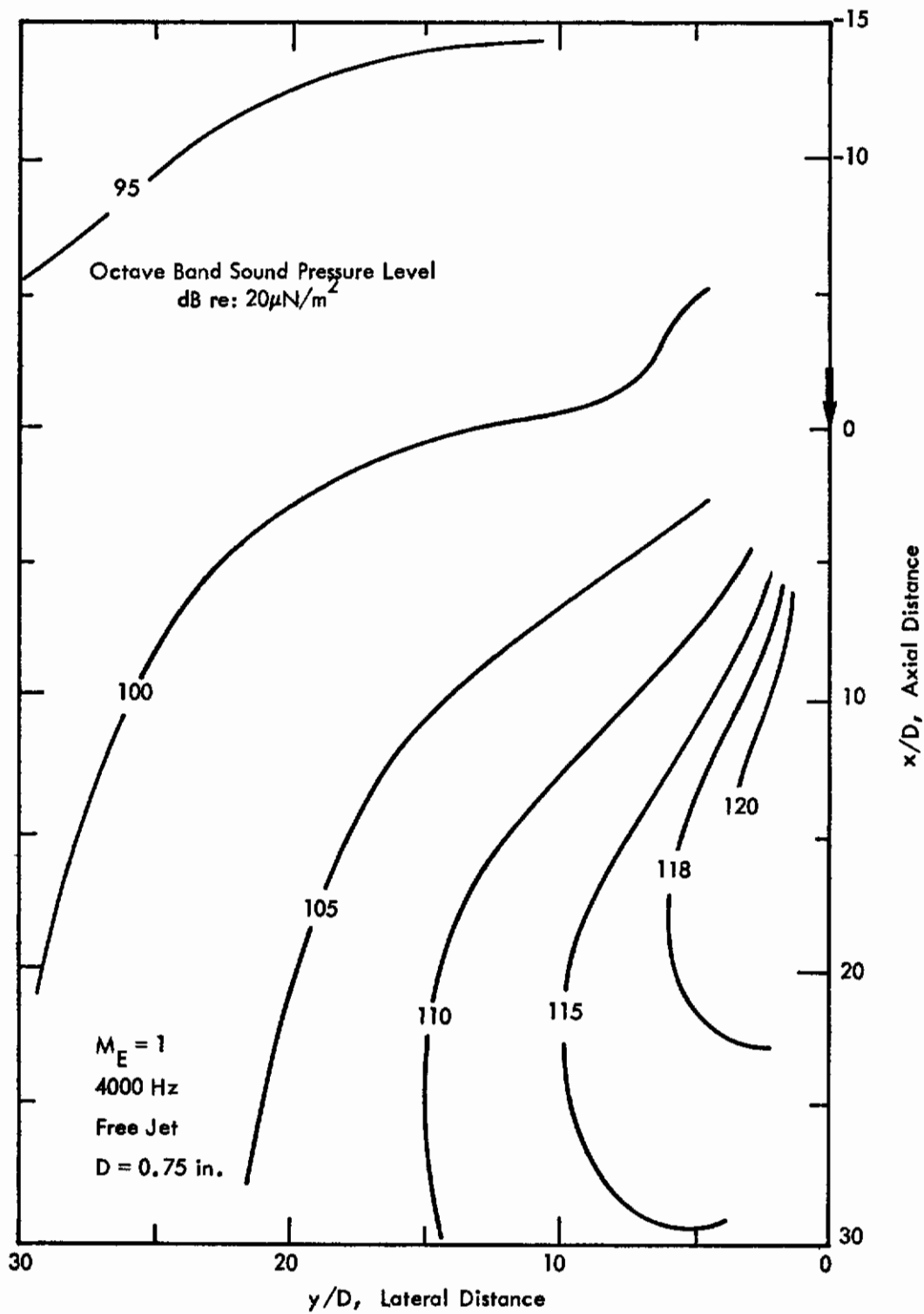


Figure 37. Contours of Constant Octave Band Sound Level for Free Ambient Air Jet. (From Appendix C.)

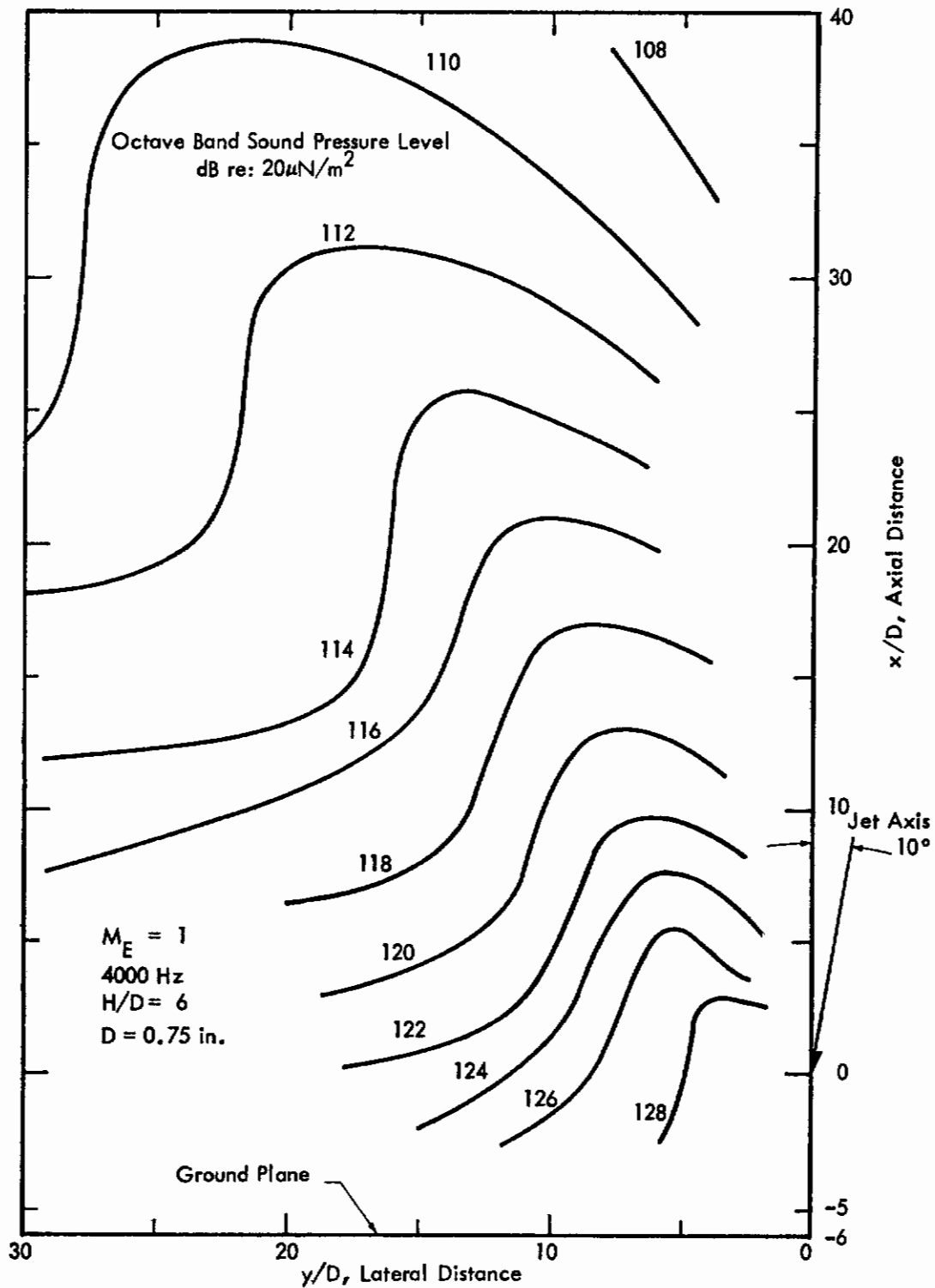


Figure 38. Contours of Constant Octave Band Sound Level for VTOL Ambient Air Jet (from Appendix C)

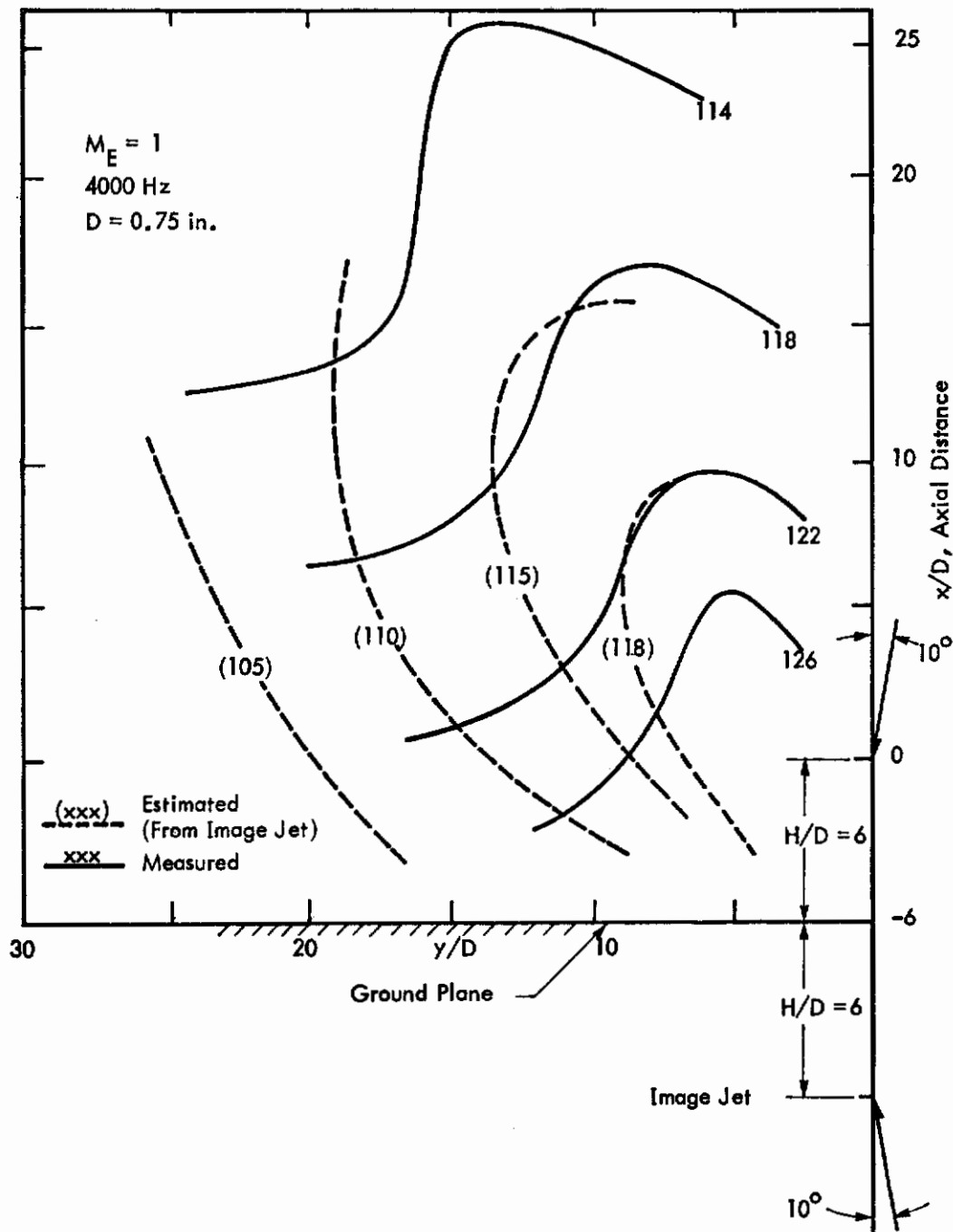


Figure 39. Comparison of Estimated (Dashed Lines) and Measured (Solid Lines) Contours of Octave Band Sound Level at 4000 Hz for Mach 1 Ambient Air VTOL Jet at 6 Nozzle Diameters Elevation and 10° Offset from Vertical. (From Appendix C.)

Figures 40 and 41 show typical results from some of the other model VTOL near field studies. Figure 40(a) and (b) illustrates the shift in position of overall sound level contours of fixed values as a function of nozzle elevation while Figure 40(c) shows the change in near field levels at specific locations for a supersonic model VTOL air jet.³⁷ In this case, the image jet concept does not appear to fit the observed contour pattern for the VTOL condition as well as for the sonic jet case illustrated earlier. One qualitative explanation for this is that the noise generation for the supersonic jet was shown to extend over a greater length of the jet (see Figure 18). Thus, the equivalent "image" jet is also more extended so that the ground reflection pattern will be diffused over a wider range of nozzle elevation while the other sources such as noise from the impinging jet will be more concentrated.

Both Figures 40 and 41 show that near field sound levels tend to approach a maximum value of 10 to 20 dB relative to the free field condition as nozzle elevation is decreased. Figure 41 indicates that this peak seems to occur at small nozzle elevations for high frequencies and at greater elevations for low frequencies.⁴ This is a very important result since it means that maximum near field sound levels on VTOL jet aircraft structure would have to be defined in terms of an envelope of maximum levels at each frequency band over the range of nozzle elevations encountered during a lift-off.

To evaluate this important effect more completely, the available VTOL model data were analyzed for the relationship between frequency, nozzle elevation and change in near field noise level. A series of 9 near field locations for VTOL model tests were selected for which measured data were available. At each location, the change in octave band level at preselected values of the nondimensional frequency or Strouhal number was determined as a function of nozzle elevation. The results were then plotted in the form shown in Figure 42. Each plot is for a particular value of the Strouhal number (S_N). Collectively, they cover the range from 0.06 to 1.0. Nozzle elevation (H) is expressed in terms of the potential core length (X_{\uparrow}). To further differentiate between the various experiments analyzed, data from heated air jets or rockets are shown by closed symbols* while open symbols represent ambient air jets. Each of the isolated data points in the figure represents a measured value at a single measurement point as indicated in the legend at the end of the figure. The combined data bar and line represents the average of the results from the ambient air jet model tests in this report (Appendix C). The length of the bar signifies the complete range of the measured values of the change in level as observed over 8 of the measurement locations defined in the legend. These locations cover a rectangular area from 0 to -20 diameters aft of the nozzle exit and from 2.5 to 25 diameters laterally from a vertical line through the jet exit plane.

*This coding not applicable for results from Appendix C.

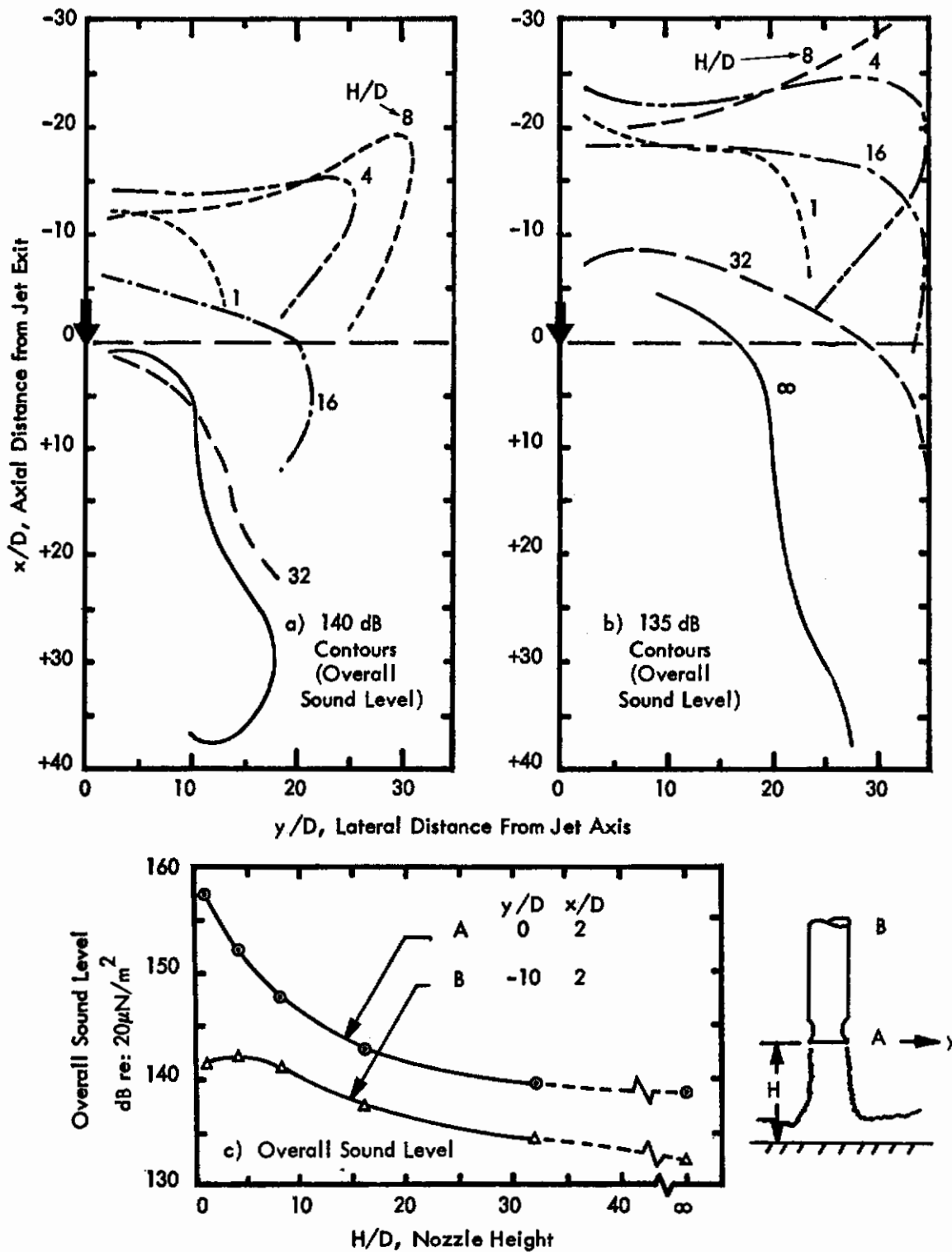


Figure 40. Change with Nozzle Height in Position of Near Field Contours (a, b) and Overall Sound Level (c) for Mach 1.88 VTOL Air Jet (Data From Reference 37).

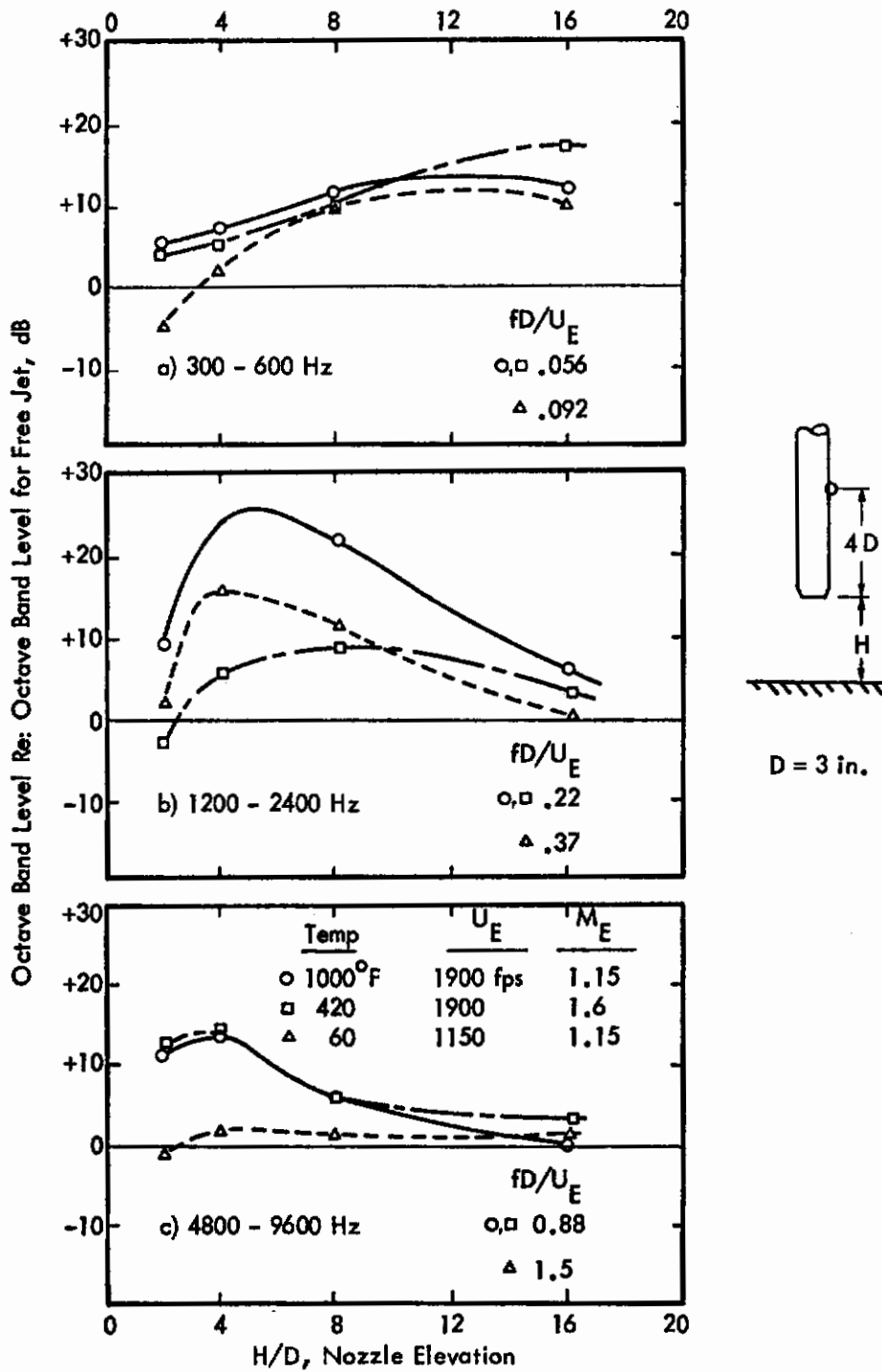


Figure 41. Change in Octave Band Level Forward of Exit for Cold and Hot Model VTOL Jet Relative to Free Field Level - $H/D = \infty$ (Data from Reference 4).

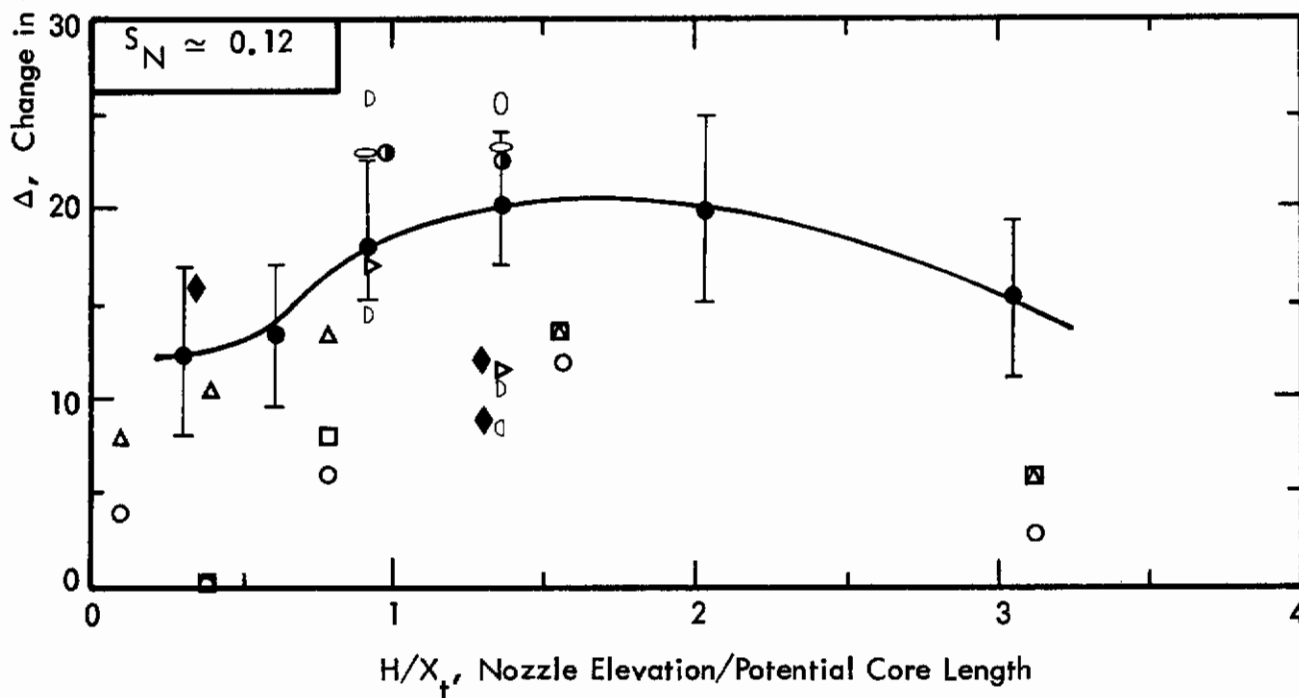
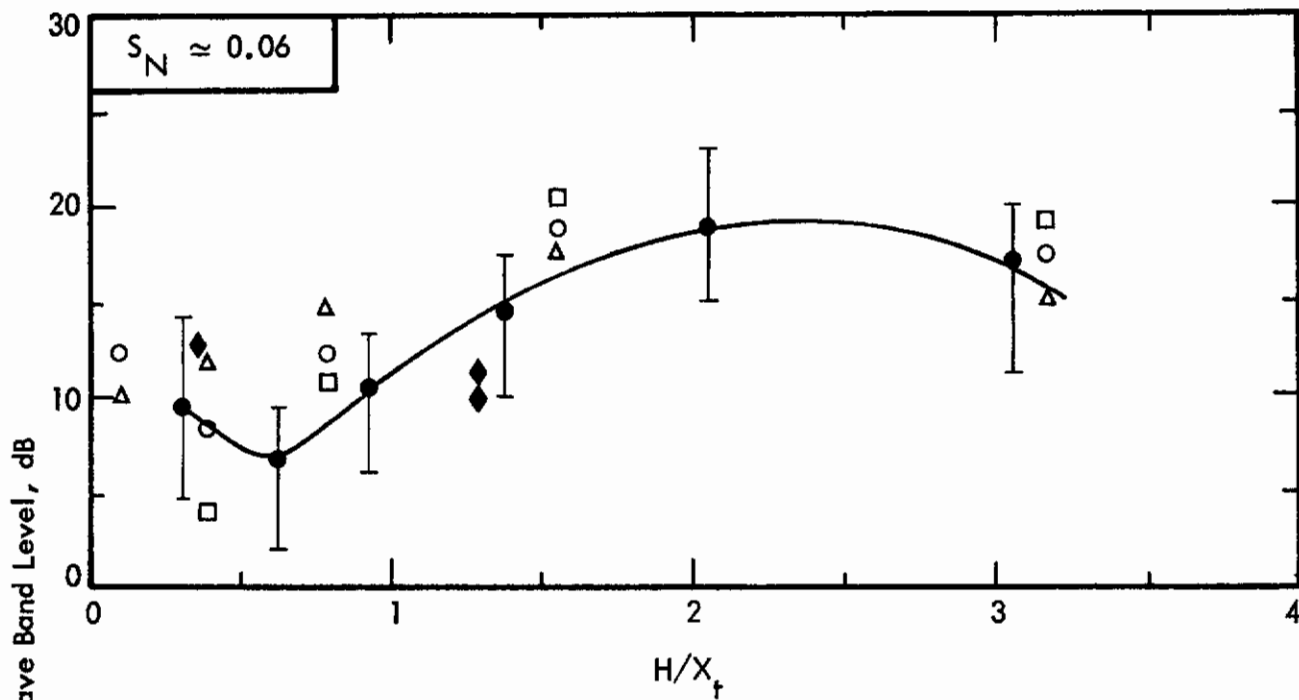


Figure 42. Summary of Model Data on Change in Octave Band Sound Level for VTOL Jet Relative to Level for Free (Undeflected) Jet. (See Legend at End of Figure)

continued ...

Contrails

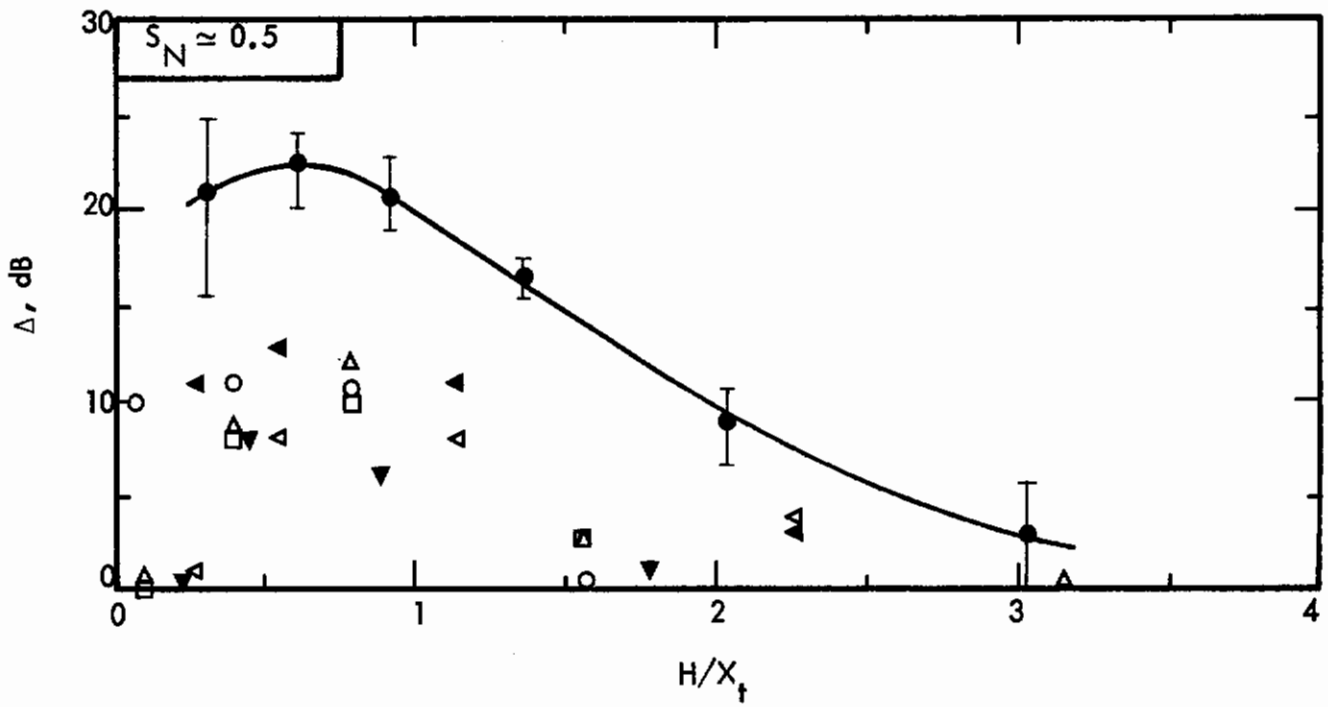
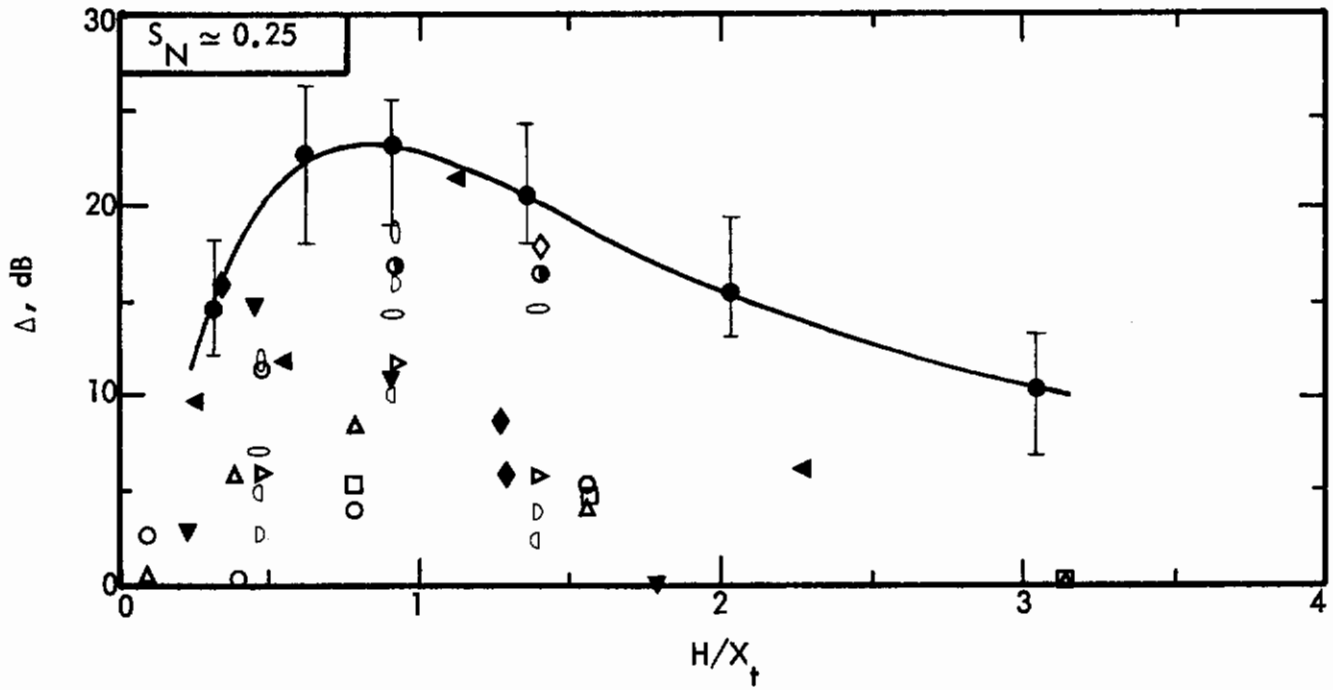
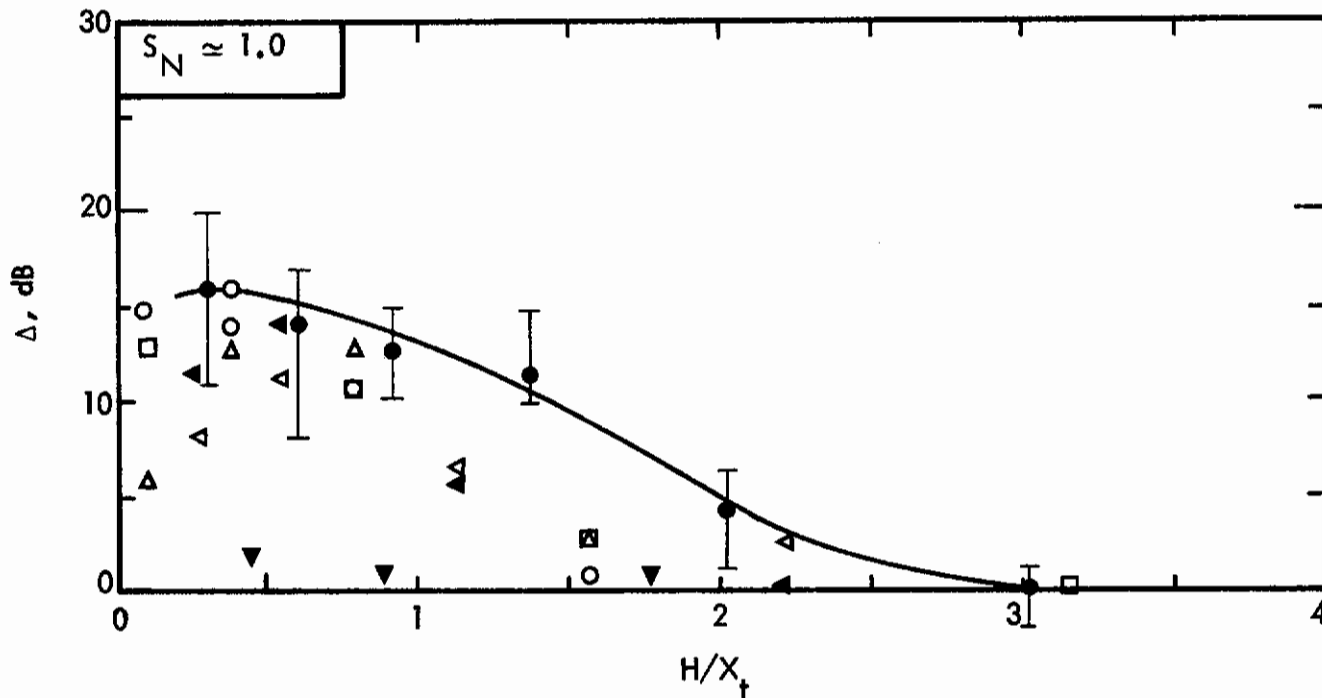


Figure 42. (Continued)



Legend for Figure 3.37

Measurement Location

x/D	2.5	2.5	10	10	10	17.5	25	25	2.5	Exit Mach No.	Ref.	Type of Jet
y/D	0	-10	-4	0	-10	-10	0	-20	-20			
Symbols	○	□	◊	△	◐	●	◇			3.25	38	Rocket
	○	□	△	◐	●	◇			1.88	37	Ambient Jet	
	○	□	△	◐	●	◇			1	40	Ambient Jet	
	△								1.15	4	Ambient Jet	
	▲								1.15	4	Heated Jet	
	▼								1.6	4	Heated Jet	
	← ● →								1			This Report - Ambient

Figure 42. (Concluded)

Two basic observations can be made about these data.

- A general pattern becomes clear for the position of the maximum value of the difference (Δ) between near field VTOL and free jet octave band levels as a function of normalized frequency and nozzle elevation. It is not surprising to find that for a Strouhal number of about 0.2, the peak value of Δ is reached when the nozzle elevation is nearly equal to X_1 . This is the approximate centroid of the "source" location for the peak frequency noise from a jet.¹⁵
- The model data from this report generally show a greater value of Δ than other published results for values of the Strouhal number greater than 0.12. There is no obvious reason for this difference. However, it should be noted that the model data in this report were obtained with a jet aimed at 10 degrees off the vertical to simulate real VTOL operations while all of the other data were obtained with nominally vertical jets. The measurements were also made in the "downstream" plane for this oblique VTOL jet. It was shown in part 1 of this section that such an oblique incidence would tend to increase the wall jet velocity slightly in the "preferred" downstream flow direction, and hence the noise from the wall jet itself. This may be part of the reason for the difference between the previous results and those reported in Appendix C. The latter represent a more comprehensive set of data on model VTOL jets than any previously available and are therefore utilized for the development of the VTOL near field noise prediction method.

Figure 43 shows a brief sample of these data for other Mach numbers. The trend in elevations for which the maximum value of Δ occurs is still the same but there is an indication that its magnitude varies slightly with exit Mach numbers.

Figure 44 shows the variation in the maximum value of Δ over the near field region studied and for the full range of nozzle elevations considered. While these figures illustrate results for only one frequency and Mach number, they are representative of the general lack of significant spatial variation in the maximum value of Δ observed for all of the results reported in Appendix C.

Finally, Figure 45 illustrates one example of the general correlation between the change in octave band power levels between a VTOL and a free jet and the corresponding average change in near field octave band sound pressure levels. For this example, the relative change in octave band power levels for three different exit Mach number collapses to essentially one curve, when frequency is expressed in terms of Strouhal number. It is clear from this figure that the other sources of noise in the VTOL jet contribute to the observed changes in near field levels since ground reflection alone should not change the sound power spectrum by more than 3 dB due to possible effects of radiation efficiency.

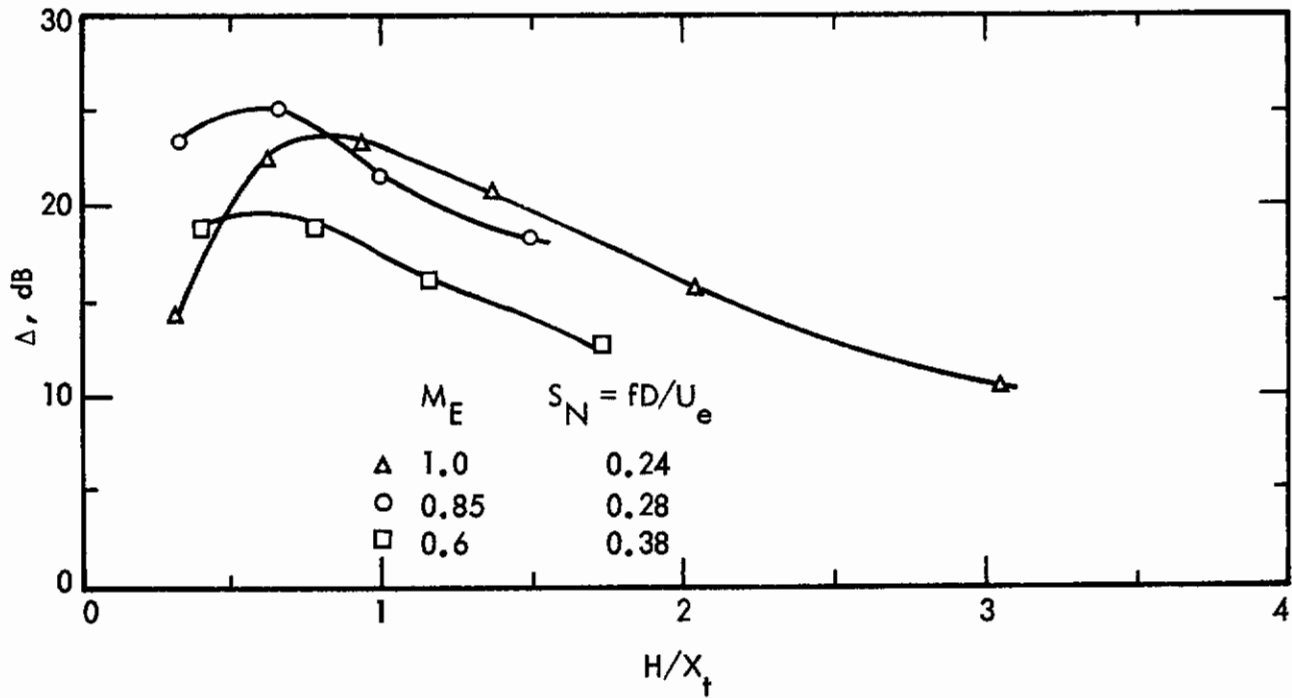


Figure 43. Variation in Δ (Change in Near Field Octave Band Levels Re Free Jet) in 4000 Hz Octave Band for 3 Different Mach Numbers. (Data From Appendix C.)

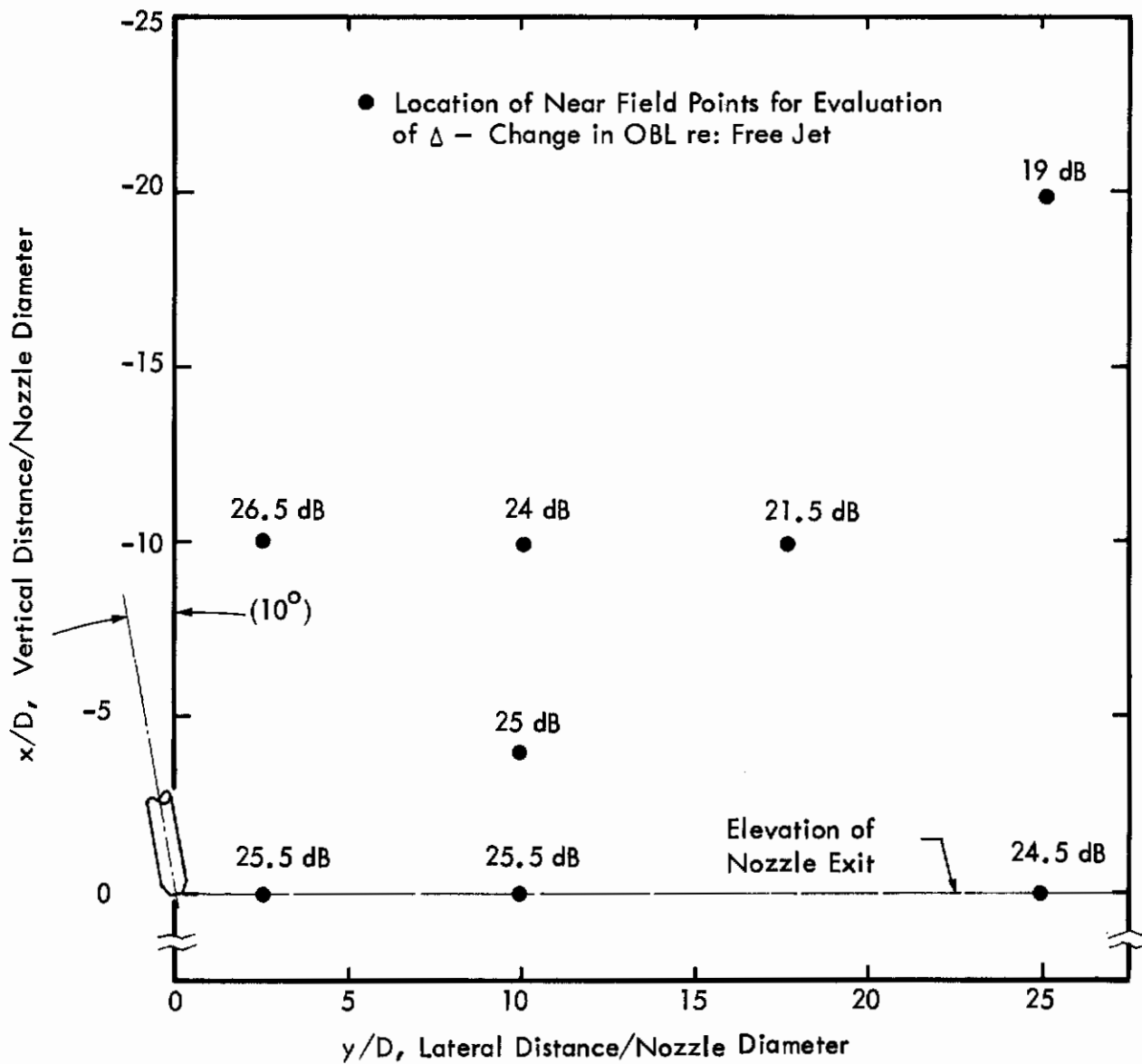


Figure 44. Variation Over Near Field Region of Maximum Value of Δ at 4000 Hz. (For Mach 1 Ambient Air Jet, $fD/U_e = 0.24$ - Data from Appendix C.)

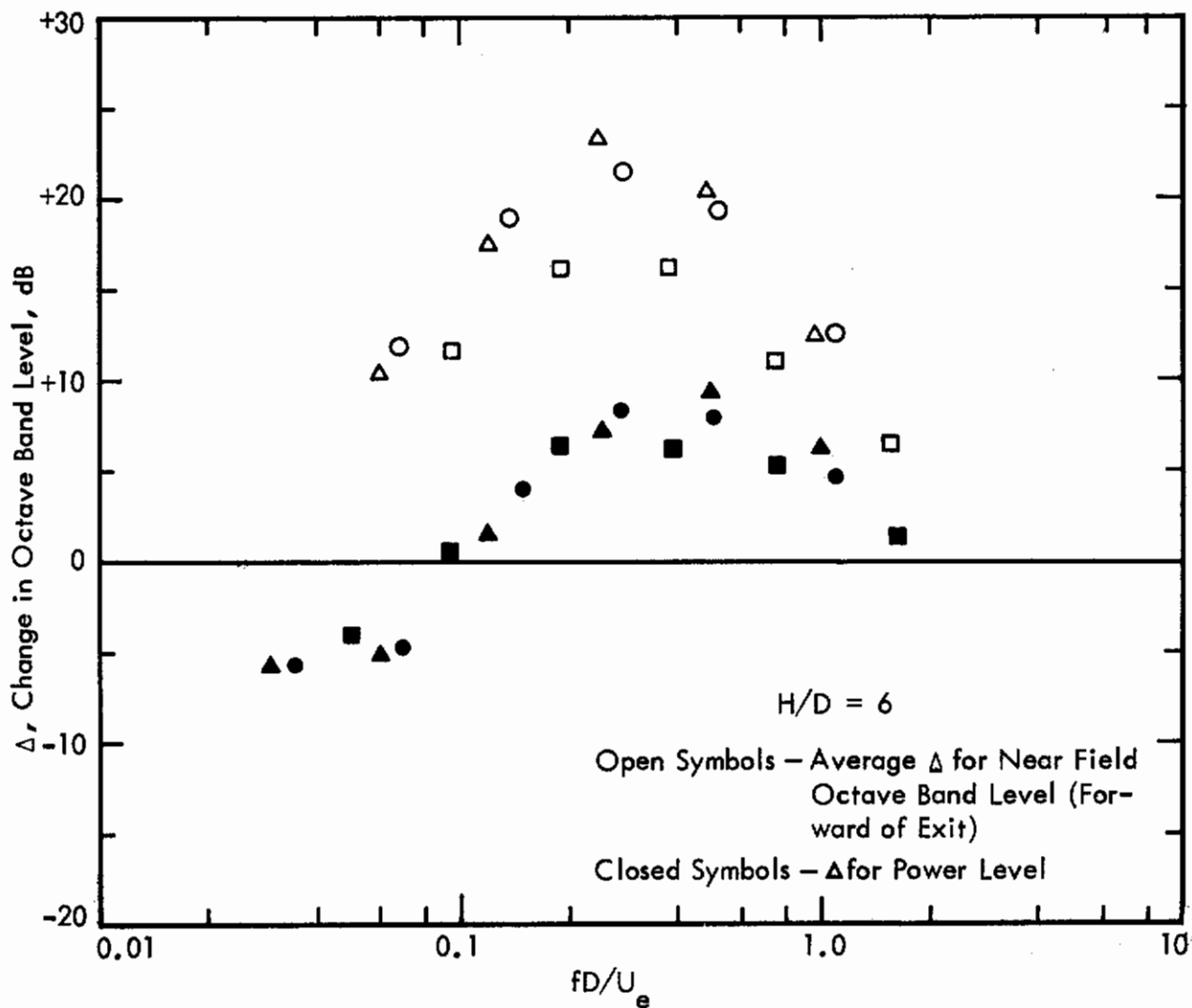


Figure 45. Change in Octave Band Power Levels and Near Field Octave Band Levels Relative to Free (Undelected) Jet for VTOL Ambient Air Jet at 6 Nozzle Diameters Elevation. (Δ for Mach 1, O for Mach 0.85, \square for Mach 0.6 – Data from Appendix C.)

To establish the starting point of a possible prediction method for the near field, the preceding figure has been generalized to define the envelope of maximum values of Δ (for any nozzle elevation) as a function of dimensionless frequency. The results, based entirely on the model data from this report, are shown in Figure 46. The envelope of the change in octave band power levels, designated by the lower line, has a nearly constant value of 3 dB at low frequencies. More significant, however, is the fact that the Δ values for power level collapse onto a single line for Mach numbers from 0.6 to 1.0. The added hump in the Δ curve for power levels at higher frequencies can be considered as representing the relative frequency spectrum of the excess power for the VTOL jet discussed earlier. The envelope for the Δ for the near field octave band sound pressure levels – the upper line in Figure 46 – could then be considered as a correction factor to be applied to free jet near field octave band sound pressure levels in regions forward of the jet exit in order to estimate the approximate envelope of the maximum levels on the VTOL structure.

Before finalizing a prediction method, the additional noise sources for the VTOL jet need to be considered and a comparison made of any prediction method with available full scale data. Perhaps this can explain, in part, the wide range of the Δ term in Figure 42 for the various sets of available model data.

To summarize so far,

- A simple intensity-addition model for the effects of ground reflection shows encouraging agreement with model data in a restricted region near the jet axis.
- The other sources of noise in a VTOL jet are considered responsible for the simple reflection model failing to fully describe the near field of the VTOL jet.
- Available model data on near field sound levels of VTOL jets relative to levels for a free jet is internally consistent in showing similar patterns relating the position of the maximum change in octave level in terms of the nozzle elevation, in core lengths, and the Strouhal number.
- However, data from various studies differ significantly in the magnitude of the relative change in octave band sound pressure levels from the free to VTOL jet.

6. OTHER NOISE SOURCES OF VTOL JETS

The remaining possible sources of noise will be considered in the sequence illustrated by the chart in Table I.

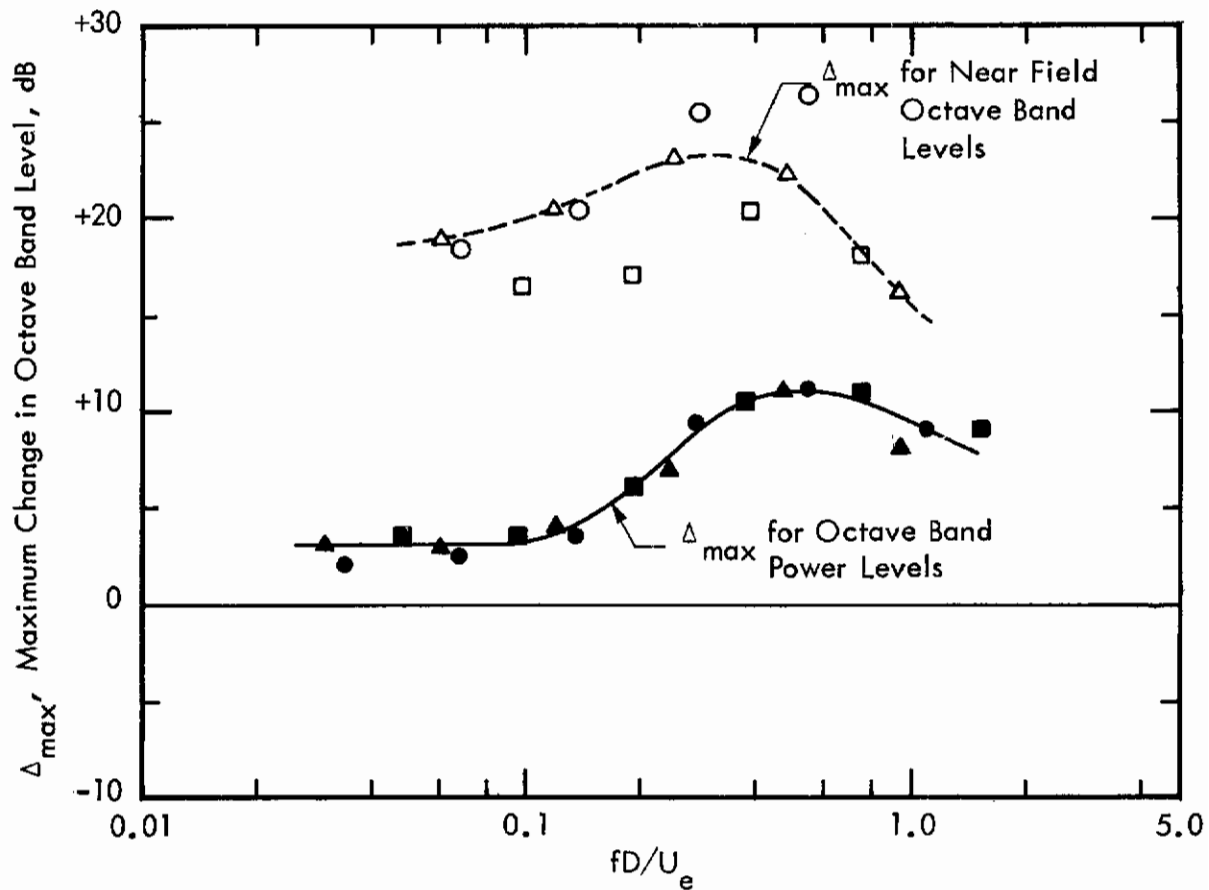


Figure 46. Envelope of Maximum Value of Change in Octave Band Levels for Model VTOL Jet Relative to Levels for Free Jet. (Δ for Mach 1, O for Mach 0.85 and □ for Mach 0.6 – Data from Appendix C.)

a. Radiation from Impingement Area

Turbulence in a jet impinging on a rigid plate can be expected to generate noise due to the fluctuating normal forces acting on the surface. This is a dipole noise source whose acoustic power (W_a) may be conveniently expressed in the form^{51, 28}

$$W_a = \frac{1}{12\pi\rho_o c_o^3} \overline{\left(\frac{\partial F}{\partial t}\right)^2} \quad (34)$$

where

ρ_o, c_o = ambient density and speed of sound, respectively

and

$\overline{\left(\frac{\partial F}{\partial t}\right)^2}$ = mean square value of the rate of change of the fluctuating force.

We can use the data from Reference 12 on pressure fluctuations under a jet reviewed in part 2(c) of this section, to estimate the magnitude of this term as follows. Its rms value can be given as:

$$\frac{\tilde{\partial F}}{\partial t} \approx 2\pi f_c \tilde{F} \quad (35)$$

where

f_c = a characteristic frequency of the fluctuation

$\tilde{F} = \tilde{p} \cdot A_c$, rms force

\tilde{p} = rms pressure under the impinging jet

and

A_c = correlation area or area within which fluctuating pressure is essentially in-phase.

The three parameters, f , \tilde{p} and A_c , can be estimated as follows.

From Figure 16 and the preceding text, the peak frequency (f_c) of the fluctuating pressure for jets at 0.5 to 7 diameters elevation is approximately

$$f_c \approx 0.23 U_e / D$$

where U_e , D = jet exit velocity and exit diameter, respectively.

From Figure 15, the maximum rms fluctuating pressure under the impinging jet occurs for $H/D = 7$ (for the Mach 0.12 jet measured) and has the value¹²

$$\tilde{p} = 0.134 \left(\frac{1}{2} \rho U_e^2 \right)$$

where ρ = the jet density.

Finally, the correlation area (A_c) could be estimated as¹²

$$A_c \approx \frac{\pi}{4} (0.8 D)^2 = 0.64 A_e$$

where A_e = jet exit area.

Substituting these relationships back into Equation (34), the estimated acoustic power in watts generated by this source could have a maximum value of about

$$W_a \approx 1.1 \times 10^{-4} \rho^2 A_e U_e^6 / \rho_o c_o^3, \quad \text{watts} \quad (36)$$

when English units are used to describe the jet variables.

This estimate can be put into better perspective by relating it to the expression for acoustic power of the free jet itself. The result is that the estimated maximum value of the acoustic power due to impingement noise (for an ambient air jet where $\rho \approx \rho_o$), would be equal to

$$W_a \approx 3 \left[W_a (\text{jet}) \right] / \left(\frac{U_e}{c_o} \right)^2 \quad (37)$$

This shows the surprising result that for a sonic ambient jet, the impingement noise power would be 3 times that of the free jet and 6 times greater for an ambient Mach 0.7 jet.*

The mean square pressure in the field of this dipole noise source will be given by the well-known directivity pattern for a dipole source.²⁸

$$\overline{p^2} = \frac{\overline{p_o^2}}{R^2} \cos^2 \beta \quad (38)$$

where

β = angle relative to the dipole source axis – the jet axis for a vertical jet

$\overline{p_o^2}$

= mean square space average pressure of the source at unit distance.

Thus, the impingement noise would tend to be a maximum along a vertical line above the impingement point where $\beta = 0$ or 180 degrees. Diffraction effects by the wall jet would probably alter this directivity at propagation angles off the vertical axis.

This estimate of impingement noise probably establishes a maximum upper bound since as nozzle elevation increases or decreases from the value $H/D = 7$, the fluctuating pressure under the jet will decrease according to Figure 15. Furthermore, if a higher Mach number jet had been measured, the turbulence in the jet and hence the maximum fluctuation pressures would have decreased.^{2,3}

Nevertheless, it appears that impingement noise can be a major source of noise for a VTOL jet at critical nozzle elevations. The directivity pattern for this source will tend to increase levels along the jet axis over what would be predicted on the basis of ground reflection alone. This is consistent with the experimental data and helps to explain some of the differences between predicted near field levels based on ground reflection models and observed values.

To summarize, the net effect of impingement noise is expected to be significant at nozzle elevations comparable to the jet noise source location and to offer a further transitory complication to the change in near field levels as nozzle elevation changes. The source is expected to be most significant for subsonic ambient jets.

*Note that this type of Mach number sensitivity was not evident in the measured excess power for the model VTOL jet data from Appendix C.

b. Direct Radiation by Wall Jet

The basic theory for radiation of noise by turbulent flow over a rigid boundary has been set down by Curle.⁵⁹ However, simple considerations of kinetic energy dissipation in a wall jet and in a normal conical jet will suffice here to show that wall jet noise should be significant only for regions close to the wall jet flow itself.

Since the dissipation of energy by a turbulent mixing flow generates noise, the relative noise power $W(X)$ generated in an elemental volume at a position X in such a flow can be defined by

$$W(X) = E(X) \cdot \eta \quad (39)$$

where

$E(X)$ = the rate of mechanical flow energy dissipated in this element

η = the efficiency for conversion of some of this dissipated energy to noise

The rate of dissipation of mechanical energy in the flow will be proportional to

$$E(X) \propto M(X) U(X)^3 \quad (40)$$

where

$M(X)$ = mass in the flow at X

$U(X)$ = velocity at X

For both conical and wall jets, these parameters vary to a first approximation as indicated in the following^{28,14,12}

<u>Mixing Region</u>	<u>Fully-Developed Flow</u>
$M(X) \sim \text{constant}$	$M(X) \propto X$
$U(X) \sim \text{constant}$	$U(X) \propto 1/X$
$E(X) \sim \text{constant}$	$E(X) \propto 1/X^2$

The position variable (X) for the conical jet is the distance to the virtual origin of the similarity region of the flow, while for the wall jet it is essentially equal to the radius outward from the centerline. (Note that it was shown in part 1 of this section that the initial mixing region in a wall jet only extends out about 1.5 jet diameters.)

Thus, the rate of dissipation of mechanical flow energy for both types of jets is initially constant in the mixing region and falls off as the inverse square of the general position variable X in the fully developed flow region.

Now, since noise generation by turbulence has an acoustic efficiency (η) proportional to the acoustic Mach number ($U(X)/c_0$) to the 5th power, then the total acoustic power generated in each element of volume at a position X should vary in the same way for both the conical and wall jets. However, the local acoustic intensity passing through the boundary area ($A(X)$) of a volume element in the fully developed flow region will be quite different since:

- for the conical jet $A(X) \approx 2 X \tan \phi \Delta X$
where ϕ = half-angle of boundary of jet, ΔX = length of element
- for the wall jet $A(X) \approx 2 X \Delta X$

Thus, the rate of increase of radiating area for the conical jet is proportional to $X \tan \phi$, much less than the rate of increase of radiating area for the wall jet. The net result is that if both jets start with the same initial kinetic energy, the shorter length of the mixing zone for the wall jet (about 1.5 D instead of 5 to 8 D for the conical jet) and the accompanying higher rate of increase for the bounding area of the fully developed region of the wall jet will result in a short region of high noise levels near the jet impingement point and lower sound levels along the fully developed flow region. The argument here is highly simplified but serves to rank the relative significance of the near field levels for the two sources of jet noise.

Another important point to note is the relative exchange of kinetic energy and hence noise power generation between the primary jet and the wall jet.

For the subsonic jet, until the nozzle elevation is reduced to less than the core tip length (X_c), approximately 80 percent of the jet noise power is still radiated. This is within 1 dB of the total power available from the free jet (ignoring the effect of source location for various frequencies). On the other hand, all other things being equal, the noise power of the wall jet should have a nearly constant value for smaller elevations than X_c , but should decrease very rapidly as nozzle elevation is increased beyond this point. The initial velocity (U_{\max_0}) of the wall jet is decreasing as approximately

$1/H$ at higher elevations and the total acoustic power from the wall jet can be assumed to be proportional to (U_{\max_0}) so that its acoustic power would fall off as $(1/H)^6$. This

tradeoff between noise power generation by the primary jet and wall jet is illustrated conceptually in Figure 47(a).

Contrails

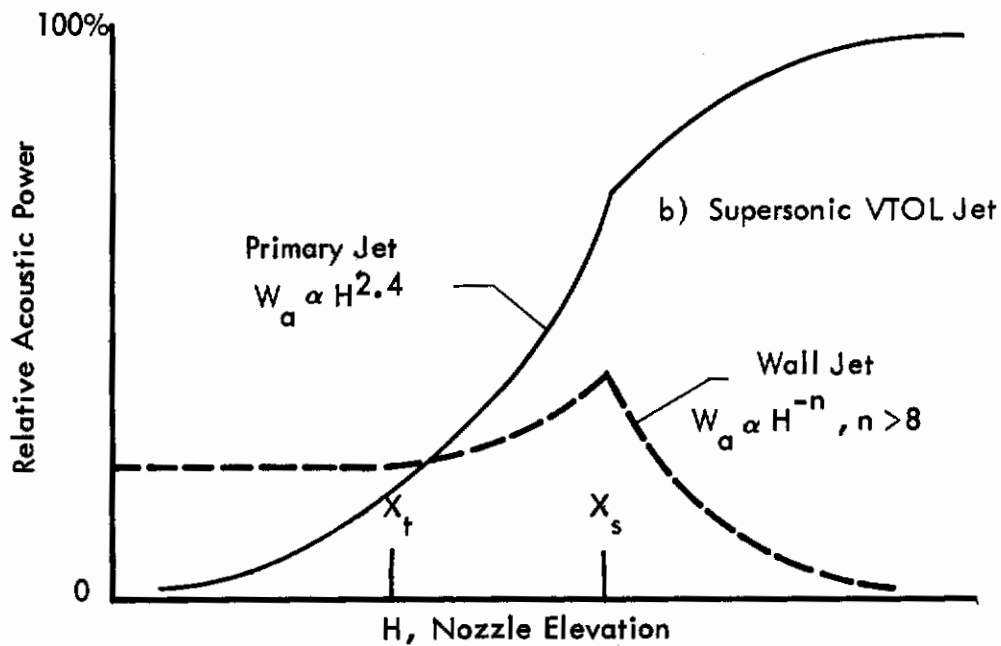
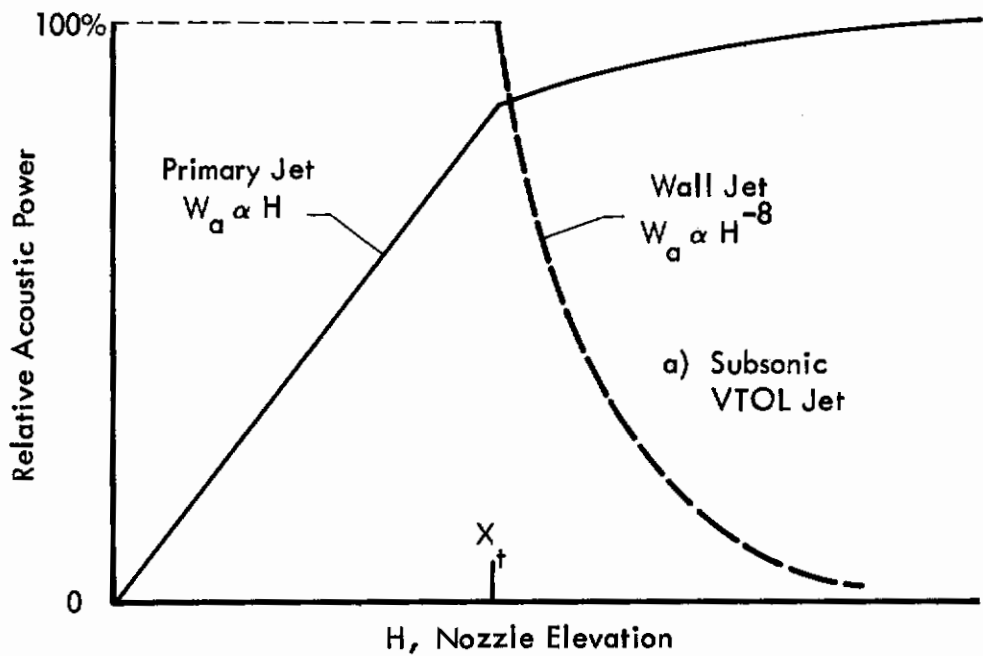


Figure 47. Simplified Illustration of Growth in Total Acoustic Power (W_a) Generated by Primary Jet and by Wall Jet as Nozzle Elevation Increases. (Based on Idealized Versions of Power per Unit Length, Figure 18, Velocity Decay of Wall Jet, Figure 8, and Wall Jet Velocity for Supersonic Jet, Figure 14, and Assuming Acoustic Power Proportional to U^8 in all Cases.)

For a supersonic jet, the tradeoff is more complex for two reasons –

- (1) The initial velocity of the wall jet is expected to decrease as the nominal impinging jet velocity increases due to the velocity jump across a standing shock above the ground.
- (2) The noise power generation within the supersonic jet itself varies with axial position in a more complex fashion. A typical case for this situation is illustrated conceptually in Figure 47(b).

Just as was found for impingement noise, the noise from the wall jet is predicted to be less significant, relative to noise from the primary jet, for supersonic jets than for subsonic jets. For the former, only when the nozzle elevation is less than the potential core length (or the source position for each frequency), will the contribution by the wall jet be significant.

c. Vortex Noise from Deflector Vanes

Some VTOL jet aircraft employ deflector vanes in the cruise engine nozzles to direct the exhaust gases downward during vertical takeoff.⁴³ Vortices shed by the engine exhaust passing over these vanes are a source of broadband noise that bears consideration. There are, in fact, three possible sources of noise involved:⁶⁰

- (1) Dipole-type noise generated by vortex shedding, assuming the deflector vanes are operating in smooth flow;
- (2) Dipole-type noise generated by initial turbulence passing over the vanes;
- (3) Quadrupole-type noise from the turbulent wake downstream of the vanes.

Although the exhaust flow in a VTOL jet will not be smooth in the ideal sense, available experimental data indicate that the first component (vortex shedding) is likely to be dominant for this case and is the only source considered here.⁶⁰

Sharland has developed the following expression for the noise power for this source, assuming uniform flow over the blades.⁶⁰

$$W_a = \frac{\rho U_e^6 (Re)^{-0.4} S}{120 c_o^3} \quad (41)$$

where

ρ = gas jet density

Re = Reynolds number based on the cord of the deflected vane

S = product of vane cord and span

The source would have a dipole directivity pattern similar to that given by Equation (38) with the source axis perpendicular to the vane flow surface.

To evaluate the potential significance of this source, the estimated acoustic power was computed for a particular VTOL aircraft which employed turning vanes and for which measured sound power data were available.⁴³ Based on maximum engine conditions for this aircraft and assuming an effective area (S) of about 1.5 ft² per nozzle, the estimated acoustic power for this noise source was about 10 dB below the measured values. If the source were significant, a broad peak in the measured spectrum would have been expected at a frequency approximately equal to

$$f_c \approx 0.2 U_e / b \quad (42)$$

where b = characteristic thickness of turning vanes in direction normal to flow.

No such peak was discernable in the available spectrum measurements for a range of feasible values for b . Therefore, it was concluded from this rough estimate of the acoustic power for vortex noise that it would not be expected to be a significant source of near field noise levels for VTOL aircraft.

d. Discrete Ring Tones

Under certain conditions, intense discrete frequency "whistles" were observed during the course of the model VTOL jet tests reported in Appendix C. These were called "ring tones" and have been definitely observed in other VTOL model studies, or may be present in some of the reported results.^{37, 38, 41, 4, 38} While it will be shown that this source of noise is probably not significant for full scale VTOL jets, the issue is not clear and, equally important, it was felt desirable to emphasize the potential presence of these tones for future model studies.

In all tests where this discrete tone was apparent or suspected, its frequency was roughly equal to

$$f_R \approx \frac{c_o}{\pi D} \quad (43)$$

Contrails

At this frequency, the acoustic wavelength is equal to the circumference of the jet exit. However, the mechanism for generation of the discrete tone is expected to involve a feedback process between the generation at the nozzle lip and jet flow impinging on the ground.⁶¹ Thus, flow velocity was also slightly influential in changing the frequency. This effect and the influence of nozzle height can be summarized as follows, according to the results from this report.

- The ring tone was observed repeatedly only when the exit Mach number of the ambient jet was 0.85 or 1.0, the two highest velocities used, with exit velocities of 910 and 1045 ft/sec respectively.
- The tone did not occur for nozzle elevations greater than 6 nozzle diameters, but at this elevation and at 4 and 2 nozzle diameters, the frequency of the ring tone was normally constant for a given exit Mach number.
- For an exit Mach number of 0.85, the fundamental of the ring tone normally occurred in the 6300 Hz 1/3 octave band. (The nozzle diameter was 0.75 inch.) For an exit Mach number of 1.0, the ring tone normally occurred in the 5000 Hz 1/3 octave band. This slight decrease in frequency for a higher flow velocity implies a critical feedback delay time which varies in a nonlinear fashion with flow velocity.

A typical 1/3 octave band spectrum analysis at one measurement point, with the ring tone present and the ring tone suppressed, is shown in Figure 48. With the ring tone present, the fundamental and second harmonic are obvious with some indication of the presence of a third harmonic. The method of suppression involved adding a very slight protuberance at the edge of the nozzle lip. The directivity pattern of the ring tone fundamental observed at a radius of 34 nozzle diameters is shown in Figure 49. This shows that the fundamental and second harmonic both have different complex directivity patterns each with at least 2 maxima in a 90 degree quadrant.

The ring tone increased the 1/3 octave band level, at the fundamental frequency, from 5 to as much as 21 dB. In general, the greatest amplification was observed for the Mach 0.85 condition at $H/D = 2$ (average 12 dB increase due to the ring tone) and for the Mach 1.0 condition at $H/D = 6$ (average 9.5 dB increase).

Since this discrete tone could be so readily suppressed by a minor modification to the exit profile, it is expected that the normal exit profile of a full scale VTOL jet will be such as to prevent the generation of this tone.

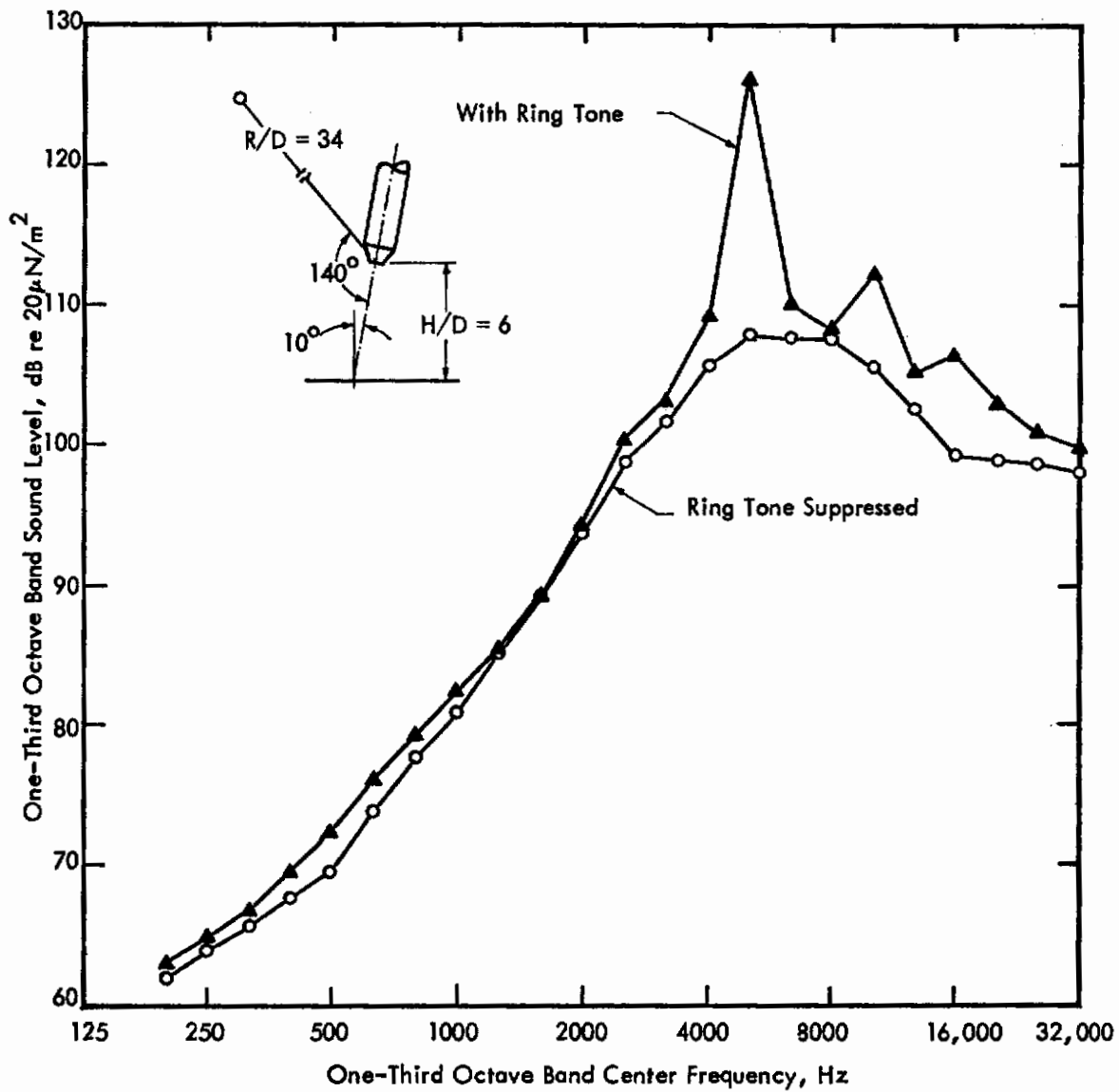


Figure 48. Typical One-Third Octave Band Spectrum Measured with and without Ring Tone Present. Exit Mach No. = 1.0, Exit Velocity = 1045 ft/sec., Exit Diameter = 0.75 in.

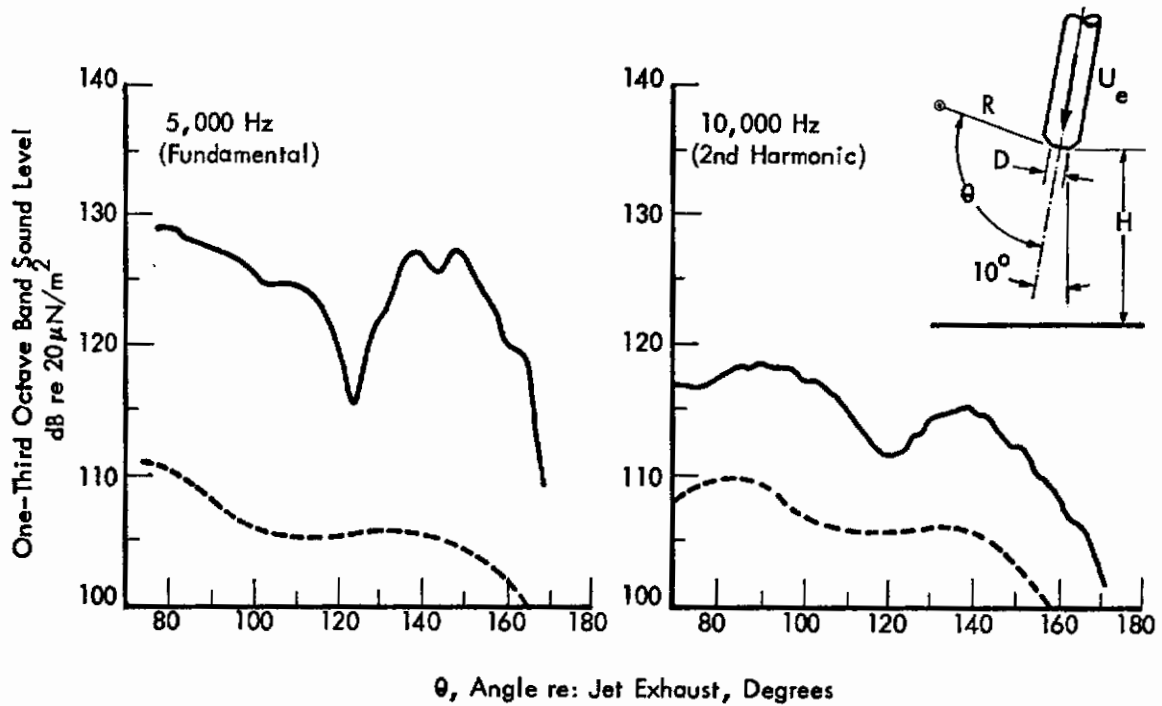


Figure 49. Typical Example of One-Third Octave Band Levels vs Angle to Exhaust of VTOL Jet with Ring Tone (Solid Lines) and with Ring Tone Suppressed (Dashed Lines). $M_E = 1.0$, $U_e = 1045$ ft/sec, $H/D = 6$, $D = 0.75$ in., Radius from Jet Exit, $R/D = 34$

e. Shock-Turbulence Interaction Noise

Passage of turbulence through a shock wave is an experimentally observed source of noise from supersonic jets, particularly unheated jets, operating off of their design pressure ratio.^{62, 63} Since a supersonic VTOL jet is expected to generate a strong standing shock just above the ground, noise from jet turbulence passing through this standing shock could be significant. However, the power level and near field sound level data for supersonic VTOL model jets summarized earlier show no clear evidence of any such noise. Therefore, no further consideration is given to this noise source.

f. Buffeting Noise

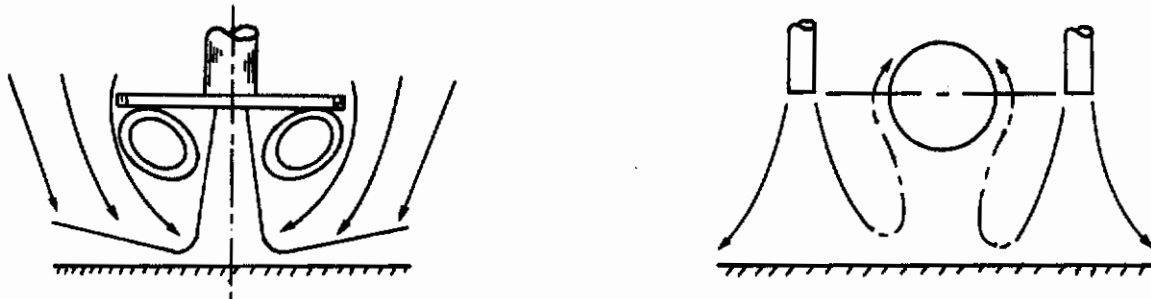
A VTOL jet exhausting vertically from underneath or to each side of a fuselage can generate the type of recirculating flow illustrated in Figure 50. This can cause buffeting "noise" or aerodynamic pressure fluctuations on the surface of the structure. Since the actual flow pattern depends so strongly on the structure-engine exhaust geometry, it is not feasible (or desirable) to establish a general prediction method for this source of sonic loading. When it occurs, it can be sufficiently severe to require modifications to the engine mounting design to reduce the severity of the buffeting. An indication of the potential magnitude of the problem may be obtained as follows. Experimental data on flow velocities in this "upflow" region indicate maximum values of 10 to 20 percent of the jet exit velocity. If the ratios of rms fluctuating pressures to jet exit dynamic pressures observed under a VTOL jet are used to estimate the buffeting pressures, then, according to Figure 15, these could range from 0.02 to 0.13 times the dynamic pressure at the exit plane. Assuming the average reduced velocities in the "upflow region" are 15 percent of the exit velocities, then a rough estimate of the range of the rms buffeting pressures (P) would be given by

$$\frac{\tilde{P}}{1/2 \rho U_e^2} \approx 0.003 \text{ to } 0.02$$

where $1/2 \rho U_e^2$ can be estimated by $1/2$ (Engine Thrust/Exit Area). Choosing a typical value of 28 psi for thrust per unit exit area for turbojet or low bypass ratio turbofan engines, one obtains the following rough estimate of the range of maximum values of the rms buffeting pressures.

$$\tilde{P} \sim 0.042 \text{ to } 0.28 \text{ psi}$$

or 143 to 160 dB re $20 \mu\text{N/m}^2$.



a) Single Jet

b) Two Jets

Figure 50. Illustration of Typical Sources of Buffeting on VTOL Aircraft Structure from Recirculation or Upflow from Jet Exhaust (From Reference 9)

This indicates substantial sonic loads are entirely possible from this type of buffeting. New VTOL jet aircraft configurations for which possible backflow conditions have not been studied before, in either full or model scale, should be evaluated experimentally for questionable backflow problems. Peak frequencies of these buffeting loads can be expected to occur in the structural response range of 100 to 1000 Hz but, again, model studies are called for when available design information is inadequate to evaluate the buffeting loads.

7. DEVELOPMENT OF A PREDICTION MODEL

From the preceding analysis of noise sources for VTOL jets, a tentative ranking can be made of the relative significance of the major noise sources. Until additional full scale data are available, this ranking must be considered as only preliminary. In descending order of significance, they are:

- Ground-reflected noise from the undeflected portion of the jet exhaust.
- Wall jet noise (primarily for subsonic jets).
- Jet impingment noise (primarily for subsonic jets).
- Direct radiation by the undeflected jet.

This is a very broad generalization since it ignores the fact that the relative dominance of each source will vary at least with the position of an observation point in the near field and the nozzle elevation above the ground.

A brief qualitative review of what has been established, observed or postulated about this relative dominance of the sources is in order at this point as a guide for selecting a near field noise prediction model.

a. Qualitative Review of Source Predictions

The total power, far field directivity and near field contours for noise from a typical turbojet engine are reasonably well known (see part 3 of this section). The effect of reduced exit temperatures and lower velocities on the near field noise is less well established. However, for a first approximation, data are available for scaling near field levels in terms of jet velocity.³⁶

For nozzle elevations equal to or greater than the core tip length, this component of the noise and the related ground reflected noise should be readily predictable. The available VTOL jet noise data indicate this combination of sources is probably dominant at these elevations. The change in their noise levels at lower nozzle elevations is at least qualitatively predictable on the basis of current knowledge of the noise source distribution in a jet (e.g., Figure 47 of Reference 15).

The predicted noise from jet impingement suggests that it would have a maximum value for nozzle elevations of the order of the axial position of the source. However, the initial predictions of the magnitude of this source indicate that its strength, relative to the jet noise, should increase as the jet Mach number decreases. This Mach number sensitivity was not observed in the VTOL jet data in Appendix C but is possibly present to some degree in other test results (see Figure 19). Due to its dipole nature, the major influence of this source would be in areas near the jet axis — in the lobe of maximum noise.

The remaining contributor to VTOL jet noise is the wall jet. In fact, the wall jet becomes the prime candidate for the major source at low nozzle elevations for subsonic jets. The evidence for this conclusion is substantial.

- The excess power of the sonic or subsonic VTOL jet approaches a constant value as nozzle elevation becomes less than the core tip length (Figure 19). Only the wall jet noise source is expected to have this characteristic.
- The peak frequency of the excess power falls at a value of fD/U of about 0.5 (Figure 46). This is higher than expected for either jet noise or impingement noise. It corresponds, in fact, to a value expected for a wall jet peak frequency on the basis of the limited data on spectra of pressure fluctuations under a wall jet (Figure 16).
- The near field contours for the VTOL jet (Figure 39), and directivity indices at 24 nozzle diameters, indicate a peak radiation near 90 degrees to the jet axis — near the boundary of the wall jet.

The major unknown for the wall jet is its maximum contribution to near field levels. It appears to have a higher maximum acoustic efficiency than the primary jet by a factor of about 8 to 12 dB for sonic or subsonic jets (Figure 19). However, the near field directivity of the wall jet noise is not well-defined over the full range of nozzle elevations encountered during lift-off.

Alternate prediction methods that were considered to account for these sources are briefly summarized below.

b. Contour Summation Method

Both the first and last sources listed at the beginning should be predictable. According to the analysis of ground reflection for a VTOL jet covered in part 4 of this section, all that would be required for these two sources are a set of contours to define free field sound levels, preferably for individual octave bands. Then, by folding these contours about the ground plane "mirror," the estimated direct and reflected

fields could be added (on an intensity basis). Pursuing the same approach, it would be conceptually possible to add in the effect of jet impingement noise and wall jet noise using the same method by constructing contours of estimated level for each of these sources. A refinement of this method could consist of breaking the distributed jet exhaust and wall jet into source regions to allow a piece-wise construction of the near field in a manner similar to the method outlined by Eldred.¹⁵

While this basic approach offers the potential of being the most accurate, it was not considered further for two reasons:

- The potential accuracy would be difficult to realize at this point until wall jet and impingement noise are more clearly defined for VTOL jets.
- The method would tend to be complex, even if the sources were well defined, due to the complex change in the sources as a function of nozzle elevation (e.g., Figure 47).

c. Total Sound Field Contour Method

This method would consist, essentially, of a single set of contours of the near field levels for a VTOL jet which included all of the above sources. This is one method commonly used for defining near field levels for conventional jets.^{15, 36, 46} Again, for lack of definitive data on the individual sources or an adequate data base of full scale measurements, this approach is not considered feasible at this time for use as a prediction model.

Variations on this approach could consist of a definition of band levels in the near field, relative to the overall power spectrum level, supplemented by definition of the noise source location. This is similar to the type of approach commonly used for defining sound levels of rockets during the initial launch phase.⁶⁴ Although a deflected jet is also involved in this case, the jet or rocket exhaust is normally deflected approximately 90 degrees and the direct radiation from the jet, before or after its deflection, is the dominant noise source. This method has been thoroughly evaluated by and supported with extensive rocket noise data. No such extensive data base exists for VTOL jets.

d. The Δ Method

This method would consist of establishing a definition of the maximum increase in sound level, over free jet values, experienced in the near field during lift-off. The approach utilizes existing data on near field levels for conventional (horizontal) jets. The Δ correction factors would inherently include all of the complex interactions and transitions from one dominant source to another to establish maximum design levels for the

near field. It would thus tend to provide conservative results for design purposes. This is the method chosen for this report. The Δ correction factors will be specified as a function of nozzle elevation for various nondimensional frequencies.

e. Development of the Δ Method

A comprehensive near field noise survey of a J57-P21 turbojet engine operating at 100 percent military power ($U_e = 1930$ ft/sec) was utilized for baseline contours of undeflected jet noise levels.³⁶ The measurements were reported in 1/3 octave band levels and were made over a concrete surface within 30 to 40 nozzle diameters of the engine. The measured contours for individual bands (at octave intervals) were corrected for ground reflection effects. The latter were obtained from the table of correction factors for ground reflection for a monopole source given in Appendix D. A monopole source is a suitable model for application to ground reflection corrections in the horizontal plane of a jet. The contours were corrected to a reference condition of a rigid plane with incoherent reflections, i.e., a 3 dB increase over free field levels. Figure 51 shows a typical example of the original and corrected contours for one octave band. The corrected contours include minor extrapolations to extend the span of the contours to the jet axis in accordance with the general trend of noise contours for an axisymmetric source. The final octave band level contours are presented in Section 6 for five frequencies covering a range of Strouhal numbers from 0.12 to 2, plus the overall level.

To correct the contour values in the region forward of the nozzle exit for lower engine velocities, a velocity exponent is used in the expression

$$OBL_2 = OBL_1 + 10n \log \left(\frac{U_{e2}}{U_{e1}} \right) \quad (44)$$

where

OBL_1, OBL_2 = the octave band levels at exit velocities U_{e1} and U_{e2} respectively, and

$n = 5$ when octave band levels are plotted on the nondimensional frequency scale fD/U_e .

This method of scaling the levels, in the forward quadrant of a jet, is based on a detailed evaluation of velocity exponents for scaling near field sound levels by Hermes

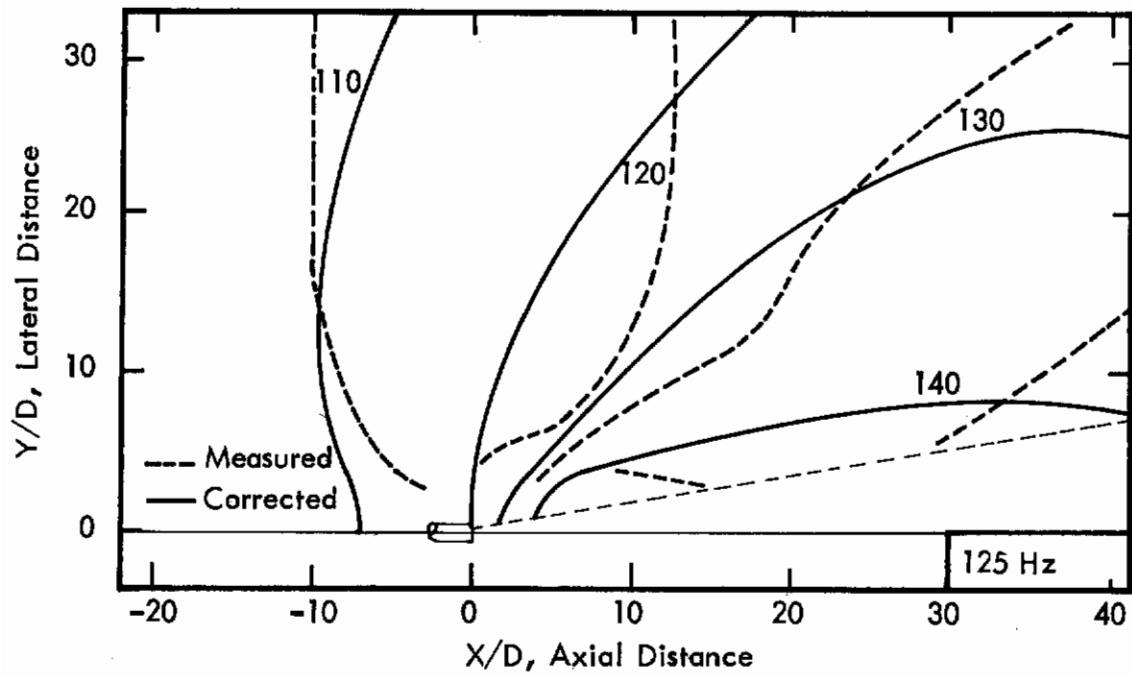


Figure 51. Illustration of Effect of Correcting Measured Octave Band Level Contours for Ground Reflection ("Measured" Contour from Reference 36)

and Smith.³⁶ A value of $n = 5$ was used for scaling overall levels (or octave band sound pressure levels plotted versus Strouhal number, fD/U).³⁶ An alternate procedure can be used for scaling near field levels for turbofan-powered VTOL aircraft operating at different engine power settings. A characteristic feature of this type of engine is that as engine power is reduced, the acoustic power of the relatively cold fan exhaust decreases more slowly than that of the primary (hot) jet. Since the total noise power is a function of the exit velocities of both the primary and bypass exhaust, it is awkward to use "jet velocity" as the scaling parameter. Thus, it was found that scaling near field noise levels by engine thrust is more practical for turbofan engines.

The shift in the frequency spectrum of the baseline undeflected jet noise with velocity or thrust is handled by a graphical procedure outlined in Section VI. This method for scaling the baseline levels neglects any change in the shape of the near field contours forward of the nozzle exit that could occur due to changes in jet exit temperature. However, the far field directivity of Mach 1 jets has been shown to be substantially independent of exit temperature for angles to the jet exhaust greater than 90 degrees.¹⁵

The next and most important step in the prediction method is to define the change (Δ) in near field octave band sound pressure levels for the deflected VTOL jet relative to the levels for the undeflected jet. This Δ factor has been selected on the basis of the model results summarized by Figures 42 and 46 in part 5 of this section. Two adjustments were made for the design curves.

- The model results reported in Appendix C employed a free jet with no significant reflection from any boundary surfaces. Thus, to normalize these model data to the case of a horizontal jet over a ground plane, 3 dB was added to the baseline levels resulting in a 3 dB reduction in Δ .
- The limited data for heated model VTOL jets indicate that the change in near field sound pressure levels relative to the undeflected jet is generally less than for an ambient jet. Unfortunately, no full scale or model data exists to define effects of temperature on excess power of VTOL jets. The only evidence of a possible effect of temperature on power is indirect and based on comparison of measured power levels for a full scale VTOL jet with calculated power levels for the undeflected case.⁴³ This analysis indicated that the excess power of heated VTOL jets is also less than for ambient jets. Thus, the estimated Δ for heated jets was reduced by 0 to 3 dB below the values estimated solely from the ambient jet data in Appendix C.

Figure 52 summarizes the values of Δ from the model tests in Appendix C with the first 3 dB correction included. The design curves in Section VI will be based on the maximum values (Δ_{\max}) of these curves regardless of the nozzle elevation and with the

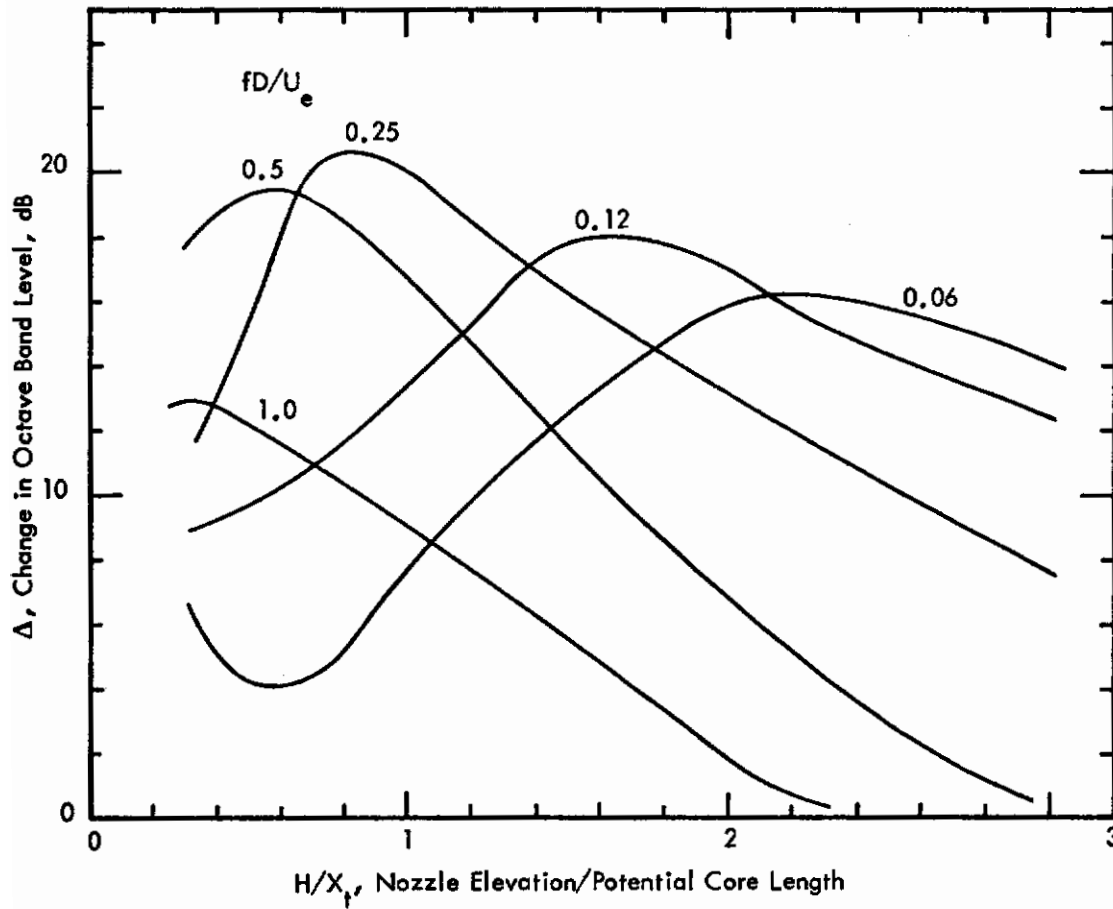


Figure 52. Adjusted Values for Δ from the Ambient Air Model Tests in Appendix C

additional estimated correction for temperature for heated jets. The change in Δ relative to its maximum value will also be given to permit an evaluation of the near field noise levels at a specific nozzle elevation.

The spatial variation in the maximum value of Δ was shown earlier to be very small. Further verification of this seemingly gross approximation is provided by values of Δ listed in Table III. This shows the measured values from the results in Appendix C at 8 test points in the near field for a Mach 1 jet at 6 nozzle diameters elevation. The average variation of individual points about the mean value for a given frequency is about ± 2 dB. The slight tendency toward a spatial pattern for the values of Δ is not considered significant for this first generation prediction model.

TABLE III

Measured Values of the Change in Octave Band Level (Δ) Relative to Levels
for an Undeflected Jet. $H/D = 6$, $M_E = 1.0$
(From Tests Described in Appendix C)

Position		Freq, Hz \rightarrow	Δ , dB				
			1,000	2,000	4,000	8,000	16,000
X/D	Y/D	$S_N \rightarrow$	0.06	0.12	.25	.50	1.0
0	2.5		12	16	24	19.5	12.5
-10	2.5		13	18	25	21.5	15
-4	10		11	18	24.5	21	13
0	10		13.5	23	25.5	23	13
-10	10		10	16.5	24	20.5	10
-10	17.5		8	16	21	19.5	11
0	25		6	15	19	19	15
-20	25		11	19.5	24.5	20.5	11
Average Δ			10.6	17.8	23.4	20.6	12.6

$S_N = fD/U_e$, Normalized Frequency

A final element of the prediction model will provide an approximate correction to the estimated near field levels to account for local shielding on the back side of fuselage or wing structure. The correction factors used are based on measured values of sound wave diffraction on the shadow side of solid obstacles.⁶⁵

f. Comparison of Predictions with Full Scale Data

Only one set of full scale data was available for making valid comparisons of predicted versus measured near field noise levels for VTOL jet aircraft.⁴³ The only other set of data on near field VTOL noise levels available was obtained with the VTOL jets exhausting into a duct for suppression of noise and backflow.⁵

The full scale data were obtained on the fuselage, wing and tail structure of a P1127 experimental VTOL aircraft powered by a turbofan engine with dual exhaust ducts for both the secondary (cold) and primary (hot) exhaust. When operating in a hover-stop position, the four exhaust ducts are oriented toward the ground as indicated in Figure 53. The test point locations examined are also identified in the figure. The prediction model outlined in part 7(e) and presented in detail in Section VI was applied to a prediction of the octave band levels at these test points for the nominal maximum power condition employed for this static tie-down test. The aircraft was positioned with the hot nozzles at an elevation of about 9.7 single nozzle diameters above the ground. The results are shown in Figure 54 by a comparison of predicted and measured octave band levels for this engine condition. Additional details on the engine and jet exhaust parameters are specified by the last entry in Table I, page 15.

In general, considering the simplifications made for the prediction model, the agreement between measured and predicted values is considered very satisfactory.

The variation in the near field noise levels with several engine thrust settings was also available.^{43, 66} Figure 55(a) shows how the overall levels varied with thrust. An average slope for each of the four measurement points evaluated corresponds to total engine thrust raised to the 2.75 power. This corresponds roughly to a U^6 law which is the expected result for the variation in sound levels for low velocity jet flows.

As a final evaluation of the measurements, measured far field sound power level spectra were compared with predicted values for the four undeflected jets using a well-known jet noise prediction method.^{43, 49} The results of this evaluation are shown in Figure 55(b). For these particular test conditions, the measured VTOL noise power and the estimated undeflected jet noise power are similar in the frequency range between 63 and 500 Hz but excess power in the VTOL jets is apparent at lower and higher frequencies. The excess power at high frequencies is believed to be the result of noise generation by the wall jet. It was shown earlier that the peak frequency for this noise was expected to be 2 to 3 times the peak frequency of the jet noise. The

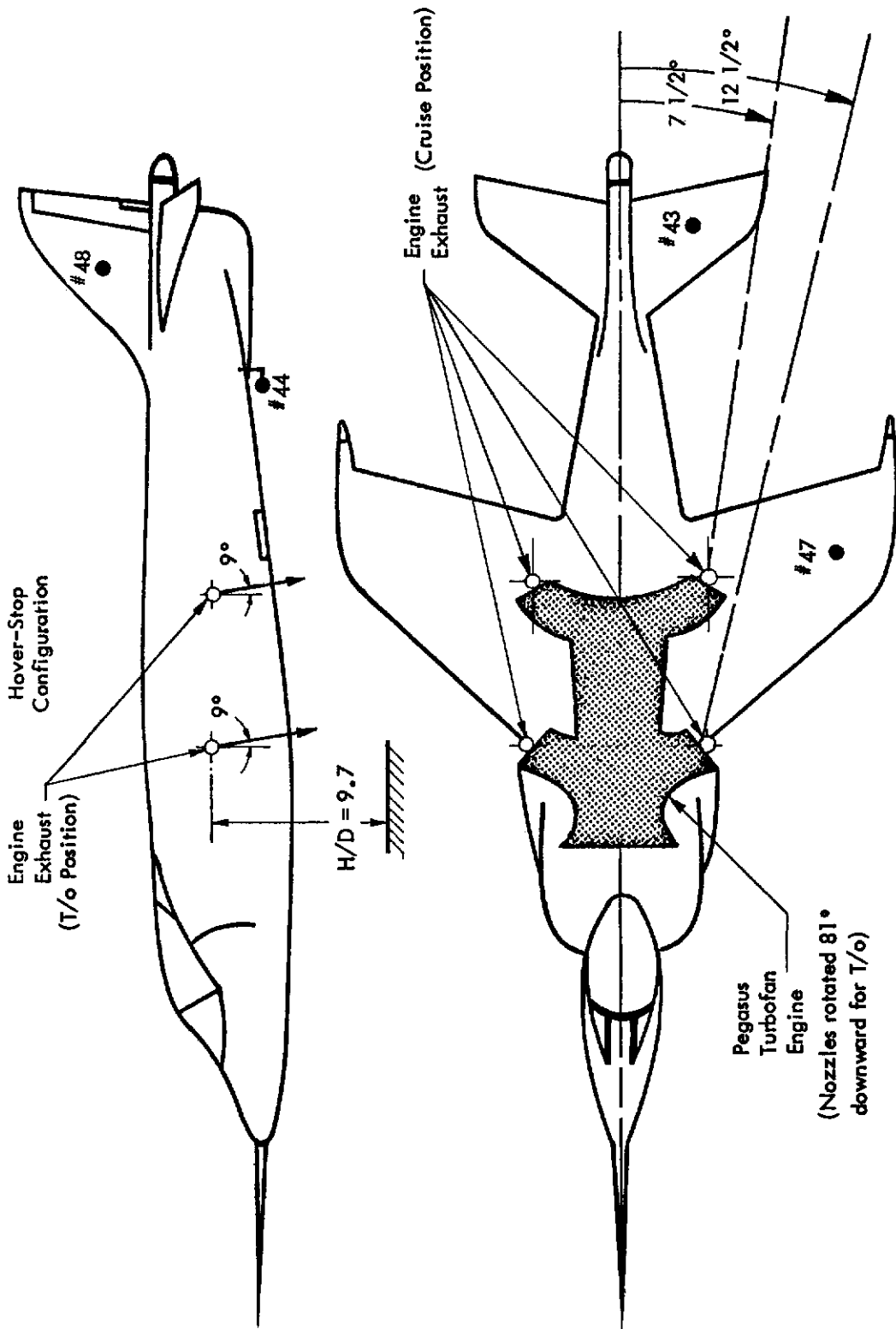


Figure 53. Nozzle Configuration and Test Point Location for the Full Scale Measurements on a P1127 VTOL Aircraft (from Reference 43).

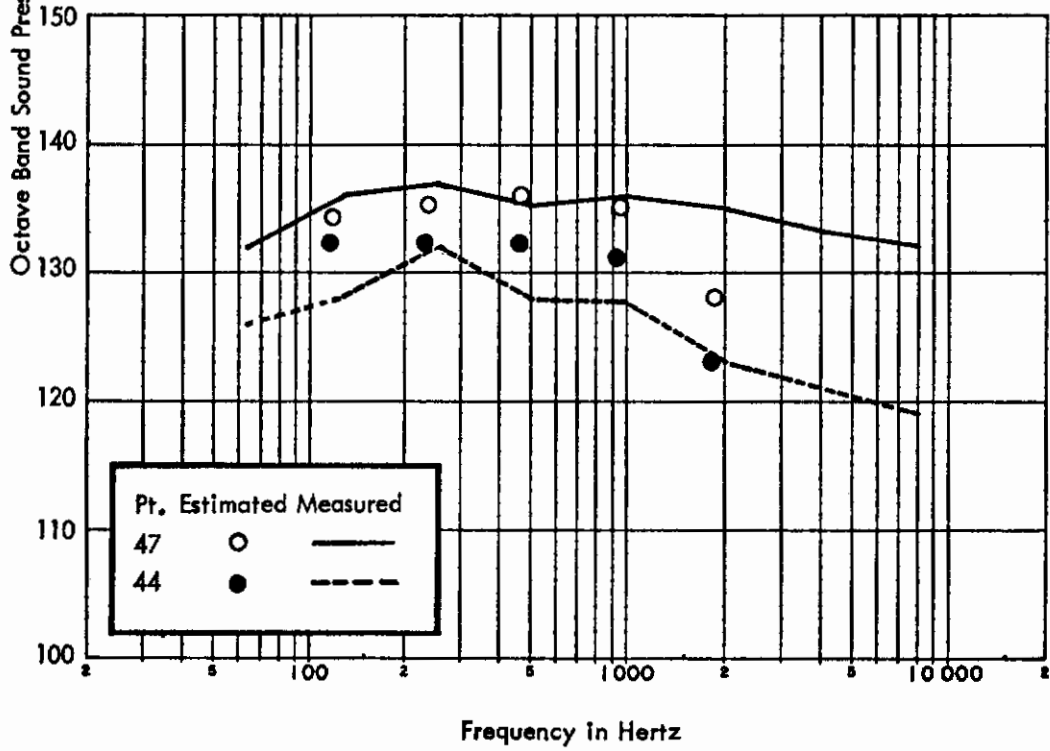
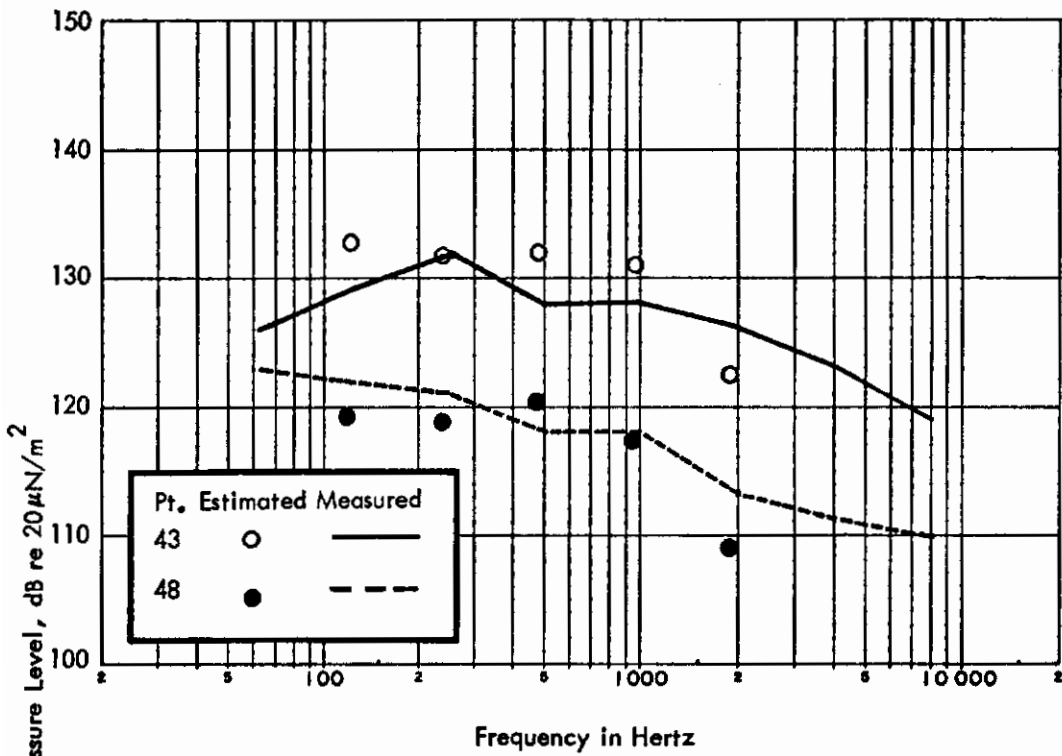


Figure 54. Comparison of Measured and Predicted Octave Band Levels on P1127 VTOL Aircraft at 92.5% Power and 9.7 Nozzle Diameter Elevation (Measured Data from Reference 43)

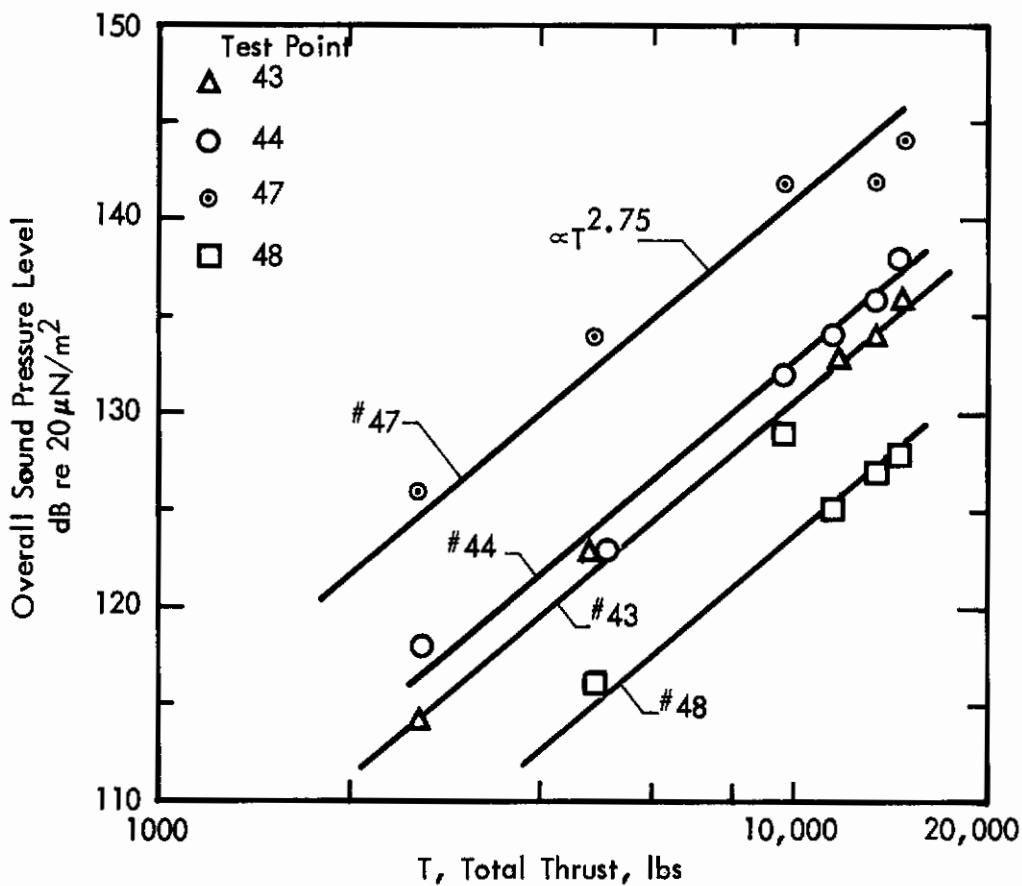


Figure 55(a). Measured Variation in Overall Sound Pressure Level with Total Engine Thrust for Noise Measurements Made on P1127 VTOL Aircraft at 9.7 Nozzle Diameter Elevation (Data from Reference 43, Measurement Locations Shown in Figure 53)

excess power at low frequencies cannot be explained at this time. However, the test facility did have a shallow pit directly under the aircraft but not directly exposed to the jet exhaust stream. The possibility of cavity excitation by the wall jet flow is considered one likely source of this low frequency power.

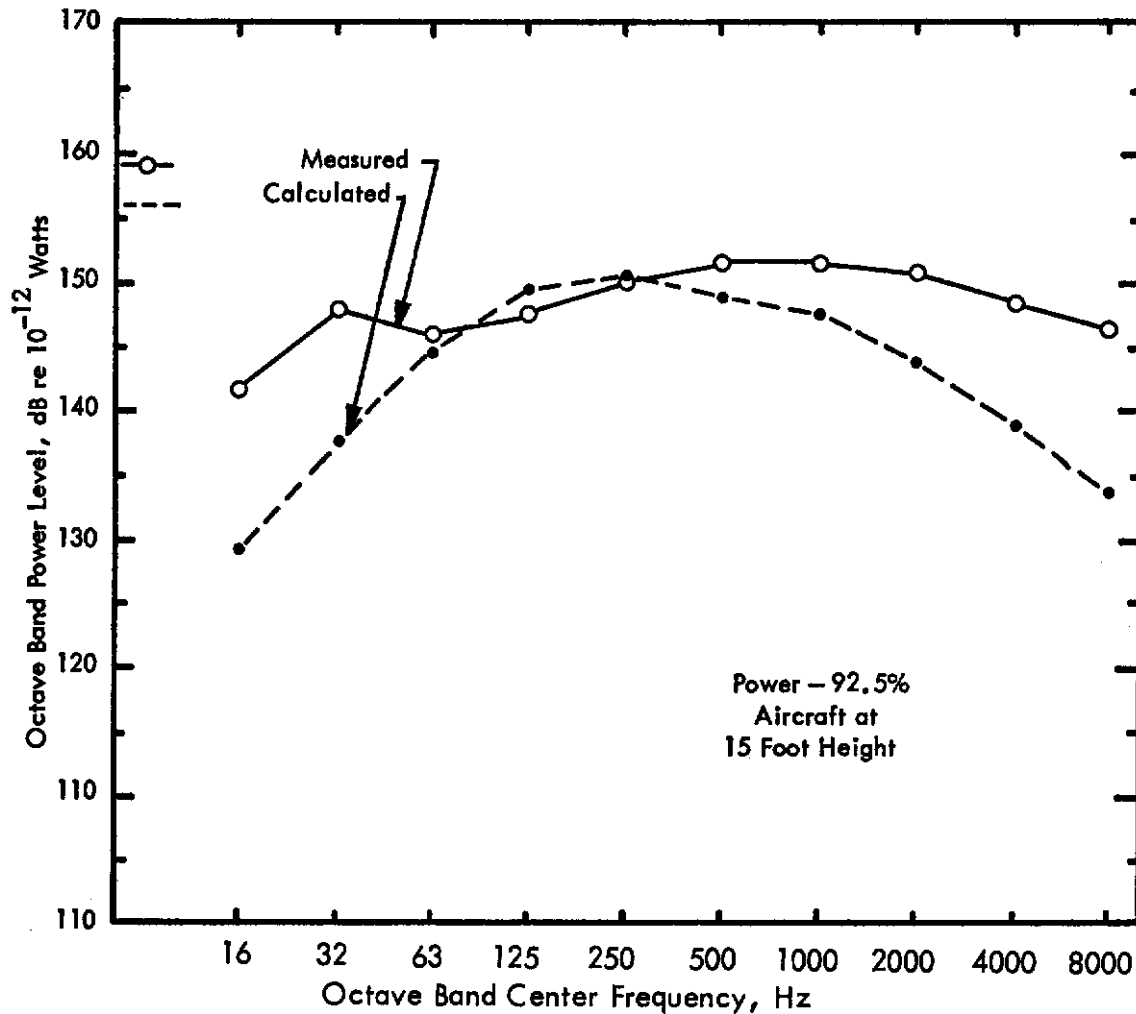


Figure 55(b). Comparison of Measured and Calculated Octave Band Power Levels for P1127 VTOL Aircraft (Measured Data from Reference 43. Predicted Levels Based on Reference 49 for Free Jet Noise Power of Bypass and Primary Exhaust Streams)

SECTION IV

NEAR FIELD NOISE OF PROPELLER SYSTEMS

1. FREE ROTORS AND PROPELLERS

Propeller systems are divided into two groups for this report: free rotors and ducted fans. Noise prediction methods for the first group are considered in the following paragraphs.

a. Review of Propeller Noise Prediction Methods

The predominant sound field components generated by rotating blades result from the load distribution carried by the blades during their rotation. Such loads induce dipole-type acoustic sources whose strength is proportional to the time rate of change of the force imposed on the fluid medium by the passing blade. The steady lift and drag forces on a set of rotating blades are the simplest to estimate, and form the basis of Gutin's theory which was the predecessor to most of the current theories.⁶⁷ The Gutin approach initiated the "effective radius" concept whereby the total thrust and drag of a propeller are considered to initiate separate dipoles, with orthogonal axes, and of strengths determined by the rate of change of pressure on the medium, induced by the passing blade's chordwise distribution of the thrust and drag loads at the "effective radius" section. This Gutin approach contains only the far field terms of the dipole source theory and has been found to provide an accurate estimate of the lower order harmonic levels.

The discrepancy of the theory for higher order harmonic level estimation was found to be of considerable interest in the case of helicopter rotor noise and this problem was examined in detail by Lawson and Ollerhead, following Lawson's rigorous study of the effects of source motion on radiated sound fields.^{68,69} The latter methods allowed the inclusion of fluctuating blade loads, in addition to the steady loads, as sound source terms, and significantly improved the estimates of the higher order harmonics of helicopter rotor noise. In propeller theory, however, very little attention has been given to the higher harmonic content due to its relative insignificance in both subjective and structural applications, for blade tip Mach numbers above about 0.5. Consequently, the Gutin method has been retained for propeller harmonic noise prediction, with the influence of forward speed included by Garrick and Watkins.⁷⁰ All higher frequency noise has been categorized as "vortex noise" and treated in an empirical manner based on Yudin's studies.^{71,72,73} A recent detailed examination of this higher frequency content indicated the predominance of harmonics in the typical vortex noise bands for low speed propellers ($M_t < 0.5$).⁷⁴ This latter study provides methods for predicting both the harmonic and broadband far field noise content in the vortex noise frequency domain, although the exact origins of the harmonic source levels are as yet unexplained.

The near field noise of propellers, which is of interest for structural design only, has not received such detailed attention in experimental or theoretical study. Of the available literature on the subject, the work of Hubbard and Regier is the only source of direct comparison between experimental data and classical theory, which they derived as a near field form of Gutin theory.⁷³ While the comparison showed good agreement for the data available, later prediction methods by Franken, et al, and Marte and Kurtz have been derived by semi-empirical approaches based on experimental data, due to the complexity of the computational work involved in the classical approach.^{32,75}

Of these studies, only the classical derivation by Lawson is perfectly general.⁶⁹ That is, it includes both near and far field terms and accounts for the motion of steady and fluctuation force components. Lawson's result for the density perturbation in the far field for a dipole in arbitrary motion is:

$$\rho - \rho_0 = \left[\frac{(x_i - y_i)}{4\pi(1 - M_s)^2 c_0^3 s^2} \left\{ \frac{\partial F_i}{\partial t} + \frac{F_i}{(1 - M_s)} \frac{\partial M_s}{\partial t} \right\} \right] \quad (45)$$

and additionally,

$$\rho - \rho_0 = \left[\frac{1}{4\pi(1 - M_s)^2 c_0^2 s^2} \left\{ \frac{F_i (x_i - y_i)}{s} \frac{(1 - M_s^2)}{(1 - M_s)} - F_i M_i \right\} \right] \quad (46)$$

for the near field. Note that the pressure fluctuation $p - p_0 = c_0^2 (\rho - \rho_0)$, to the first order. In these expressions, the square brackets indicate evaluation of the enclosed terms at a proper retarded time, M_i is the component of the source Mach number (M) in the i direction, and M_s is the component in the direction of the observation point at coordinates y_i some distance s from the source. F_i is the component of the point force at coordinates x_i in the i direction. Application to rotating blade systems requires consideration of the rotor geometry, which can be simplified to a system of rotating point sources (Figure 56), and a knowledge of the aerodynamic loads (F_i) which can be expressed as steady and fluctuating thrust (T) and drag (D) components. While the steady loads are usually accurately defined for use in the acoustic problem, the unsteady loads are extremely difficult to predict in terms of general design features. Consequently, for a general prediction method, the best approach is to calculate the sound pressure of the first harmonic which is predominantly dependent on the steady loads, and relate all higher-harmonic sound levels to that of the fundamental by means of some empirical method. Considering steady loads only, Equation (45) reduces to the Gutin equation for the acoustic pressure in the far field of a static propeller, i.e.,

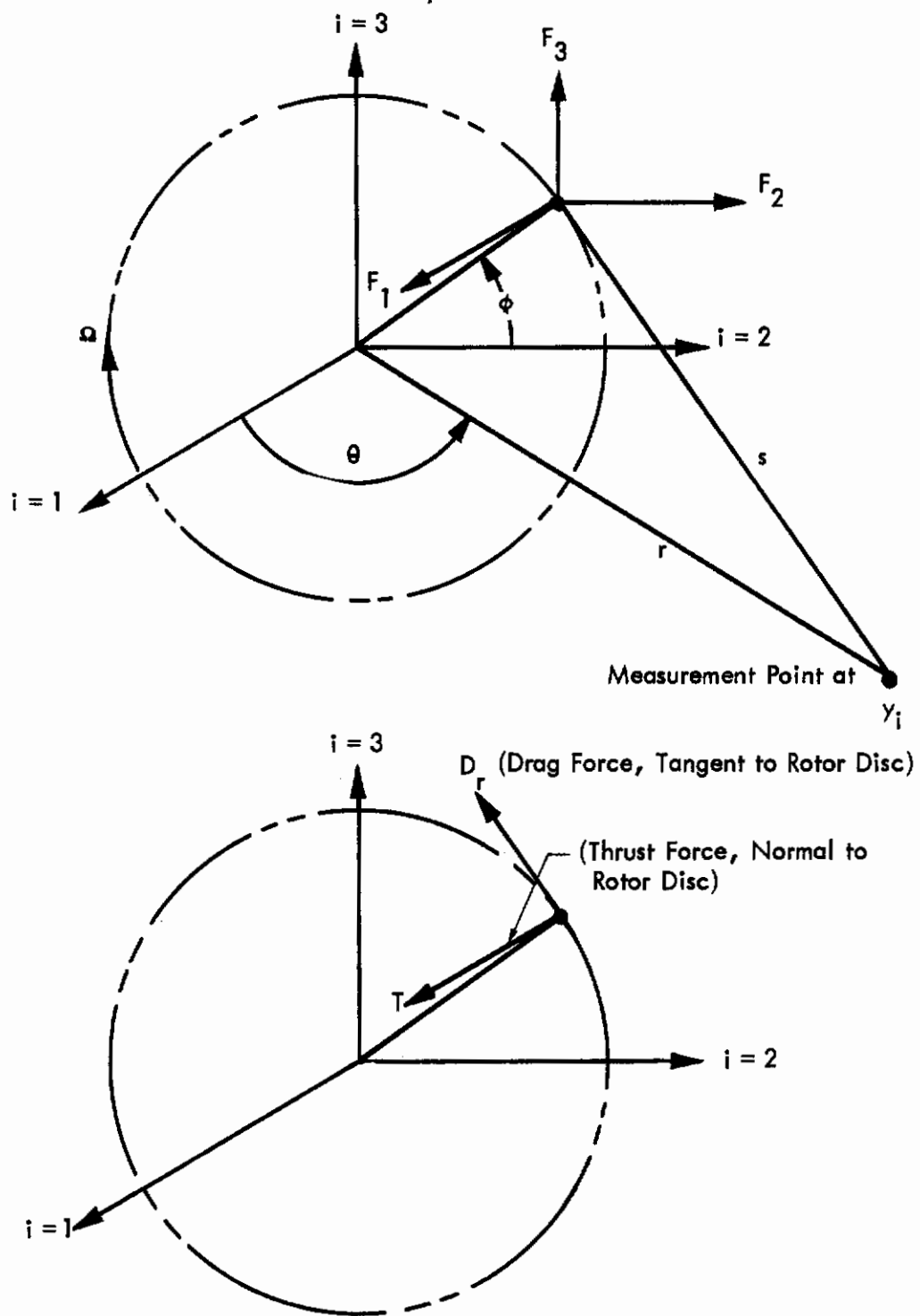


Figure 56. Spatial Coordinate System for Rotor Noise Calculations

$$p_m = \frac{mB \Omega}{2\pi c_o r} \left\{ T \cos \theta - D_r \right\} J_{mB} (mB M \sin \theta) \quad (47)$$

For the near field, Equation (46) can be rewritten as:

$$p = \left[\frac{1}{4\pi(1-M_s)^2 s^2} \left\{ \frac{r(1-M^2)}{s(1-M_r)} (T \cos \theta + D_r \sin \theta \sin \Omega t) \cdot M D_r \right\} \right] \quad (48)$$

for the propeller case. This requires evaluation at retarded time increments, as in Equation (46), which can be accomplished by digital numerical computation. Hubbard and Regier's solution to include the near field pressure assumed a single point loading on each blade and is:

$$p = \frac{e^{-ikc_o t}}{4\pi^2} \int_0^{2\pi} \left(T \left(\frac{x}{s} \right) + D_r \left(\frac{y}{s} \right) \sin \phi \right) \cdot \left(\frac{ik}{s} + \frac{1}{s^2} \right) e^{-i(mB \phi + ks)} d\phi \quad (49)$$

which requires integration over the period of the blade rotation angle $0 < \phi < 2\pi$. Equations (48) and (49) give instantaneous pressure amplitudes and must therefore be converted to harmonic rms values for sound pressure level estimates.

While Equations (45) through (49) do not lend themselves to simple computations, they provide some clues to the form of an empirical approach to a simplified prediction method. The first obvious simplification suggested by the theory is for the estimation of sound levels in the plane of the rotor disc. For the static case (at lift-off, where the required loads are maximum), theory suggests that the in-plane sound pressures are dependent on the drag component only, and hence can be based on the shaft horsepower (P_H) and blade tip Mach number (M_t) in the form

$$p \sim P_H / (M_t A_d)$$

where A_d is the disc area. In the far field, an additional Mach number dependency is expected because of the frequency dependency of the radiation term. In the near field, however, the pressure is essentially hydrodynamic and such velocity dependency is not expected, except at high subsonic tip Mach numbers, where additional effects influence the total pressure field. Similarly, the inverse influence of blade numbers, which is complex in the far field, as is indicated by the presence of the Bessel function in

Equation (47), may be regarded as being relatively simple in the near field for first harmonic level estimation. As illustrated in Figure 57, in the polar region of maximum pressure (within ± 15 degrees of the disc plane), the near field pressures can be expected to be more closely dependent on loading for a single blade than on the simultaneous interaction of the instantaneous components from all of the blades. Thus, the drag per blade should be used. Therefore, the resulting expression for the in-plane pressure field in close proximity to the propeller tip radius can be expected to be of the form:

$$p \sim \frac{P_H}{M_t A_d B} (r - r_o)^{-2} \quad (50)$$

where r is the radius to the observation point, r_o is the (effective) source radius and B is the number of blades.

The comparable empirical expression for the near field in-plane overall sound level, as given by Franken et al is:³²

$$p \sim \frac{P_H M_t^{1.83}}{A_d B} (r - r_o)^{-(1.67 - 1.22 M_t)} \quad (51)$$

and that of Marte and Kurtz, derived from Reference 32, is⁷⁵

$$p \sim \frac{P_H^\alpha M_t^{1.83}}{A_d B} (r - r_o)^{-(1.67 - 1.22 M_t)} \quad (52)$$

where

$$\alpha = 0.75, \text{ for } P_H > 400 \text{ horsepower}$$

$$= 0.65, \text{ for } P_H \leq 400 \text{ horsepower}$$

Comparison of these last two expressions with Equation (50) shows a greater tip Mach number dependency than expected, and a distinct deviation from the expected decay exponent with distance. A further discussion of these equations is made in the following where the prediction methods are reexamined with respect to experimental data.

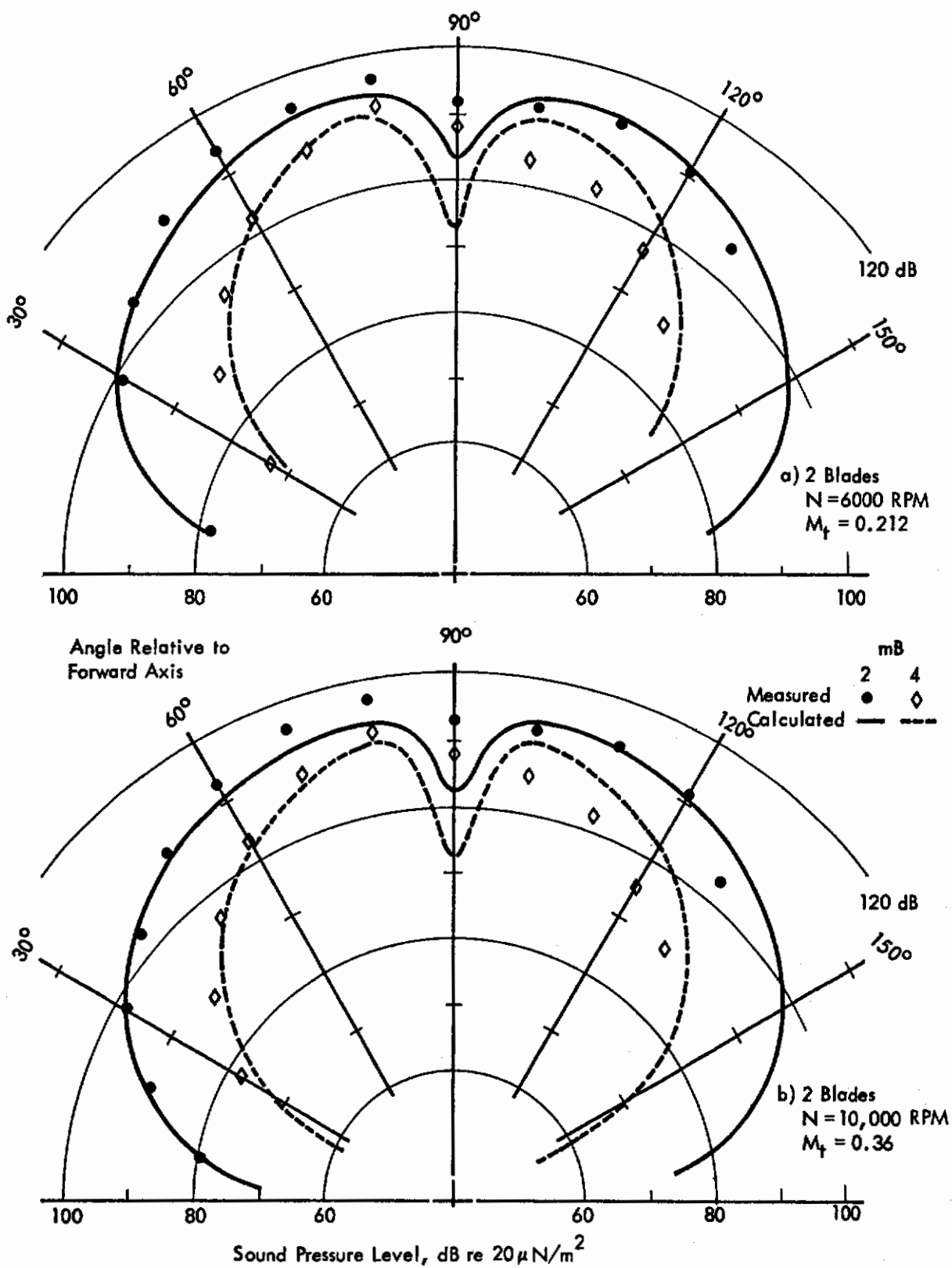


Figure 57. Comparison of Theory and Experiment for First Two Harmonics of 2 and 3 Bladed Model Propellers ($R/D = 0.55$, $D = 0.75$ feet, Data from Appendix B)

Contrails

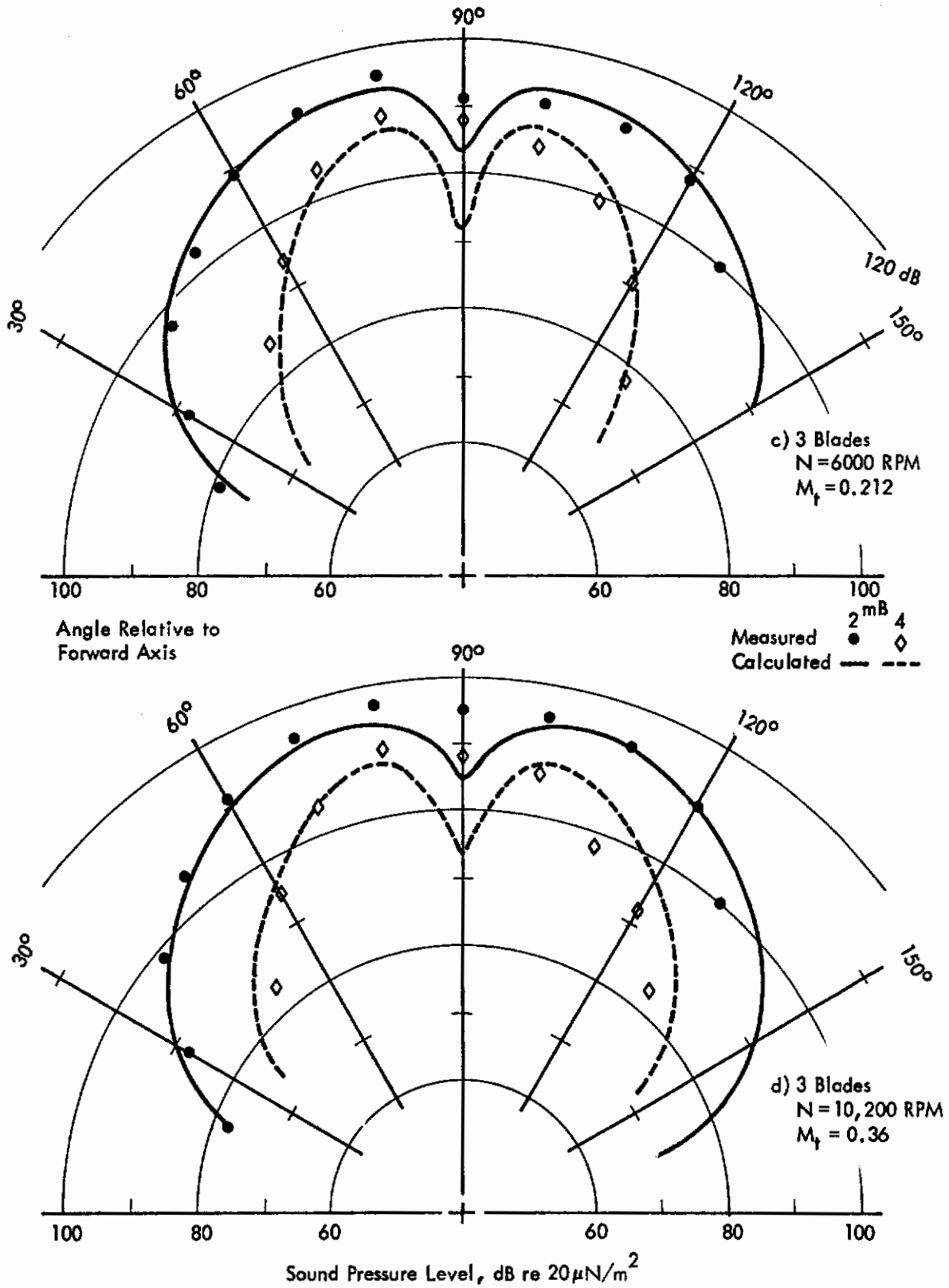


Figure 57. (Concluded)

b. Comparison with Experimental Data

A review of available literature on propeller noise yielded very little comprehensive experimental near field data. In particular, where noise data are available, the necessary information on propeller operating loads (thrust, horsepower or torque, etc.) is not always quoted. Lack of detail in the spatial definition of the near sound field is also a limiting feature of available experimental results and imposes considerable restraints on interpretive usage for sound level prediction purposes. These problems have been approached in the present study by the use of as much data on full-scale propellers as is available and by supplementing these data with detailed measurements of the near sound field of two small model propellers. A description of the latter experimental program is given in Appendix B.

The data on full-scale propeller noise to be used in the present study are contained in References 32 and 76 through 79, and additional data supplied by the Air Force Flight Dynamics Laboratory, Wright-Patterson Air Force Base. The latter data were obtained on a 100-inch diameter, 6-blade propeller at various blade pitch settings and rotational speeds, and were supplied in the form of one-third octave spectra from which only the first blade passage harmonic was distinguishable. Thrust data were also supplied, and torque levels have been estimated for each test case.

The model propeller data were obtained for two 9-inch diameter configurations, with 2 blades and 3 blades respectively. These data were obtained to provide detailed information on the spatial characteristics of the near sound field, and are complemented by thrust and torque estimates based on total-head wake surveys and torque balance measurements.

Equation (48) was programed for digital computation of the near field harmonic levels and the results are compared with the model propeller experimental data in Figure 57. The theoretical results shown were computed by applying the total blade loading at the 0.8 radius station on the blade. This simplification, first introduced by Gutin for far field cases, was found to provide closer agreement with experimental data (over the total Mach number range) than that given by a distribution of the blade loading over five radial stations. As illustrated by the comparisons, the theory provides a good estimate of the first two harmonic levels, except in a spatial region close to the disc plane. This discrepancy was found by Hubbard and Regier in their correlations and is known to occur also in far field estimations derived from Gutin theory. A further peculiarity noted in the model propeller data which can also be found in some full scale propeller cases is the occurrence of the maximum harmonic level in front of the disc plane. Theory suggests that the near field directivity pattern should be symmetrical about the disc-plane, for low tip speeds, and should develop into the well-known skew-cardioid pattern with a maximum at about 15 degrees behind the disc-plane for high tip Mach numbers. The reasons for these variances between theory and experiment are not

sufficiently understood to include their consideration in the theoretical model. Whereas the sound field asymmetry problem does not induce large errors relative to the theoretical field, the in-plane levels are underestimated by a significant margin (up to 8 dB) and require closer examination for parametric dependency.

A summary of the experimental data cases used in the following correlation analysis is given in Table IV. These cases represent experimental data in which sound measurements have been obtained in the near field, with corresponding performance data. Additional data obtained by Wright-Patterson Air Force Base on the 6-blade propeller at higher blade pitch settings is considered to be inapplicable due to probable stall conditions.

Examination of the in-plane first harmonic noise data of the various propellers first requires a collapse of the data to a common field point. Unfortunately, in all of the full scale propeller test results, only one field position has been used which can be regarded as truly near field (i.e., within one diameter of the hub center). Other data points generally lie in a region where the sound field is in transition between the near field and the far field. Referring to the small, model propeller data, obtained at field radii of 0.555, 0.67 and 0.83 propeller disc diameters from the hub center, the effective source radius (r_0) can be evaluated as that which exhibits in inverse square law decay of the mean square harmonic pressure with distance when this distance from the source is expressed as $(r - r_0)$. Figure 58 shows that the effective source radius is approximately 0.35 of the tip radius, which agrees with the results of Hubbard and Regier in their correlation. Using the value of $r_0/D = 0.35$, and correcting the measured sound levels to a common field point at $r/d = 0.6$, the first harmonic levels in the disc plane can be examined for their dependency on the thrust and drag blade loads by the following equations:

$$L_T = \text{SPL} - 20 \log T + 40 \log D + 20 \log B \quad (53a)$$

$$L_D = \text{SPL} - 20 \log P_H + 40 \log D + 20 \log B + 20 \log M_t \quad (53b)$$

(In these equations, D is the propeller diameter, in feet.) The values of L_T and L_D (in dB) are plotted relative to the blade tip Mach number (M_t) in Figure 59 for all available in-plane, near field experimental data. Although the quantity of data available for conversion to L_T is less than that for the L_D conversion, due to lack of operating thrust quantities, the trend indicated by Figure 59 shows that the in-plane level is reasonably correlated with blade thrust as evidenced by the collapse of data to within a 4 dB range shown in Figure 59(a). Conversely, the wide scatter in Figure 59(b) indicates little correlation with drag. The data in Figure 59(a) encompass propeller configurations with 2 to 6 blades, and with diameters from 0.75 to 11.16 feet. They enable representation of the first harmonic level in the disc-plane by the following equation:

TABLE IV

SUMMARY OF PROPELLER NOISE NEAR FIELD EXPERIMENTAL DATA CASES					
Source	Propeller Geometry		Operating Conditions		
	Dia. (ft)	Blades	M_t	Thrust (lb)	P_H
WPAFB (Ref. 66)	8.33	6	.195	213	44.4
			.220	297	73
			.270	404	116
			.315	527	172
			.350	668	248
			.385	832	342
			.405	934	408
NACA TN 4068 (Ref. 78)	11.17	2	.59	1490	570
			.64	1850	710
			.66	2500	960
			.66	2800	1030
			.72	3100	1200
NACA Rep. 996 (Ref. 73)	4.0	2	.75	*	37
			.75	*	51.5
			.75	*	103
			.9	*	75
			.9	*	88.6
			.9	*	127
NACA TN 3202 (Ref. 76)	3.92	2	.7	*	36
			.9	*	96
Boeing (1954) (Ref. 79)	15.0	4	.35	*	94
			.65	*	1103
			.73	*	2100
			.75	*	4553
			.765	*	6879
			.775	*	8915
			.785	*	8850
			.8	*	9127
Wyle (App B)	0.75	2	.212	1.03	.078
			.286	1.82	.150
			.36	2.42	.34
			.423	4.1	*
			.53	6.45	*
Wyle (App B)	0.75	3	.177	.98	.058
			.212	1.37	.096
			.286	2.82	.272
			.36	4.28	.520
			.47	7.6	*

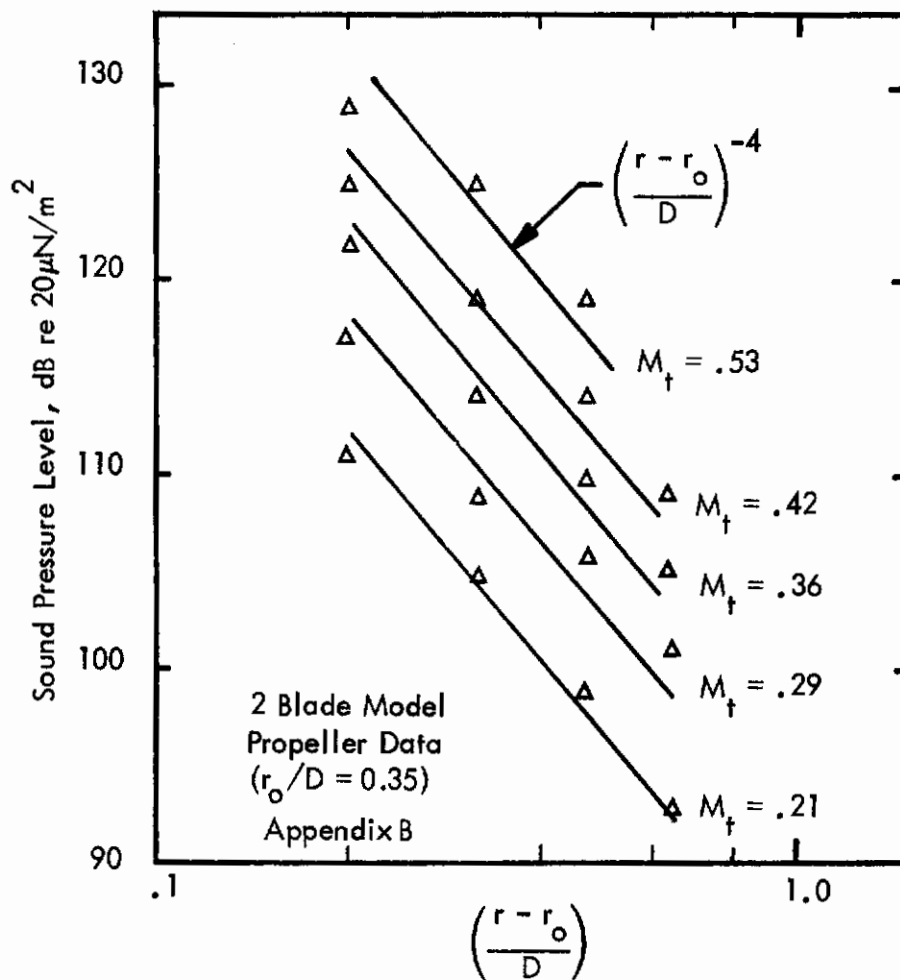


Figure 58. Effect of Distance From Effective Source on Propeller Noise First Harmonic Levels

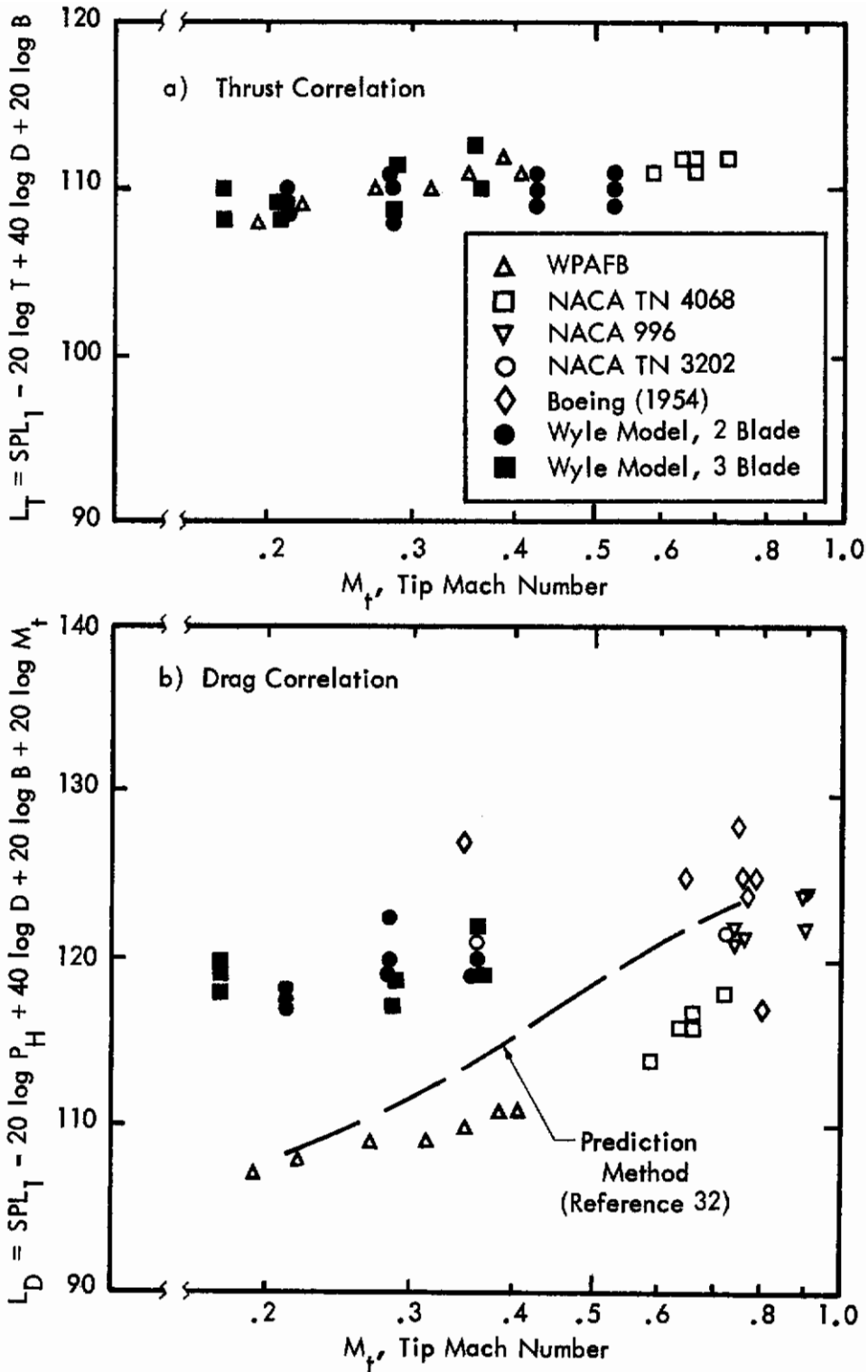


Figure 59. Dependence of the In-Plane Near Field Corrected First Harmonic Levels L_T and L_D , on Tip Mach Numbers

$$\text{SPL}_1 \text{ (at } r/D) = 110 + 20 \log T - 40 \log D - 20 \log B - 40 \log \left(\frac{r/D - 0.35}{0.25} \right) \quad (54)$$

where

T = the total thrust in lbs

D = the propeller diameter in feet

and

r = the distance from the hub center to the observation point, in feet.

This result was derived from data measured at radial positions of $r/D \leq 0.8$. Due to the complexity of the sound field in the transition range of $1.0 < r/D < 3$, where the radiation (far field) pressure amplitudes tend to approach and exceed the hydrodynamic (near field) pressures, an accurate prediction method for the sound levels in this range is not attempted here. It is considered that the best approach to this problem is to calculate the far field pressures for a range of r/D (exceeding 3.0) by means of Equation (47), and for the near field range by means of Equation (54) and interpolate for values in the transition region.

The above method provides an estimate of the fundamental blade-passage harmonic level in the disc-plane. The relationship between this level and higher-harmonic levels is examined in Figure 60. The data shown in Figures 60(a) and (b) were obtained from Reference 78 and the model propeller tests (Appendix B), respectively, and indicate that at a fixed r/D position in the near field, the roll-off rate of the harmonics is not significantly affected by the tip Mach number for $0.2 \leq M_t \leq 0.7$. Comparison of Figures 60(b), (c) and (d) indicates the effect of radial distance on the roll-off rate and a final collapse of this effect is presented in Figure 61. At tip speeds greater than $M_t = 0.7$, the roll-off rate decreases as $M_t = 1.0$ is approached, as illustrated in References 73 and 76. Data from these references has been used to provide the high tip speed range of Figure 61.

The directionality of the near sound field of large scale propellers has been examined in References 73, 76, 77 and 78 for regions close to the disc-plane. These studies have indicated that the maximum level of each of the first few harmonics occurs within ± 15 degrees of the disc-plane and is typically about 4 dB greater than the in-plane level. Typical examples of the directionality patterns obtained (at a constant radius) for the small model propellers are presented in Appendix B. These test results indicate that the first harmonic maximum occurs at about 15 degrees forward of the disc-plane and is again about 4 dB greater than the in-plane level. In this spatial region, it can therefore be postulated that the best approach to a prediction method is to assume that the maximum

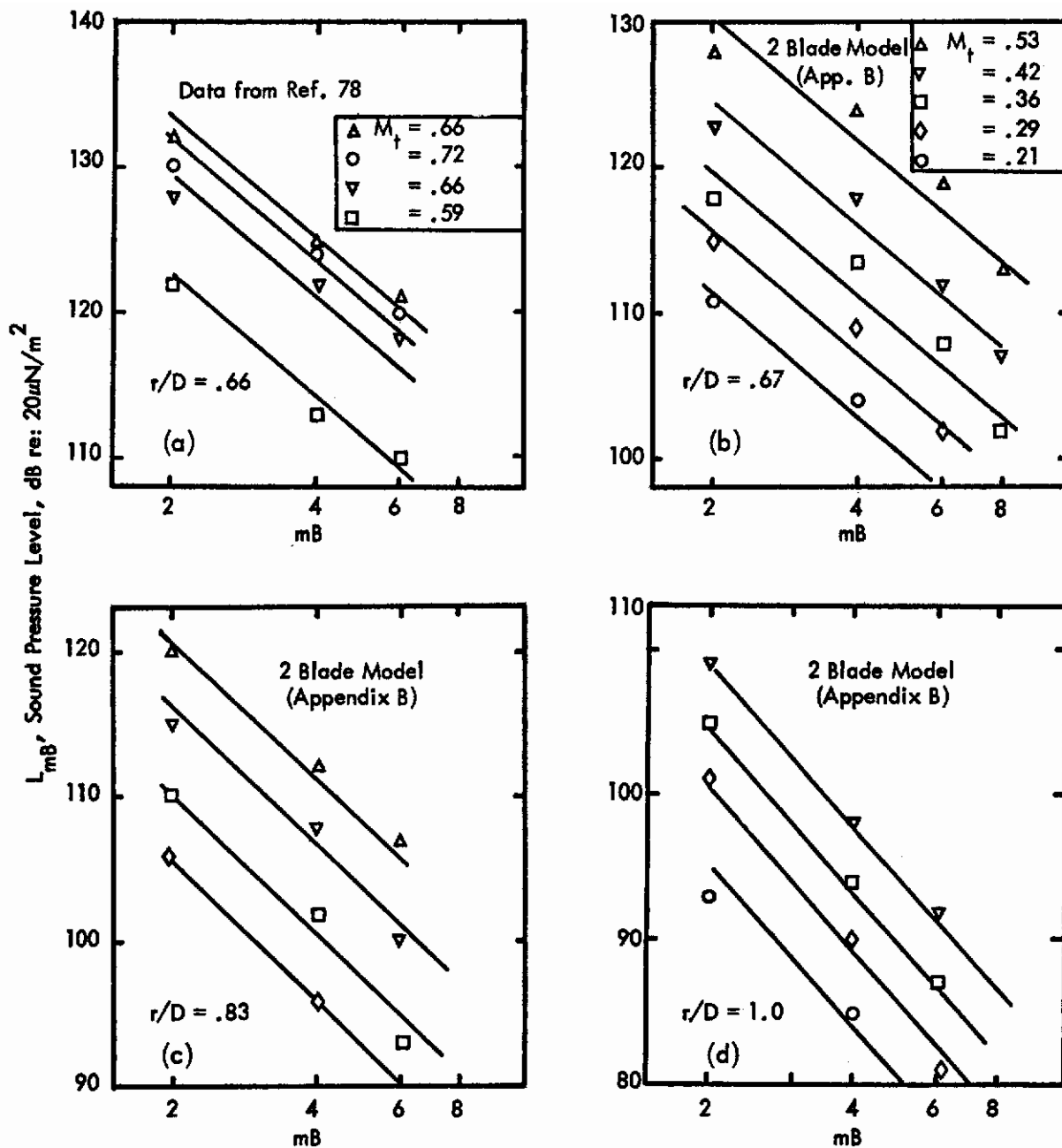


Figure 60. Decay of Propeller Noise Harmonics at Different Tip Speeds and Near Field Radii (In-Plane Levels)

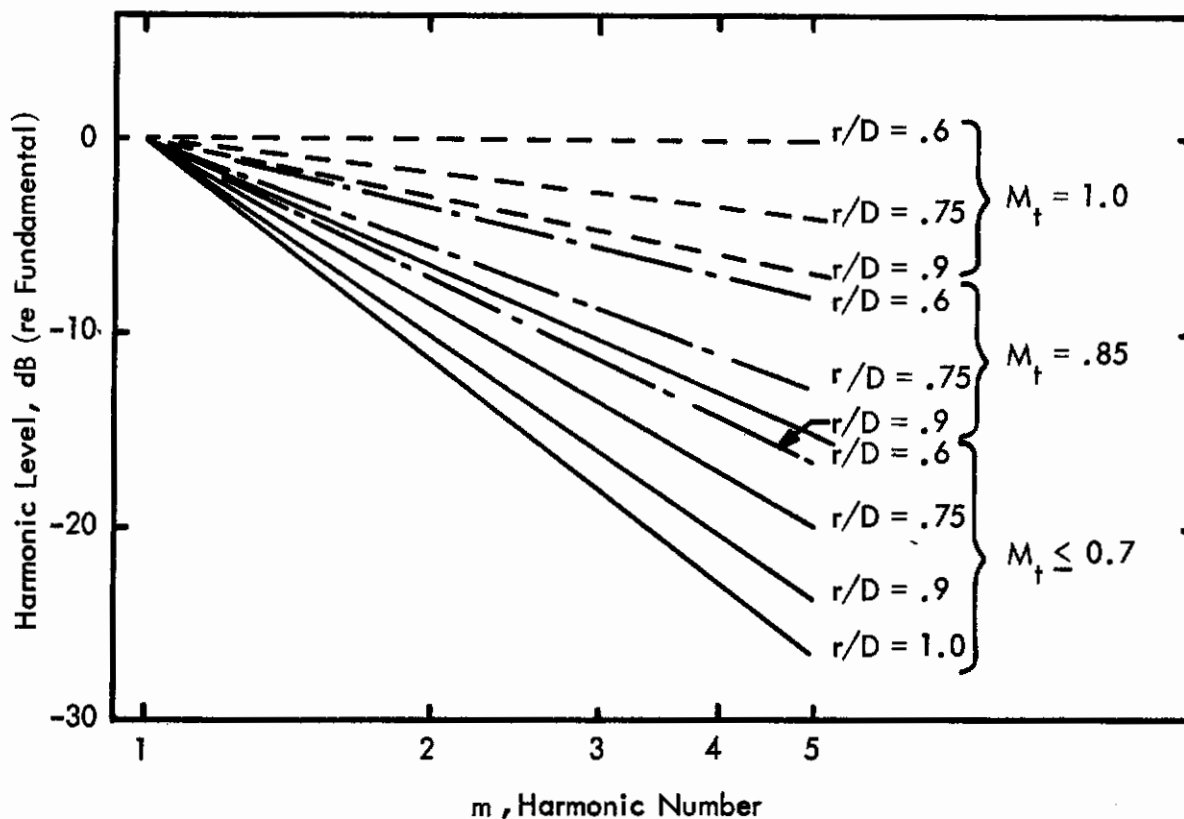


Figure 61. Harmonic Level Decay with Normalized Field Radius as a Function of Harmonic Number

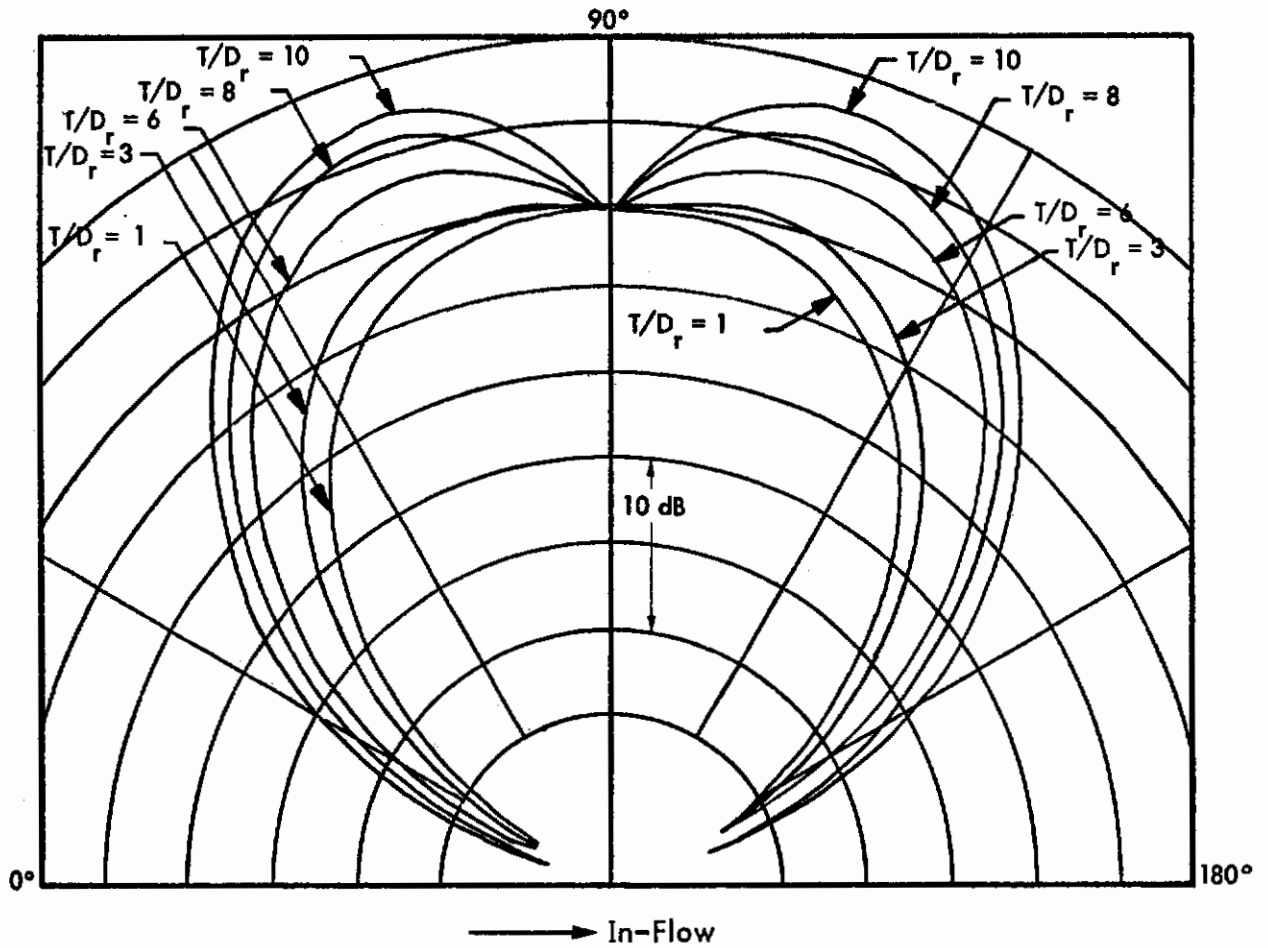
level of the first harmonic will occur at ± 15 degrees from the disc-plane and will be 4 dB greater than the level given by Equation (54). For higher harmonics, the levels estimated for the disc-plane position can be assumed to be constant over a region of ± 10 degrees from the plane.

At other azimuthal positions on a constant radius, forward and aft of the disc, the lower harmonic levels are known to decay rapidly as the axis is approached. The characteristics of the decay are, in theory, dependent on the blade tip speed and the thrust-to-drag ratio as indicated by the separated effects shown in Figures 62(a) and (b), derived from Equation (48). The comparisons between theory and experiment shown in Figure 57 indicate that good agreement exists at angles greater than ± 15 degrees from the disc. It is therefore preferable to retain the theoretical directionality patterns for the region outside ± 15 degrees, and to relate them to the maximum levels (at ± 15 degrees) estimated by the above method. A closer examination of Figures 62 (a) and (b) reveals that there is very little difference between the directionality patterns when either tip Mach number (M_t) or thrust-to-drag ratio (T/D) is varied if the curves are modified to have a maximum at ± 15 degrees, and if the region very close to the axis is considered as being insignificant because of the very low sound levels expected. It is also apparent that the directionality patterns are almost identical in the forward and aft quadrants when related to the same reference level at ± 15 degrees. Thus, the effects of M and T/D can be unified and superimposed to give a single directionality pattern for the angular region $15 \text{ degrees} \leq \psi \leq 80 \text{ degrees}$, where ψ is the angle forward or aft of the disc plane. Although this is true of any individual sound harmonic, the pattern is distinctly dependent on the product of the harmonic order (m) and blade number (B). A series of patterns corresponding to different values of mB have been derived by means of Equation (48) and are presented in Figure 63. These will be used in the noise prediction method described in part 2 of Section VI.

2. DUCTED FANS

a. Review of Theory

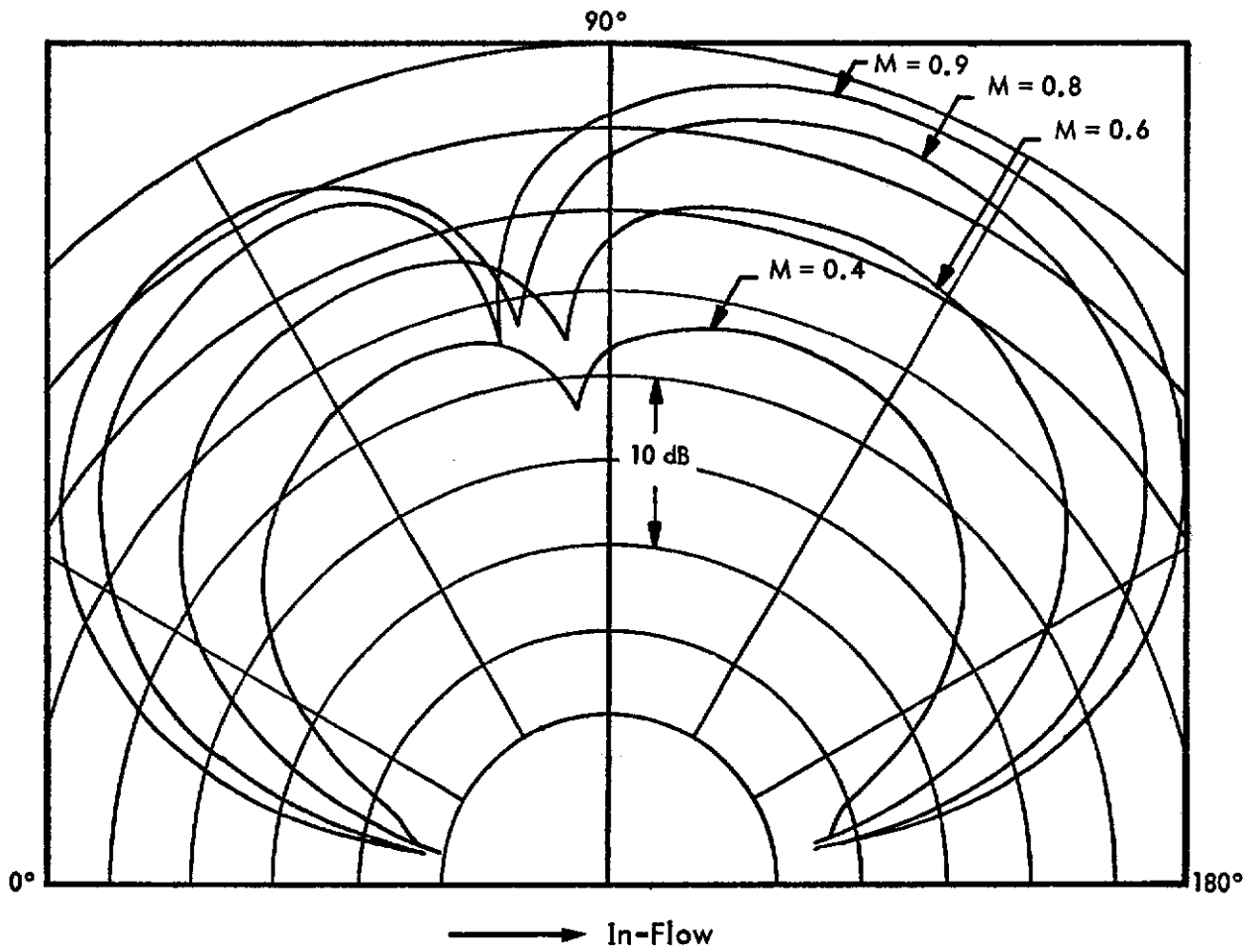
The preceding discussion of free rotors and propellers, in part 1 of this section, considered the case in which the sound generated by the blades is radiated directly to free space. The present part considers the influence on the sound field imposed by the constraints of a shroud or duct, as is the case in VTOL propulsion systems such as the ducted propeller, tip-turbine lift fans and other propeller-fan configurations. These systems can be of tilt-duct or fan-in-wing design. The former can be simply considered as a duct system radiating to free space, whereas the latter is more alike to a fan radiating from a semi-infinite baffle. Research into the more detailed sound field characteristics is presently receiving much attention, but, as in the case of free propellers, is more concerned with far field levels. It is therefore the intent of the following to review the main findings of previous studies of ducted fan noise characteristics and to apply them to the subject of near field noise prediction.



(a) Effect of Thrust/Drag Ratio
(Constant M_t)

Figure 62. Effects of Thrust/Drag Ratio and Blade Velocity
on Propeller Noise Directivity (Theory)

Continued



(b) Effect of Blade Mach Number at 0.8 Radius Station
(Constant T/D_r)

Figure 62. (Concluded)

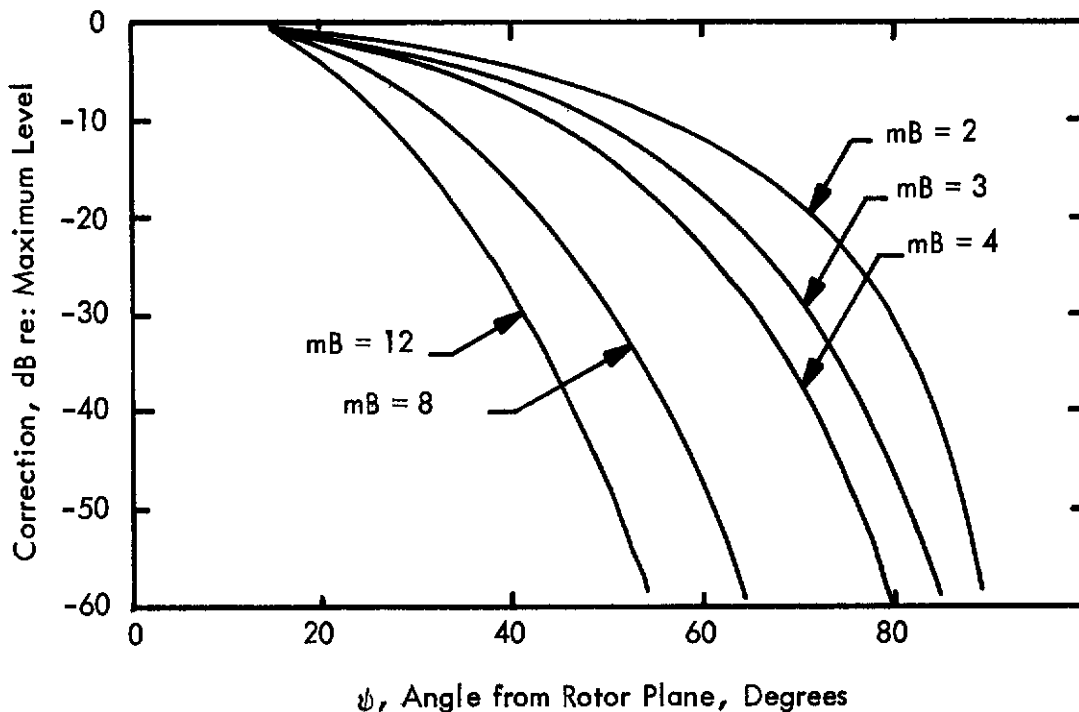


Figure 63. Directionality Corrections for mB Harmonics (r/D constant)

The primary differences between the sound generation/radiation principles of free and ducted rotor systems can be generally stated under two categories of duct effects. First, the aerodynamic field at the rotor is modified, which in turn changes the blade loading. Secondly, the duct acts as an acoustic wave guide which contains preferential frequency characteristics associated with the acoustic modes of the constrained field within the duct.

Concerning the aerodynamic effects, the most practical approach is to assume that the noise source strength is adequately described in terms of the pressure rise across the rotor. The modeling of this with respect to radial distribution is further discussed in the light of the acoustic transmission mode theory. It is worth noting at this stage, that the total thrust developed by a ducted fan, at static or very low forward speed conditions, comprises two components — that arising from the pressure rise through the propeller disc, and that developed by the duct flow momentum. In other words, the thrust developed by the rotating blade can be as low as 50% of the total developed static thrust. As advance-ratio is increased, the duct drag increases, such that at typical cruise velocities the total thrust can be regarded as equal to the propeller generated component. Therefore, for acoustic modeling, it is important that only the thrust forces from the propeller be considered, particularly at lift-off where the total thrust is much greater than the propeller thrust.

In most lift-fan systems considered for VTOL aircraft, the frequencies of the fan blade passage harmonics are within a range of high-order acoustic modes of the duct. The sound sources feed sound energy into these modes, which then transmit the sound along the duct, and the sound is finally radiated to free space from the duct extremities. It is in the transmission process, between the rotor and the duct extremities, that the most significant effects of the duct constraints can occur. These effects have been extensively examined by Tyler and Sofrin who laid the practical foundation of most current research studies into fan and compressor duct transmission theory.⁸⁰ The basic implications of duct transmission theory are now briefly discussed, and the significant features relevant to noise prediction methodology are presented.

Consider the case of a simple infinite length cylindrical duct with zero mean flow. The uncoupled acoustic modes of such a system can be expressed in terms of the sound pressure at cylindrical coordinates (r, θ, x) as:

$$p_{\ell, n} = A_{\ell, n} \cos(\ell \theta + \phi_{\ell, n}) J_{\ell} \left(k_{\ell, n}^{(r)} r \right) e^{-(\omega t - k_{\ell, n}^{(x)} x)}$$

where (ℓ, n) is the (tangential, radial) order of the mode, and $k^{(r)}$ and $k^{(x)}$ are the radial and axial components of the wave number vector. If this mode is driven at radian frequency ω , then the relationship between $k^{(r)}$ and $k^{(x)}$ is, (neglecting $k^{(\theta)}$ as of low order):

$$k^{(x)} = \left[\left(\frac{\omega}{c_0} \right)^2 - \left(k^{(r)} \right)^2 \right]^{1/2} \quad (55)$$

and the transmission exponent, $+ik^{(x)}x$, can be real and negative if $\frac{\omega}{c_0} < k^{(r)}$. Thus the mode pressure amplitude will decay exponentially with axial distance (x) if the mode is driven at a frequency below its "cut-off" value of $k^{(r)} \cdot c_0$. The transmission loss along the duct can be written as:

$$TL = 8.68 \overline{k_x} \text{ (dB per unit length)} \quad (56)$$

when $\overline{k_x} = -ik^{(x)}$ is real. To evaluate this transmission loss in practical systems, it is necessary to identify the mode of interest (ℓ, n) and to find the value of $k^{(r)}$ for that mode in the duct.

Tyler and Sofrin, in their study of axial compressor noise found that the sound energy generated by a rotor at the blade passage frequency and each higher harmonic is transmitted by modes of tangential order $\ell = mB$, where m is the harmonic number and B is

the number of blades.⁸⁰ If a secondary set of vanes or stator blades are sufficiently close to the rotor to create interaction effects, then $\ell = mB \pm SV$, where S is any integer and V is the number of vanes. This only partly solves the identification problem as the radial order, n , is still unspecified. In recent experimental studies of the transmission modes in a ducted propeller, the predominant harmonics were found to decay at rates corresponding to the theoretical values for $(mB, 0)$ modes, as shown in Figure 64.⁸⁴ This suggests a gross simplification of the evaluation procedure, as only the $(mB, 0)$ modes need be considered for the cut-off characteristics in applications to simple ducted rotors.

The value of $k^{(r)}$ for a given mode is determined by the boundary conditions at the duct wall. For a rigid wall, with radius R , the radial particle velocity component must be zero at the wall, and hence:

$$\partial \left(J_{\ell} \left(k_{\ell, r}^{(r)} \cdot R \right) \right) / \partial \left(k_{\ell, r}^{(r)} \cdot R \right) = 0, \text{ at } r = R \quad (57)$$

giving $(k_{\ell, r}^{(r)} \cdot R)$ and therefore $k^{(r)}$, as roots of this equation. A much more complicated equation arises for annular ducts and ducts with complex boundary conditions, as reported in References 80 through 84, for example, although the basic principles of the cut-off effect are as described above.

The design stage of the lift-fan propulsion systems can now be categorized according to whether the rotors operate above or below the cut-off conditions of the duct. It has been demonstrated by Lowson and by Ollerhead and Munch that for simple fan systems above cut-off, the acoustic influence of a small-length duct can be neglected and the noise prediction method is identical to that of a free rotor, with the correct aerodynamic forces used.^{85,86} It can therefore be postulated that the near field of such systems can be treated by the method derived in part 1 of this section, using the rotor-thrust component only. The acoustic theory for systems operating below cut-off is more complex due to the need for transformation of the source field to the duct-end plane. The only simple approach available for present purposes is to retain the free-rotor prediction method, and to apply a correction to the harmonic levels corresponding to the transmission loss calculated through Equation (56). The use of the single-point equivalent source position at $r/D \approx 0.35$ can also be retained because the radial pressure distribution of $(mB, 0)$ duct modes is concentrated toward the outer duct sections. In fan systems which have closely spaced rotor and stator-vane combinations, additional sources of noise (other than the steady blade loads) are created by the fluctuating forces induced on the rotor and stator blades. The studies presented in References 85 and 86 have shown that the radiated harmonic levels of such systems should be estimated by the summation of the rotor and stator noise components. A detailed calculation procedure for far field levels, arising from each of the rotor and stator stages of a fan or compressor, is given in Reference 86. For present purposes, it is considered

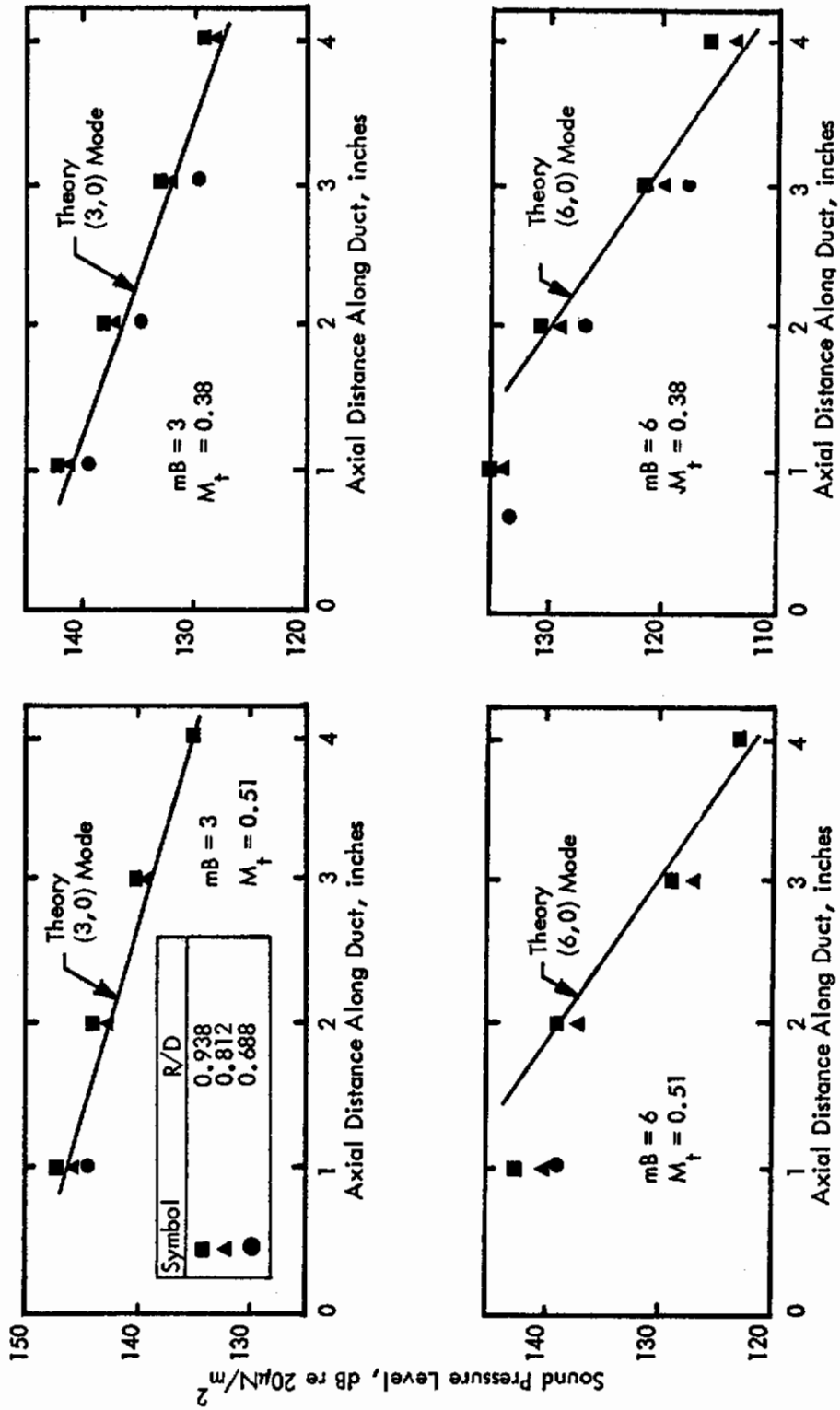


Figure 64. Comparison of Measured and Theoretical Decay of Harmonic Sound Levels in a Propeller Duct (from Reference 84)

adequate to apply an empirical correction to the simple-rotor estimates to account for the interaction effects. Such a correction procedure has been adopted by Smith and House in their prediction method for noise from gas-turbines.⁸⁷ The radiated noise level for a rotor-stator combination was found to increase, as the ratio of the rotor-stator separation distance (d) to the downstream blade chord (c) decreased from a value of $d/c = 2$, at a rate given by $-20 \log (d/c)$. The additive correction to a free-rotor estimate can therefore be expressed as,

$$\Delta \text{dB} = 3 - 20 \log (d/c), \quad \text{for } d/c < 2.0 \quad (58)$$

The first step in rotor noise estimations should therefore be to determine whether the rotor blade passage harmonics are above or below cut-off. For a given cylindrical or annular duct, the roots of the indicial equations – that is, the product of the cut-off wave number and the duct radius – can be derived from first principles or extracted from various reports. These can be compared directly with the product of wave number values (corresponding to each harmonic frequency) and the duct radius. Note that:

$$k = \frac{2\pi f}{c_0} \quad (59)$$

Hence, for each frequency $f_m = \frac{mB N}{60}$ (Hz)

$$k_m = \frac{mB M_t}{R} \quad (60)$$

where R is the duct radius and B is the number of blades.

Thus, the test for each frequency is whether

$$mB M_t < (k_{\ell}^{(r)} \cdot R)$$

and, when true, the transmission loss over a length equal to the duct radius R is:

$$\text{TL (dB per unit multiple of length } R) = 8.68 \sqrt{(k_{\ell}^{(r)} \cdot R)^2 - (mB M_t)^2} \quad (61)$$

TABLE V

Cut-Off Values of $(k_{\ell}^{(r)} \cdot R)$ for Duct Sound Transmission (from Reference 80)							
Hub-to-Tip Radius Ratio σ	$\ell = (mB) \text{ or } mB \pm SV $						
	2	3	4	8	12	16	32
0	3.06	4.2	5.3	9.7	14.0	18.1	34.6
.25	3.01	4.2	5.3	9.7	14.0	18.1	34.6
.50	2.69	3.9	5.2	9.6	14.0	18.1	34.6
.75	2.30	3.5	4.6	9.5	13.9	17.9	34.6

<p>m = blade passage harmonic order B = number of blades V = number of vanes</p>	<p>R = outer (tip) radius S = any integer (0, 1, 2, 3,)</p>
---	---

Table V contains the values of $(k_{\ell}^{(r)} \cdot R)$ for various hub-to-tip ratios. It is seen that cut-off, and hence a decaying transmission field, always occurs for a single rotor at subsonic tip speeds ($M_t < 1$). For cases in which rotor-stator interaction occurs, the value of the cut-off root should be taken for the lowest value of $(mB - SV)$, rather than for mB . Thus, a simple ducted rotor with 12 blades, operating at $M_t = 0.8$, $N = 4000$ rpm, will generate a sound field in the duct which decays at 88 dB per unit length R at the fundamental frequency ($m = 1$, $f = 800$ Hz) and at 150 dB per unit length R at the second harmonic ($m = 2$, $f = 1600$ Hz). For a typical duct length, between rotor disc and duct extremity of 0.2 of the duct radius, the transmission loss in each harmonic would be:

$$m = 1, mB = 12, TL = 17 \text{ dB}$$

$$m = 2, mB = 24, TL = 32 \text{ dB}$$

However, if the system included a set of 20 guide vanes, very close to the rotor disc, the following estimates would be given.

For $m = 1$, $|mB - SV| = 8$ and $k_{\ell}^{(r)} R > mB M_t$, then $TL \approx 2.4 \text{ dB}$

For $m = 2$, $|mB - SV| = 4$ and $k_{\ell}^{(r)} R < mB M_t$, then $TL \approx 0 \text{ dB}$

The latter case would require the incremental correction for rotor-stator interaction, i.e., $3 - 20 \log (d/c)$ dB, and the noise prediction method would incorporate all duct effect corrections to the free rotor sound level estimates. Additionally, the directivity pattern employed for a harmonic which is cut-off should be that corresponding to the lowest value of $|mB - SV|$, rather than mB as shown in Figure 63.

b. Comparison with Experimental Data

Only one source of near field noise data for lift fan systems has been found in available literature.⁴⁰ These data provide spatial contours of the blade passage and third harmonic levels of a model tip-turbine lift-fan with various mounting arrangements relative to the ground plane. A summary of the design features of this system, and the measured harmonic levels at a radius of $r/D = 1.0$, are presented in Table VI.

TABLE VI
Measured Near Field Noise Levels (at $R/D = 1.0$) of a Tip-Turbine Fan
(Reference 87)

			Sound Pressure Levels, dB re $20 \mu\text{N/m}^2$			
Fan Mount	Thrust (lb)	Ground-Plane Distance	In Disc-Plane		Maximum	
			Bpf	3rd Harm.	Bpf	3rd Harm.
Shroud	320	6 Diameters	128	136	130	136
		4 Diameters	128	130	130	134
		2.25 Diameters	126	132	128	132
Cruise	326	2.25 Diameters	126	132	132	138
		6.00 Diameters	124	132	130	138
		None	127	134	134	140
Fan Diameter = 8.00 inches Spinner Diameter = 4.90 inches Outer Scroll Diameter = 14.16 inches Bpf = 8,400 Hz, 3rd Harm. = 25,200 Hz			Number of Fan Blades = 22 Number of Vanes = 24 rpm = 22,850			

From these data, the following estimates are made:

Fan hub-to-tip ratio = 0.61

Fan tip Mach numbers = 0.71

Rotor-stator separation, $d/c \sim 1.0$

For the first noise harmonic, $m = 1$

$$m b M_t = 0.71 \cdot 22 = 15.6$$

$$|mB - SV| = 2, \text{ and } k_2^{(r)} R = 2.7$$

so that

$$m b M_t \gg k_2^{(r)} R$$

and, therefore, the attenuation is zero.

From Equation (54), the disc-plane level of the first harmonic at $r/D = 1.0$ is

$$\text{SPL} = 110 + 20 \log (320) - 40 \log (0.67) - 20 \log (22) - 40 \log (2.6) = 123.5 \text{ dB}$$

The correction for rotor-stator interaction is

$$\Delta \text{dB} = +3 \text{ dB}$$

Therefore, the expected first harmonic level in the plane of the fan is 126.5 dB, which compares well with the measured levels of 124 to 128 dB.⁴⁰ The expected maximum level is 131.5, as compared to measured maxima of 128 to 134 dB.

The measured third harmonic levels are higher than the fundamental levels, and therefore will not be predicted accurately by the present prediction method, as shown in Figure 61 for $M_t = 0.7$. The discrepancy can be due to inadequate accounting for the fluctuating loads on the rotor-stator combination, or may be due to the sound radiated from the tip-turbine which has the same harmonic frequencies as the fan and operates at a tip Mach number of 1.26. A more detailed study of these effects is required to improve higher harmonic level predictions for such fan-turbine systems.

SECTION V

NOISE REDUCTION CONCEPTS FOR VTOL AIRCRAFT

Little, if any, noise reduction technology has been developed for specific application to reduction of near field noise levels for VTOL aircraft. One possible exception is the design of VTOL jet engine exhaust configurations to minimize buffeting loads and engine recirculation of exhaust gases. Aircraft propulsion system noise reduction has concentrated primarily on quieting of transport aircraft to minimize community noise problems. Application of these noise reduction techniques to VTOL aircraft would, in some cases, provide a corresponding beneficial reduction in noise levels on the structure. This section briefly reviews a few of these noise reduction techniques.

1. JET NOISE REDUCTION

Since one of the primary design objectives of VTOL jet propulsion systems is to achieve a maximum ratio of thrust to engine weight, the inherent high thrust to weight ratio of turbofan engines, coupled with their noise reduction potential, makes such engines prime candidates for application to VTOL aircraft. The jet noise reduction is due to a decrease in effective exhaust velocity of the combined primary and secondary flows for the same thrust that is achieved by pure turbojets.

Figure 65 illustrates a typical comparison in far field octave band sound pressure levels during takeoff of commercial aircraft achieved with current turbofan engines and pure turbojet engines. To allow a rough comparison on a constant thrust basis, the levels have been normalized approximately to a 10,000 lb thrust engine, as indicated on the ordinate scale. (This is intended only as an approximate means of scaling noise level with thrust for purposes of this graph.)

Assuming near field sound levels follow the same relative trend indicated in Figure 65, the potential noise reduction in the frequency range of 100 to 1000 Hz (of primary interest for structural loads), when changing from pure turbojet lift engines to turbofan engines, could be:

- 3 to 6 dB for turbofan engines with a low bypass ratio
- 13 to 17 dB for turbofan engines with a high (>6) bypass ratio.

A more conservative estimate for the latter would indicate a noise reduction of about 10 to 12 dB, based on the trends noted in Section III for overall sound power levels for a full scale VTOL jet versus exit velocity. According to Figure 21, for example, a 2 to 1 reduction in effective jet velocity (readily achieved in going from a pure

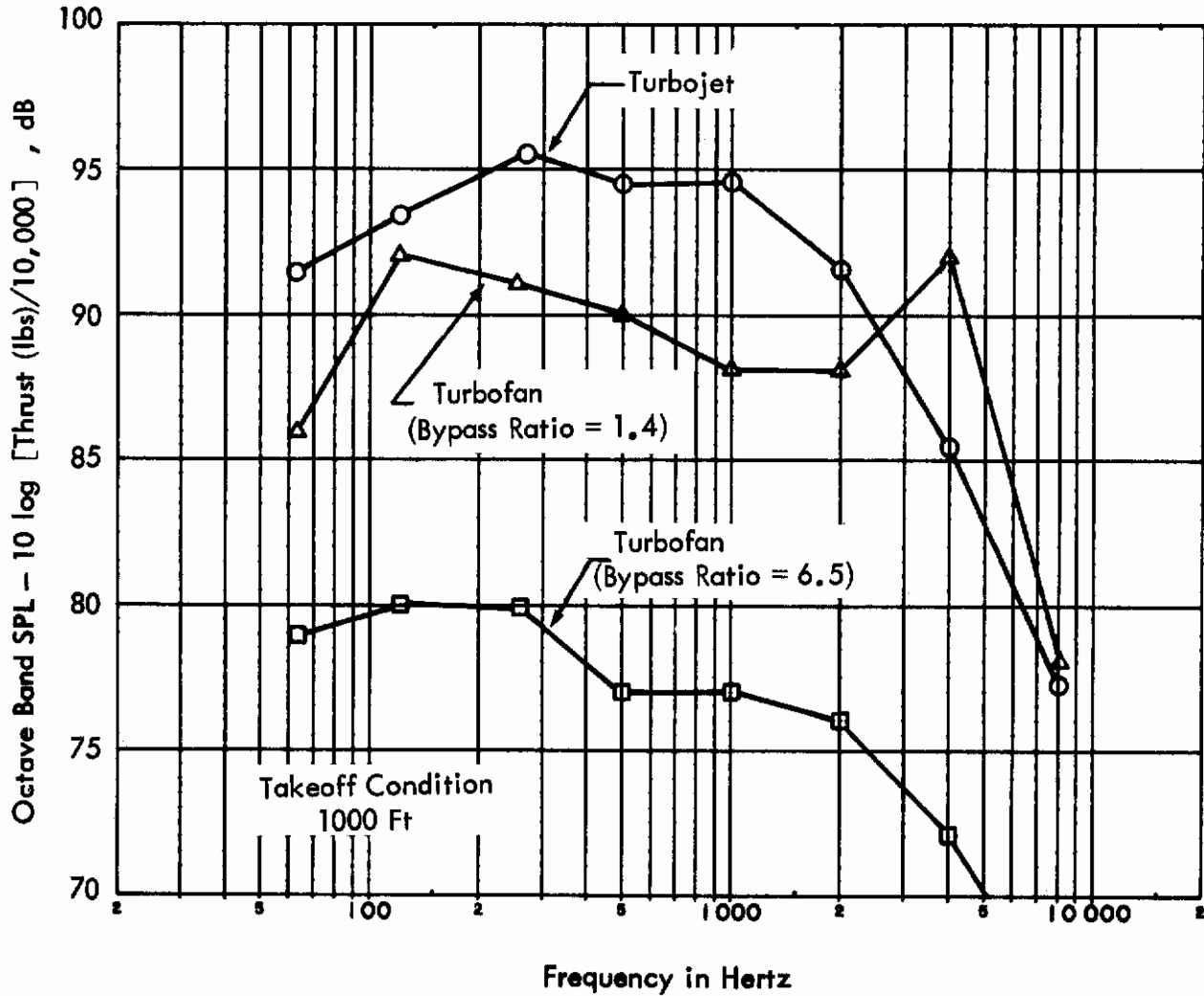


Figure 65. Typical Example of Maximum Octave Band Sound Levels at 1000 Ft Slant Range (Normalized to 10,000 lb Thrust) During Takeoff of Current Commercial Aircraft with Turbojet and Turbofan Engines. (From References 88 and 89)

current-technology turbojet to a high bypass ratio turbofan) would reduce overall sound power levels by about $10 \log (2)^4$ or 12 dB.

Near field sound levels will not necessarily scale directly as far field sound levels due to the major influence of the engine mounting and primary-secondary exhaust configuration. Nevertheless, the large bypass ratio turbofan engines are able to extract sufficient kinetic energy from the primary jet to drive the fan system, and thus reduce exit velocities to about 1000 ft/sec. Such marked reduction in exit velocity would probably offer a greater potential near field noise reduction than one could expect to obtain by any other practical method of jet noise suppression for VTOL jet aircraft.^{90,91}

There is one possible exception to this generalization of the dominant noise reduction benefit of high bypass turbofan engines for VTOL aircraft. Jet noise suppression of 5 to 10 dB has been achieved with various types of nozzles such as multi-tube or corrugated types which enhance the mixing of a jet with the atmosphere. The net result can be a substantial reduction in the effective length of the potential core. This by itself could offer a significant noise reduction for a jet-powered VTOL aircraft by insuring that the peak noise levels in the near field would occur at a lower nozzle elevation above the ground. If this elevation for peak noise was close to the normal minimum elevation before lift-off, the duration of peak noise level exposure during lift-off could be reduced. However, such a concept would require evaluation, since it is also possible that the net effect could be an increase in time of exposure if the initial acceleration and elevation for peak noise were not optimum.

Extended ground testing of prototype jet-powered VTOL aircraft presents special problems which dictate the need to consider noise suppression devices for this operation.⁵ Although some full-thrust engine testing should certainly be done under simulated operational conditions (i.e., exhaust deflected over flat ground), unrealistic sonic fatigue damage could result from repeated static tethered full-thrust testing without the use of special exhaust deflectors and test pads with non-reflecting surfaces to minimize near field noise levels.

2. FAN NOISE REDUCTION

Extensive work has been carried out to reduce discrete-frequency turbomachinery noise of the turbofan engine.⁹² This has generally consisted of adding absorbing liners to inlet and outlet ducts to attenuate this high frequency noise before it is radiated. The performance of a typical example of this type of noise reduction treatment is illustrated in Figure 66.⁹⁰

Since the primary objective of this type of noise reduction design is to reduce the subjectively annoying high frequency noise associated with most turbofan engines, the frequency range of maximum attenuation is generally near or above the upper limit of

primary concern for aircraft structural loads. Thus, current technology for reduction of discrete frequencies from fan-in-wing type VTOL aircraft, for example, would have to be extended to a lower frequency range to be of significant benefit for VTOL structure. Unfortunately, this extension to lower frequencies would generally involve increasing the depth and hence weight of the treatment. Until more specific VTOL designs are available which might utilize this noise reduction technique, it is difficult to assess its practicality for VTOL applications solely for near field noise reduction. Nevertheless, the basic engineering technology and design approaches are reasonably well understood and developed so that the application to any VTOL design should not present new problems aside from possible weight penalties.

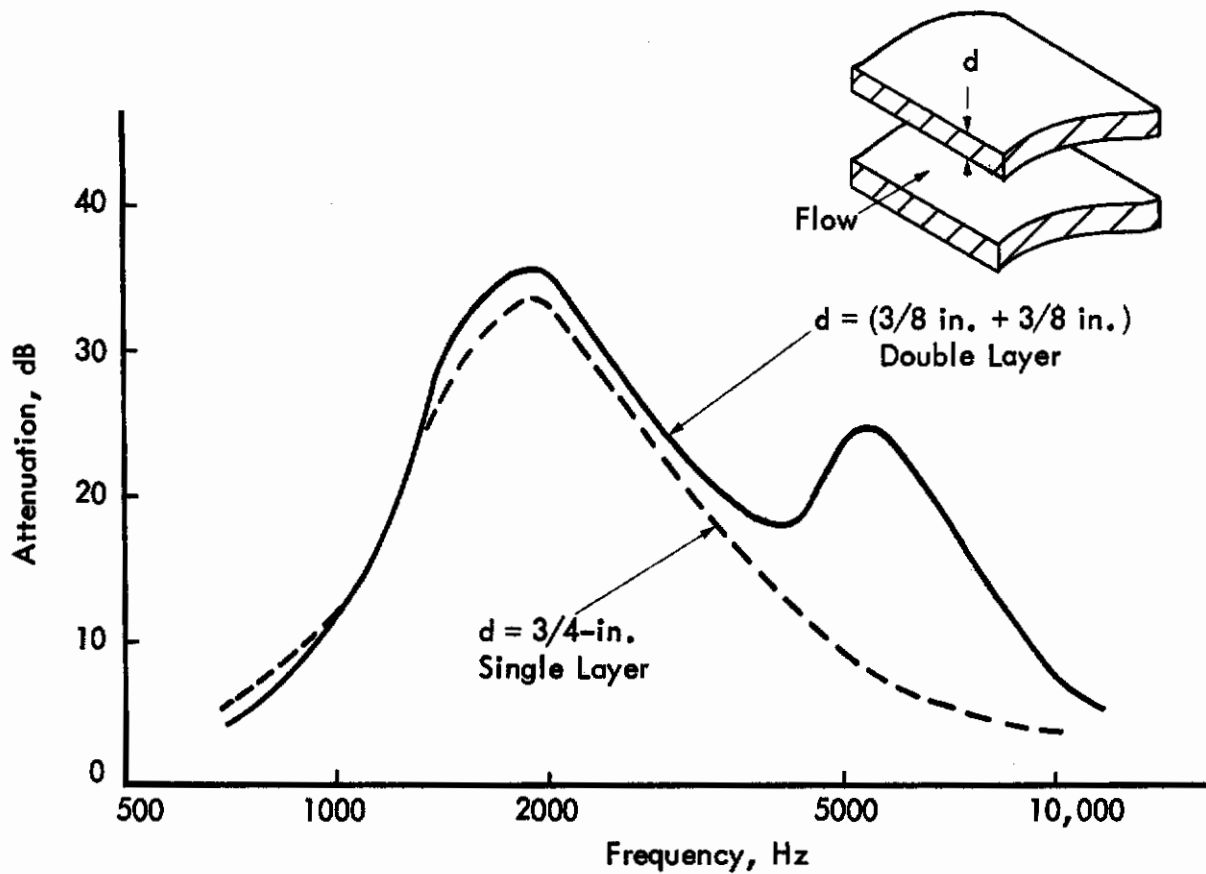


Figure 66. Illustration of Typical Attenuation of Fan Noise Source Achieved by Duct Lining (Reference 90)

Another more fundamental method is also available for fan noise reduction. It is also the technique that could offer the greatest noise reduction benefit for the lowest weight. This involves optimizing the turbomachinery design (i.e., inlet guide vane configuration, rotor-stator spacing, etc.) to minimize the basic noise generation. (See Section IV for additional details.)

3. ROTOR OR PROPELLER NOISE REDUCTION

Again, motivated by the desire to reduce far field noise levels, significant advances have and are being made in the reduction of rotor or propeller noise from helicopters.^{93,94} An illustration of some of these noise reduction programs for helicopters is presented in Figure 67. An example of the noise reduction benefits attained in one case is shown in Figure 68.

The most direct and efficient methods for propeller and rotor noise reduction involve reducing the blade tip speed and reducing either the total load on each blade or the load per unit blade area. There are obvious limits to the application of these techniques. These limits include aerodynamic stall (which gives a sudden noise increase) and the weight/performance requirements for economic operation. Thus, most research effort has been aimed at deriving more subtle approaches to design, whereby the above methods can be implemented and improved upon with negligible performance penalty. Some of the more successful of these methods are:

- Larger blade area
- Increased number of blades
- Variable geometry blades (changeable camber in flight)
- Modified blade tip shapes

All of these have either resulted from, or have been optimized by combined efforts in acoustic, aerodynamic and materials research. In particular, the noise reduction potential from increasing the number of blades and blade area has been known for quite some time, but this approach has only recently become practical due to the development of lightweight propeller construction materials and fabrication techniques. Blade tip shape modifications have undergone extensive investigation for both aerodynamic and acoustic benefits, including reduction of blade slap.

Major activity in noise reduction pursued by the industry has included work on both propeller/rotor noise reduction and engine exhaust noise reduction. The latter will ordinarily be less significant from a structural loads standpoint. However, if required, well developed methods for muffling of piston-powered or turbine-powered engine exhaust noise are available.^{93,94}

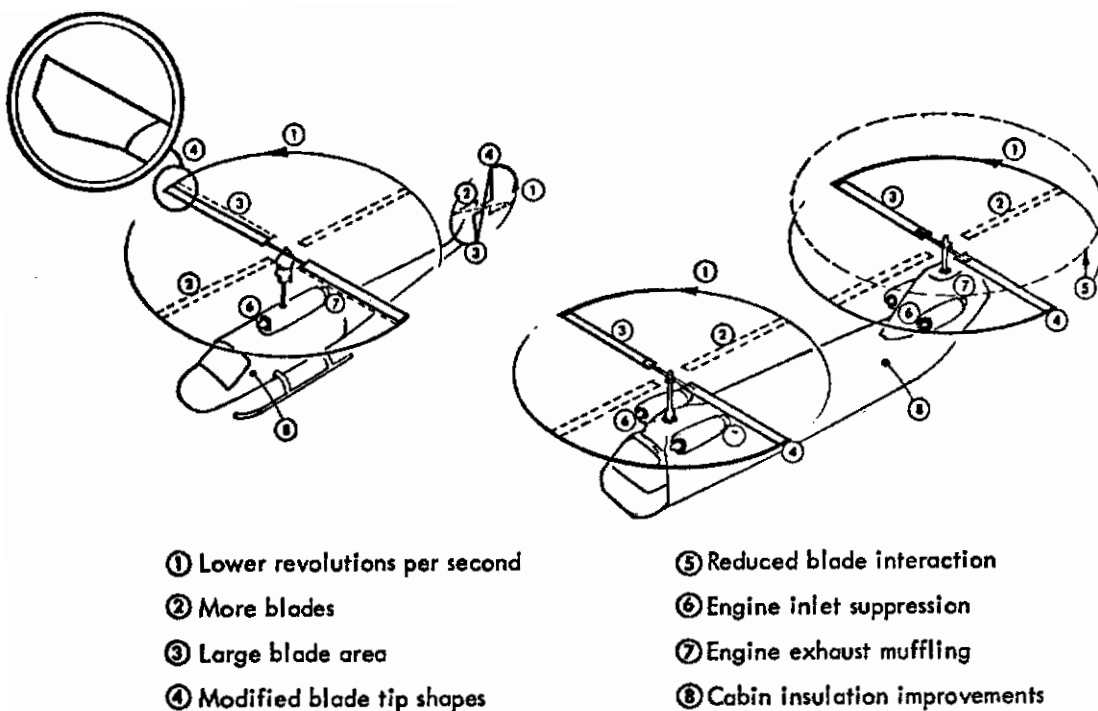


Figure 67. Current Design Approaches to Helicopter Noise Reduction
 (Reference 93)

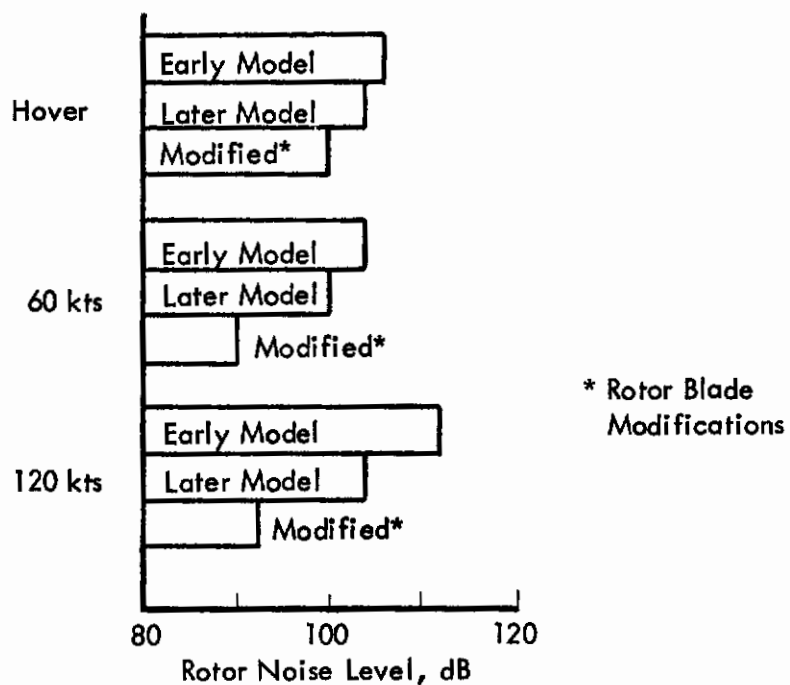


Figure 68. Demonstrated Noise Reduction of a Heavy-Helicopter Twin-Rotor System for Hover and Two Flight Speeds
 (Reference 94)

SECTION VI

NEAR FIELD NOISE PREDICTION METHODS

This section summarizes the basic results of this report in the form of prediction methods for near field noise levels of jet-powered and rotor/propeller-powered VTOL aircraft. The prediction methods were designed to be suitable for hand calculations at preliminary design stages of VTOL aircraft.

Development of the prediction methods was supported by an in-depth review of the existing state-of-the-art and by additional data taken specifically for this report. However, the constraint of keeping the prediction methods simple prevented, in some cases, inclusion of additional refinements suggested by the backup analysis in Sections III and IV. These refinements may be helpful for developing improvements to the prediction methods in the future or may be useful now for carrying out a more detailed near field noise prediction applying methods beyond the scope of this section. The estimated accuracy of the prediction methods presented in this section is ± 5 dB.

1. PREDICTION OF VTOL JET NEAR FIELD NOISE LEVELS

The near field region for noise from a VTOL jet is assumed, for this report, to consist of the rectangular volume which bounds the aircraft. This will normally not extend beyond about 30 nozzle diameters from the VTOL nozzles in any direction. The prediction method involves two basic operations:

- Estimate the near field noise in octave band sound pressure levels in the vicinity of the structure assuming there is no ground plane under the vertically directed jets.
- Add a correction factor Δ , dB to these estimates of the noise levels for the undeflected jet to define the expected octave band noise levels for VTOL operation.

This correction factor will be specified by its maximum value Δ_{\max} , regardless of the exit nozzle elevation or by Δ as a function of the nozzle elevation. In either case, the correction term will vary with frequency expressed in the non-dimensional form (the Strouhal number, S_N) given by:

$$S_N = \frac{fD}{U_e} \quad (62)$$

where

f = center frequency of an octave band

D = jet exit diameter

U_e = jet exit velocity

Step-by-step procedures to carry out these two basic operations are defined in the following.

a. **Sound Pressure Levels for the Undeflected Jet**

Contours of constant octave band sound pressure level in a plane containing the jet axis are given in Figure 69 for non-dimensional frequencies of $S_N = 0.125, 0.25, 0.5, 1$ and 2 . These contours apply directly to jet engines with exit velocities U_e close to 1930 ft/sec and exit total temperatures close to 1600°R or exit Mach numbers close to 1.13. A procedure for conversion to other exit velocities will be specified in the following.

Prediction Method

(1) The required input parameters are

D - The exit diameter of the jet (ft)

U_e - the exit velocity of the jet (ft/sec)

X, Y - the coordinate locations of the desired observation point(s) in a rectangular coordinate system with the origin at the jet exit and the positive X axis along the downstream direction of the flow (ft).

For VTOL jet aircraft for which the actual jet engine nozzle diameter is not available, the diameter D may be approximated by:

$$D \approx K \sqrt{\text{Thrust (lb)}} \quad , \text{ ft} \quad (63)$$

where

$K = 0.018$ for turbojets or low bypass ratio turbofans

0.038 for high bypass ratio turbofans (with coaxial flow)

Contrails

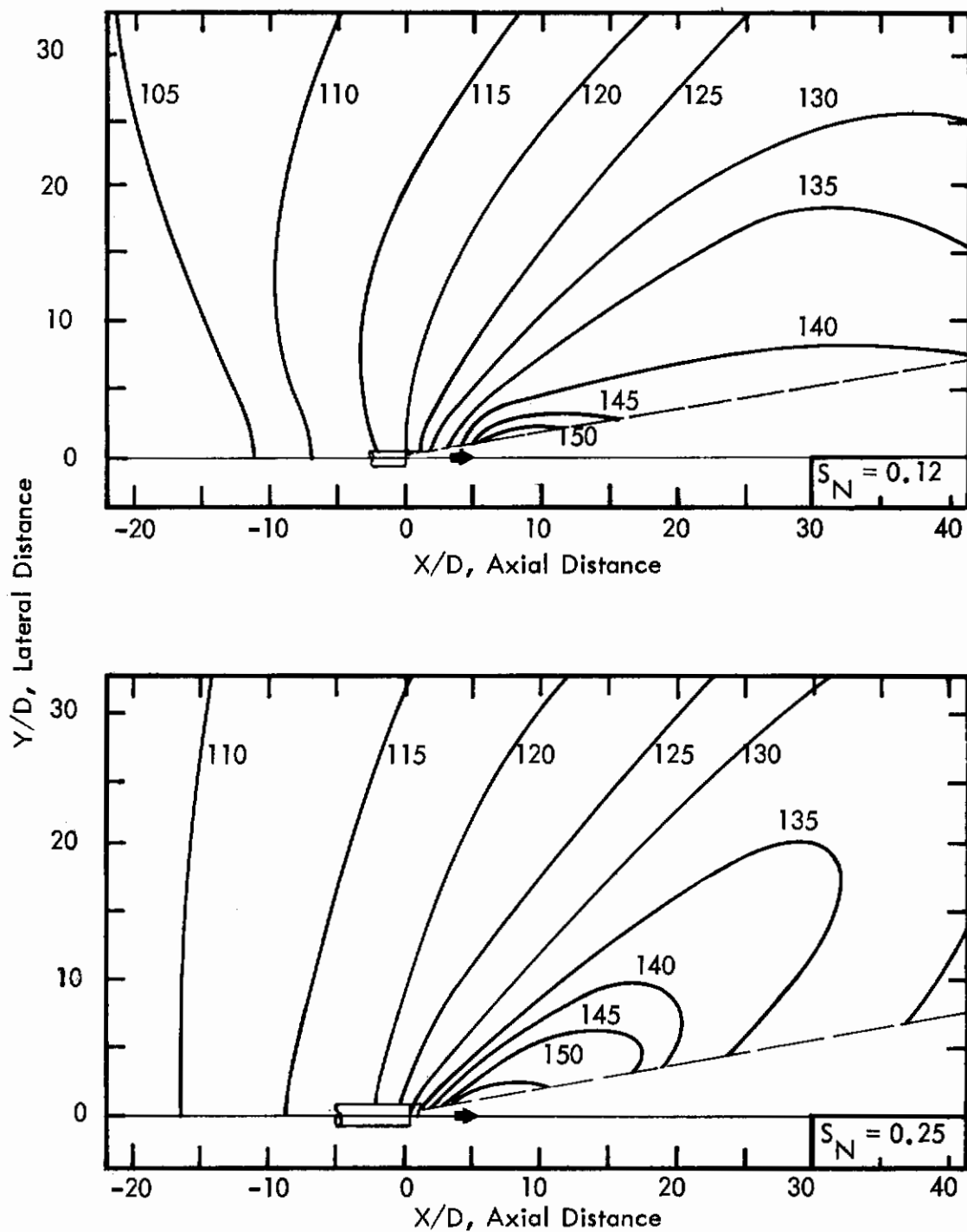


Figure 69. Contours of Octave Band Sound Pressure Level in dB re: $20\mu\text{N}/\text{m}^2$ for Free Jet with Exit Velocity of 1930 ft/sec and Exit Mach Number of 1.13 (Adopted from Reference 36 with Corrections for Ground Reflection).

Contrails

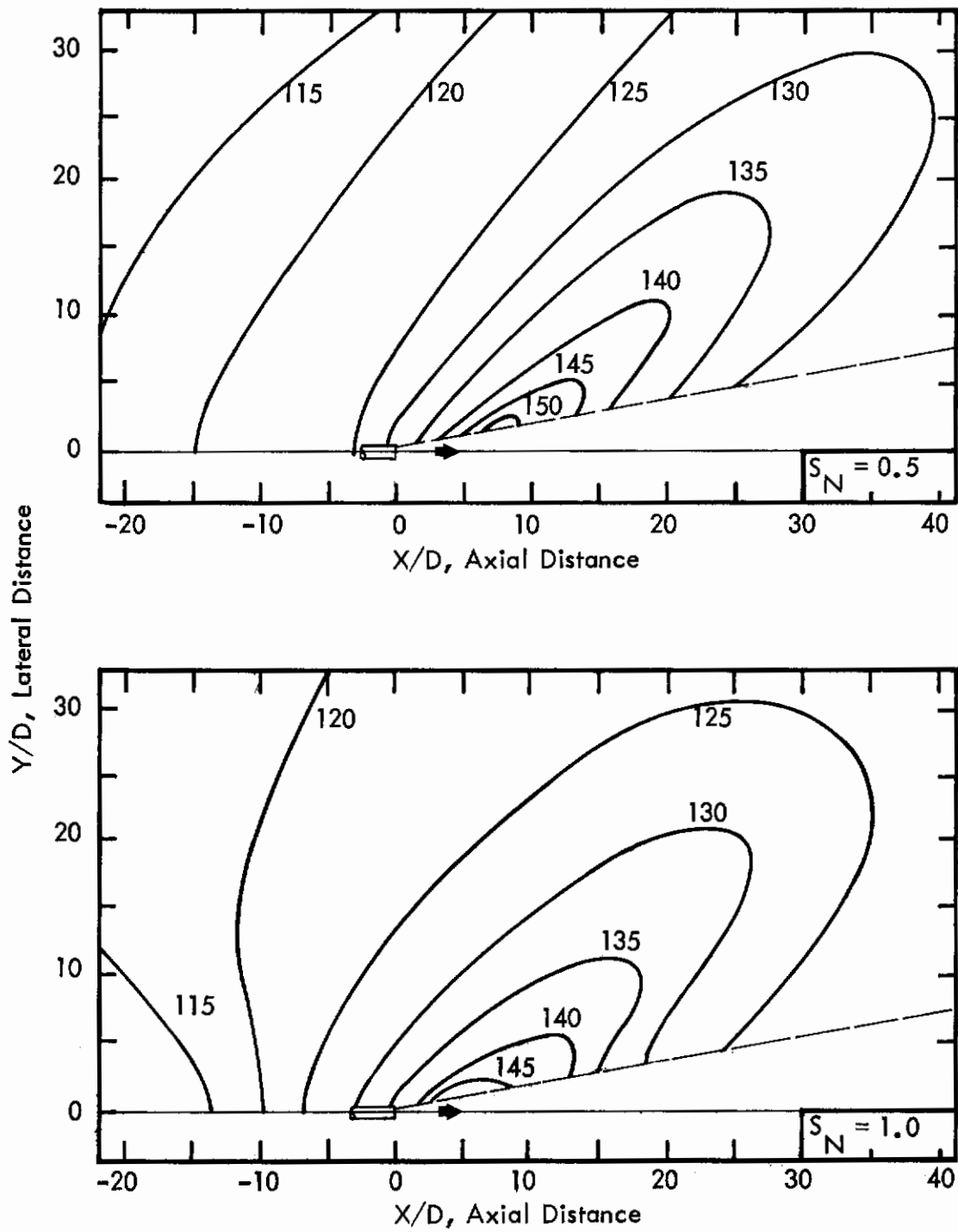


Figure 69 (Continued)

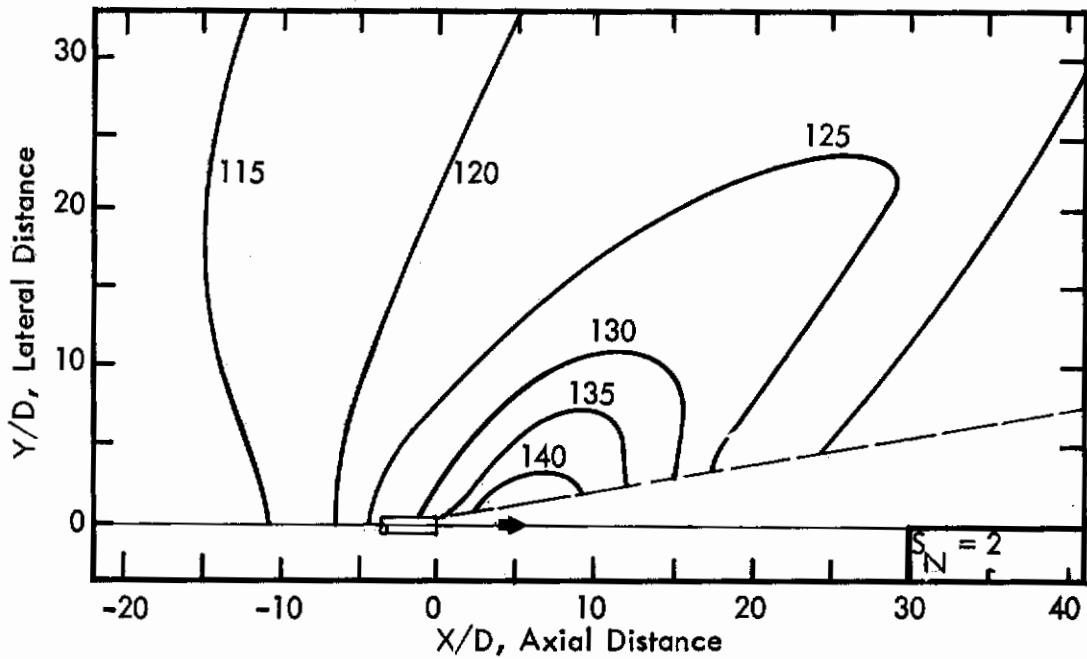


Figure 69 (Concluded)

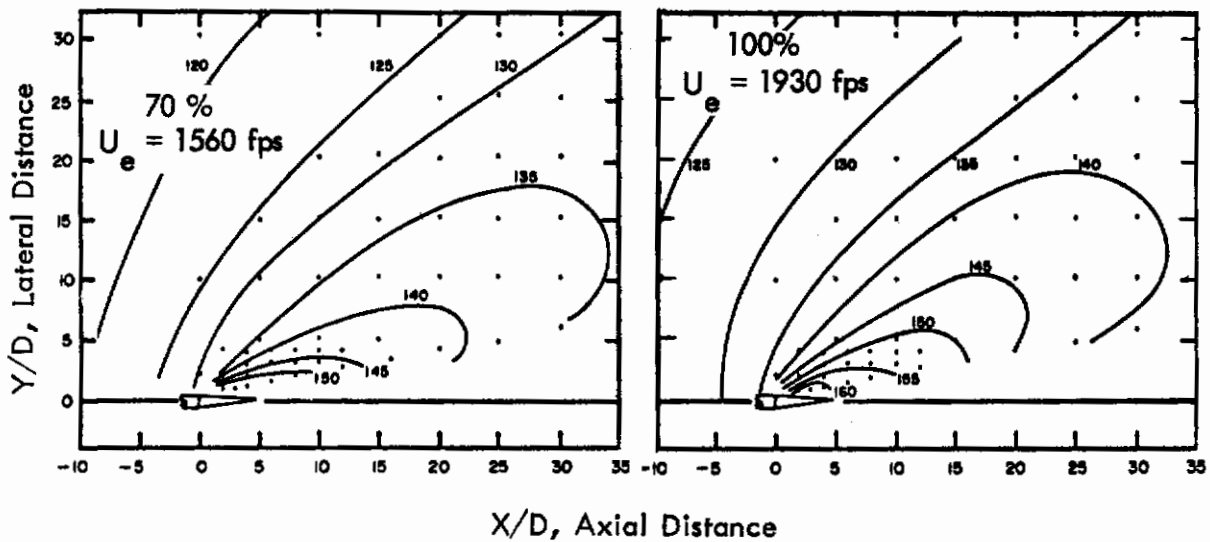


Figure 70. Contours of Overall Sound Pressure Level in dB re: $20\mu\text{N}/\text{m}^2$ for Same Jet as in Figure 69 at Two Power Settings (from Reference 36)

- (2) Compile or plot a matrix of field points at the desired values of X and Y and convert these coordinates to the dimensionless ratios X/D and Y/D.
- (3) Enter Figure 69 for each desired value of X/D and Y/D and for the desired dimensionless frequencies (S_N) and read the corresponding octave band levels (L_o). If only overall sound pressure levels are desired, use Figure 70.
- (4) For jet engines operating with exit velocities (U_e) different from 1930 ft/sec, add the following velocity correction, C_v , to each octave band level (or overall level for the 100 percent power condition).

$$C_v = 50 \log_{10} (U_e/1930), \quad \text{dB} \quad (64)$$

For turbofan engines with non-coaxial exhausts of the primary (hot) and secondary (cold) flow, determine the velocity correction for each nozzle separately and continue to treat each nozzle as a separate source as long as their levels are within 10 dB of each other.

For turbofan engines with coaxial exit flow, compute an equivalent exit velocity U'_e by

$$U'_e = 32.2 \left[\frac{\text{Total Thrust, lbs}}{\text{Total Weight Flow, lb/sec}} \right], \quad \text{ft/sec} \quad (65)$$

Use this equivalent velocity to determine the velocity correction with the preceding expression.

b. Sound Pressure Levels for the VTOL Jet

The VTOL jet near field sound pressure levels are determined by applying the following Δ corrections to the preceding sound pressure levels.

Prediction Method

- (1) The required input parameters are the same as in part (a) of this section plus the following additional parameter if the variation in near field levels with nozzle elevation is desired.

$$M_E = \text{exit Mach number}$$

For turbojet engines, M_E is typically in the range of 1.0 to 1.2 for maximum (non-afterburning) power settings. For bypass turbofan engines, M_E may be

Contrails

approximated by a value of 0.8 for both primary and secondary nozzles. Actual values will vary depending on engine design and bypass ratio.

- (2) Enter Figure 71 to determine the value for the maximum correction factor Δ_{\max} , independent of nozzle elevation, at each frequency expressed in terms of the non-dimensional Strouhal number. If the variation in Δ with nozzle elevation is not required, skip the next two steps.

- (3) Compute the nozzle elevation H , relative to the potential core length X_f by

$$H/X_f = H/3.45 D_E \left[1 + 0.38 M_E \right]^2 \quad (66)$$

D_E is the fully expanded jet diameter and, for turbojet and turbofan engines, may be assumed equal to the exit diameter D .

- (4) Enter Figure 72 at the value of H/X_f and S_N desired to determine the value of Δ relative to its maximum value, $(\Delta - \Delta_{\max})$. Compute Δ by adding Δ_{\max} from step 2 to this quantity.

- (5) For each value of S_N , add the correction factor Δ or Δ_{\max} to the corresponding values of undeflected jet levels to determine the VTOL sound pressure levels L_v . That is

$$L_v = L_o + C_v + \Delta \text{ (or } \Delta_{\max}\text{)}, \quad \text{dB} \quad (67)$$

- (6) Compute the actual frequency corresponding to each Strouhal number by

$$f = S_N \cdot U_e/D, \quad \text{Hz} \quad (68)$$

- (7) Plot the values of L_v at these frequencies, draw a smooth line between the points and then interpolate from the graph the values of L_v at the standard octave band frequencies (i.e., 63, 125, 250, 500, 1000, etc.).

- (8) For structural surface sound pressure levels, add 6 dB to each value if the surface is flat, or 3 dB for curved surfaces exposed to the source at frequencies in Hz greater than $360/$ (shortest dimension of structure normal to wave front in ft). At these same frequencies, for surfaces in the shadow of the source, subtract 5 dB from each octave band level. The shortest dimension is taken in a plane roughly normal to the incident sound.

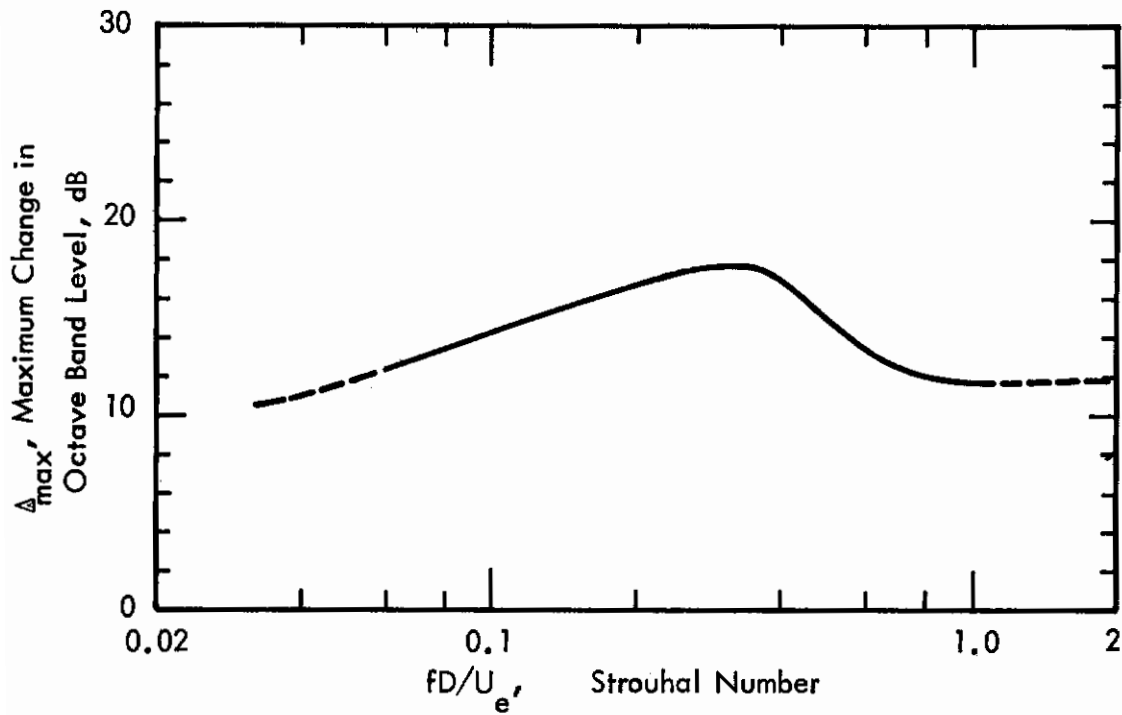


Figure 71. Δ_{\max} , Maximum Change in Near Field Octave Band Sound Pressure Levels for VTOL Jets Relative to Levels for Undeflected Jets.

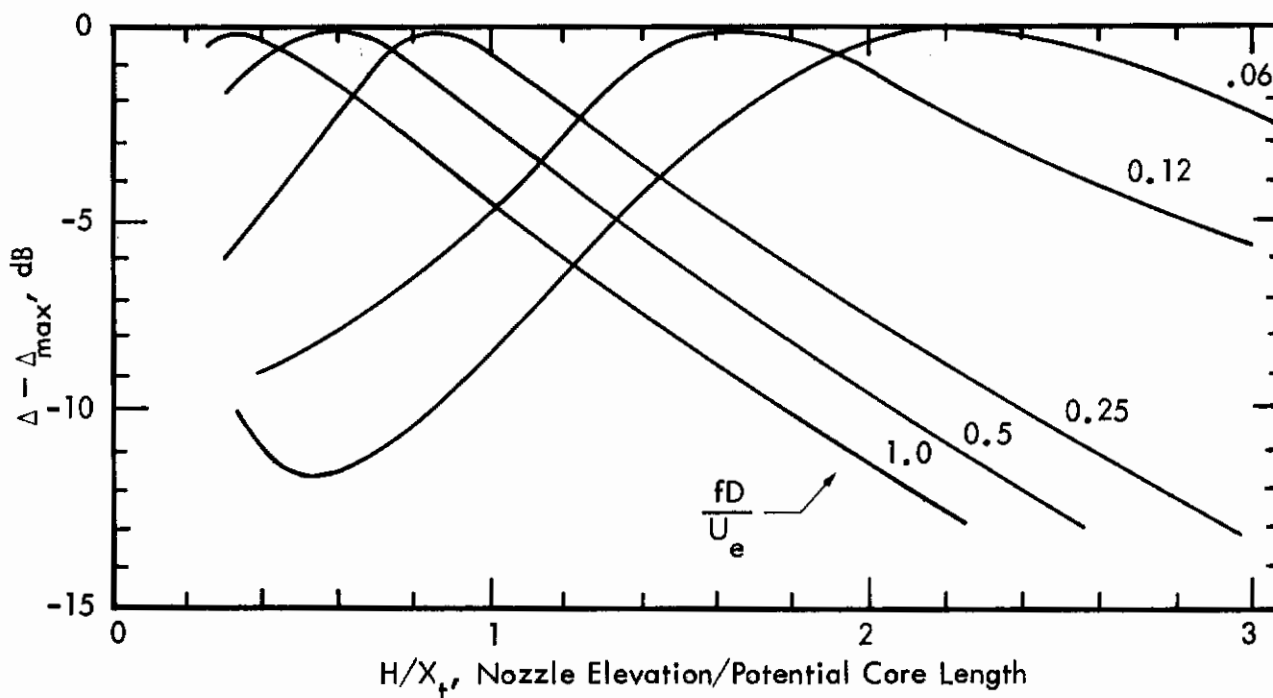


Figure 72. Change in Δ Relative to its Maximum Value for Near Field of VTOL Jet as a Function of Nozzle Elevation and Normalized Frequency

- Δ = Change in Near Field Octave Band Level for VTOL Jet Relative to Level for Undeflected Jet
- f = Center Frequency of Octave Band
- D = Jet Exit Diameter
- U_e = Exit Velocity

- (9) Compute the approximate overall sound pressure level L_{vo} by adding, logarithmically, the new values of L_v of each frequency. That is

$$L_{vo} = 10 \log_{10} \left[\sum_i^n \text{antilog} (L_{vi}/10) \right], \quad \text{dB} \quad (69)$$

where $L_{vi} = L_v$ at i^{th} frequency.

- (10) Repeat the preceding steps for additional exit nozzles located on the same side of the aircraft as the observation points being considered.
- (11) For further changes in engine power, add the following correction to the overall level

- For Turbojet Aircraft

$$C_v = 50 \log \left[U'_e / U_e \right], \quad \text{dB} \quad (70)$$

where U'_e and U_e are the new and original exit velocities respectively.

- For Turbofan Aircraft

$$C = 27.5 \log \left[T'/T \right], \quad \text{dB} \quad (71)$$

where T' and T are the new and original total engine thrusts respectively.

- (12) If desired, compute the time history of the noise levels on the structure during takeoff by changing the nozzle elevation H with time (t) in seconds by

$$H = H_o + 16.1 \left[(T/W) - 1 \right] T^2, \quad \text{ft}$$

where

$$H_o = \text{initial nozzle elevation at } t = 0 \quad (72)$$

T/W = initial thrust to weight ratio for the aircraft. Normally, T/W is about 1.1 to 1.3 for VTOL aircraft.

For nozzle elevations greater than about $5X_t$, the near field levels will no longer be significantly influenced by the ground and will also decrease due to the effect of source motion. Thus, for higher elevations, the near field levels may be taken from part (a) of this section with the correction in dB, $20 \log [1 - (\text{Flight Mach No.})]$ subtracted from the levels.

2. PREDICTION OF PROPELLER/ROTOR NEAR FIELD NOISE LEVELS

For this section, the near field of a rotor or propeller is the spatial region within a radius of one rotor-diameter from the center of rotation. In this region, the predominant noise components occur at the blade passage frequency (f_1 (Hz)) and at multiples thereof (f_2, f_3 , etc.). These frequencies are calculated from

$$f_m = \frac{m \times B \times N}{60}, \quad \text{Hz} \quad (73)$$

where

$m = 1, 2, 3$, etc.

$B =$ number of blades

$N =$ rotational speed (revolutions per minute)

a. Free Propellers

The noise level prediction method presented here requires the first harmonic level (L_1 (dB) at f_1 (Hz)) to be found by means of Figures 73 and 74 for a position in the plane of the propeller at the desired radius from the propeller center. The level at other azimuthal positions on this radius, and the levels of other harmonics (for $m = 2, 3$ and 4) at any desired azimuth, will be calculated by the use of corrections (Δ dB) applied to the value of L_1 .

Prediction Method

(1) The required parameters are:

B - the number of blades on each propeller

T - the total thrust developed by each propeller (lb)

N - the rotational speed of the propeller (in rpm)

D - the propeller/rotor diameter (ft)

M_t - the blade tip Mach number

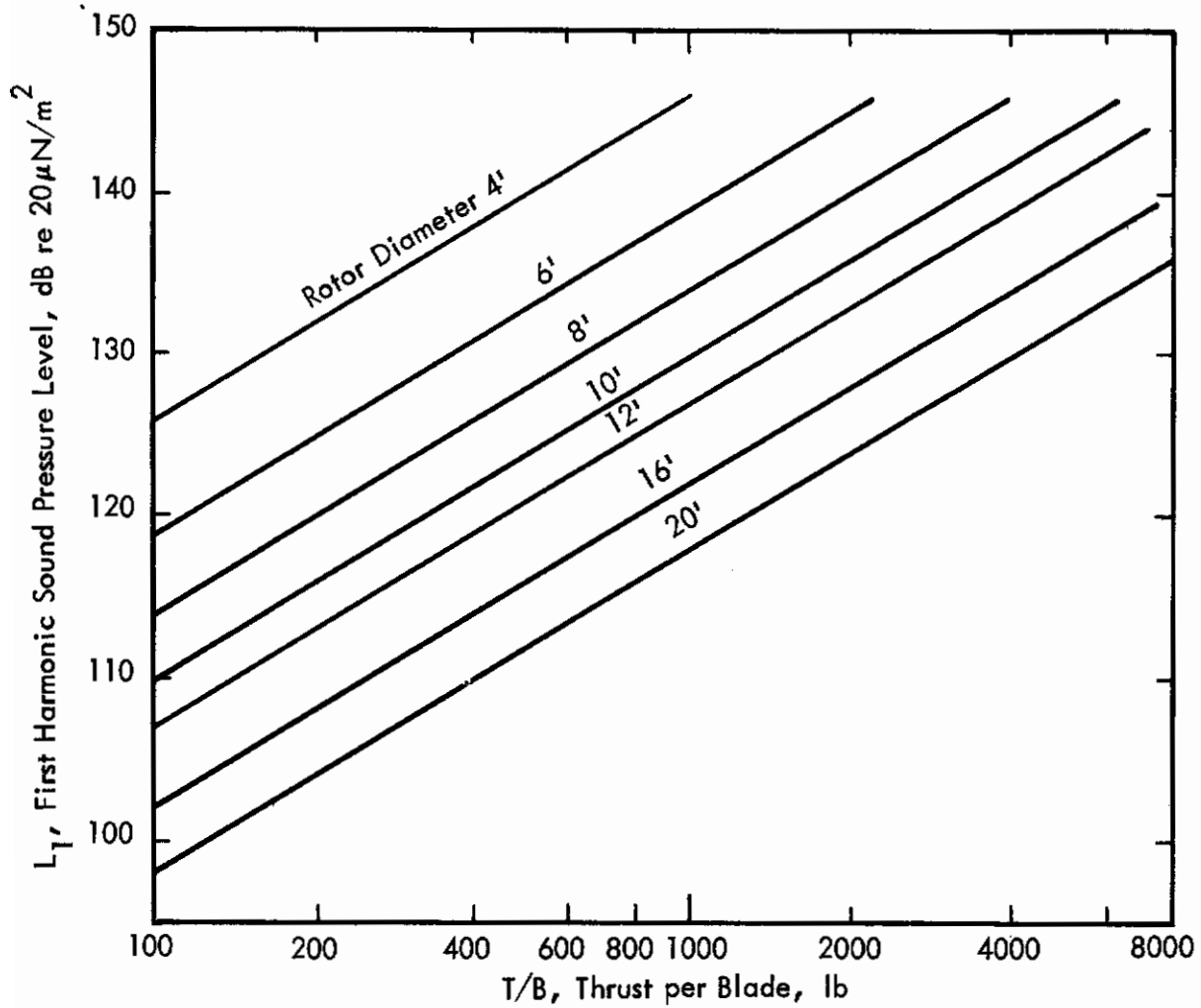


Figure 73. Partial Sound Pressure Level, L_1 in Terms of Rotor Diameter and Thrust per Blade

For VTOL aircraft, the maximum thrust is generated at takeoff. In this case, the following approximations can be used to give a preliminary estimate of the sound levels:

$$T \approx \text{Aircraft gross weight/number of propellers}$$

and

$$M_t \approx \frac{\pi DN}{60 \times 1120} \quad (74)$$

- (2) Compile or plot a matrix of field points at which sound level estimates are required. For each point, calculate the radius, r (ft) from the center of the propeller, and the aximuthal angle, ψ (degrees) from the disc-plane of the propeller. Sound levels will now be estimated for each point at coordinates $(r/D, \psi)$.
- (3) From the estimated thrust per blade (T/B) and propeller diameter (D) , find level L_1 from Figure 73 or from

$$L_1 = 110 + 20 \log_{10} (T/B) - 40 \log D, \quad \text{dB} \quad (75)$$

- (4) For the desired field point radius (r/D) , find incremental level $\Delta L^{(1)}$ from Figure 74 or from

$$\Delta L^{(1)} = -40 \log_{10} [r/D - 0.35] - 6, \quad \text{dB} \quad (76)$$

- (5) For each of the harmonic frequencies $f_m = \frac{m \times B \times N}{60}$, Hz, find the incremental level $\Delta L_m^{(2)}$ from Figure 75 for the appropriate values of M_t and r/D , respectively.

- (6) For $\psi = 0$, that is, for levels in the disc-plane, the sound pressure levels, SPL_m (dB re $20 \mu\text{N}/\text{m}^2$) at each frequency f_m (Hz) are given by

$$\text{SPL}_m (r/D, 0^\circ) = L_1 + \Delta L^{(1)} + \Delta L_m^{(2)}, \quad \text{dB} \quad (77)$$

- (7) For $\psi \neq 0^\circ$, that is, for levels outside the disc-plane, the sound pressure levels, SPL_m (dB re $20 \mu\text{N}/\text{m}^2$) at each frequency f_m (Hz) are given by

$$\text{SPL}_m (r/D, \psi) = L_1 + \Delta L^{(1)} + \Delta L_m^{(2)} + \Delta L_{mB, \psi}^{(3)}, \quad \text{dB} \quad (78)$$

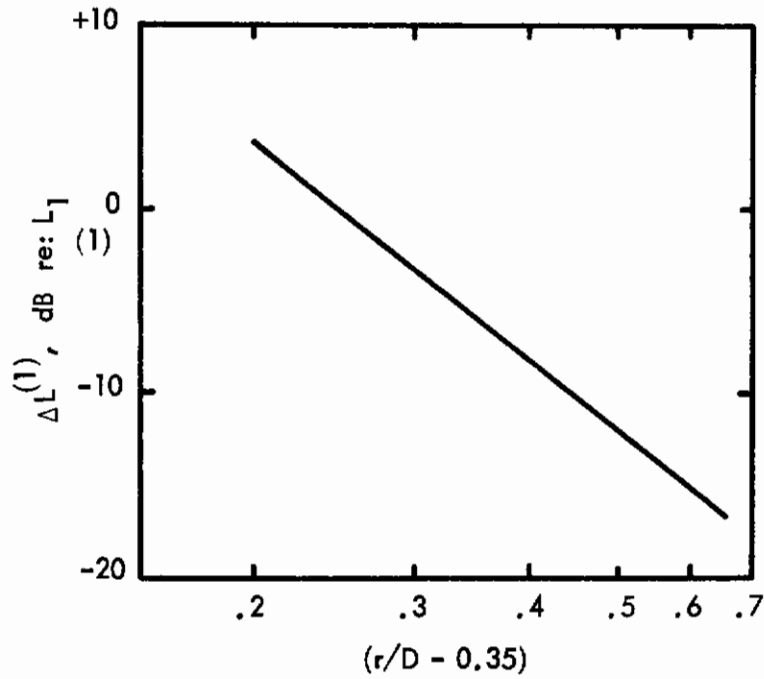


Figure 74. Sound Level Correction, $\Delta L^{(1)}$, for Required Observation Radius from Rotor Center, r/D .

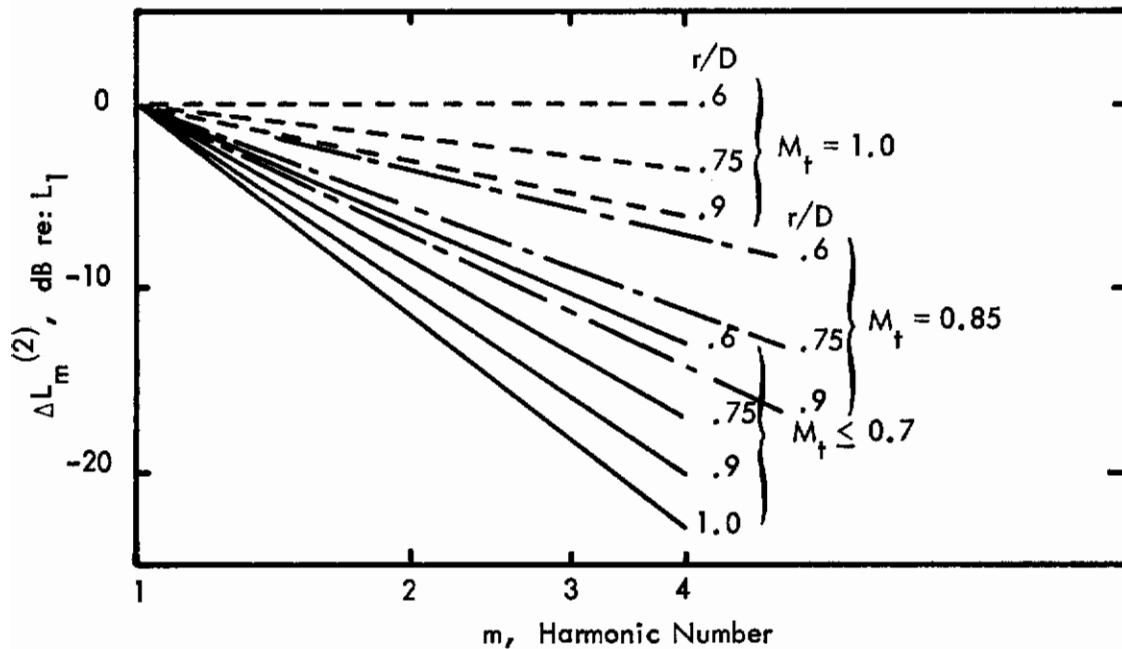


Figure 75. Sound Level Correction, $\Delta L^{(2)}$, for Harmonic Order m , in terms of Tip Mach Number M_t , and Observation Radius, r/D

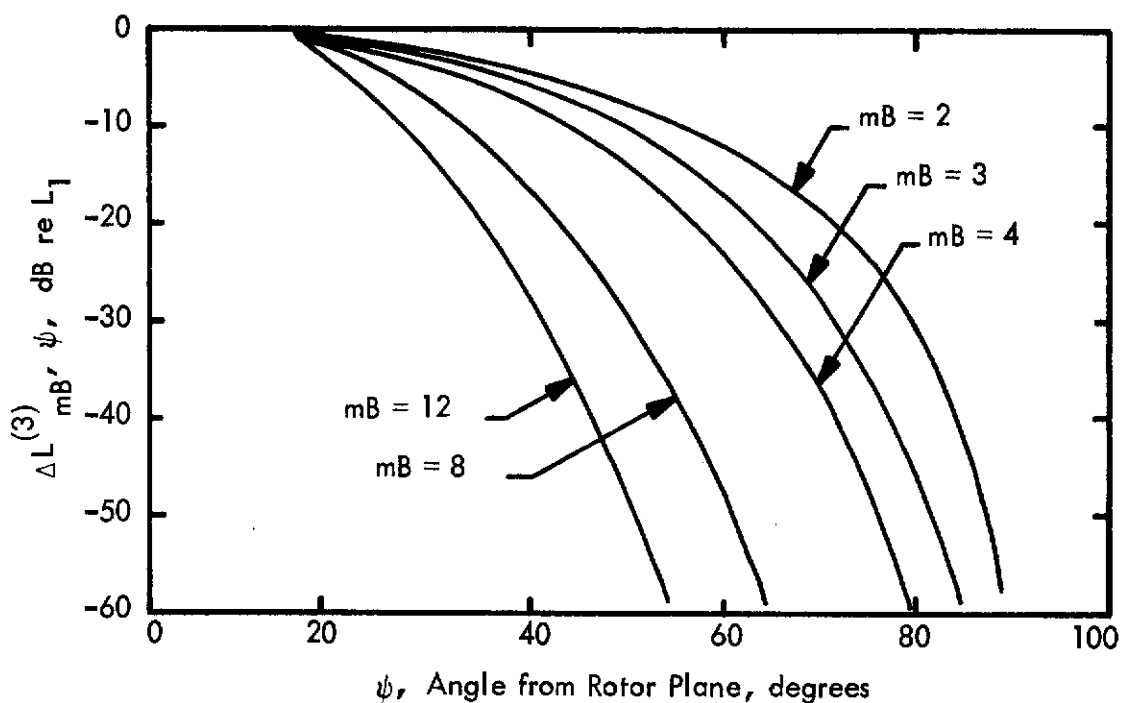


Figure 76. Sound Harmonic Level Correction $\Delta L_{mB, \psi}^{(3)}$ for Azimuthal Angle, ψ Degrees, from Rotor Plane. (m = Harmonic Order, B = Blade Numbers).

where $\Delta L_{mB, \psi}^{(3)}$ is obtained from Figure 76 for the appropriate values of mB and ψ , respectively.

- (8) For structural surface sound pressure levels, add 6 dB to each value if the surface is flat, or 3 dB for curved surfaces. (See step 8 in part 1(b) of this section.)
- (9) For field points at $1.0 < r/D < 3.0$, calculate levels for $r/D = 0.6$, by steps 1 through 7, and for $r/D = 3.0$ by Equation 46. Plot these sound pressure levels on a linear ordinate scale of sound levels and a logarithmic abscissa scale of $(r/D - 0.35)$. Draw a straight line with a slope of -12 dB per doubling of the abscissa scale through the point for which $r/D = 0.6$. Draw another line with a slope of -6 dB per doubling of the abscissa scale through the point for which $r/D = 3.0$. Draw a fairing curve, tangential to these two lines at points for which $r/D = 1.0$ and 3.0 , and read the sound level for the required value of r/D from this composite interpolation curve. Apply corrections in step 8 for surface pressure levels.

b. Corrections for Ducted Systems

For systems in which the rotor is shrouded by a duct, the following corrections are made to the free-rotor levels estimated by the method in part 2(a) of this section.

- Duct-Transmission Loss (TL_m)
- Rotor-stator Interaction (Δ_s)
- Directionality Corrections

The additional design parameters required for estimation of these corrections are:

V = the number of stator vanes in close proximity to the rotor disc.

(d/c) = the separation distance between the rotor and stator blades (trailing edge to leading edge) divided by the chord of the downstream blade.

(x/R) = The axial duct-length between the rotor disc and the duct leading-edge, divided by the duct radius (R).

σ = the hub-to-tip radius ratio of the duct.

Prediction Method

- (1) Calculate the sound harmonic levels for a field point in the disc-plane, at the required r/D , by steps 1 through 6 of part 2(a) of this section, i.e.,

$$\text{SPL}_m(r/D, \psi = 0^\circ) = L_1 + \Delta L^{(1)} + \Delta L_m^{(2)}, \quad \text{dB} \quad (79)$$

These levels require the following duct corrections.

- (2) Calculate the duct transmission loss, TL_m , as follows:

- If $d/c < 2.0$, find the lowest value of $\ell = |mB - SV|$, for each harmonic order m .

$$S = 0, 1, 2, 3, \text{ etc.}$$

If $d/c \geq 2.0$, or if no stators are present, $\ell = mB$, for each harmonic order m .

- For each harmonic order (m), find the value of $(k_\ell^{(r)})_R$ from Table V, page 143, for appropriate values of σ and ℓ .

If

$$m\text{BM}_t \geq (k_\ell^{(r)})_R$$

then

$$\text{TL}_m = 0$$

if

$$m\text{BM}_t < (k_\ell^{(r)})_R$$

then

$$\text{TL}_m = 8.68 (x/R) \sqrt{(k_\ell^{(r)})_R^2 - (m\text{BM}_t)^2}, \quad \text{dB} \quad (80)$$

- (3) Calculate the rotor-stator interaction (Δ_s), as follows:

if

$$d/c \geq 2.0,$$

then

$$\Delta_s = 0$$

if

$$d/c < 2.0,$$

then

$$\Delta_s = 3 - 20 \log (d/c), \quad \text{dB} \quad (81)$$

- (4) The corrected sound pressure levels in the disc-plane, at the required r/D , are,

$$\text{SPL}_m (r/D, \psi = 0^\circ) = L_1 + \Delta L^{(1)} + \Delta^{(2)}_m - \text{TL}_m + \Delta_s, \quad \text{dB} \quad (82)$$

where the first three terms are found from part 2(a) of this section.

- (5) For $\psi \neq 0^\circ$, that is, for levels outside the disc-plane, the sound pressure levels are corrected to:

$$\text{SPL}_m (r/D, \psi) = \text{SPL}_m (r/D, 0^\circ) + \Delta L^{(3)}_{mB, \psi}, \quad \text{dB} \quad (83)$$

where $\Delta L^{(3)}_{mB, \psi}$ is obtained from Figure 76 for the appropriate values of ℓ (instead of mB) found in step 2, and for angle ψ .

- (6) For structural surface sound pressure levels, add 6 dB to each value if surface is flat, or 3 dB for curved surfaces. (See step 8 in part 1(b) of this section.
- (7) For field points at $1.0 < r/D < 3.0$, estimate the levels by step 9 in part 2(a) of this section.

SECTION VII CONCLUSIONS

Propulsion systems for VTOL aircraft have been grouped into the two broad categories of jet-type and propeller-type propulsion systems and, for each type, methods have been defined for predicting near field noise levels on the aircraft structure.

1. PREDICTION METHODS FOR JET-TYPE PROPULSION SYSTEMS

The prediction method developed for VTOL jets is supported by a review of the basic flow structure of free and deflected (wall) jets, along with an analysis of potential noise sources for the latter. The dominant sources in the near field were found to be, in approximate order of importance,

- Ground-reflected noise from the near field noise of the undeflected jet.
- Jet noise from the radially deflected flow of the wall jet formed by the engine exhaust.
- Noise of the impinging jet exhaust.
- Direct radiation by the undeflected jet.

Other potential sources of noise, such as vortex noise generated by turning vanes in a VTOL jet nozzle, shock-turbulence noise for a supersonic VTOL jet, or discrete ring tones from a VTOL jet close to the ground were found to be insignificant or not representative of sources expected in full scale VTOL jets.

Due, primarily, to the complexity of the resulting near field noise of a VTOL jet, classical prediction methods or semi-empirical methods based on a piece-wise construction of the noise field from its separate distributed sources was not considered feasible or desirable for this first-generation prediction method. The Δ method, was therefore developed which corrects the near noise field for a free undeflected jet by a factor which accounts for the observed change in near field levels for a VTOL jet relative to a free jet. The Δ correction term was found to vary primarily with frequency and nozzle elevation. The maximum value of Δ occurred for nozzle elevations comparable to the location of the source in a free jet. The correction term did not vary substantially over space in the near field region forward of the VTOL jet exit.

Comparison of predicted near field levels and limited measurements on a full scale VTOL aircraft showed very satisfactory agreement.

2. PREDICTION METHODS FOR PROPELLER-TYPE PROPULSION SYSTEMS

The method for prediction of near field sound pressures of rotating-blade systems has been derived by a combination of empirical collapse of experimental data and classical theory. It was found that the sound pressures in the rotor plane were not accurately predicted by rotating point force theory, but agreement between estimated and measured levels at angles greater than 15 degrees from the rotor plane was satisfactory. The in-plane levels were found to collapse well on a parametric basis of thrust level per disc area per blade, and this dependency provides the in-plane absolute level for the prediction approach. Harmonic roll-off rates and the maximum levels at out-of-plane angles have been derived from the experimental data. Directivity patterns have been developed from the rotating point force theory and referenced to the maximum level at ± 15 degrees from the rotor plane.

Corrections to the above method have been derived for the estimation of ducted fan noise levels. These corrections include rotor-stator interaction effects and duct dispersive attenuation effects. Good agreement was obtained with measured blade passage tone levels of a tip-turbine lift fan.

The prediction methods developed in this report were supported by unique experimental data on propeller noise and VTOL jet noise summarized in Appendices B and C respectively. Correction factors for ground reflection of noise from a point source are tabulated in Appendix D, along with the corresponding computer program listing.

REFERENCES

1. vonGierke, H.E., "Aircraft Noise Sources," Chapter 23, Handbook of Noise Control, C.M. Harris, ed., McGraw-Hill Book Co., N.Y. (1957).
2. Lawrence, J.C., "Intensity, Scale and Spectra of Turbulence in Mixing Region of Free Subsonic Jets," NACA Report 1292 (1956).
3. Lighthill, M.J., "Jet Noise," AIAA Journal 1:1507-1517 (1963).
4. Morgan, W.V., Sutherland, L.C., Young, K.J., "The Use of Acoustic Scale Models for Investigating Near Field Noise of Jet and Rocket Engines," WADD Tech. Report 61-178, April 1961, AD 268 576.
5. Lockheed-Georgia Co., Lockheed Aircraft Corp., "XV-4B Acoustic Sonic Fatigue and Vibration Final Report." Report No. ER-10073, February 1969.
6. Hunt, F.V., "Velocity-Strain Ratio for Vibrating Elastic Bodies." J. Acoust. Soc. Amer. 32, 1123-1128 (1960).
7. Beranek, L.L., "Airplane Quieting II - Specification of Acceptable Noise Levels," Trans. Am. Soc. Mech. Eng. 69:97 (1947).
8. Glauert, M.B., "The Wall Jet," J. Fluid Mech. 1, 625-643 (1956).
9. Skifstad, J.G., "Aerodynamics of Jets Pertinent to VTOL Aircraft," U.S. Air Force Aero Propulsion Laboratory Report, AFAPL-TR-69-28, March 1969, AD 853 494.
10. Hodgson, T.H., "Pressure Fluctuations in Shear Flow Turbulence," College of Aeronautics Note 129, Cranfield, England.
11. Lyon, R.H., et al, "Aerodynamic Noise Simulation in Sonic Fatigue Facility," U.S. Air Force Flight Dynamics Laboratory Report AFFDL-TR-66-112, November 1966.
12. Strong, D.R., Siddon, T.E. and Chu, W.T., "Pressure Fluctuations on a Flat Plate with Oblique Jet Impingement," University of Toronto Institute of Aerospace, Tech. Note 107, February 1967.
13. Schlichting, H., "Boundary Layer Theory," Translated by J. Kestin, McGraw-Hill Book Co., Inc., N.Y., pp 592-596 (1960).

Contrails

14. Maestrello, L. and McDaid, E., "Acoustic Characteristics of a High Subsonic Jet," AIAA 8th Aerospace Sciences Meeting, Paper No. 70-234, January 1970.
15. Eldred, K.M., et al, "Suppression of Jet Noise with Emphasis on the Near Field," ASD-TDR-62-578, February 1963.
16. Ollerhead, J.B., "On the Prediction of the Near Field Noise of Supersonic Jets," NASA CR-857, August 1967.
17. Anderson, A.R. and Johns, F.R., "Nondimensional Characteristics of Free and Deflected Supersonic Jets Exhausting into Quiescent Air," Report NADC-ED-5401 (1954).
18. Potter, R.C. and Crocker, M.J., "Acoustic Prediction Methods for Rocket Engines, Including the Effects of Clustered Engines and Deflected Exhaust Flow," NASA CR-566, October 1966.
19. Ames Research Staff, "Equations, Tables and Charts for Compressible Flows," NACA Report 1135 (1953).
20. Sutherland, L.C., "Future Trends in Acoustic Environments of Manned Space Vehicles," Paper presented before Acoustical Society of America, San Francisco, October 1960.
21. Potter, R.C., "An Investigation to Locate the Acoustic Sources in a High Speed Jet Exhaust Stream," Wyle Laboratories Report WR 68-4 (1968).
22. Johanneson, N.H., "The Mixing of Free Axially Symmetrical Jets of Mach Number 1.40," British A.R.C. 18, 967, January 1967.
23. Nagamatsu, H.T. and Horvay, G., "Supersonic Jet Noise," AIAA Paper No. 70-237, presented before 8th Aerospace Sciences Meeting, N.Y., January 1970.
24. Eggers, J.M., "Velocity Profiles and Eddy Viscosity Distributions Downstream of a Mach 2.22 Nozzle Exhausting into Quiescent Air," NASA TN D3601, September 1966.
25. Lighthill, M.J., "Sound Generated Aerodynamically," The Bakerian Lecture, 1961, Proc. Roy. Soc. (London) A267, 157-182 (1962).
26. Lilley, G.M., "On the Noise From Air Jets," Aeronautical Research Council, 20, 376, N. 40-F.M. 2724, September 1958.

Contrails

27. Ffowcs Williams, J.E., "The Noise from Turbulence Convected at High Speed," Trans. Roy. Phil. Soc. (London) A255, 469-503 (1963).
28. Ribner, H.S., "The Generation of Sound by Turbulent Jets," Adv. Appl. Mech. 8, 104-178, Academic Press, Inc., N.Y. (1964).
29. Pao, S.P., "A Generalized Theory on Noise Radiated by Supersonic Turbulent Shear Layers," Wyle Laboratories Report WR 70-1, February 1970.
30. Ribner, H.S., "On the Strength Distribution of Noise Sources Along a Jet," UTIAS Report No. 51, April 1958.
31. Powell, A., "Similarity and Turbulent Jet Noise," J. Acous. Soc. Amer. 31, 812-813 (1959).
32. Franken, P.A., et al, "Methods of Flight Vehicle Noise Prediction," WADC Tech. Report 58-343, November 1958.
33. Howes, W.L., "Similarity of Near Noise Fields of Subsonic Jets," NASA TR-R-94 (1961).
34. Morgan, W.V. and Young, K.J., "Studies of Rocket Noise Simulation with Substitute Gas Jets and the Effect of Vehicle Motion on Jet Noise," ASD TDR 62-787, March 1963.
35. Simcox, C.D. and Grande, E., The Boeing Company, personal communication, July 1971.
36. Hermes, P.H. and Smith, D.L., "Measurement and Analysis of the J57-P21 Noise Field," AFFDL-TR-66-147, November 1966, AD 403 713.
37. Oas, Stanley, "The Acoustic Near Field of a Model Air Jet Simulating Vertical Takeoff," Boeing Co. Document No. D2-2463 (1958).
38. Cole, J.N., England, R.T., and Powell, R.G., "Effects of Various Exhaust Blast Deflectors on the Acoustic Noise Characteristics of 1,000-Pound-Thrust Rockets," WADD Tech. Report 60-6, September 1960.
39. Marsh, A., "Noise Measurements Around a Subsonic Air Jet Impinging on a Plane, Rigid Surface," J. Acous. Soc. Amer., 33, 8, August 1961.
40. Plumlee, H.E., et al, "Near Field Noise Analysis of Aircraft Propulsion Systems with Emphasis on Prediction Techniques for Jets," AFFDL TR 67-43, August 1967.

Contrails

41. Potter, R.C. and Ollerhead, J.B., Wyle Laboratories, Unpublished data (1968).
42. Flemming, M. and Scholten, R., "Noise Problems of VTOL with Particular Reference to the Dornier DO 31," The Aeronautical Journal of the Royal Aeronautical Society, Vol. 73, pp 647-653.
43. Smith, D.L. and McFarland, S.L., Jr., "The Acoustic Environment of a Deflected-Jet VTOL Aircraft," WPAFB TM-70-1-FYA, September 1970.
44. Waterhouse, R.V. and Berendt, R.D., "Reverberation Chamber Study of the Sound Power Output of Subsonic Air Jets," J. Acous. Soc. Amer., 30, pp 114-121 (1958).
45. Eldred, K.M., "Review of Noise Generation of Rockets and Jets," J. Acous. Soc. Amer., 32, 1502(A), (1960).
46. Howes, W.L., "Similarity of Far Field Noise of Jets," NASA TR-R-52 (1960).
47. Lassiter, L.W., and Hubbard, H.H., "Experimental Studies of Noise from Subsonic Jets in Still Air," NACA TN-2757, August 1952.
48. Plumlee, H.E., et al, "Effect of Jet Temperature on Jet and Pure Tone Noise Radiation," NASA CR-1472, November 1969.
49. Society of Automotive Engineers, Aerospace Information Report (AIR) 876, "Jet Noise Prediction," July 1965.
50. Grande, E., "Refraction of Sound by Jet Flow and Jet Temperature; Extension of Temperature Range Parameters and Development of Theory," NASA CR-840, August 1967, also UTIAS Tech. Note No. 110 (1966).
51. Ffowcs Williams, J.E., "Jet Noise at Very Low and Very High Speed," AFOSR-UTIAS Symposium on Aerodynamic Noise, Toronto, Canada, May 1968.
52. Cole, J.N., et al, "Noise Radiation from Fourteen Types of Rockets in the 1000 to 130,000 Pounds Thrust Range," WADC Aero Medical Lab, TR 57-354, December 1957.
53. Franken, P.A., "A Theoretical Analysis of the Field of a Random Noise Source Above an Infinite Plane," NACA TN-3557, November 1955.
54. Howes, W.L., "Ground Reflection of Jet Noise," NASA TR-R-35 (1959).

Contrails

55. Ingard, K.V., and Lamb, C.I., "The Effect of a Reflecting Plane on the Power Output of Sound Sources," J. Acous. Soc. Amer., 29, pp 743-744, June 1951.
56. Bies, D.A., "Effect of a Reflecting Plane on an Arbitrarily Oriented Multipole," J. Acous. Soc. Amer., 33, pp 286-288, March 1961.
57. Ribner, H.S., "Reflection, Transmission and Amplification of Sound by a Moving Medium," J. Acous. Soc. Amer., 29, pp 435-441, April 1957.
58. Wareing, J.T., "Increasing V/STOL Aircraft Size Increases Downwash Severity," SAE Journal, 77:pp 56-57, April 1969.
59. Curle, N.J., "The Influence of Solid Boundaries Upon Aerodynamic Sound," Proc. Roy. Soc. A, 231, 505-514 (1955).
60. Richards, E.J., and Mead, D.J. (ed) "Noise and Acoustic Fatigue in Aeronautics," John Wiley and Sons, Ltd., London (1968).
61. Powell, A., "Vortex Action in Edge Tones," J. Acous. Soc. Amer., 34, 163, (1962).
62. Powell, A., "Noise of Choked Jets," J. Acous. Soc. Amer., 25, 385, (1953).
63. Ribner, H.S., "Acoustic Energy Flux from Shock-Turbulence Interaction," UTIAS Tech. Note 108, July 1967.
64. Franken, P.A., et al, "Methods of Space Vehicle Noise Prediction," WADC Tech. Report 58-343, Vol. II, September 1960.
65. Sutherland, L.C., (ed), "Sonic and Vibration Environments for Ground Facilities - A Design Manual," Wyle Laboratories Research Staff Report WR 68-2, March 1968.
66. Smith, D.L., Air Force Flight Dynamics Laboratory, (personal communication), (1970).
67. Gutin, L., "On the Sound Field of a Rotating Propeller," Physiks Zeitschrift der Sowjetunion Band A Heft 1 (1936) pp 57-71. Translated as National Advisory Committee for Aeronautics TM 1195, October 1948.
68. Lawson, M.V. and Ollerhead, J.B., "Studies of Helicopter Rotor Noise," USA-AVLABS TR68-60 (1968).

69. Lawson, M.V., "The Sound Field for Singularities in Motion," Proceedings of the Royal Society of London, Vol. 286, Series A, pp 559-572 (1965).
70. Garrick, I.E. and Watkins, C.E., "A Theoretical Study of the Effect of Forward Speed and Free-Space Sound Pressure Field Around Propellers," National Advisory Committee for Aeronautics, Report 1198 (1954).
71. Yudin, E.Y., "On the Vortex Sound from Rotating Rods," Zhurnal Tekhnicheskoi Fiziki, Vol. 14, No. 9 p 561, 1944. Translated as National Advisory Committee for Aeronautics TM 1136, March 1947.
72. Hubbard, H.H., "Propeller Noise Charts for Transport Airplanes," NACA TN 2968, June 1953.
73. Hubbard, H.H. and Regier, A.A., "Free-Space Oscillating Pressures Near the Tips of Rotating Propellers," NACA Report 996 (1950).
74. Brown, D. and Ollerhead, J.B., "Propeller Noise at Low Tip Speeds," AFAPL-TR-71-55, September 1971.
75. Marte, Jack E. and Kurtz, D.W., "A Review of Aerodynamic Noise from Propeller Rotors and Lift Fans," JPL Tech. Report 32-1462 (1970).
76. Hubbard, H.H. and Lassiter, L.W., "Oscillating Pressures Near a Static Pusher Propeller at Tip Mach Numbers up to 1.20 with Special Reference to the Effects of the Presence of the Wing," NACA TN-3202, July 1954.
77. Vogeley, A.W. and Kurbjun, M.C., "Measurements of Free-Space Oscillating Pressures Near a Propeller at Flight Mach Numbers to 0.72," NACA TN-3417, May 1965.
78. Kurbjun, M.C., "Effects of Blade Plan Form on Free-Space Oscillating Pressures Near Propellers at Flight Mach Numbers to 0.72," National Advisory Committee for Aeronautics, TN-4068, August 1957.
79. Waite, W., "Turbo-prop Noise Tests," Unpublished Boeing Company data, March 1954.
80. Tyler, J.M. and Sofrin, T.B., "Axial Flow Compressor Noise Studies," SAE Transactions, pp 309-332 (1961).
81. Morfey, C.L., "Rotating Pressure Patterns in Ducts: Their Generation and Transmission," J. Sound and Vibration, Vol. 1, No. 1, pp 60-87, January 1964.

Contrails

82. Morfey, C.L., "A Review of the Sound-Generating Mechanisms in Aircraft-Engine Fans and Compressors." Paper presented at AFOSR-UTIAS Symposium on Aerodynamic Noise, Toronto, May 1968.
83. Rice, E.J., "Attenuation of Sound in Soft Walled Circular Ducts." Paper presented at AFOSR-UTIAS Symposium on Aerodynamic Noise, Toronto, May 1968.
84. Brown, D., "Investigation of the Influence of Duct-Mounted Helmholtz Resonators on the Sound Field of a Model Ducted Propeller," NASA CR-1653, September 1970.
85. Lawson, M.V., "Theoretical Studies of Compressor Noise," NASA CR-1287 (1969).
86. Ollerhead, J.B. and Munch, C.L., "An Application of Theory to Compressor Noise," NASA CR-1519 (1970).
87. Smith, M.J.T. and House, M.E., "Internally Generated Noise from Gas Turbine Engines, Measurement and Prediction," Trans. ASME, J. Engr. for Power April 1967, pp 177-190. Paper presented at Gas Turbine Conference (Zurich, Switzerland), ASME 66-GT/N-43, March 1966.
88. Bishop, D.E. and Horonjeff, R.D., "Procedures for Developing Noise Exposure Forecast Areas for Aircraft Flight Operations," FAA-DS-67-10, Federal Aviation Administration, August 1967.
89. McPike, A.L., "Community Noise Levels of the DC-10 Aircraft," presented at 12th Anglo-American Aeronautical Conference, Calgary, Alberta, Canada, July 1971. Douglas Paper 5957, Douglas Aircraft Company.
90. Russell, R.E. and Kester, J.D., "Aircraft Noise. Its Source and Reduction," Society of Automotive Engineers - Department of Transportation Conference on Aircraft and the Environment, Washington, D.C., February 8-10, 1971.
91. Kramer, J.J., "The NASA Quiet Engine," NASA TM-X-67884, National Aeronautics and Space Administration, September 1971.
92. "NASA Acoustically Treated Nacelle Program," NASA SP-220, National Aeronautics and Space Administration, September 1971.
93. Holmes, D.R. and Cox, C.R., "Noise Reduction Possibilities for a Light Helicopter," SAE National Aeronautic and Space Engineering and Manufacturing Meeting, Los Angeles, California, October 6-10, 1969.

94. Duke, F.H. and Hooper, W.E., "The Boeing Model 347 Advanced Technology Helicopter Program," 27th Annual National V/STOL Forum of the American Helicopter Society, Washington, D.C., May 1971.
95. Eldred, K.M., et al, "Far Field Noise Generation by Coaxial Flow Jet Exhausts," Contract No. FA68WA-1889, Federal Aviation Administration Report No. FAA-RD-71-101,I and II, November 1971.

APPENDIX A

SUMMARY OF REPRESENTATIVE VTOL AIRCRAFT⁽¹⁾
(CURRENT OR PROPOSED)⁽²⁾

Manufacturer	Model	Type	Weight		Propulsion				Approximate Dimensions		
			Maximum Takeoff K lb	Empty K lb	Takeoff Engines		Cruise Engines		Wing Span feet	Length feet	Height feet
					Number	Thrust ⁽⁴⁾ K lb	Number	Thrust ⁽⁴⁾ K lb			
JET											
Bell	X-14A		3.3	3.2	2	5.36	-	-	35.8	26	10.7
Dessault	Mirage III-V				8	35.2	1	11.7-20.5			
Domier	DO 31-E DO 231 C,D		60.5	~55	8 12	35.2 120+	2	31.0	59	65.2	28.5
Hawker-Siddeley	Harrier GR MK-1		<22	12.2	1	19.0	-	-	29	50±5	12
Lockheed	XV-4B	Fan in Wing	12.8	8.5	4	<12.0	2	<6.0	27.1	34	12.5
Ryan	XV-5B		2	5.36							
VFW-Fokker	VAK 191B		2	11.15	1	9.92	20	53.5	14		
					Propeller						
					Number	SHP	Blades	Diameter			
PROP											
Bell	X-22A	Tilting Duct	18.0	(16)	2	5000	4	7'	39	3.96	20.7
Canadair	CL-84-1	Tilt Wing	12.6	8.8	2	3000	2	14'	33.3	47.2	14.1
Lockheed	XH-51A	Compound Rotor and Jet	4.1	2.8	1	500 ⁽³⁾	1	35'	-	40.7	8.2
LTV	XC-142A	Tilt Wing	31.8		4	15.5					
Nord	500	Shrouded Prop			2	634		23'	62.7	73.6	25.3
VFW-Fokker	VC 400		61.7		4	2100	3				

(1) Aviation Week and Space Technology, March 8, 1971.

(2) Excluding Helicopters.

(3) Also 2600 lb Thrust Jet.

(4) Total Static Thrust for all Engines.

APPENDIX B

PROPELLER NEAR FIELD NOISE EXPERIMENTS

B.1 INTRODUCTION

Early in the course of this program, it became obvious that very little comprehensive near field acoustic data pertaining to propellers, rotors or fans existed in the literature. In order to obtain near field noise data under controlled conditions, a limited experimental study was conducted of the near field noise of two 9-inch diameter model propellers in a semi-anechoic facility. This study was limited to obtaining rotational harmonic noise data for a model propeller operating at various tip speeds and with different numbers of blades. Two-blade and three-blade tractor-type propellers were used for the study, providing data at tip speeds in the range of $0.2 \leq M_t \leq 0.5$.

B.2 TEST FACILITIES

The model tests were conducted in a semi-anechoic chamber (7 ft x 8 ft x 9 ft) which was free of reflections for frequencies down to approximately 250 Hz. The propeller was mounted on the end of a shaft which was driven by an electric motor mounted outside of the chamber. To support the shaft, which was approximately four feet long, a high-speed bearing was mounted on a support approximately 2.5 propeller diameters behind the propeller. This support, as well as other reflective surfaces in the room, were covered with a two-inch layer of grade AA fiberglass blanket. Figure B-1 illustrates the installation details.

A microphone was positioned at a given radial point on a boom and the boom was driven azimuthally by a 1-rpm reversible motor. The design of this boom system and its location in the test chamber was based on the requirements for minimum interference with the aerodynamic and acoustic fields in close proximity to the propeller.

The instrumentation system employed is schematically illustrated in Figure B-2. Since the primary intent of this study was to examine the variation of the rotational harmonics with radial and azimuthal position, an X-Y plotter was used to plot the sound pressure level against azimuth angle at given radii from the hub. A 1/3-octave filter set was used to separate the individual harmonics of rotational noise. A narrower band filter (1% bandwidth) was first tried in order to obtain greater resolution of harmonics, but was rejected because small motor speed variations due to line voltage fluctuations caused large fluctuations of the measured level in the 1% bandwidth. A graphic level recorder/analog voltage readout device was used as a high slew-speed, true-rms log converter to drive the Y-axis input of the X-Y recorder.

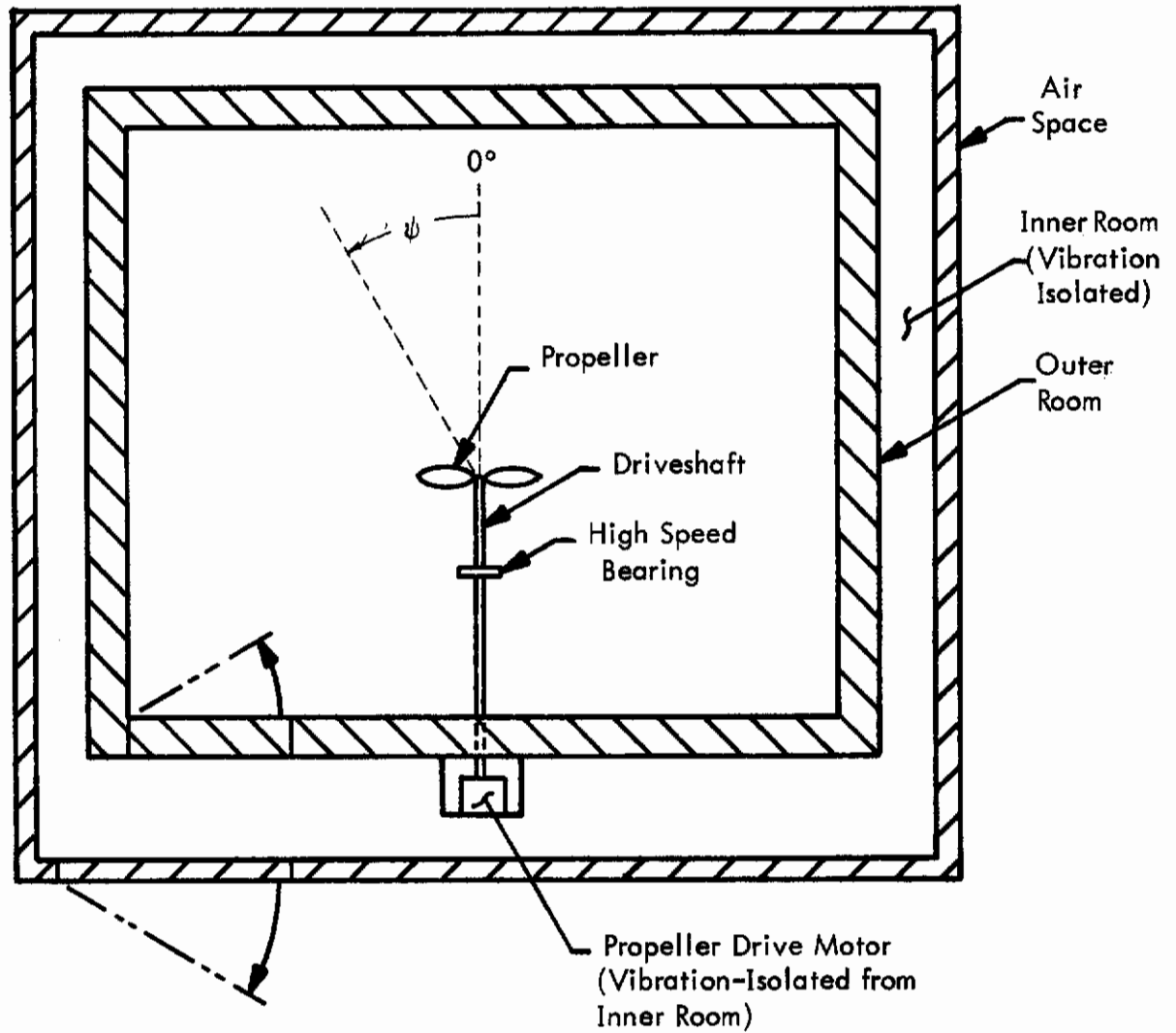


Figure B-1. Model Propeller Installation (Top View)

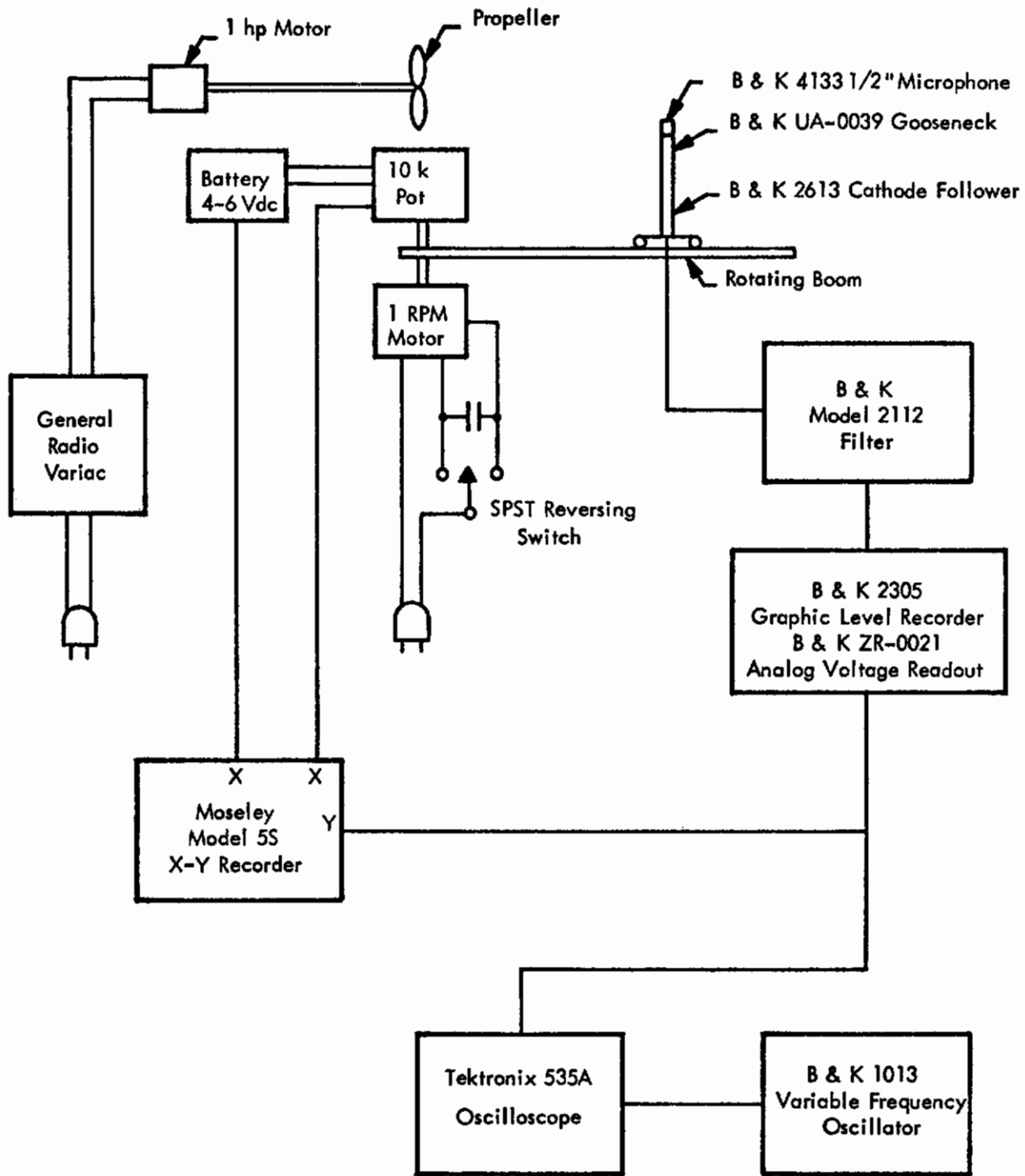


Figure B-2. Model Study Instrumentation

The X-axis drive was obtained from a linear-taper potentiometer (rotated by the microphone boom) which provided an output voltage to the X-Y recorder proportional to the azimuth location of the microphone. The propeller speed was determined by comparing the fundamental rotational frequency with an oscillator tone by means of Lissajous patterns on the oscilloscope.

B.3 TEST PROCEDURES

Each test operation and sound measurement was controlled from outside of the test chamber. Periodic checks, both of the microphone and of the azimuth position indication, were made to insure overall system calibration. For each propeller, the microphone was set at a specified radius from the propeller hub center and swept from 0° to approximately 160° at the rate of 6° per second. The 1/3-octave filter was first set at the band containing the fundamental blade passage frequency, and then at each successive harmonic, for each sweep of the microphone boom. This procedure provided the levels of the first four or five harmonics as a function of position around the propeller. The number of harmonics which could be accurately plotted was, of course, limited by the filter bandwidth — that is, the highest harmonic plotted was that which solely occupied a 1/3-octave pass band. This procedure was followed for each propeller, tip speed setting and microphone radius.

The thrust developed at each test condition was determined by a total-head wake pressure survey. The radial distribution of the total pressure rise immediately behind the propeller disc was measured by means of a total-head tube and manometer, and the incremental thrust calculated by

$$dT = 2\pi r (\Delta H) dr$$

where $2\pi r dr$ is an elemental annulus area and ΔH is the total pressure rise over the annulus element.

The operating propeller torque was initially estimated from these thrust values by calculation of the induced velocities and corresponding induced drag. These estimates were later verified by means of a torque balance, incorporated in the experimental assembly.

B.4 TEST RESULTS

Figures B-3 through B-8 show the on-line plotted measurements of the propeller near field sound pressure levels, as obtained for each of the first few harmonics of the blade passage frequency by azimuthal sweeps of the boom microphone. Figures B-3 through B-6 were obtained with a two-blade model, and correspond to measurement radii of 0.555, 0.667, 0.83 and 1.0 propeller diameters, respectively. Figures B-7 and B-8 show data obtained with a three-blade model, at measurement radii of 0.55 and 0.677

Contrails

propeller diameters respectively. Each figure contains data for a range of blade tip speeds. Thrust and absorbed-horsepower values corresponding to each of these test conditions are tabulated in Table IV in Section IV.

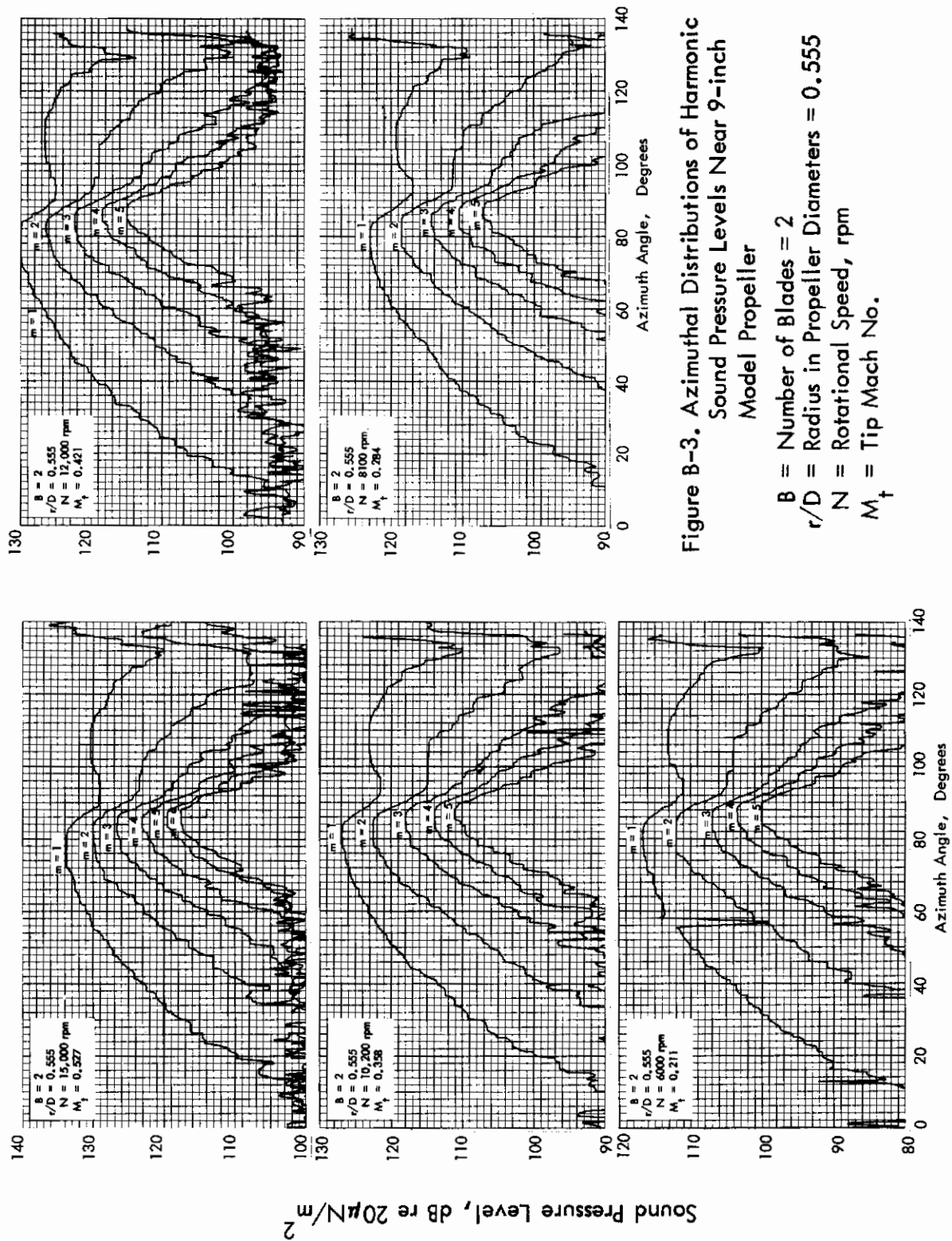


Figure B-3. Azimuthal Distributions of Harmonic Sound Pressure Levels Near 9-inch Model Propeller

B = Number of Blades = 2
 r/D = Radius in Propeller Diameters = 0.555
 N = Rotational Speed, rpm
 M_t = Tip Mach No.

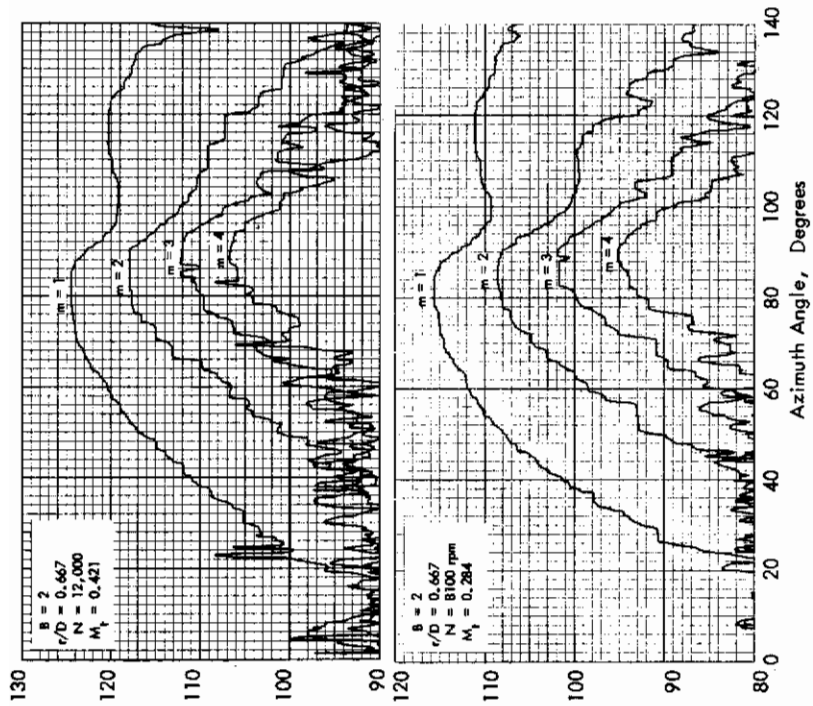
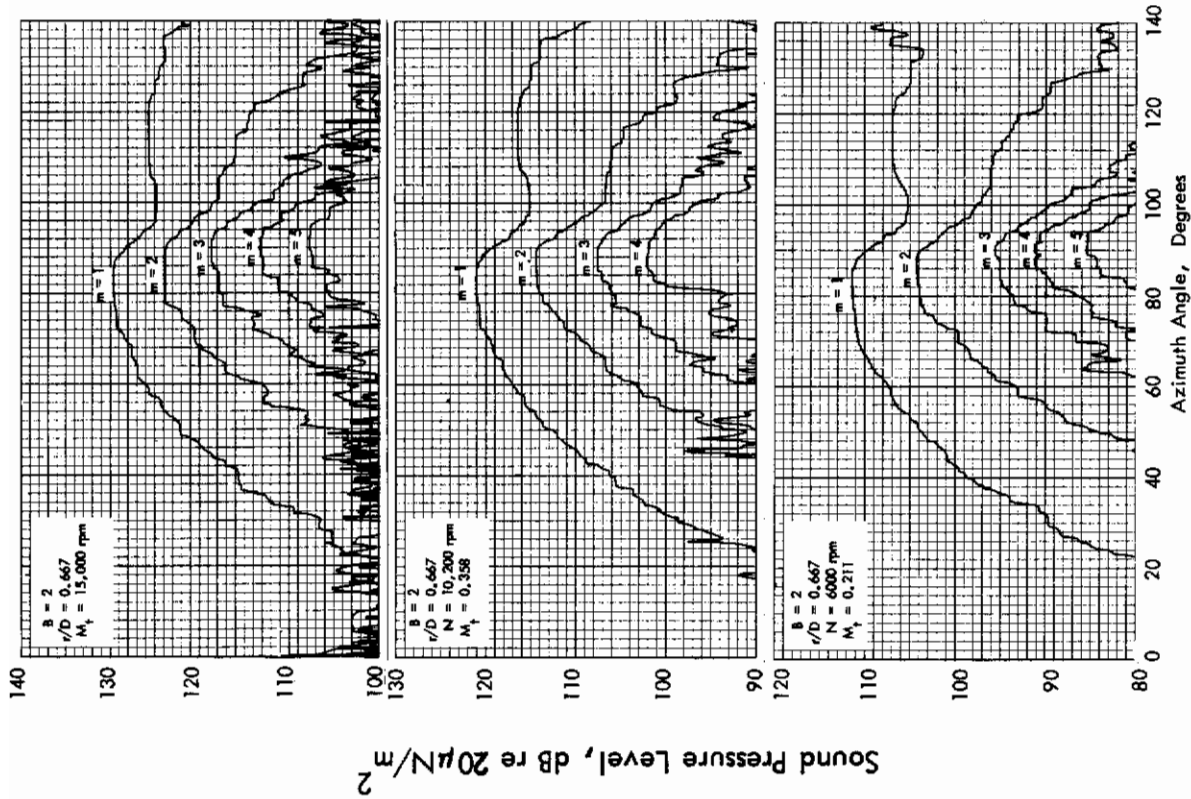


Figure B-4. Azimuthal Distributions of Harmonic Sound Pressure Levels Near 9-inch Model Propeller

$$B = 2$$

$$r/D = 0.667$$



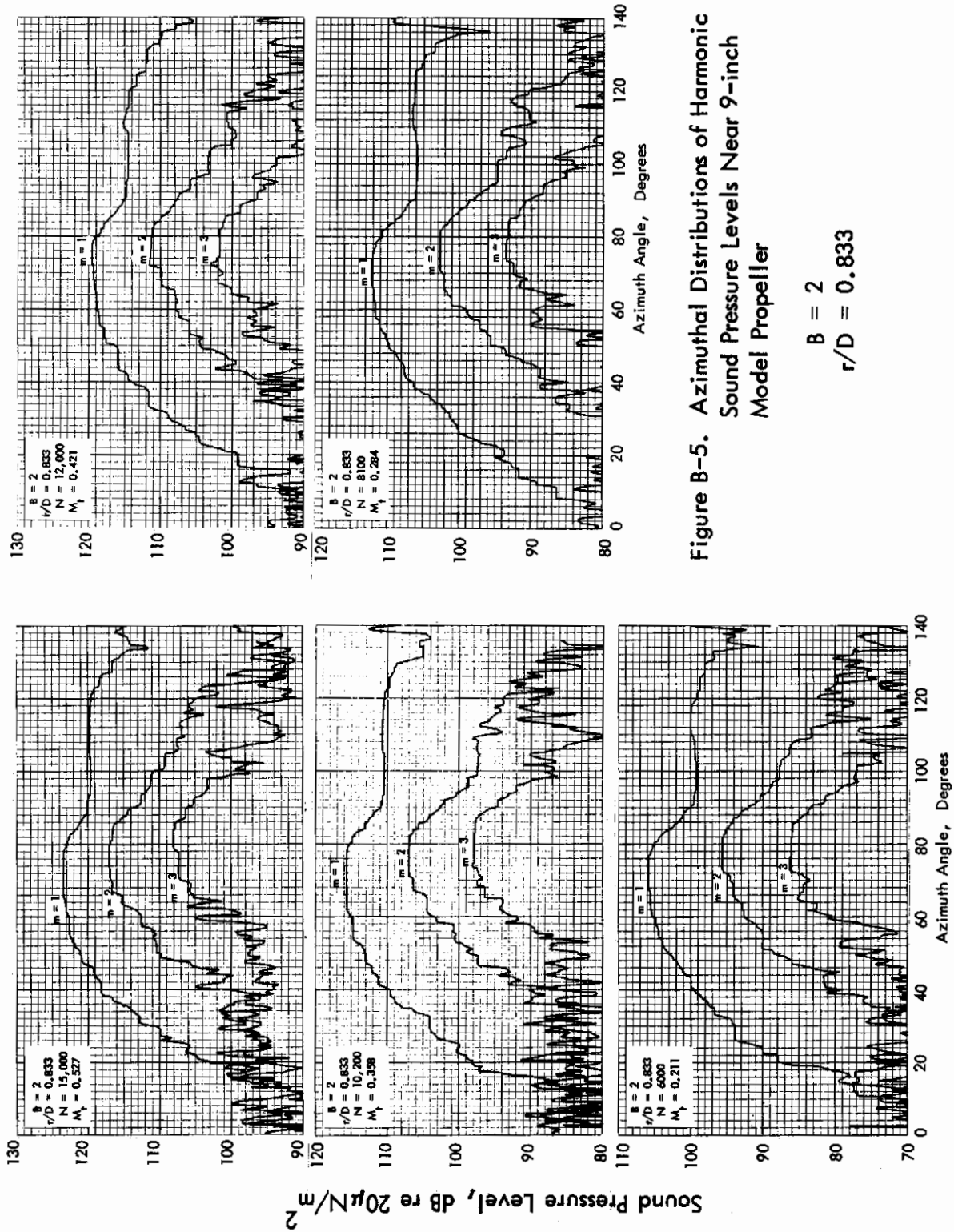


Figure B-5. Azimuthal Distributions of Harmonic Sound Pressure Levels Near 9-inch Model Propeller

$$B/D = 2$$

$$r/D = 0.833$$

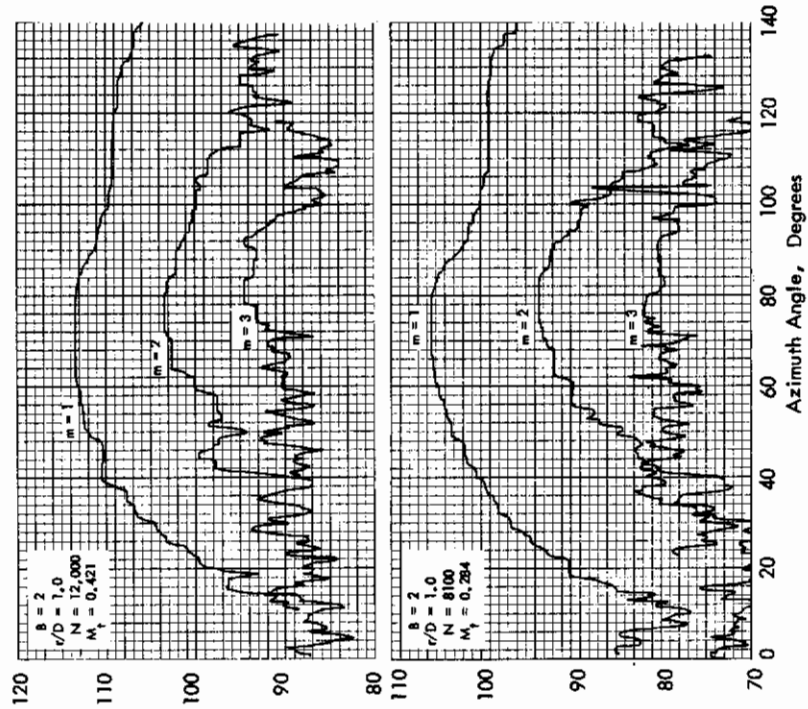
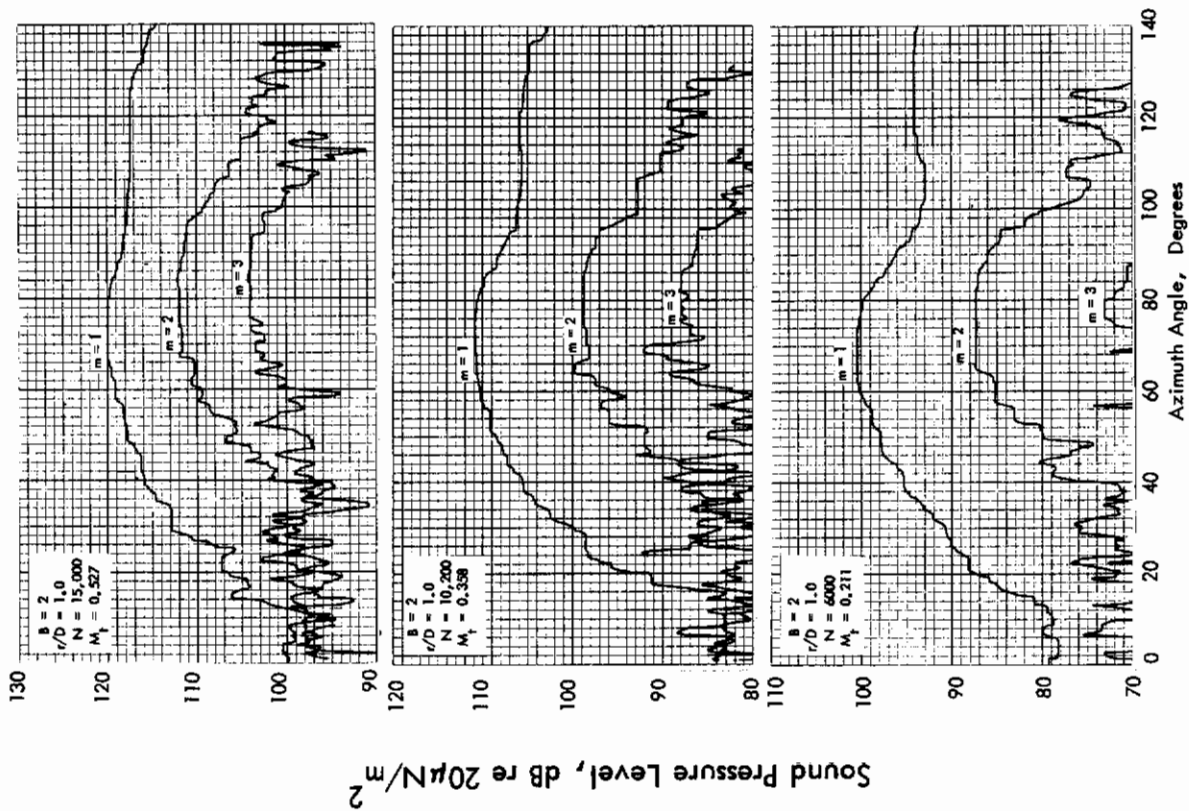


Figure B-6. Azimuthal Distributions of Harmonic Sound Pressure Levels Near 9-inch Model Propeller

$B = 2$
 $r/D = 1$



Sound Pressure Level, db re $20 \mu N/m^2$

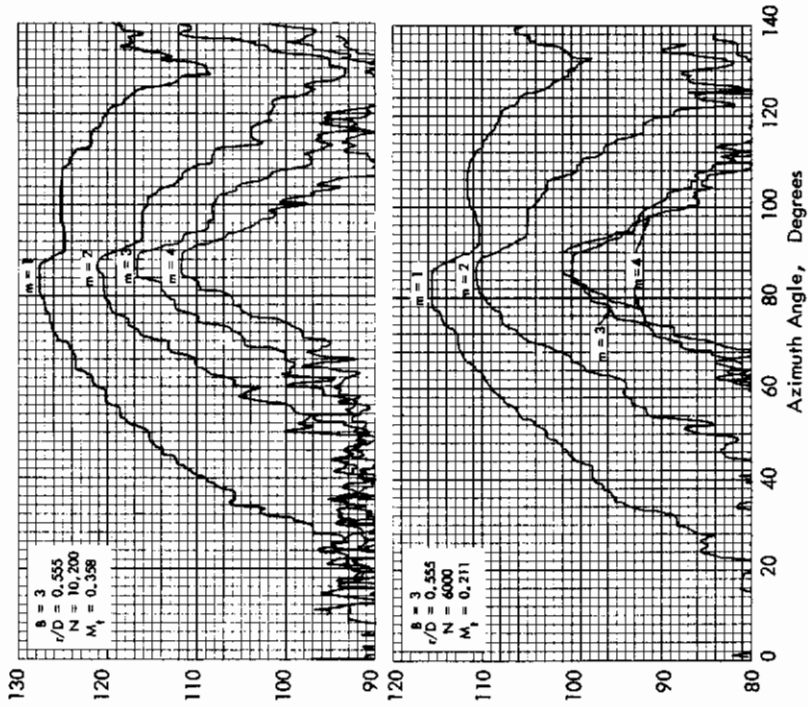
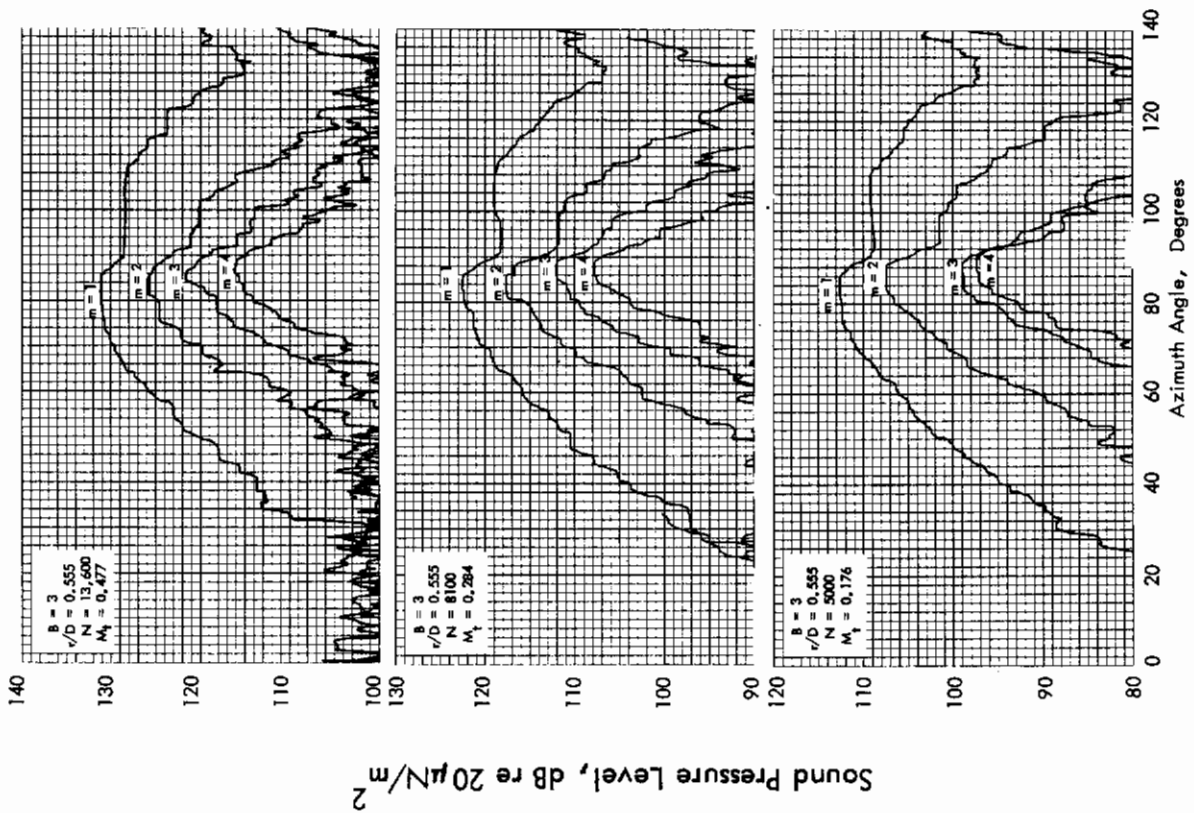


Figure B-7. Azimuthal Distributions of Harmonic Sound Pressure Levels Near 9-inch Model Propeller

$B = 3$
 $r/D = 0.555$



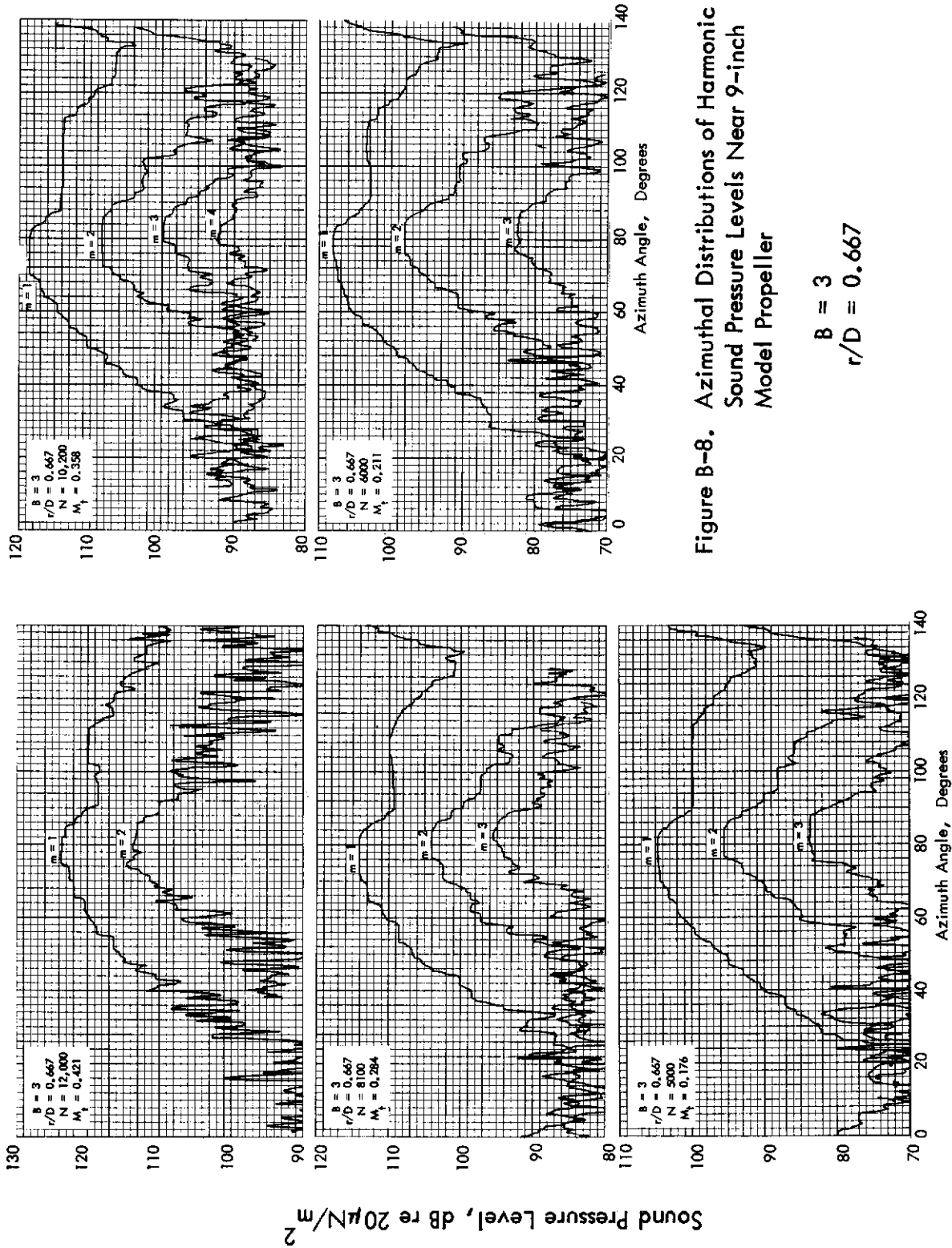


Figure B-8. Azimuthal Distributions of Harmonic Sound Pressure Levels Near 9-inch Model Propeller

$$B = 3$$

$$r/D = 0.667$$

APPENDIX C

SUMMARY OF EXPERIMENTAL STUDY OF MEAN FLOW PROPERTIES
AND NOISE GENERATION BY SIMULATED VTOL JET

C.1 INTRODUCTION

An experimental model jet program was conducted to support the development of near field noise prediction methods for jet-powered VTOL aircraft. The experimental effort consisted of a brief study of the mean flow properties of a simulated VTOL jet and an extensive series of acoustic measurements in the near field of a horizontal free jet and the same jet directed against a ground plane. Major findings from these experiments are summarized in this Appendix.

C.2 MEAN FLOW MEASUREMENTS

a. Test Facilities

Mean flow velocity and velocity profile measurements were made on an ambient subsonic air jet exhausting through a 0.625-inch diameter nozzle at a maximum exit velocity of 207 ft/sec. The internal diameter of 0.625 inches was constant for a distance of 0.25 inches upstream of the exit plane, then flared gradually within 1.25 inches into a 1.25-inch diameter supply plenum. The outside diameter of the nozzle was 0.69 inches at the exit plane and increased abruptly to a 1.81-inch flange diameter at 0.5 inches upstream of the exit plane. A pitot tube with an outside diameter of 0.0625 inches connected to a water manometer was used to determine the velocity pressure (q). The velocity (U) was computed from the incompressible flow expression $q = 1/2 \rho U^2$ with ρ assumed constant at 0.0022 lb/sec²/ft⁴ at the exit temperature of 100°F.

For vertical positions of the jet, used to simulate VTOL operation, the nozzle assembly was mounted to a lead screw mechanism allowing precision control of vertical height above a ground plane. The ground plane consisted of a polished aluminum sheet firmly supported by a rigid table.

Except at the lowest velocities, the estimated overall accuracy of the measurements is ± 5 percent.

b. Results for Velocity Decay Measurements

The decay in maximum centerline or axial velocity of the free jet is shown by the upper line in Figure C-1. The axial velocity was constant out to a distance of

approximately 4 nozzle diameters. This agrees closely with the expected length of the potential core for an exit Mach number of 0.18 (see Figure 9 in Section III). Beyond an axial distance (X) of about 7 nozzle diameters, the axial velocity decay varies as $1/X$ as expected.

A simple empirical expression which very closely approximates this velocity decay at all axial positions is given by

$$U_c = U_e \left[1 + \left(\frac{X}{1.5X_t} \right)^6 \right]^{-1/6} \quad (C.1)$$

where

U_e = exit velocity of jet

X = axial position

X_t = length of potential core (see part 2 of Section III)

The axial velocity for the free jet, predicted by this expression, is also shown in Figure C-1. For the simulated VTOL condition, the maximum radial velocity in the wall jet was determined over a radial distance from 0.5 to 10 nozzle diameters for nozzle exit heights from 0.5 to 8 diameters above the ground plane. The results are shown by the lower line in Figure C-1. Out to a radial distance of about 1 to 1.5 nozzle diameters, and for nozzle elevations equal or greater than 1 diameter, the radial velocity was very nearly equal to the axial velocity (U_c) of the free jet at an axial distance (X/D) equal to the nozzle elevation (H/D) of the VTOL jet. At the lowest nozzle elevation ($H/D = 0.5$), the radial velocity close to the impingement point was about 12 percent higher than the nozzle exit velocity of the free jet.

At radial distances greater than about 3 nozzle diameters, the maximum velocity decayed approximately as $1/R^{1.3}$ for all nozzle heights. The velocity decay exponent was based on fitting the data by eye with a straight line and is considered a representative value within about ± 0.1 for the jet velocity and nozzle elevation range investigated.

c. Results for Velocity Profile Measurements

Velocity profile measurements were made at 2.5, 5, 10 and 20 nozzle diameters downstream for the free jet and at radii of 1, 3 and 6 diameters for the deflected (wall) jet at a nozzle height of 4 diameters. The results are shown in Figure C-2.

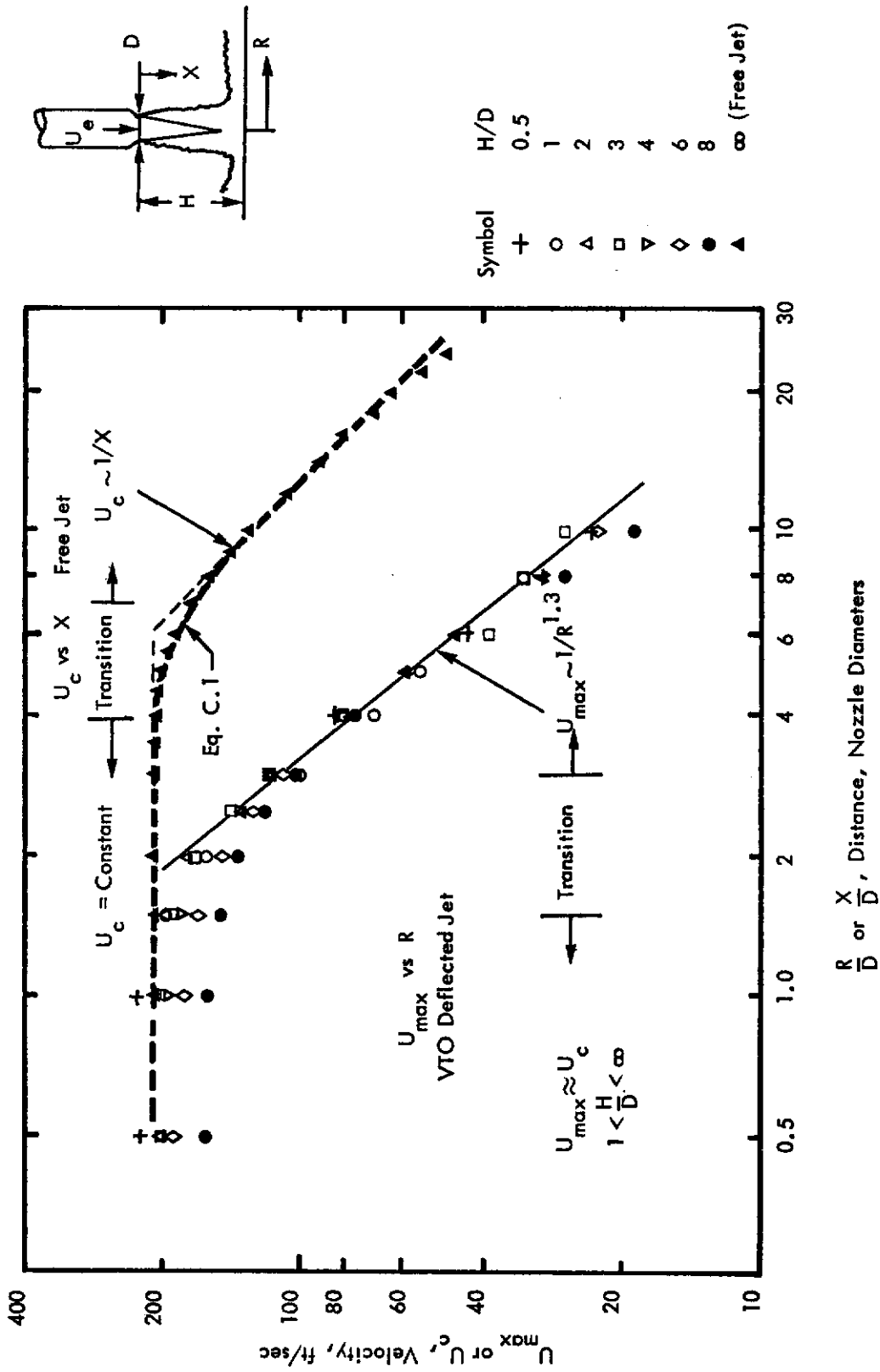


Figure C-1. Decay in Axial Velocity (U_c) of Free Jet or Maximum Radial Velocity (U_{max}) of Simulated VTOL Jet (Mach 0.18, Total Temperature = 100 Degrees F).

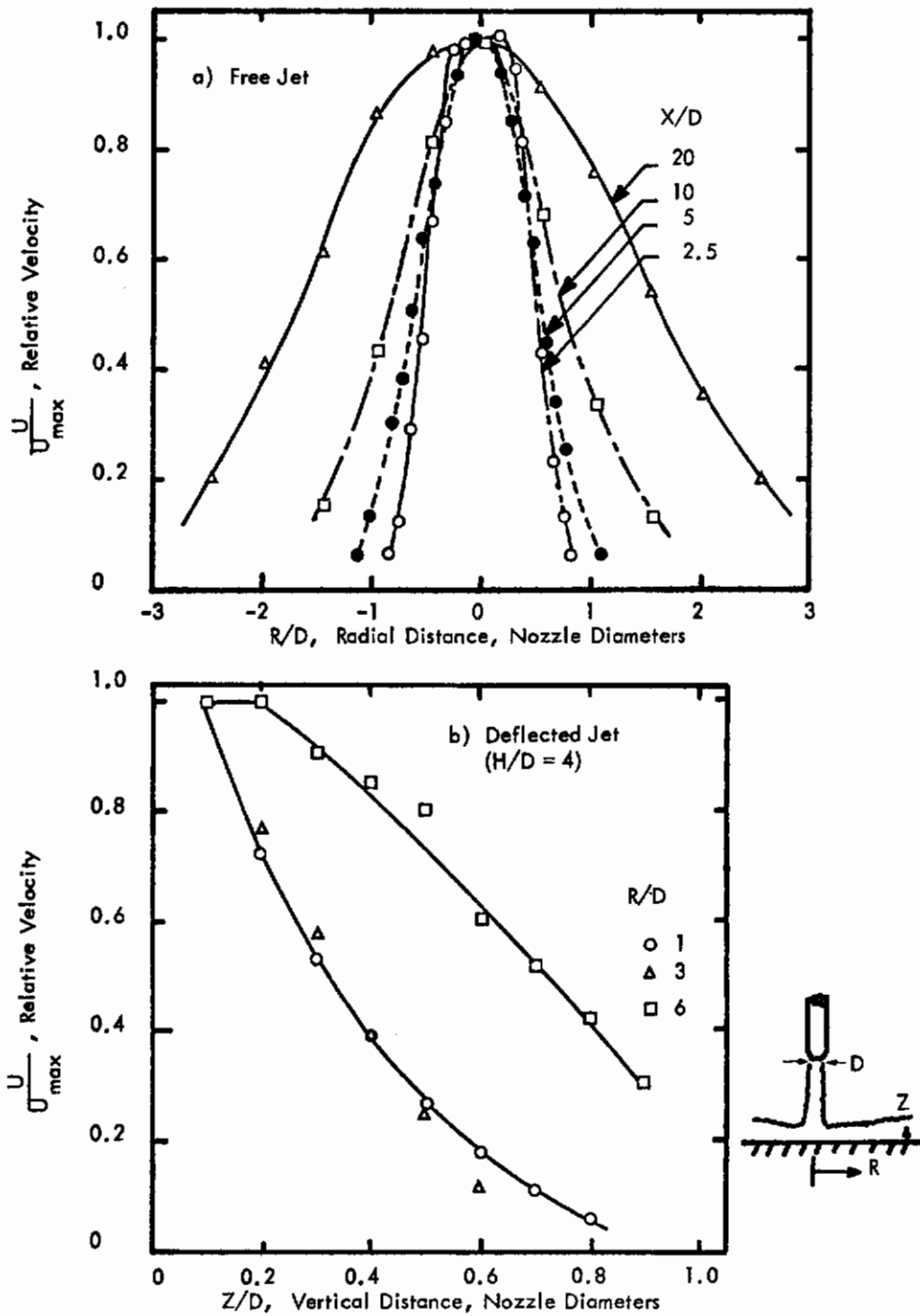


Figure C-2. Velocity Profiles Through Free and Deflected Jet

For the free jet, the velocity profiles exhibit the expected trend in flow similarity. This is most apparent at the two farthest axial positions where the jet is fully developed. For the wall jet, the limited vertical profile measurements indicated that the outer flow boundary did not increase significantly for radii less than about 3 diameters from the impingement point and then increased nearly linearly with radii beyond this point.

d. Velocity Decay for Oblique Incidence

To evaluate the effect of changing the incidence angle of the flow from 90 degrees, limited measurements were made with jet incidence angles relative to the ground plane of 80 and 70 degrees. The vertical nozzle height was fixed at 4 diameters and radial velocity measurements were taken at various radii from the measurement point and at various azimuth angles in the ground plane. For an incidence angle of 80 degrees, the maximum radial velocity at a radial distance of 2 diameters did not vary significantly with azimuth angle and was essentially the same as for a vertical jet at the same radial position.

By decreasing the incidence angle (β) to 70 degrees (20 degrees off vertical), and taking measurements out to larger radii, significant changes in radial velocity with azimuth angle were noted. The results have been summarized, in part, in Figure 10 in Section III of the report. It was found that the initial radial velocity of the wall jet was nearly independent of azimuth angle and equal to the same initial value previously noted for 90 degree incidence. However, at radii of 3 or more diameters, the maximum radial velocity changed with azimuth angle but decayed with velocity at approximately the same rate as for normal incidence. The observed change with azimuth angle (δ) for $\beta = 70$ degrees would be described to a first approximation by the semi-empirical expression.

$$U_{\max}(\delta) = U_{\max}(90^\circ) [1 + \cos\beta \cos\delta] \quad (\text{C.2})$$

where

$$U_{\max}(90^\circ) = \text{maximum radial velocity for } \beta = 90 \text{ degrees at same radius in fully developed flow region } (R/D > 3)$$

$$\beta = \text{incidence angle of jet axis}$$

$$\delta = \text{azimuth angle}$$

The expression is compared in Figure C-3 with the observed change in radial velocity at $R = 3$ and 4 diameters from the impingement point. A linear plot of the dynamic

pressure along the radial line for $\delta = 0$ degrees and 180 degrees is shown in Figure C-4. This shows that for an incidence angle of 70 degrees, the maximum dynamic pressure actually occurs about 3/4 nozzle diameters downstream of the impact point. By using small flow tufts and by varying the angle of the pitot tube, it was clearly established that this offset was a true shift in the region of maximum radial velocity but that the origin for the radial flow still fell at the geometric impact point at the intersection of the jet axis with the ground plane.

C.3 ACOUSTIC TESTS

The acoustic tests on a model VTOL jet were conducted in a 15,000 cubic foot anechoic room. The suitability of the room for acoustic measurements such as were undertaken in this program is illustrated by Figure C-5. These data show that the decay in octave band levels follow an inverse square law over the frequency bandwidth and measurement positions employed for this experimental program.

a. Acoustical Data Acquisition System

The noise was measured by the system shown in Figure C-6. For most of the measurements, the microphone was slowly traversed by a motor-driven boom over a segment of a circle centered on the nozzle exit for free (undeflected) jet tests and centered at a fixed height of 11.5 inches above the ground for deflected VTOL jet tests.

The radius of the circular segment and the angle swept were varied over the range required to cover the near field of the jet (i.e., within about 35 nozzle diameters from the exit). The microphone was a half-inch condenser microphone, Bruel and Kjaer, Type 4133, aligned to present the diaphragm at normal incidence to the noise from the jet. The system was calibrated before and after each day's run and remained stable throughout the tests within 1 dB.

The microphone traverse mechanism contained a microswitch trip mechanism which was actuated at five degree intervals. These five degree intervals were marked on the level recorder trace by the event marker. This provided a synchronized index signal of microphone position on the level recorder. One sweep of the microphone boom was made, typically over a 30-second period, for each fixed octave band setting of the spectrum analyzer.

b. Model Jet

The model jet consisted of ambient air exhausting through a 0.75-inch convergent nozzle which terminated a 4-inch plenum chamber. Air was supplied through a flow straightener to the plenum chamber system by a stable plant air supply. The jet was operated at ambient conditions giving a total temperature of approximately $85^{\circ}\text{F} \pm 10^{\circ}$ throughout the runs.

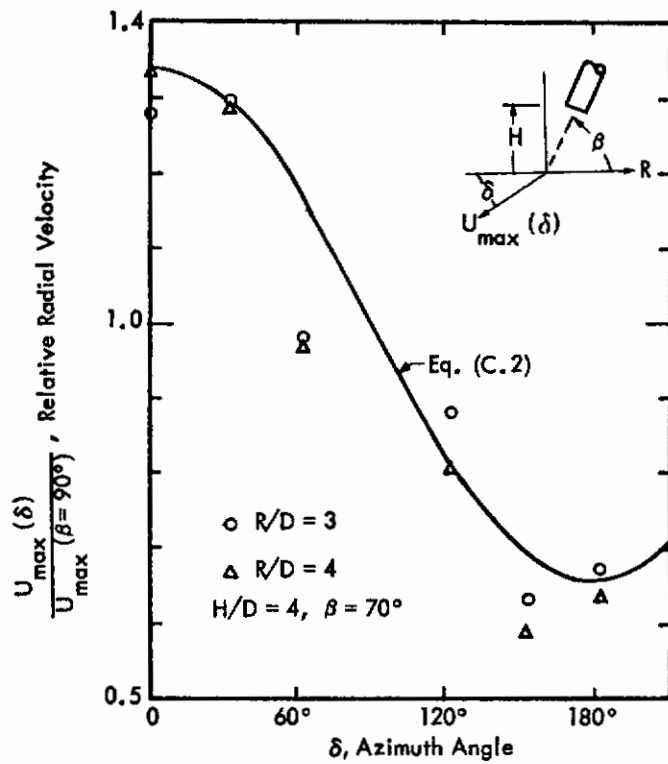


Figure C-3. Variation with Azimuth Angle of Maximum Radial Velocity in Fully Developed Flow Region for Oblique Incidence.

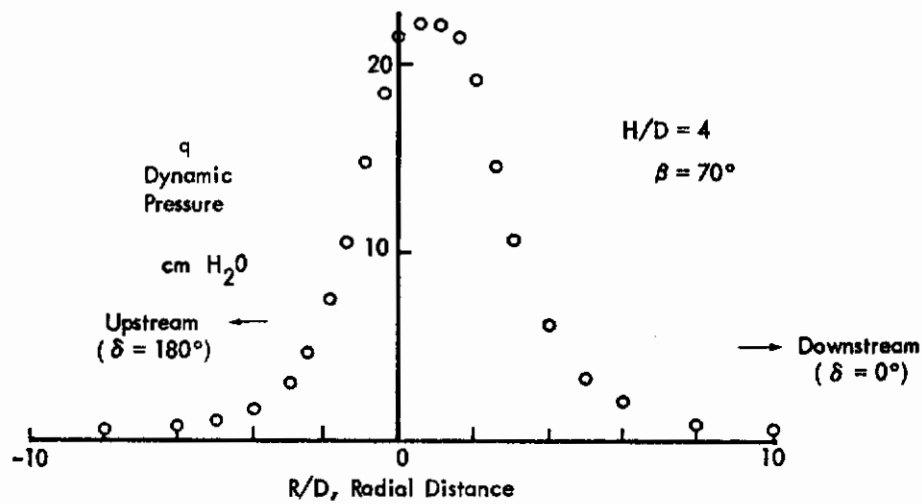
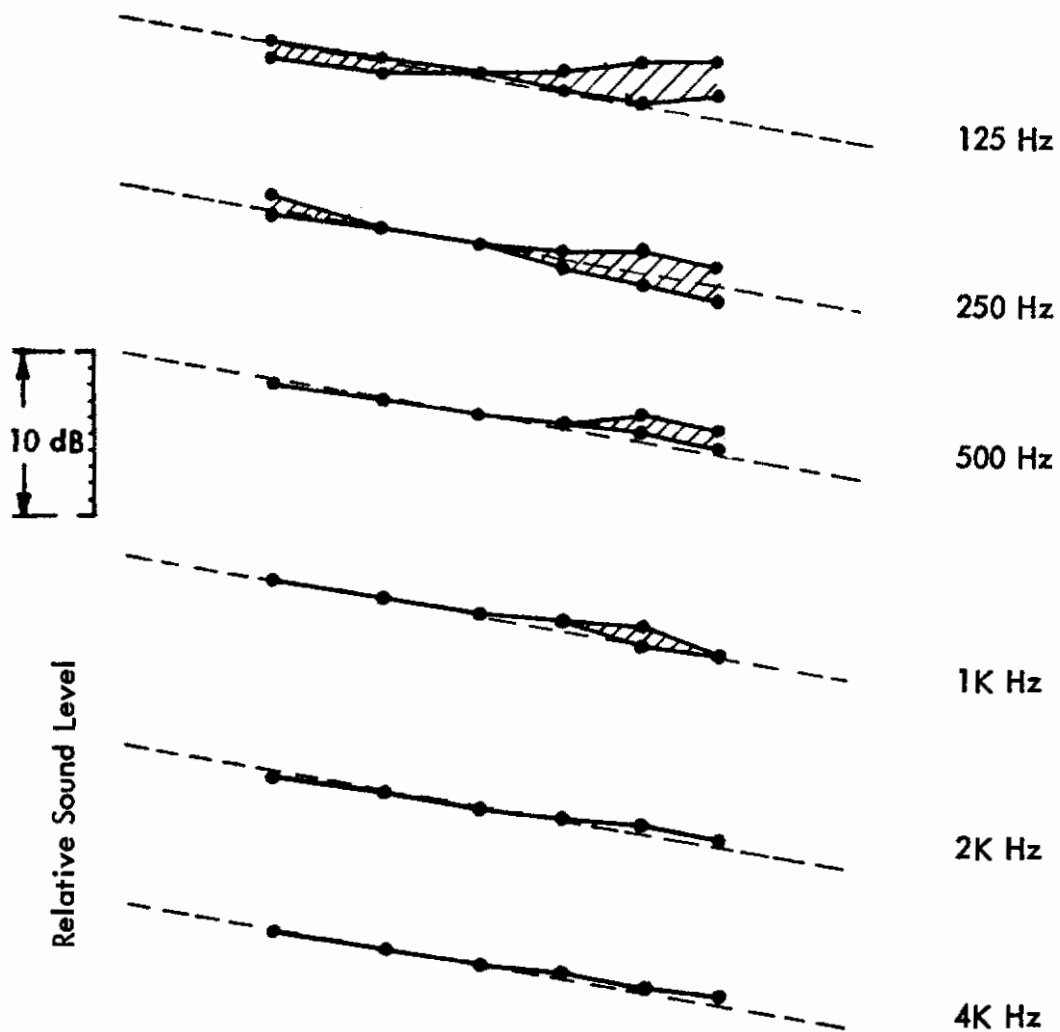


Figure C-4. Variation in Dynamic Pressure of Radial Flow Along Radial Line of Symmetry for Wall Jet with Oblique Incidence Jet

Contrails



The broken lines indicate a slope of 6 dB per doubling of distance.
The hatched area indicates the level variation found over a 120° sweep of the microphone boom.

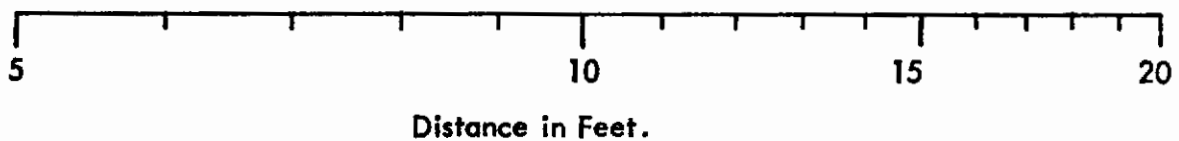


Figure C-5. Inverse Square Law Measurements in the Anechoic Room Using Full-Octave Bands of Random Noise

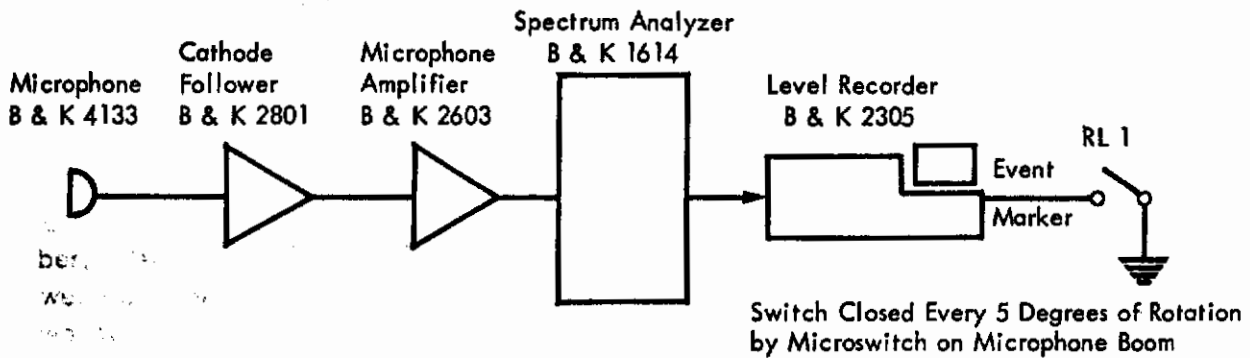


Figure C-6. Block Diagram of Acoustic Data Acquisition System

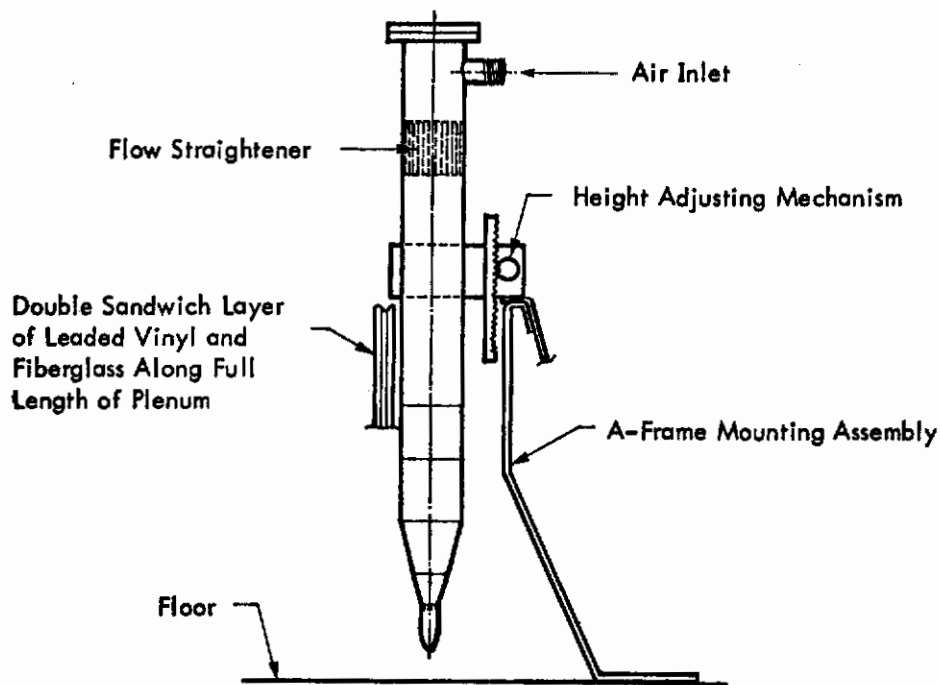


Figure C-7. Model Nozzle and Plenum Chamber Assembly Setup to Simulate VTOL Operation

The mass flow of air to the nozzle was monitored for all tests to insure stable conditions. The total temperature in the nozzle settling chamber was measured with a thermocouple probe and recorded on a standard temperature recorder. Total pressure in the plenum chamber was monitored by a calibrated water manometer. As shown in Figure C-7, the nozzle and chamber were mounted on an A-frame assembly with a lead screw mechanism to allow adjustment of the vertical distance between the nozzle and the ground plane. The latter consisted of a layer of 3/4-inch plywood nailed to a supporting lattice foundation of 2-inch by 6-inch joists. For the undeflected free jet tests, the nozzle assembly was placed in a horizontal position about 5 feet above the ground plane. The latter was covered with a layer of fiberglass for these tests to minimize ground reflection. The plenum chamber was wrapped with a double sandwich layer of leaded vinyl and fiberglass to minimize noise or reflections from the plenum wall.

A total pressure profile of the flow at the nozzle exit plane, shown in Figure C-8, indicates that the exit flow profile was free of velocity defects and showed only a very small boundary layer at the exit plane.

c. Results

Octave band sound pressure levels were graphically recorded over a frequency range from 250 to 31,500 Hz for pressure ratios of 1.27, 1.6 and 1.89 corresponding to exit Mach numbers of 0.6, 0.85 and 1.0 respectively. Flow parameters for the model tests are summarized in the following table.

TABLE C-1

Flow Parameters for Model VTOL Tests			
Mach Number	0.6	0.85	1.0
Total Pressure, psig	4.0	8.8	13.1
Total Temperature, °F	85°F (±10°)	—————→	
Exit Density, lb/ft ³	0.078	0.083	0.087
Weight Flow, lb/sec	0.150	0.22	0.267
Nominal Exit Area, ft ²	0.00312	—————→	
Effective Exit Area, ft ²	0.00292	0.00290	0.00292

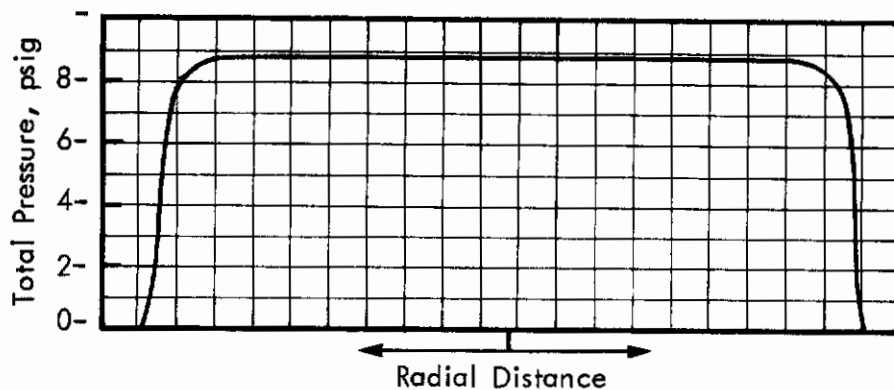


Figure C-8. Graphic Record of Total Pressure Profile at Exit Plane of Nozzle with Exit Mach Number of 1.0 (data from Reference 95).

Data were obtained in the near field of the jet for a horizontal configuration (free undeflected jet) and for simulated VTOL conditions at elevations of 2, 4, 6, 9, 13.3 and 20 diameters. In order to more accurately simulate typical full scale jet exhaust conditions, the impingement angle of the VTOL jet was set at 80 degrees instead of 90 degrees. Preliminary runs at both angles indicated that the difference in near field sound levels for the two incidence angles was small. Power level spectra and directivity data for the nozzle assembly in a horizontal position had been measured for this jet at a radius of 170 diameters in an earlier program.⁹⁵ Results are shown in Figures C-9 and C-10.

To define the near field sound levels, the graphic records of octave band levels were read at 5 to 15 degree intervals of the angular position of the microphone and translated onto x-y coordinate plots with the origin of the axes at the jet exit. Contours were then constructed through the measured data points to define near field noise contours. A typical record of the raw octave band level data as a function of angle is shown in Figure C-11 for two octave bands. A typical contour map of the sound levels, including the measured levels from which the contours were drawn, is shown in Figure C-12.

Figure C-13 presents representative contour plots constructed for the undeflected jet while Figures C-14 to C-17 present corresponding contour plots for the simulated VTOL jet. Periodically during the tests, a one-third octave band analysis was made at fixed near field locations to verify the detailed spectrum shape. With the exception of those tests for which discrete ring tones were observed, the spectrum shape was regular and exhibited no irregularities. A typical example of the spectrum with and without a ring tone present was shown in Section III on Figure 48, page 103.

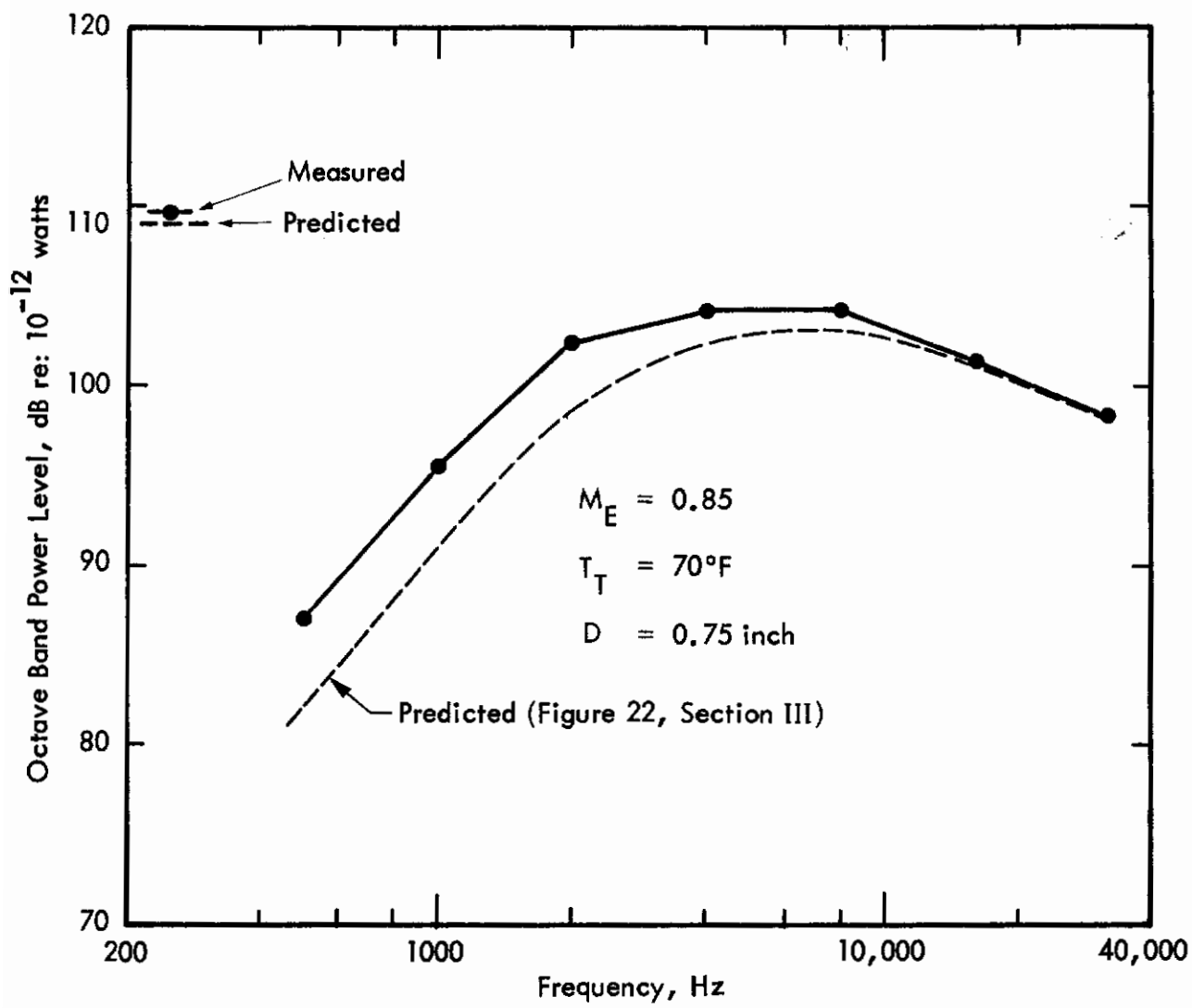


Figure C-9. Octave Band Power Level Spectra for Model Jet (from Measurement at 170 Diameter Radius, Reference 95)

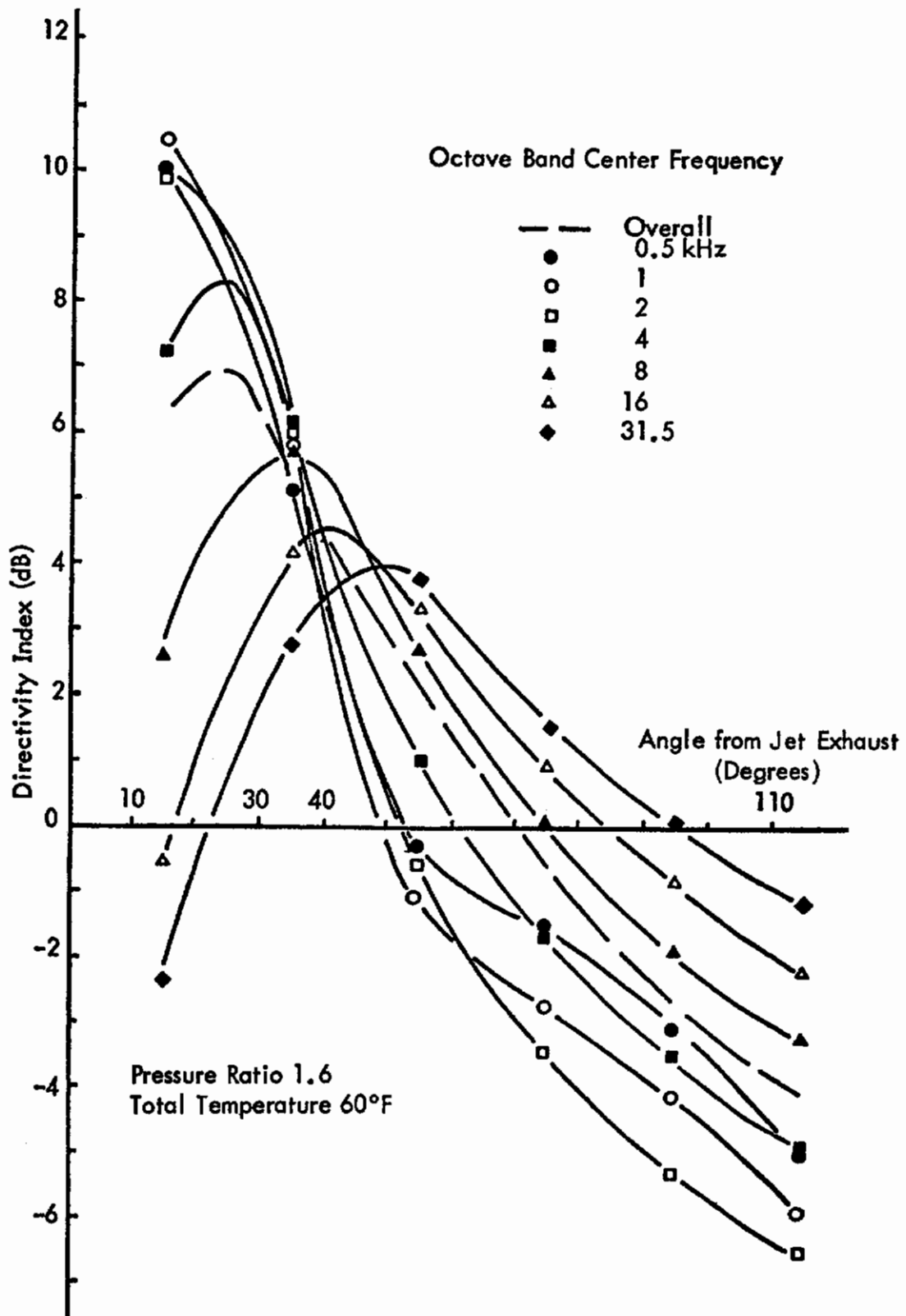


Figure C-10. Directivity Pattern for Horizontal Free Jet at 170 Nozzle Diameters (from Reference 95).

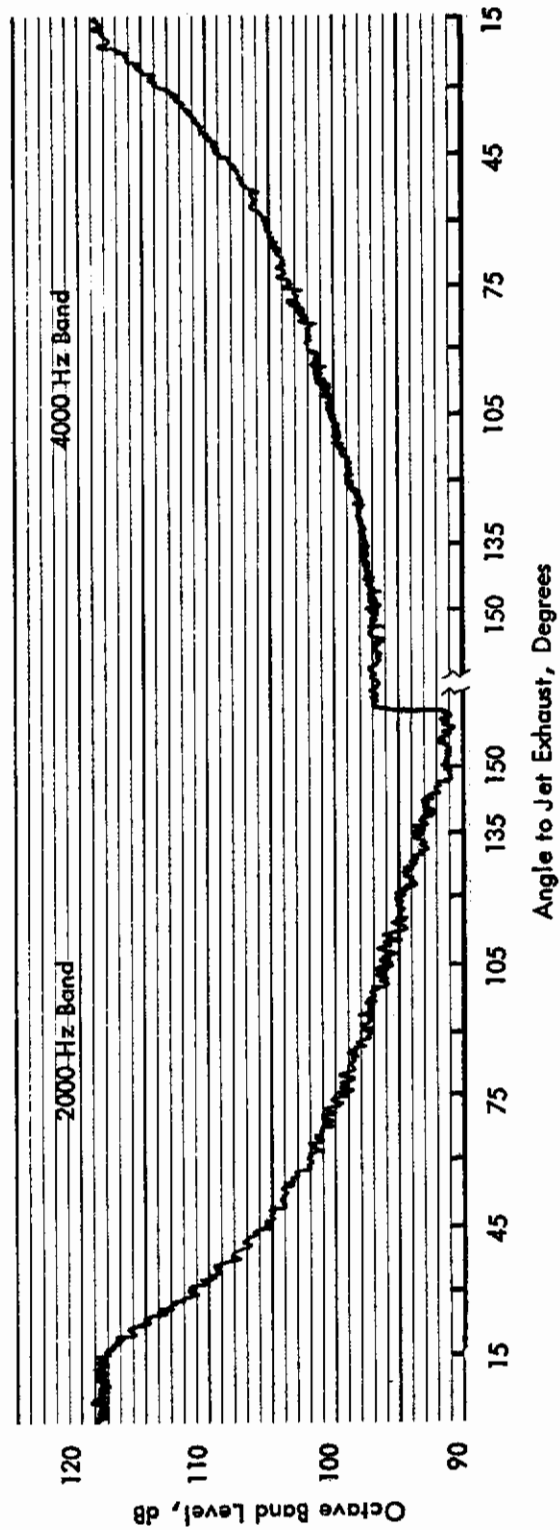


Figure C-11. Typical Graphic Record of Angular Variation in Octave Band Level, Horizontal Jet, Mach 0.85, Microphone Radius 13.3 Nozzle Diameters

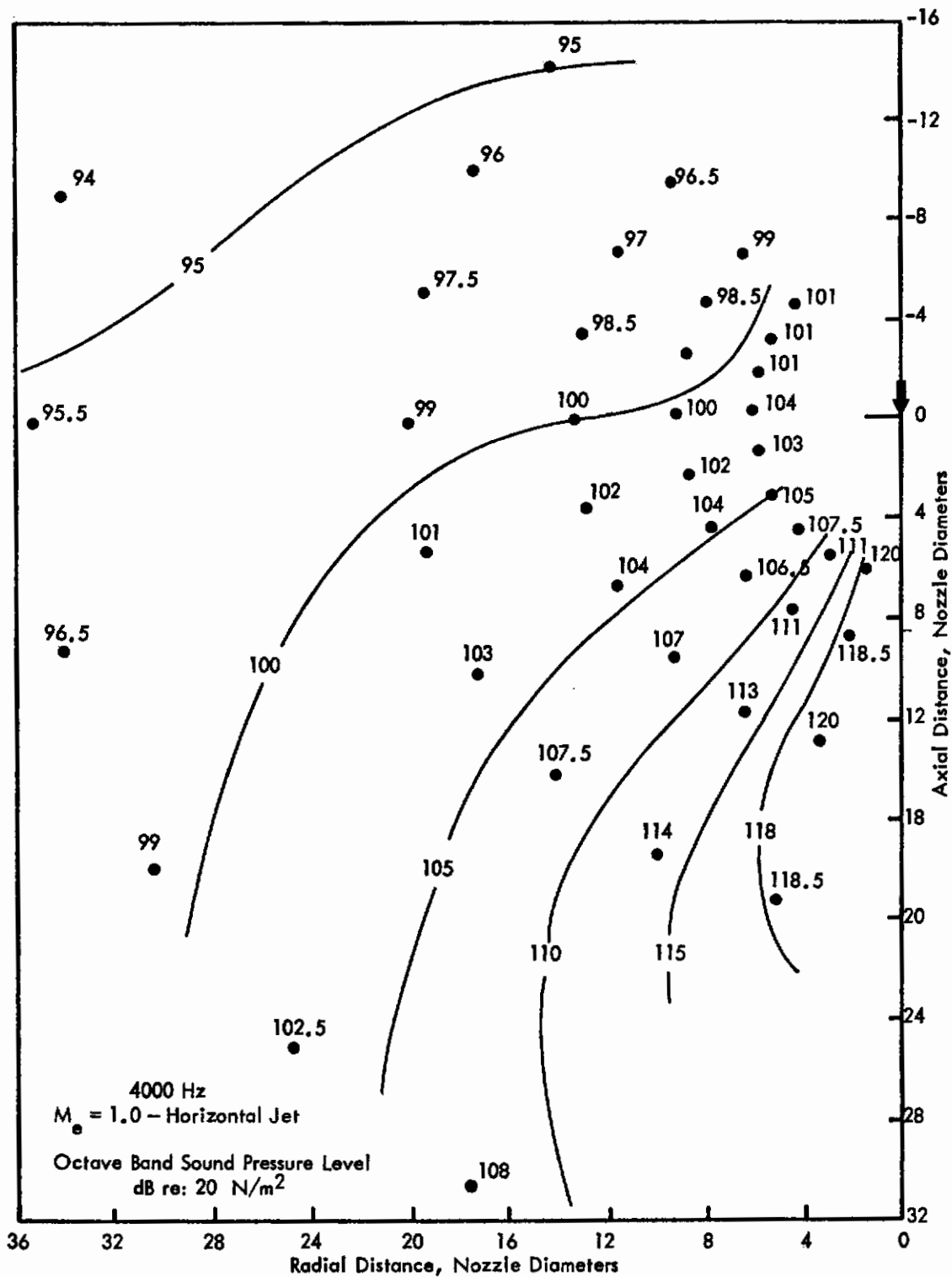


Figure C-12. Typical Octave Band Sound Level Contours

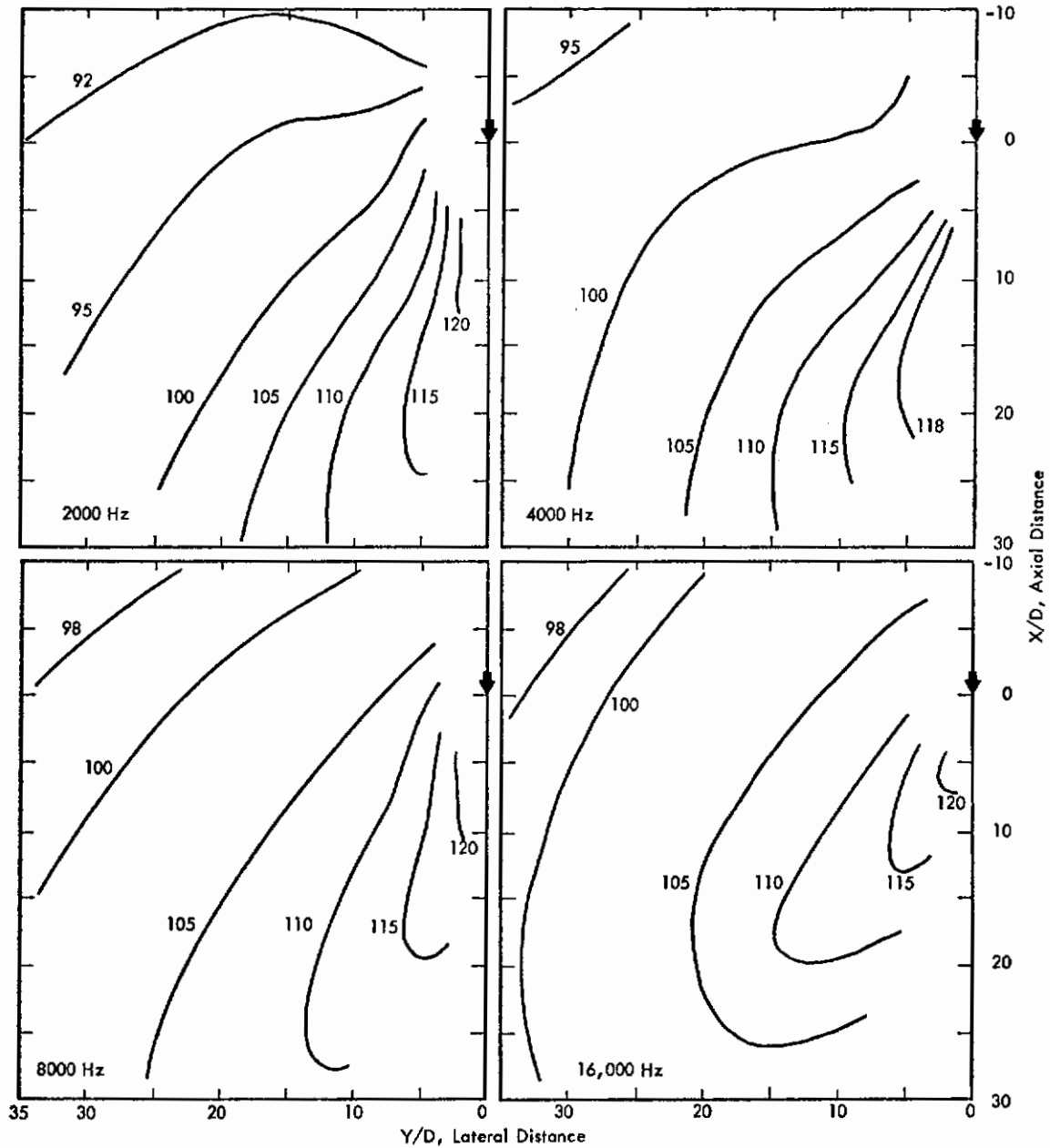


Figure C-13. Contours of Octave Band Sound Pressure Level, dB re $20 \mu\text{N}/\text{m}^2$, Mach 1, Free Horizontal Jet.

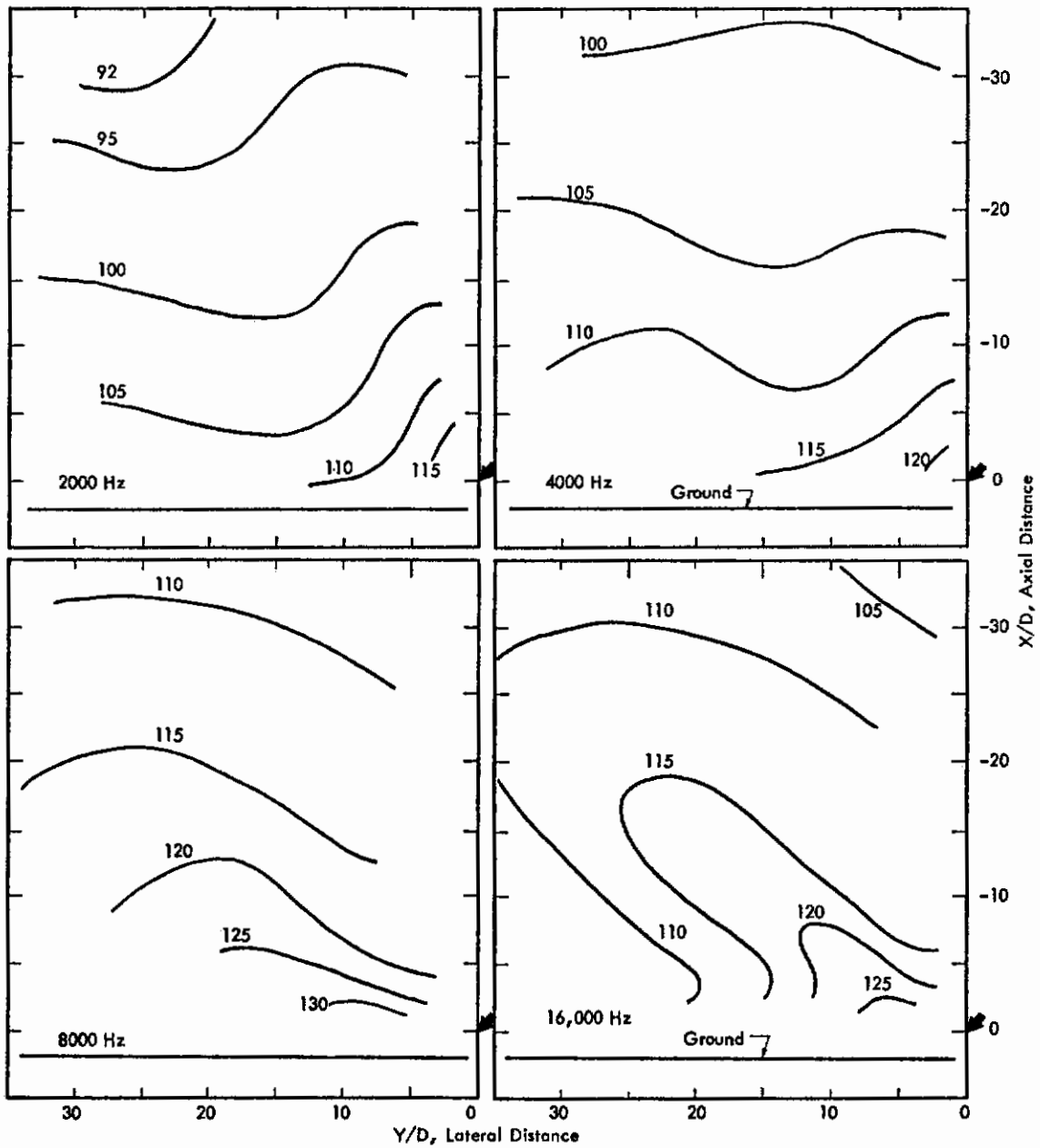


Figure C-14. Contours of Octave Band Sound Pressure Level, dB re $20 \mu\text{N}/\text{m}^2$
 Mach 1, VTOL Jet, H/D = 2, Jet Impingment Angle, 80° .

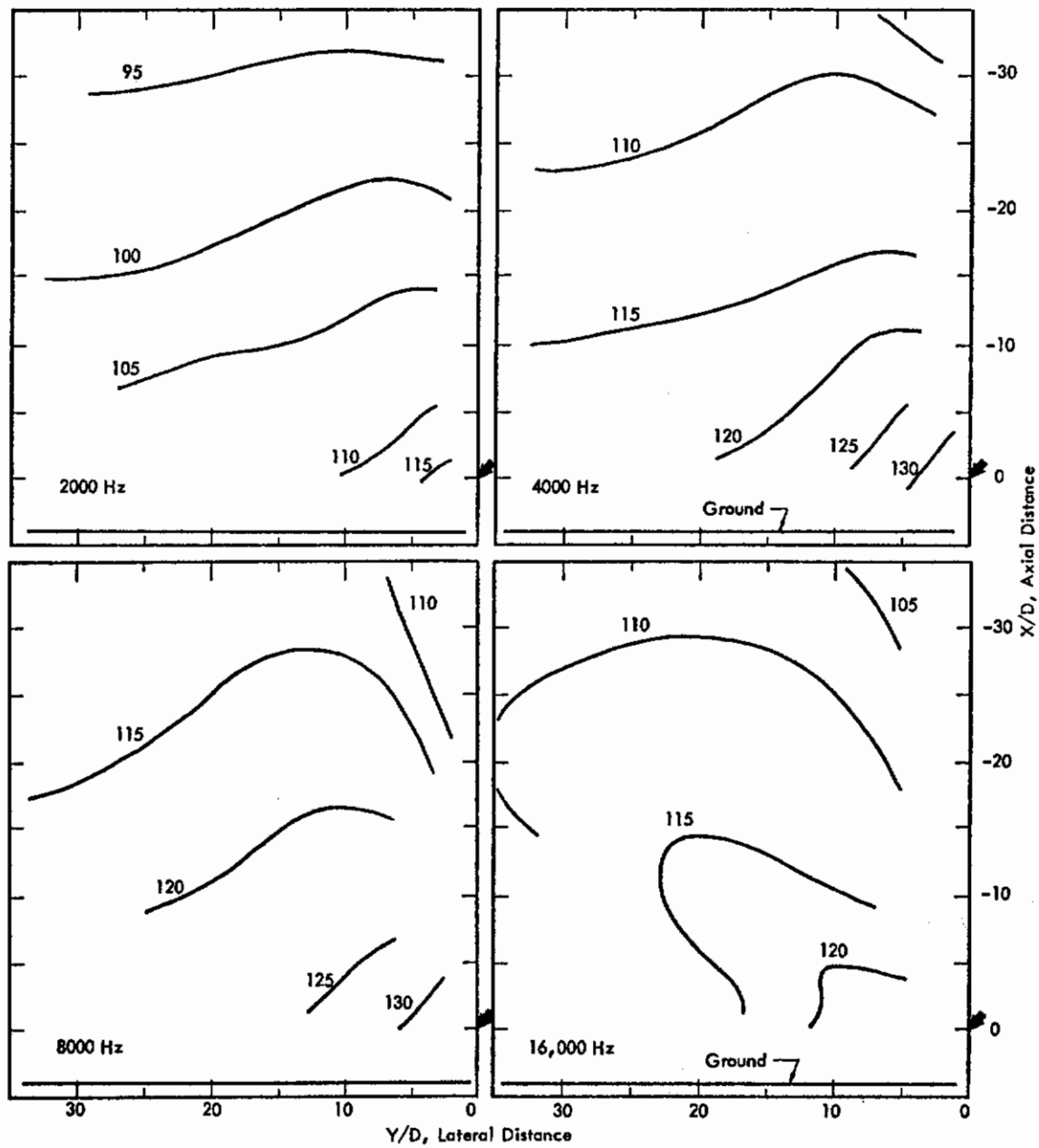


Figure C-15. Contours of Octave Band Sound Pressure Level, dB re $20 \mu\text{N}/\text{m}^2$
 Mach 1, VTOL Jet ($H/D = 4$), Jet Impingement Angle = 80° .

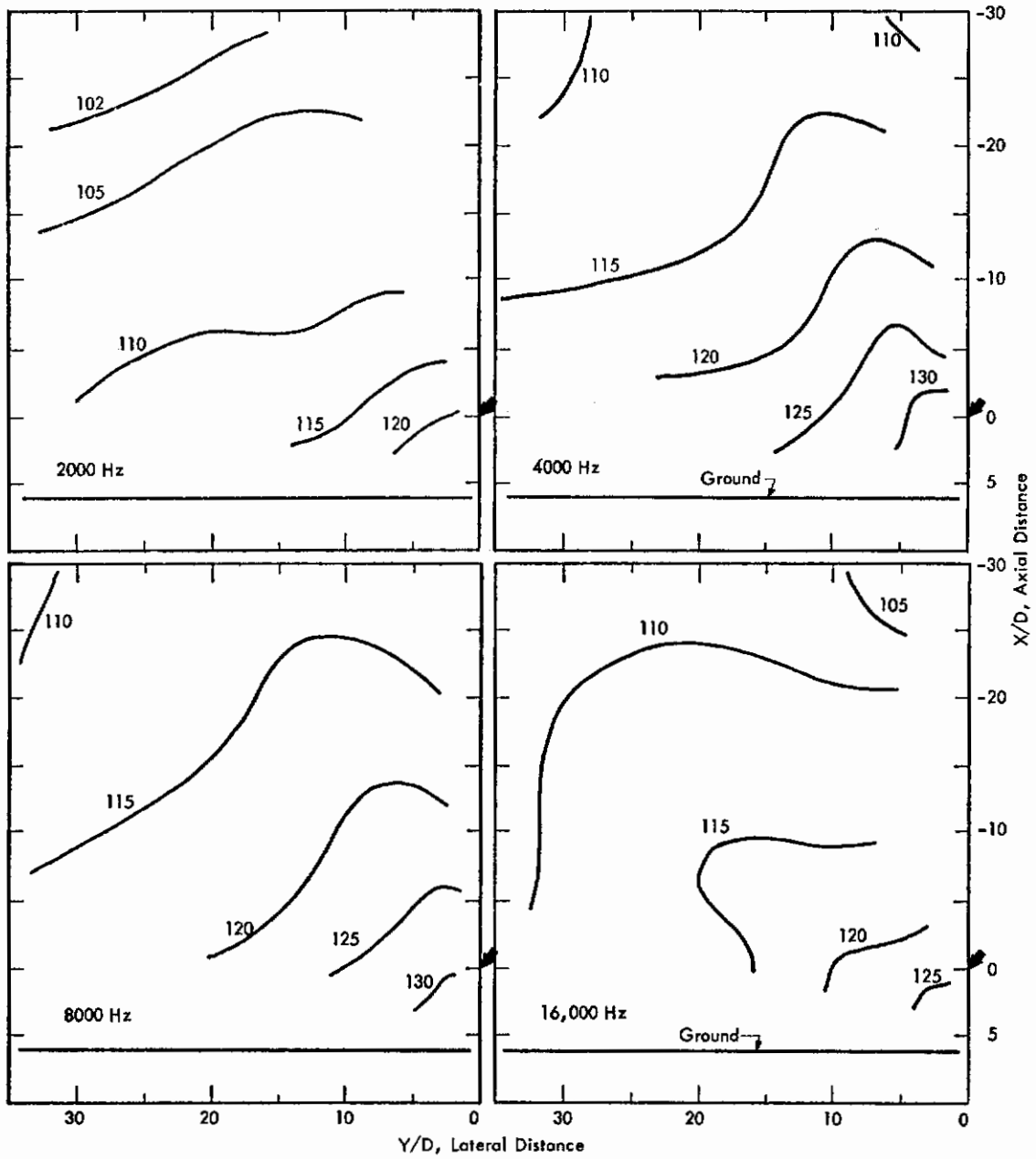


Figure C-16. Contours of Octave Band Sound Pressure Level, dB re $20\mu\text{N/m}^2$
 Mach 1, VTOL Jet ($H/D = 6$), Jet Impingment Angle = 80° .

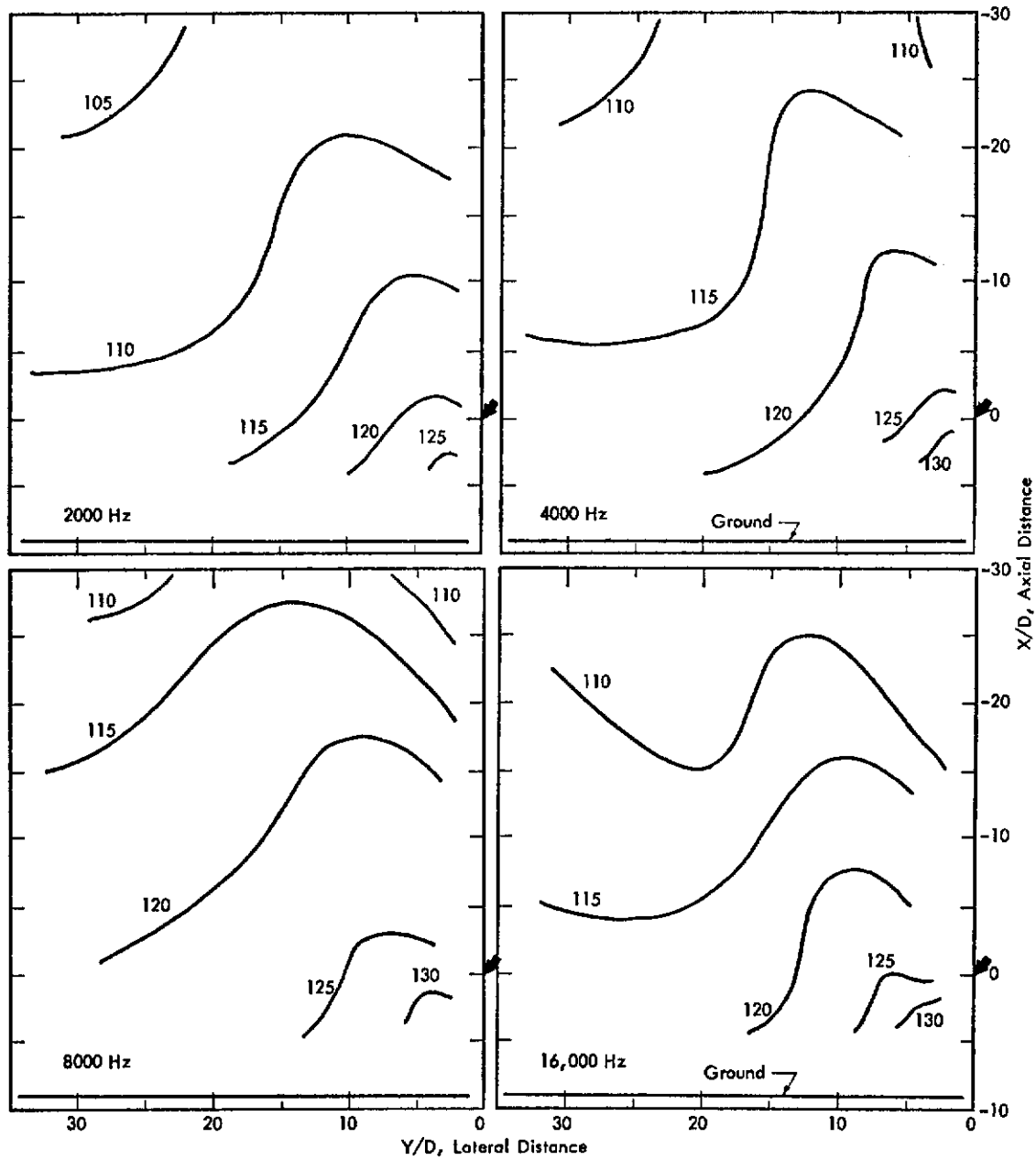


Figure C-17. Contours of Octave Band Sound Pressure Level, dB re $20 \mu\text{N/m}^2$ Mach 1, VTOL Jet ($H/D = 9$), Jet Impingement Angle = 80° .

APPENDIX D

TABLES AND COMPUTER PROGRAM FOR REFLECTION OF OCTAVE BANDS
OF WHITE NOISE FROM A RIGID REFLECTING PLANE

Tables and the computer program utilized for their generation are provided for calculating the change in octave band levels due to ground reflection from a rigid plane for a point source which simulates the directivity of a:

- Non-directional monopole source
- Jet noise source

The computer program prints tables in a geometrically arranged matrix array of either or both of the following quantities. The relevant equations are derived in part 4 of Section III of the main text. The geometry of the problem is illustrated in Figure D-1.

$$A = 10 \log \left[\frac{\text{Mean Square (Direct + Reflected Pressure)}}{\text{Mean Square Direct Pressure}} \right], \quad \text{dB} \quad (\text{D.1})$$

The change in sound level due to introduction of the rigid reflecting plane.

$$B = L_o - 20 \log \left(\frac{R}{H} \right) + 10 \log D(\theta), \quad \text{dB} \quad (\text{D.2})$$

The sound level at a position R, θ , in the absence of a reflecting plane, of a point source with a directivity factor $D(\theta)$, and space average sound level L_o at a reference distance H . For printout, the polar coordinates are converted to rectangular coordinates x and y .

To simulate a jet noise source, the computer program assumes a directivity factor for the point source of the following form (see Equation (30) in Section III).

$$D(\theta) = \frac{K (1 + \cos^4 \theta)}{\left[(1 - M_c \cos \theta)^2 + \alpha^2 M_c^2 \right]^{5/2} \left[1 + C_4 e^{-C_5 \theta} \right]} \quad (\text{D.3})$$

Tables

Tables are provided for the case of a monopole source only. Table D-I presents a set of matrix tables of A (Equation (D.1)) for a monopole source for the following range of variables.

- For each table:

$$x/H = -2 \text{ to } +1 \text{ in steps of } 0.2$$

$$y/H = 0 \text{ to } 6 \text{ in steps of } 0.6$$

- Separate tables are provided for:

$$H/\lambda = 0.25, 0.5, 1, 2, 4, 8 \text{ and } 100$$

The case of $H/\lambda = 100$ approximates the condition for which phase effects are negligible in the reflection and the total direct and reflected sound fields are added on an intensity basis.

Table D-II presents a matrix table of $A + B$ for $H/\lambda = 100$ with the reference space average sound level of the direct sound field (L_0) arbitrarily set equal to 50 dB.

For convenience, by suitable choice of the intervals for the rectangular position variables x/H and y/H , the tabular values appear in a geometrically scaled pattern normalized by the source height H . For any table, the positions x and y may be normalized in terms of wavelength by multiplying the x/H and y/H values by H/λ .

Computer Program

The computer program, listed in Table D-III, is written in FORTRAN IV adopted for use on a remote computer terminal utilizing direct input to a TYMSHARE (Registered Trademark) time-sharing computer service. Minor modifications will be required to adopt the program to conventional FORTRAN IV-compatible computers which do not use a remote terminal on-line input. The following instructions apply to its use with the TYMSHARE remote terminal system. The program is self-instructing and when loaded into the central processor, requests only one additional input from the terminal.

- Input File Name

The user types the file name on which is stored the following variables separated by commas (,).

XL,	Lowest Value of x/H
XH,	Highest Value of x/H
XD,	Interval in x/H
YL,	Lowest Value of y/H
YH,	Highest Value of y/H
YD,	Interval in y/H
MC,	Value of M_c in Equation (D.3)
AL,	Value of α^2 in Equation (D.3)
C4,	Value of C_4 in Equation (D.3)
C5,	Value of C_5 in Equation (D.3)
K,	Value of K in Equation (D.3)
LO,	Value of L_0 in Equation (D.2)
G,	Value of γ , incidence angle (in radians) of "jet" axis. (See Figure D-1.)
ICODE,	An integer from 1 to 7 to define the output form desired as defined below.
NU,	Value of H/λ

The input file may be extended to allow additional cases to be run for different values of H/λ with or without a change in output code in the following manner.

For no change in output code, add additional values of NU (H/λ) after the first value, separating each by a comma (,).

For a subsequent change in output code for any values of NU except the first, add, in the same manner, the following:

Contrails

-ICODE, the negative of the new desired output code

NU, etc. the new values of NU for new output code

This extension may be continued for as many new values of NU and ICODE as desired for the same values of all other variables. The output code allows the following combinations of output for a given value of NU.

<u>ICODE</u>	<u>Matrix Tables Printed</u> <u>(See Equations D-1, D-2)</u>
1	A
2	A and B
3	A and A + B
4	A, B and A + B
5	B
6	B and A + B
7	A + B

- **Special Instructions**

For the case of a monopole, set K and $G(\gamma) = 0$. This sets the directivity index to unity and properly orients the coordinates for a non-directional source.

For a B or A + B output table, the value of LO (L_0) should be less than about 80 to maintain at least one space between rows.

For a geometrically scaled printout on a standard teletype terminal or computer printer, the interval YD ($\Delta y/H$) must be three times XD ($\Delta x/H$).

The program prints out the values of MC through K, G and NU at the top of each table where AL (α^2) is identified as ALPHA and $G(\gamma)$ is identified as GAMMA.

Contrails

The value of K may be selected arbitrarily but, for physically rational results, should be adjusted so that the integral of $D(\theta) \cdot \sin \theta$ from 0 to π is unity. Suitable values of the directivity parameters in Equation (D.3) which satisfy this constraint are given in part 4 of Section III to simulate far field directivity of an ambient air jet and a turbojet engine.

After inputting the first file name, the computer prints the requested tables and then requests a new file name. Any number of additional files may thus be provided for new cases with new directivity constants.

Termination of the program is executed by the normal abort procedure for the remote terminal system.

TABLE D-1

CHANGE IN OCTAVE BAND LEVEL DUE TO REFLECTION FROM RIGID PLANE
FOR MONOPOLE SOURCE AT ELEVATION H WITH
WAVELENGTH λ AT CENTER FREQUENCY OF BAND

		Vertical Distance (Decibels)												
		X/H	Y/H (Lateral Distance)											
		0.0	.6	1.2	1.8	2.4	3.0	3.6	4.2	4.8	5.4	6.0		
$\frac{H}{\lambda} = 0.25$	Source →	-2.0	-3.4	-3.7	-4.2	-4.3	-3.4	-2.0	-.6	.6	1.5	2.3	2.8	
		-1.8	-3.2	-3.5	-4.1	-4.1	-3.0	-1.5	-.1	1.0	1.9	2.6	3.2	
		-1.6	-3.1	-3.4	-4.0	-3.8	-2.5	-.9	.4	1.5	2.3	3.0	3.5	
		-1.4	-2.9	-3.2	-3.8	-3.4	-2.0	-.3	1.0	2.0	2.8	3.3	3.8	
		-1.2	-2.6	-3.1	-3.7	-3.0	-1.3	.3	1.5	2.5	3.2	3.7	4.1	
		-1.0	-2.3	-2.9	-3.4	-2.4	-.6	.9	2.1	2.9	3.5	4.0	4.3	
		-.8	-2.0	-2.7	-3.1	-1.8	.1	1.6	2.6	3.4	3.9	4.3	4.6	
		-.6	-1.6	-2.4	-2.7	-1.0	.9	2.2	3.2	3.8	4.3	4.6	4.8	
		-.4	-1.2	-2.2	-2.1	-.1	1.7	2.9	3.7	4.2	4.6	4.9	5.1	
		-.2	-.6	-2.0	-1.3	.9	2.5	3.5	4.2	4.6	4.9	5.1	5.3	
Plane →	0	⊕	-1.7	-.2	1.9	3.3	4.1	4.6	4.9	5.2	5.3	5.5		
	.2	-.8	-1.0	1.2	3.0	4.0	4.6	5.0	5.2	5.4	5.5	5.6		
	.4	-.6	.5	2.6	3.9	4.7	5.1	5.3	5.5	5.6	5.7	5.8		
	.6	1.4	2.5	4.0	4.8	5.2	5.5	5.6	5.7	5.8	5.8	5.9		
	.8	4.0	4.5	5.1	5.5	5.7	5.8	5.9	5.9	5.9	5.9	6.0		
	1.0	6.0	6.0	6.0	6.0	6.0	6.0	6.0	6.0	6.0	6.0	6.0		
	$\frac{H}{\lambda} = 0.5$	Source →	-2.0	2.0	2.2	2.5	2.7	2.5	1.6	.3	-1.5	-3.4	-4.8	-5.1
			-1.8	1.9	2.1	2.5	2.6	2.2	1.1	-.5	-2.5	-4.3	-5.1	-4.6
			-1.6	1.7	2.0	2.4	2.5	1.8	.5	-1.5	-3.6	-5.0	-4.8	-3.6
			-1.4	1.6	1.9	2.3	2.2	1.3	-.4	-2.7	-4.6	-5.1	-4.0	-2.4
-1.2			1.4	1.8	2.2	1.9	.6	-1.5	-3.9	-5.1	-4.3	-2.7	-1.2	
-1.0			1.2	1.6	2.1	1.5	-.3	-2.9	-4.9	-4.7	-3.0	-1.3	.0	
-.8			1.0	1.5	1.9	.8	-1.6	-4.3	-5.0	-3.4	-1.5	.0	1.1	
-.6			.8	1.4	1.5	-.2	-3.2	-5.1	-3.8	-1.7	.0	1.2	2.1	
-.4			.6	1.3	.9	-1.7	-4.7	-4.3	-1.9	.0	1.4	2.3	3.0	
-.2			.3	1.1	-.2	-3.6	-4.7	-2.2	.0	1.5	2.6	3.3	3.8	
Plane →	0	⊕	.7	-2.0	-4.8	-2.5	.1	1.8	2.9	3.6	4.1	4.4		
	.2	.3	-.5	-4.1	-2.8	.3	2.1	3.2	3.9	4.4	4.7	5.0		
	.4	-.8	-3.0	-2.8	.6	2.6	3.7	4.4	4.8	5.1	5.3	5.4		
	.6	-2.9	-1.7	1.4	3.3	4.3	4.9	5.2	5.4	5.5	5.6	5.7		
	.8	2.4	3.4	4.5	5.1	5.5	5.6	5.8	5.8	5.9	5.9	5.9		
	1.0	6.0	6.0	6.0	6.0	6.0	6.0	6.0	6.0	6.0	6.0	6.0		
	$\frac{H}{\lambda} = 1$	Source →	-2.0	.4	.3	.4	1.2	1.8	1.8	1.7	2.3	3.2	3.8	4.0
			-1.8	.3	.2	.4	1.3	1.8	1.6	1.9	2.7	3.6	4.0	3.9
			-1.6	.2	.1	.5	1.4	1.7	1.6	2.2	3.2	3.8	3.9	3.6
			-1.4	.2	.1	.6	1.5	1.5	1.7	2.7	3.6	3.9	3.7	3.0
-1.2			.1	-.0	.7	1.5	1.4	2.0	3.2	3.8	3.7	3.1	2.1	
-1.0			.0	-.1	.8	1.4	1.4	2.6	3.6	3.8	3.2	2.1	.6	
-.8			-.0	-.1	1.0	1.2	1.8	3.2	3.7	3.3	2.2	.5	-1.4	
-.6			-.1	-.0	1.0	1.1	2.5	3.5	3.4	2.2	.4	-1.7	-3.8	
-.4			-.1	.1	.9	1.5	3.2	3.4	2.3	.3	-2.1	-4.3	-5.0	
-.2			-.1	.3	.7	2.4	3.3	2.3	.1	-2.7	-4.8	-4.7	-3.2	
Plane →	0	⊕	.4	1.3	3.1	2.3	-.3	-3.5	-5.1	-3.8	-1.9	-.3		
	.2	.1	.3	2.5	2.2	-.8	-4.5	-4.5	-2.2	-.3	1.1	2.1		
	.4	.2	1.7	1.9	-1.9	-5.1	-2.7	-.1	1.5	2.6	3.3	3.8		
	.6	1.6	.6	-4.2	-3.3	.3	2.2	3.4	4.1	4.5	4.8	5.0		
	.8	-3.9	-1.7	1.8	3.7	4.6	5.0	5.3	5.5	5.6	5.7	5.8		
	1.0	6.0	6.0	6.0	6.0	6.0	6.0	6.0	6.0	6.0	6.0	6.0		

TABLE D-1 (Continued)

	Vertical Distance X/H	Y/H (Lateral Distance)											
		0.0	.6	1.2	1.8	2.4	3.0	3.6	4.2	4.8	5.4	6.0	
$\frac{H}{\lambda} = 2$	-2.0	1.0	1.2	1.5	1.0	1.6	1.8	2.2	2.8	2.1	1.4	1.9	
	-1.8	.9	1.1	1.4	.9	1.7	1.7	2.5	2.5	1.5	1.6	2.4	
	-1.6	.8	1.1	1.2	.9	1.7	1.9	2.7	1.9	1.3	2.1	2.7	
	-1.4	.7	1.0	1.0	1.2	1.5	2.3	2.4	1.3	1.8	2.6	2.7	
	-1.2	.6	.9	.7	1.4	1.5	2.5	1.6	1.4	2.4	2.7	2.4	
	-1.0	.5	.9	.5	1.4	2.0	2.1	1.2	2.1	2.6	2.4	2.3	
	-.8	.3	.8	.6	1.2	2.3	1.2	1.7	2.6	2.4	2.3	2.9	
	-.6	.2	.6	.9	1.5	1.8	1.2	2.4	2.3	2.3	3.0	3.8	
	-.4	.1	.3	.9	2.0	.9	2.2	2.3	2.2	3.1	4.0	4.3	
	-.2	.0	.1	.9	1.1	1.7	2.2	2.2	3.3	4.1	4.2	3.7	
	Source →	0	⊕	.4	1.5	1.0	2.1	2.1	3.5	4.2	3.9	2.9	1.5
		.2	-.0	.6	.3	1.9	2.1	3.7	4.0	3.0	1.3	-.9	-3.1
		.4	.6	.1	1.6	2.3	3.9	3.2	1.0	-2.0	-4.5	-4.7	-3.3
		.6	.8	1.0	3.0	3.1	.1	-4.0	-4.6	-2.3	-.3	1.1	2.1
		.8	2.7	1.5	-3.9	-3.3	.4	2.4	3.5	4.1	4.6	4.9	5.1
Plane →	1.0	6.0	6.0	6.0	6.0	6.0	6.0	6.0	6.0	6.0	6.0	6.0	
$\frac{H}{\lambda} = 4$	-2.0	1.1	1.1	1.1	1.4	1.3	1.8	2.2	2.0	2.2	2.7	2.5	
	-1.8	1.0	1.0	1.1	1.6	1.5	1.9	1.8	2.3	2.3	2.7	2.0	
	-1.6	.9	.8	1.1	1.5	1.7	2.1	1.8	2.1	2.8	2.1	2.3	
	-1.4	.8	.7	1.0	1.1	1.5	1.7	2.1	2.4	2.3	2.1	2.7	
	-1.2	.7	.6	.9	1.1	1.8	1.6	2.0	2.6	1.9	2.6	2.4	
	-1.0	.6	.4	1.1	1.3	1.7	2.0	2.5	1.8	2.5	2.4	2.9	
	-.8	.5	.4	1.0	1.3	1.4	2.0	2.0	2.3	2.4	2.9	3.3	
	-.6	.3	.4	.7	1.6	1.7	2.3	2.0	2.3	2.9	3.2	2.1	
	-.4	.2	.3	.9	1.2	2.1	1.6	2.3	2.8	3.0	1.8	2.0	
	-.2	.1	.5	1.2	1.4	1.4	2.2	2.8	2.7	1.6	2.4	3.0	
	Source →	0	⊕	.3	.9	1.7	2.1	2.8	2.2	1.8	2.8	2.8	2.5
		.2	.1	.6	1.6	1.9	2.8	1.5	2.4	2.8	2.4	2.9	3.8
		.4	.1	.8	1.6	2.6	1.6	2.7	2.4	3.3	4.2	4.4	3.9
		.6	.5	1.1	1.2	2.5	2.4	3.9	4.3	3.3	1.6	-.6	-2.9
		.8	1.7	1.8	3.5	3.6	.4	-3.8	-4.6	-2.3	-.2	1.2	2.2
Plane →	1.0	6.0	6.0	6.0	6.0	6.0	6.0	6.0	6.0	6.0	6.0	6.0	
$\frac{H}{\lambda} = 8$	-2.0	.9	1.0	1.1	1.5	1.7	1.8	2.0	2.1	2.2	2.3	2.5	
	-1.8	.8	1.0	1.0	1.2	1.5	2.0	2.0	2.1	2.5	2.4	2.7	
	-1.6	.7	.9	1.1	1.3	1.6	1.7	2.1	2.2	2.1	2.4	2.4	
	-1.4	.6	.8	1.0	1.3	1.6	1.8	2.1	2.3	2.4	2.6	2.6	
	-1.2	.5	.7	1.0	1.3	1.5	1.9	2.2	2.3	2.6	2.4	2.5	
	-1.0	.4	.7	.9	1.3	1.7	2.0	1.9	2.4	2.2	2.5	2.7	
	-.8	.3	.5	.9	1.4	1.8	2.2	2.1	2.1	2.4	2.7	2.5	
	-.6	.2	.4	1.0	1.3	1.7	2.0	2.2	2.3	2.6	2.6	2.6	
	-.4	.1	.3	.9	1.5	1.7	2.3	2.3	2.4	2.6	2.7	2.9	
	-.2	.0	.3	.8	1.5	2.0	2.2	2.3	2.6	3.0	2.3	2.7	
	Source →	0	⊕	.3	.9	1.6	2.1	2.0	2.4	2.8	2.3	2.8	2.8
		.2	.1	.5	1.0	1.8	1.8	2.5	2.0	2.8	2.3	3.5	2.6
		.4	.3	.8	1.5	1.9	2.6	2.6	2.8	3.2	1.8	2.4	3.1
		.6	.8	1.2	1.8	2.3	3.0	2.0	2.5	3.0	2.6	3.0	3.8
		.8	1.3	1.8	1.8	2.8	2.6	4.0	4.4	3.5	1.7	-.5	-2.8
Plane →	1.0	6.0	6.0	6.0	6.0	6.0	6.0	6.0	6.0	6.0	6.0	6.0	

TABLE D-1 (Concluded)

	Vertical Distance X/H	Y/H (Lateral Distance)										
		0.0	.6	1.2	1.8	2.4	3.0	3.6	4.2	4.8	5.4	6.0
$\frac{H}{\lambda} = 100$	-2.0	1.0	1.0	1.2	1.4	1.6	1.8	2.0	2.2	2.3	2.4	2.5
	-1.8	.9	.9	1.1	1.3	1.6	1.8	2.0	2.2	2.3	2.4	2.5
	-1.6	.8	.9	1.1	1.3	1.6	1.8	2.0	2.2	2.3	2.5	2.5
	-1.4	.7	.8	1.0	1.3	1.6	1.9	2.1	2.2	2.3	2.5	2.5
	-1.2	.6	.7	1.0	1.3	1.6	1.9	2.1	2.3	2.4	2.5	2.6
	-1.0	.5	.6	.9	1.3	1.6	1.9	2.1	2.3	2.4	2.5	2.6
	-.8	.3	.5	.9	1.3	1.7	2.0	2.2	2.4	2.5	2.6	2.6
	-.6	.2	.4	.9	1.3	1.7	2.0	2.2	2.4	2.5	2.6	2.7
	-.4	.1	.4	.9	1.4	1.8	2.1	2.3	2.5	2.6	2.6	2.7
	-.2	.0	.3	.9	1.5	1.9	2.2	2.4	2.5	2.7	2.7	2.7
Source →	⊕ 0	⊕	.3	1.0	1.6	2.0	2.3	2.5	2.6	2.6	2.7	2.8
	.2	.1	.5	1.2	1.8	2.2	2.4	2.6	2.7	2.8	2.7	2.8
	.4	.3	.7	1.5	2.0	2.3	2.5	2.6	2.7	2.8	2.8	2.9
	.6	.7	1.2	1.9	2.3	2.6	2.7	2.8	2.8	2.9	2.8	2.8
	.8	1.6	1.9	2.4	2.7	2.8	2.8	3.0	3.0	3.0	3.0	3.2
Plane →	1.0	6.0	6.0	6.0	6.0	6.0	6.0	6.0	6.0	6.0	6.0	6.0

TABLE D-2

OCTAVE BAND LEVEL FOR MONOPOLE SOURCE OF WHITE NOISE
AT ELEVATION H ABOVE RIGID PLANE WITH SPACE AVERAGE
OCTAVE BAND LEVEL = 50 dB AT RADIUS = H
($H/\lambda = 100$)

	Vertical Distance X/H	Y/H (Lateral Distance)										
		0.0	.6	1.2	1.8	2.4	3.0	3.6	4.2	4.8	5.4	6.0
	-2.0	44.9	44.6	43.8	42.8	41.7	40.7	39.7	38.8	38.0	37.2	36.5
	-1.8	45.8	45.4	44.4	43.2	42.1	40.9	39.9	39.0	38.1	37.3	36.6
	-1.6	46.7	46.2	45.0	43.7	42.4	41.2	40.1	39.1	38.2	37.4	36.7
	-1.4	47.8	47.1	45.7	44.2	42.7	41.5	40.3	39.3	38.4	37.5	36.8
	-1.2	49.0	48.1	46.4	44.6	43.0	41.7	40.5	39.5	38.5	37.7	36.8
	-1.0	50.5	49.3	47.0	45.0	43.3	41.9	40.7	39.6	38.6	37.7	36.9
	-.8	52.3	50.5	47.7	45.4	43.6	42.1	40.9	39.7	38.7	37.8	37.0
	-.6	54.7	51.9	48.3	45.8	43.9	42.3	41.0	39.8	38.8	37.9	37.1
	-.4	58.1	53.2	48.8	46.1	44.1	42.5	41.1	40.0	38.9	38.0	37.2
	-.2	64.0	54.3	49.2	46.3	44.3	42.6	41.2	40.0	39.0	38.0	37.1
Source →	⊕ 0	⊕	54.8	49.4	46.5	44.4	42.7	41.4	40.1	39.0	38.0	37.2
	.2	64.0	54.4	49.5	46.6	44.5	42.9	41.5	40.2	39.1	38.1	37.2
	.4	58.2	53.6	49.4	46.7	44.6	42.9	41.5	40.2	39.1	38.1	37.3
	.6	55.2	52.6	49.3	46.7	44.7	43.0	41.5	40.3	39.2	38.1	37.2
	.8	53.5	51.9	49.2	46.8	44.7	43.0	41.6	40.4	39.3	38.2	37.6
Plane →	1.0	56.0	54.7	52.1	49.7	47.7	46.0	44.6	43.3	42.2	41.2	40.3

TABLE D-3

LISTING FOR PROGRAM TO COMPUTE GROUND REFLECTION TABLES

```
10 DIMENSION X(50),YY(11),A(11,50),B(11,50),AB(11)
15 STRING F(10)
20 REAL K,MC,LO,NU
25 10 WRITE(1,11)
30 11 FORMAT(3/)
35 12 ACCEPT 'INPUT FILE NAME ',F
40 OPEN(3,F,INPUT,SYMBOLIC,ERR=20)
45 GO TO 30
50 20 DISPLAY 'ERROR IN FILE',F
55 GO TO 12
57 30 READ (3) XL,XH,XD,YL,YH,YD,MC,AL,C4,C5,K,LO,G,ICODE,NU
65 M=(YH-YL)/YD+1
70 N=(XH-XL)/XD+1
75 X(1)=XL
80 PI=3.1415926536
85 DO 40 I=2,N
90 40 X(I)=X(I-1)+XD
95 41 Y=YL-YD
100 DO 1000 I=1,M
105 Y=Y+YD
110 YY(I)=Y
115 DO 100 J=1,N
120 Z=X(J)
125 R=SQRT(Z*Z+Y*Y)
130 IF(R.NE.0.) GO TO 55
135 A(I,J)=-.01
140 B(I,J)=-.01
145 GO TO 100
146 55 ARG=Z/R
147 ARG=ARG*1.E+10
149 ARG=TRUNC(ARG)
149.1 ARG=ARG/(1.E+10)
150 T=(ACOS(ARG)) - G
155 TP=ATAN(Y/(2.-Z))-G
160 CALL DTHETA(K,T,MC,AL,C4,C5,D)
165 IF(D.EQ.0.) D=1.
170 IF(ICODE.EQ.5) GO TO 80
175 CALL DTHETA(K,TP,MC,AL,C4,C5,DP)
180 IF(DP.EQ.0.) DP=1.
185 TM1=SQRT(R*R+4.*(1.-Z))
190 SMALLR=SQRT(DP/D)*(R/TM1)
195 IF(TM1.NE.R) GO TO 60
200 A(I,J)=20.*ALOG10(SMALLR+1.)
205 GO TO 70
210 60 BETA=PI*NU*(TM1-R)/1.4142135624
215 C=SIN(BETA)*COS(3.*BETA)/BETA
220 A(I,J)=10.*ALOG10(1.+SMALLR*SMALLR+2.*SMALLR*C)
225 70 IF(ICODE.EQ.1) GO TO 100
230 80 B(I,J)=L0+10.*ALOG10(D/(R*R))
235 100 CONTINUE
240 1000 CONTINUE
245 GO TO (500,500,500,500,550,550,600) , ICODE
```

TABLE D-3 (Concluded)

```
249 500 L=1
250     CALL XHED(MC,AL,C4,C5,K,G,NU,YY,M,L)
255 DO 200 J=1,N
260 200 WRITE(1,210) X(J),(A(I,J),I=1,M)
265 210 FORMAT(F4.1,11F5.1)
270 GO TO (900,550,600,550) ,ICODE
275 550 CALL XHED(MC,AL,C4,C5,K,G,NU,YY,M,2)
280 DO 300 J=1,N
285 300 WRITE(1,210) X(J),(B(I,J),I=1,M)
290 IF(ICODE.EQ.2.OR.ICODE.EQ.5) GO TO 900
295 600 CALL XHED(MC,AL,C4,C5,K,G,NU,YY,M,3)
300 DO 420 J=1,N
305 DO 410 I=1,M
310 410 AB(I)=A(I,J)+B(I,J)
315 420 WRITE(1,210) X(J),(AB(I),I=1,M)
320 900 READ(3,END=950) NU
321 IF(NU.GE.0.) GO TO 41
322 ICODE=-NU
323 READ(3,END=950) NU
325 GO TO 41
330 950 CLOSE(3)
335 GO TO 10
336 336 FORMAT (1F70.64)
340 END
345 SUBROUTINE XHED(MC,AL,C4,C5,K,G,NU,X,N,M)
350 DIMENSION X(11)
351 REAL MC,K,NU
355 STRING F(12)
360 GO TO (1,2,3) ,M
365 1 F='A-MATRIX'
370 GO TO 4
375 2 F='B-MATRIX'
380 GO TO 4
385 3 F='A+B - MATRIX'
390 4 WRITE(1,5) F
395 5 FORMAT (3/,T31,A12,2/)
400 WRITE(1,10) MC,AL,C4,C5,K,G,NU
410 10 FORMAT(T6,'MC ALPHA C4 C5',7X,'K GAMMA',
6X,'NU',/,T2,5(F6.2,2X),F6.4,F8.2,2/)
411 WRITE(1,20) (X(I),I=1,N)
415 20 FORMAT(T31,'Y/H',/,T2,'X/H',11F5.1)
420 DISPLAY ' '
425 RETURN
430 END
435 SUBROUTINE DTHETA(A,B,CM,AL,C4,C5,D)
440 C=COS(B)
445 TOP=A*(1.+C**4)
450 BOT=(((1.-CM*C)**2)+AL*CM*CM)**2.5
455 BOT=BOT*(1.+C4*EXP(-C5*B))
460 D=TOP/BOT
465 RETURN
470 END
```

Unclassified
Security Classification

DOCUMENT CONTROL DATA - R & D		
<i>(Security classification of title, body of abstract and indexing annotation must be entered when the overall report is classified)</i>		
1. ORIGINATING ACTIVITY (Corporate author) Wyle Laboratories 128 Maryland Street El Segundo, California 90245		2a. REPORT SECURITY CLASSIFICATION Unclassified
		2b. GROUP
3. REPORT TITLE PREDICTION METHODS FOR NEAR FIELD NOISE ENVIRONMENTS OF VTOL AIRCRAFT		
4. DESCRIPTIVE NOTES (Type of report and inclusive dates) Final Report		
5. AUTHOR(S) (First name, middle initial, last name) Louis C. Sutherland David Brown		
6. REPORT DATE May 1972	7a. TOTAL NO. OF PAGES 222	7b. NO. OF REFS 95
8a. CONTRACT OR GRANT NO. AF 33615-69-C-1407	9a. ORIGINATOR'S REPORT NUMBER(S) AFFDL-TR-71-180	
8. PROJECT NO. 1471		
c. Task Nr 147102	9b. OTHER REPORT NO(S) (Any other numbers that may be assigned this report) WR-71-19	
10. DISTRIBUTION STATEMENT Distribution limited to U.S. Government agencies only: test and evaluation; statement applied 24 March 1972. Other requests for this document must be referred to AF Flight Dynamics Laboratory (FY), Wright Patterson AFB, Ohio 45433.		
11. SUPPLEMENTARY NOTES	12. SPONSORING MILITARY ACTIVITY Air Force Flight Dynamics Laboratory Air Force Systems Command Wright-Patterson Air Force Base, Ohio 45433	
13. ABSTRACT This report establishes a consistent set of prediction methods which may be used to estimate near field noise levels for jet powered and rotor/propeller powered VTOL aircraft operating in close proximity to the ground. The methods provided utilize available theory augmented extensively by experimental data which was available or was obtained during the program. The noise prediction methods are presented in Section VI and will allow an analysis of near field environments of VTOL aircraft using a simplified procedure suitable for manual calculations. The experimental effort carried out in the program consisted of noise measurements in the near field of a model propeller (Appendix B) and a subsonic jet in a free and vertical configuration (Appendix C). Ground reflection correction factors for a simple source are tabulated in Appendix D along with the computer program listing. The methods described in this report are intended for use by aircraft designers for the prediction of the near field noise environment of VTOL aircraft as required in MIL A 8893 Airplane Strength and Rigidity, Sonic Fatigue Resistance.		

DD FORM 1 NOV 65 1473

Unclassified

Security Classification

UNCLASSIFIED

Security Classification

14. KEY WORDS	LINK A		LINK B		LINK C	
	ROLE	WT	ROLE	WT	ROLE	WT
Noise Prediction V/STOL Aircraft Jet Noise Propeller Noise						

UNCLASSIFIED

Security Classification